ABSTRACT

Title of Document: ELECTROSPRAY-DIFFERENTIAL MOBILITY ANALYSIS OF BIONANOPARTICLES

Suvajyoti Guha, PhD, 2012

Directed By: Prof. Michael R. Zachariah, Departments of Mechanical Engineering, Chemistry and Biochemistry

The growth of the multibillion dollar bionanoparticle industry has spurred the development of new physical characterization methods. One such method, electrospray-differential mobility analysis (ES-DMA) constitutes an electrospray for aerosolization of bionanoparticles (such as viruses, gold-nanoparticles, proteins, nanoparticle-protein complexes) and an ion mobility method that operates at atmospheric conditions, and separates bionanoparticles spatially. This dissertation identifies some relevant "problem" areas for ES-DMA by reviewing selected applications.

Some such problems are: proteins while passing through ES capillaries are found to interact with it and thus produce time dependent size distributions. Further, it is thought that adsorbed proteins may subsequently desorb and influence size distributions with the ES-DMA which may concomitantly affect quantification of aggregates. These artifacts are studied systematically and it is demonstrated that ES-DMA can quantify adsorption-desorption of complex protein mixtures at high shear rates. Further, it is shown that desorbing proteins do not have a significant effect on size distributions. Another artifact of the ES takes place during the

aersolization process. Two units (called monomers) of a bionanoparticle may get encapsulated in the same ES droplet and upon drying of the droplet create artificial dimers thus affecting quantification with ES-DMA. Assuming Poisson distribution, this thesis provides a systematic approach that can be undertaken to eliminate this artifact. A third artifact arises from the low sensitivity of the DMA to size increase. When a ligand (for e.g. protein) adsorbs to a bionanoparticle it creates an increase in the size of the later, which can be used to quantify the amount of ligand adsorbed per bionanoparticle. As ligands can change conformations upon adsorption, using ES-DMA for such applications may be flawed. This issue has been identified and a solution has been provided by integrating a mass analyzer after the ES-DMA.

After correcting for these artifacts, this dissertation delves into characterization of different types of bionanoparticles and demonstrates that ES-DMA has several advantages over other traditional techniques such as transmission electron microscopy, size exclusion chromatography, analytical ultracentrifugation, dynamic light scattering and plaque assay and thus has immense potential to become a process analytical technique in biomanufacturing environments.

ELECTROSPRAY-DIFFERENTIAL MOBILITY ANALYSIS OF BIONANOPARTICLES

By

Suvajyoti Guha

Dissertation submitted to the Faculty of the Graduate School of the
University of Maryland, College Park, in partial fulfillment
of the requirements for the degree of
Doctor of Philosophy
2012

Advisory Committee:
Professor Michael R. Zachariah, Chair
Professor Gregory Jackson
Associate Professor Kenneth Kiger
Assistant Professor Santiago Solares
Associate Professor Srinivas Raghavan, Dean's representative

Dedication

To my parents Mr. Naresh Chandra Guha and Mrs. Rekha Guha and my wife Saimanti.

Acknowledgements

I would firstly like to thank my advisor Prof. Michael R. Zachariah for giving me the opportunity to work under him and making this such a memorable experience. As a result I will cherish the last four and half years' experiences for the rest of my life. He has played an instrumental role in shaping me up as a researcher as well. Besides, this work would not have been possible without his supervision. I would also like to thank Leonard F. Pease III and De-Hao Tsai to have mentored me in the first few months of the project and Dr. Michael Tarlov for having played a semi-supervisory role and having played an instrumental role in improving the quality of my publications. I am also grateful to Dr. Jackson, Dr. Kiger, Dr. Solares and Dr. Raghavan for having agreed to serve on my committee.

Over the last four and half years I have had some great colleagues. Of many, Leonard, De-Hao, Mingdong, Max, Zhou, Josh, Germarie, Dean and Vinayak deserve special mention. I would also like to thank all my friends for making the "PhD experience" such a pleasurable one. A few of them who have also become very good friends are Rishi, Aftab, Snehaunshu, Purnendu, Sachin, Baidurja, Ishita, Murthy, Rajarshi, Rashmish and Srini. I still remember the first day I arrived in US at around 1'o clock in the morning after a 37 hour long trip, Sachin and Snehaunshu were there to greet me at the airport. When I returned to their place I got to eat food that tasted just the way it is made at my home. That to a person traveling far away from his country for the first time is simply unforgettable. Thank you Sachin and Shenahaunshu for being such amazing roommates! In this regard I would also like to thank Ranjan Mehta and

Prahalad Parthangal for providing some excellent suggestions while I was on the crossroads trying to decide which school to join for pursuing my PhD.

Lastly, I would like to thank my parents without whom I would have never been what I am today. The constant support that I got from my mom in bad times and good is worth mentioning. The strict academic environment at home also played an instrumental role in shaping up my career. Finally, I would like to thank my wife for her unconditional love and support.

Table of Contents

ABSTRACT 1

Dedication ii

Acknowledgements iii

Table of Contents v

List of Figures xii

List of Tables xvii

Acronymns xviii

Chapter 1: INTRODUCTION 1

1.1 Growth trends of the bionanoparticle industry 1

1.2 Necessity of multiple analytical tools 2

1.3 Growth of ES-DMA 5

1.4 Structure and organization of this dissertation 6

Chapter 2: ES-DMA: PRINCIPLES AND OPERATION 7

2.1 Electrospray 7

2.2 Neutralization chamber 11

2.3 Differential Mobility Analysis 15

2.4 Condensation particle counter (CPC) 20

2.5 Data Interpretation 21

2.6 Operating parameters of the ES-DMA 23

2.7 Summary 26

Chapter 3: LITERATURE SURVEY 28

3.1 Viruses and bacteriophages 28

3.2Polymers and proteins 31

3.3 Nanoparticle-biomolecule conjugates 36

3.4 Advantages and limitations of ES-DMA 40

3.4.1 Advantages 40

3.4.2 Limitations 41

3.5 Summary and Motivation 42

Chapter 4: ES ARTIFACTS: ADSORPTION AND DESORPTION OF PROTEINS AND ITS EFFECTS 44

4.1 Monomeric protein adsorption-desorption to ES silica capillaries 44

4.1.1 Introduction 44

4.1.2 Materials and Methods 46

4.1.2.1 Sample preparation 46

4.1.2.2 ES-DMA 47

4.1.2.3Shear rate calculation 48

4.1.3 Proof of Principle Experiment 49

4.1.4 Surface coverage and adsorption kinetics for monomeric and multimeric proteins 51

4.1.5 Concentration and pH dependent adsorption-desorption of RmAb 55

4.1.6 Desorption rate constants 58

4.1.7 Summary 60

4.2 Oligomeric protein adsorption-desorption to ES silica capillaries 61

4.2.1 Introduction 61

4.2.2 Sample preparation 62

4.2.2.1 Protein sample preparation 62

4.2.2.2 Capillary surface preparation and passivation 62

4.2.2.3 ES-DMA 63

4.2.3 Results and Discussion 63

4.2.4 Summary 73

4.3 Influence of protein adsorption-desorption to aggregate distribution 73

4.3.1 Introduction 73

4.3.2 Materials and Methods 76

4.3.3 Results and Discussion 76

4.3.3.1 Adsorption of BSA to passivate capillaries 76

4.3.3.2 Adsorption of Gelatin to passivate capillaries 79

4.3.3.3 Effect of size distribution on passivated, partially passivated and unpassivated capillaries 81

4.3.3.4 Efficacy of gelatin passivation in repelling different protein monomers . 84

4.3.3.5 Stability of gelatin passivation 87

4.3.4 Summary 87

4.4. Protein Adsorption based Characterization: Preliminary results 88

4.4.1 Introduction 88

4.4.2 Materials and Methods 90

4.4.3 Results and Discussion 90

4.4.4 Summary 91

Chapter 5: ES ARTIFACTS: DROPLET INDUCED AGGREGATION 92

5.1 Introduction 92

5.2 Materials and Methods 94

5.2.1 Analytical Ultracentrifugation 94

5.2.2 Sample preparation 95

5.3 Results 95

5.3.1 Intrinsic monomers 97

5.3.2 Intrinsic monomers and dimers 98

5.4 Discussion 102

5.4.1 Limitations 105

5.5 Summary 107

Chapter 6: DMA ARTIFACTS: CONFORMATIONAL CHANGES OF LIGANDS UPON ADSORPTION TO NANOPARTICLES 108

6.1 Introduction 108

6.2 Materials and Methods 112

6.2.1 Sample preparation 112

6.2.2 ES-DMA-APM 113

6.3 Results and Discussion 115

6.4 Summary 120

Chapter 7: APPLICATIONS: VIRUSES 121

7.1 Introduction 121

7.2 Materials and Methods 122

7.2.1 Test article preparation 122

7.2.2 Buffer Preparation 123

7.2.3 Gold nanoparticles Preparation 124

7.2.4 ES-DMA operation and data analysis 124

7.2.5 Gold calibration approach 124

7.2.6 TEM Characterization 125

7.3 Results 126

7.3.1 Specificity 126

7.3.2 Precision, Linearity and Accuracy 128

7.3.3 Detection and Quantitation Limits 132

7.3.4 Range 133

7.3.5 Robustness 134

7.4. Discussion and Summary 135

CHAPTER 8: APPLICATIONS: PROTEINS 139
8.1 Introduction 139
8.2 Sample Preparation 141
8.2.1 Protein Sample Preparation 141
8.2.2 Size Exclusion Chromatography (SEC) 141
8.2.3 ES-DMA 143
8.3 Results and Discussion 144
8.3.1 Size distributions obtained with ES-DMA 144
8.3.2 SEC Chromatograms 148
8.3.3 Comparison of ES-DMA with SEC 149
8.4 Summary 155
CHAPTER 9: APPLICATIONS: NANOPARTICLE-PROTEIN COMPLEXES 156
9.1. Nanoparticle-protein conjugate stability 156
9.1.1 Introduction 156
9.1.2 Materials and Methods 157
9.1.2.1 Sample preparation 157
9.1.2.2 ES-DMA operation 158
9.1.2.3 TEM 159
9.1.2.4 Fluid Imaging 159
9.1.3 Results and Discussion 160

9.1.4 Summary 169

9.2 Glycan Analysis: Preliminary results 169

9.2.1 Introduction 169

9.2.2 Materials and Methods 170

9.2.3 Results and discussion 171

9.2.4 Summary 172

CHAPTER 10: CONCLUSIONS 173

10.1 Intellectual Contributions and Anticipated Benefits 173

10.2 Future Research 177

APPENDIX A: CFD simulations of a modified DMA design 180

A.1. Introduction 180

A.2 Design and Preprocessing 180

A.2.1 GAMBIT 183

A.2.2 FLUENT 184

A.3 Results and Discussion 184

A.4 Summary 187

BIBLIOGRAPHY 188

List of Figures

Figure 1.1: Global growth trends of the nanomaterial and pharmaceutical industry……...2

Figure 1.2: A list of techniques used for determining nanoparticle size…….4

Figure 1.3: (A) Published articles on ES-DMA from 1996 to 2010. (B) Number of citations (including self-citations) from 1996 to 2010…….....6

Figure 2.1: A schematic of the section of the ES that aerosolizes the analytes into the gas phase……8

Figure 2.2: The journey of the ES droplet from the tip of the ES capillary to the orifice plate……11

Figure 2.3: (A) An alpha source, typically Po-210, is used in commercial ES-DMA for neutralizing the charges on the electrospray. (B) The journey of the ES droplet and the analyte inside the neutralization chamber…….….13

Figure 2.4: (A) Size distribution of the sucrose residue size. (B) Size distribution of the ES droplet size for the same sucrose residue size……..15

Figure 2.5: Force balance on a charged analyte inside the DMA…….….17

Figure 2.6: Schematic of the operating principle of the CPC……...…….21

Figure 2.7: Steps for converting the raw data to the actual gas phase distribution……24

Figure 2.8: Actual ES-DMA experimental set up……..26

Figure 2.9: Schematic of the ES-DMA used for obtaining size distribution of bionanoparticles.....27

Figure 3.1: Molecular weight and mobility diameter correlation…….….37

Figure 4.1: Size distributions of 0.001% sucrose (v/v) mixed with 0.01 mg/mL RmAb at pH 7.0 using the ES-DMA as a function of time. 2B shows the integration of the sucrose peak and RmAb peak plotted as a function of time…….…..50

Figure 4.2: (A) Size distributions of RmAb. (B) Size distribution as a function of time. (C) Sum of the monomer and twice the dimer counts as a function of time. (D) Surface coverage as a function for RmAb……..54

Figure 4.3: (A) The total gas phase density of RmAb as a function of time expressed in equivalent capillary volumes at four different concentrations at pH 7.0. (B) Adsorbed and desorbed amounts of RmAb per unit area as a function of concentration……...…..56

Figure 4.4: Adsorbed and desorbed RmAb per unit area as a function of pH at concentration of 0.1 mg/mL……...……58

Figure 4.5: (A) Two simplest possible configurations of dimers attaching to the surface of ES capillary. (B) Projected area occupied by dimers assuming equal probability of both configurations……..……..64

Figure 4.6. (A) Size distributions of monomers and dimers of IgM as a function of capillary volumes for a bare capillary during adsorption. (B) Size distributions of monomers and dimers of IgM as a function of capillary volumes during desorption. (C) Integration of the monomer and dimer peaks obtained from size distributions at each capillary volume as a function of capillary volumes. (D) Coverage of monomer and dimers of IgM at the same conditions as a function of equivalent capillary volume……68

Figure 4.7 (A) Size distributions of monomers and dimers of IgM as a function of capillary volumes on a gelatin coated capillary surface during adsorption. (B) Size distributions of monomers and dimers of IgM as a function of capillary volumes during desorption from the same gelatin coated capillary. (C) Integration of the monomer and dimer peaks obtained from size distributions at each capillary volume as a function of capillary volumes. (D) Coverage of monomer and dimers of IgM at the same conditions as a function of equivalent capillary volume……..…….……..72

Figure 4.8: Approach taken to study the affect of aggregate distribution as a function of surface passivation…….……75

Figure 4.9: (A) Size distributions of monomers, dimers, and traces of trimers (not evident from this figure) of BSA eluting through the capillary as a function of capillary volumes. (B) Size distribution of the desorbing species as a function of capillary volumes when the protein sample is replaced with buffer. (C) Coverage of BSA adsorbed and desorbed as a function of capillary volumes……...…….78

Figure 4.10: (A) Mobility distribution of 0.10 mg/mL gelatin in 20 mmol/L ammonium acetate at pH7. (B) The coverage of gelatin on fused silica as a function of time……..80

Figure 4.11: Dimer to monomer (A) and trimer to monomer ratios (B) of four different proteins on unpassivated, gelatin passivatedand BSA passivated surfaces……..….83

Figure 4.12: Desorption of monomers of IgG (A), RmAb (B), BSA (C) and IgM (D) for the gelatin passivated (solid circle, dotted line) and unpassivated capillaries (open square, solid line) at pH 7.0……..……..86

Figure 4.13: (A) A colloidal solution with heterogenous mixture of Protein X, Y and Z. (B) Random sampling with ES droplet might induce different proteins into the same ES droplet……..……..89

Figure 4.14: (A) Size distribution of 0.1 mg/mL of Am. (B) Size distribution of the same sample during desorption……..……..90

Figure 5.1: (A) Distribution of particles in a colloidal solution (B) Electrospray sampling may create artificially induced dimers or larger aggregates……..93

Figure 5.2: (A) Size distribution of bovine IgM using ES-DMA. (B) Size distribution of bovine IgM using AUC. (C) Size distribution of hIgG using ES-DMA. (D) Size distribution of hIgG using AUC…….....…….96

Figure 5.3: Physical representation of the probability distribution of induced and intrinsic aggregate distributions from electrospray…….….99

Figure 5.4 Size distribution of BSA at 0.1 mg/mL using 2mmol/L ammonium acetate.106

Figure 6.1: Mobility increase does not take into account changes in conformation changes of protein upon adsorption to a nanoparticle…….…...110

Figure 6.2: The different steps involved that eventually provides the number of ligands adsorbed/nanoparticle using a DMA-APM system…….114

Figure 6.3: Coverages of BSA on 30 nm AuNP as a function of concentration obtained with DMA-APM (square-black), on planar Au surface obtained with QCM-D (diamond-red), using VB approach (circle-purple) and AB approach (triangle-green)…..…….116

Figure 6.4: Figure 6.4: (A) RmAb adsorbed to on negatively charged 60 nm PSL (NIST SRM 1964) quantified with DMA-APM (square, black) and comparisons with literature: IgG 2B (mouse IgG type 1) (triangle, green), IgG 7B (mouse IgG type 1) (circle, purple) and Mab-1 (asterisk, blue) and RmAb on Silica (diamond, red). (B) Coverage of RmAb at different pH values obtained using DMA-APM (square-black), and predictions based on VB (circle-purple) and AB approach (triangle-green)…….……...119

Figure 7.1: (A) ES-DMA size distributions for PR772 and TEM images of PR772 (B) untreated and heated for 30 minutes to (C) 60^{o}C and (D) 70^{o}C. (E) ES-DMA size distributions for PP7 and TEM images of PP7 (F) untreated and (G) heated for 30 minutes to 60^{o}C……....128

Figure 7.2: ES-DMA aerosol number density, N, versus solution concentration, C, for PP7 and PR772……130

Figure 8.1: The concentration and size landscape of the most popular characterization tools namely size exclusion chromatography (SEC), analytical ultra-centrifuge (AUC) and field-flow fractionation (FFF)……...…140

Figure 8.2: (A) Size distribution of RmAb for increasing incubation times at 70 ^{o}C. The inset shows a magnification of different aggregates as a function of incubation time. B) Size distribution of IgG prepared at different incubation times at 70 ^{o}C……146

Figure 8.3: (A) Percentages of the trimers, tetramers and pentamers of RmAb and (B) IgG as a function of incubation time as obtained by the ES-DMA…….……147

Figure 8.4: **(**A) Chromatograms of RmAb obtained with the SEC for heat treated samples at increasing incubation times at 70 ^{o}C. The inset shows a magnification of the aggregate region (B) Chromatograms of hIgG obtained with the SEC for heat treated samples at different incubation times at 70 ^{o}C…….…….148

Figure 8.5: (A) Normalized monomer counts for RmAb as a function of incubation time at 70 ^{o}C obtained with SEC and ES-DMA (after correcting for "droplet induced aggregation"). (B) Normalized monomer counts for hIgG as a function of incubation time 70 ^{o}C obtained with SEC and ES-DMA (after correcting for "droplet induced aggregation")……....152

Figure 9.1: Demonstrates the steps involved in preparation of AuNP-IgG sample. Step b and e will be refered to as 0× Au NP-IgG and 1× Au NP-IgG samples respectively. After Step e, c to e are repeated to prepare 2× Au NP-IgG and 3× Au NP-IgG samples……...…..158

Figure 9.2: (A) The hydrodynamic diameter of AuNP (not centrifuged) and AuNP-IgG samples as a function of centrifugation. (B) ES-DMA size distributions of the same samples. (C) The total gas phase counts (primary Y-axis) of monomers, dimers and trimers and mobility diameter (secondary Y-axis) as a function of centrifugation……..….163

Figure 9.3: TEM images of (A) AuNP-IgG 0X, the black dots represet the individual AuNP-IgG conjugates, the dark grey color patches are from citrate, and the light grey color is from the carbon background of TEM grids, (B) AuNP-IgG 1X, (C) AuNP-IgG 3X, (D) zoom up AuNP-IgG 0X (also showing patches of dark grey citrate background along with light gray carbon background) and (E) zoom up AuNP-IgG 1X…….165

Figure 9.4: (A) Simplified schematic of the internal constituents of a FLOWCAM. (B) Photographs of different conjugate aggregates for AuNP-IgG 3X sample. (C) Size distribution of centrifuged samples and of the control AuNP. (D) The integration of size distributions obtained with FLOWCAM for the AuNP-IgG conjugate and IgG samples as a function of centrifugation……..……166

Figure 9.5: Schematics of a lectin based assay for identifying glycans……..…….170

Figure 9.6: Size distributions of Au, Au-RnaseB and Au-RnaseB-ConA……...172

Figure 10.1: List of most important bionanoparticles characterized from Jan, 2008 to Feb, 2012…….…….177

Figure A1: The original DMA design……..181

Figure A2: Increase in Reynolds number with decrease in spacing between inner and outer electrodes……182

Figure A3: The modified DMA design……183

Figure A4: Computational domain and boundary conditions……..184

Figure A5: (A) Velocity contours and (B) velocity vectors in the computational domain. Magnitude of axial (C) and radial velocities (D) at 8 different sections…….186

.

List of Tables

Table 3.1 Summary of reported virus identities and mobility sizes……..29

Table 3.2 List of bionanoparticles and conjugates and the differences in results depending on equations used……...39

Table 4.1 Desorption rate constants at different concentrations and pH……...59

Table 4.2 Comparison of efficacy of gelatin passivation for each protein……85

Table 7.1 ES-DMA as compared to plaque assay……131

Table 7.2 Repeatability, intermediate precision and capillary variation statistics for ES-DMA……132

Table 8.1 Dimer/Monomer ratio for ES-DMA before and after correcting for "droplet induced aggregates" and SEC at different incubation times at 70 ^{0}C……..152

Table 8.2 Rate constants and R^2 values obtained for RmAb and IgG using ES-DMA and SEC by fitting different reaction orders……...……155

Acronymns

ES-DMA – Electrospray-differential mobility analysis
SEC – Size exclusion chromatography
AUC – Analytical ultracentrifugations
DLS – Dyanmic light scattering
TEM – Transmission electron microscopy
FFF – Fluid flow fractionation
UV-vis – Ultraviolet-visible spectrometry
SEM – Scanning electron microscopy
AFM – Atomic force microscopy
CC – Coulter counter
LO – Light obscuration
LD – Laser diffraction
XRD – X-Ray Diffraction
MS – Mass spectrometry
LC-MS – Liquid chromatography-mass spectrometry
AuNP – gold nanoparticle
IgG - Immunoglobulin
RmAb – Rituxan
hIgG – polyclonal human IgG
pAb – polyclonal IgG
mAb – monoclonal IgG
Strp – Streptavidin
QD – Quantum dot
BSA – Bovine serum albumin
IgM – Immunoglobulin M

Chapter 1: INTRODUCTION

1.1 Growth trends of the bionanoparticle industry

The nanoparticle industry is growing at a steady rate as evident from Figure 1.1 (primary Y-axis) below [1]. Curiously, the biopharmaceutical industry, a giant by its own right (Figure 1.1, secondary Y-axis), although presumably unrelated to the nanoparticle industry is also showing a steady growth [2]. As the barriers between conventional fields of science and engineering break down it becomes difficult to segregate these two areas. For example, the most important products of the biopharma industry are different drugs, such as proteins. These proteins themselves are roughly several nanometers in size and thus strictly speaking are nanoparticles or nanomaterials. In this dissertation the pharma and nanomaterial industry together will be considered as the bionanoparticle industry. In this context, bionanoparticles are being defined as nano-sized particles that are either biologically or synthetically-derived (examples, viruses and proteins) or are functionalized to integrate into a biological context (example, nanoparticle-protein complexes). Although such a definition should include non-functionalized (also referred to as unconjugated) inorganic nanoparticles such as gold, silver, etc, this dissertation avoids the discussion of such particles. Also, the words particles, nanoparticles and bionanoparticles are going to be used interchangeably throughout this dissertation.

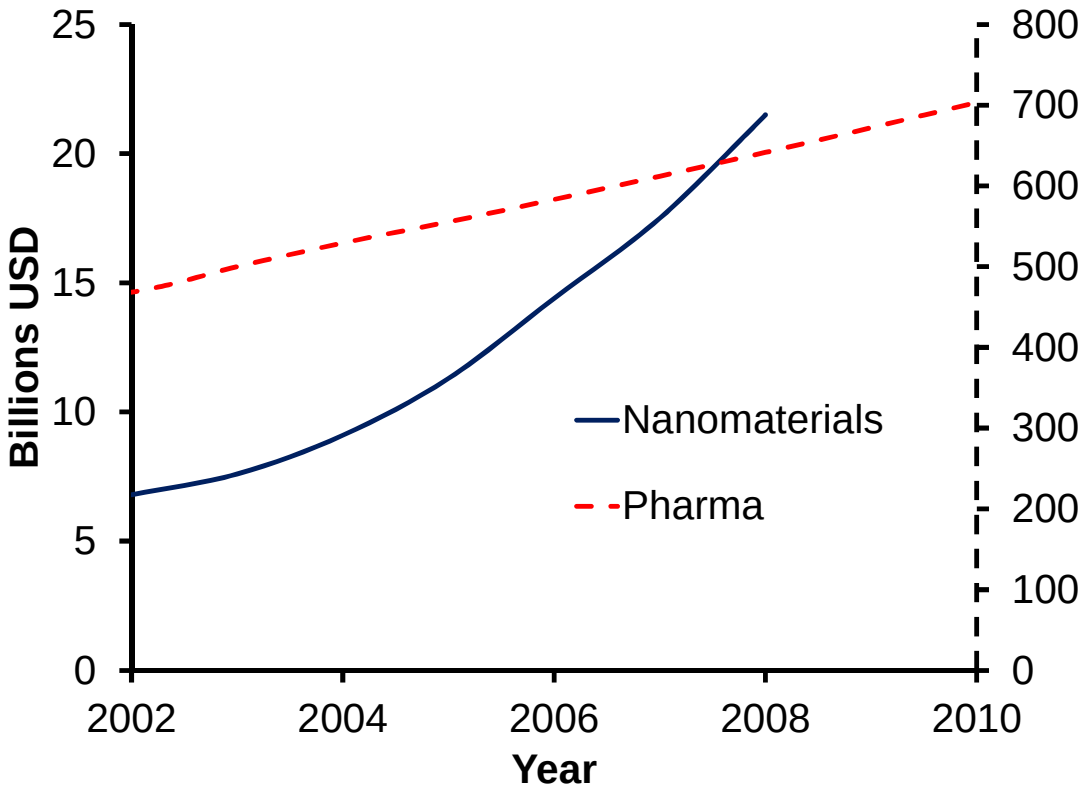

Figure 1.1: Global growth trends of the nanomaterial and pharmaceutical industry.

Given the growth potential of the bionanoparticle industry, it is imperative that it would be perhaps the most sought after and researched area for decades to come. The growth of this industry also has spurred the development of several analytical tools that can characterize bionanoparticles. This is because analytical tools act as the "eyes" necessary for efficient development and production of bionanoparticles.

1.2 Necessity of multiple analytical tools

Broadly speaking, bionanoparticle characterization can be either physical or chemical. Of the different physical properties of interest, particle size is perhaps of foremost importance. The need for better characterization of bionanoparticles in the last decade has either seen a resurgence of old techniques modified for addressing the nano-size regime or the development of completely new techniques. It is beyond the scope of this dissertation to make a comprehensive list of all such techniques. Thus

only a few of the most routinely used tools are shown in Figure 1.2. Most of these techniques provide a relative measure of size such as electrophoresis, size exclusion chromatography (SEC), analytical ultracentrifugation (AUC), Coulter counter (CC), laser diffraction (LD) etc. Some, such as transmission electron microscopy (TEM) and scanning electron microscopy (SEM) on the other hand can provide a direct measure of size and more importantly provide visual images. Although each technique has its own pros and cons almost all techniques have some or many operational disadvantages. For example, SEC is the workhorse of the pharmaceutical industry for protein characterization [3] but does not provide a direct measure of size. Inside a SEC a heterogeneous mixture of protein is passed through a column and as the extent of interaction for different proteins with the column is different, hence they elute at different times. Usually, the smaller species elute fastest and the bigger ones elute later, thus providing a measure of the different types of proteins in solution. Another cheap-easy-to-use popular technique, dynamic light scattering (DLS) is regularly used by the nanomaterial industry for obtaining the hydrodynamic size of nanoparticles and correlates it with the hydrodynamic diameter of the particle. Although it is accurate for monodispersed systems, for a polydispersed system size distributions are skewed towards larger sizes because of the strong dependence of the scattered light on size [4]. Alhough TEM provides high resolution images, it is expensive, relatively slow, and artifacts can be introduced from electron beam damage, sample preparation, and biases in particle selection for quantitative analysis. Some more discussion about the disadvantages of other analytical techniques is also discussed briefly in chapter 3. It is evident that one analytical tool cannot give all the answers and thus there is a need for characterization of bionanoparticles using multiple techniques [3, 5].

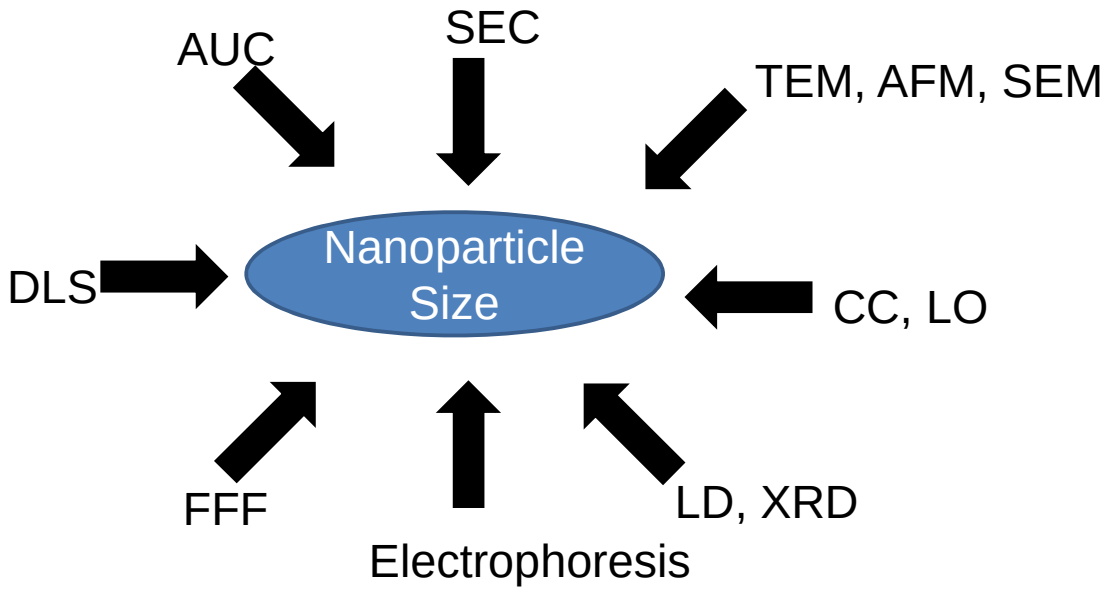

Figure 1.2: A list of techniques used for determining nanoparticle size.

Perhaps driven by the necessity to develop new techniques to characterize bionanoparticles, Stanley Kaufman, a scientist at TSI Inc., attempted to put together electrosprays (ESs) with a special type of ion mobility spectrometers called differential mobility analyzer (DMA) in the 1990s. In this regard, ESs were used in 1960s and 1970s for applications involving surface coatings, agricultural treatments, emulsions and as colloid micro-thrusters [6]. In the 1980s it was discovered that ES could also be used for aerosolizing bio-macromolecules allowing their analysis with mass spectrometers (MS) [7]. On the other hand, DMA is just one of the several ion mobility techniques and its conceptualization can be traced to the late 19^{th} – early 20^{th} century [8]. In general, all ion mobility techniques measure how fast an ion moves in a viscous medium under the influence of an electrical field, and depending on the design can probe particle sizes from sub-nanometer to several hundred micrometers. The predecessor of present day DMA was developed in 1957 to investigate charging of small particles. This DMA, further modified in 1970s, was subsequently

commercialized [8]. Although, exploratory experiments were underway even in 1994 [9], Kaufman *et al*. published a seminal paper integrating the ES and DMA in 1996, when he used this technique to determine the size of globular proteins [10]. Subsequently, researchers have used ES-DMA to characterize other bionanoparticles including polymers, viruses, bacteriophages, nanoparticles-bionanoparticle and bionanoparticle-bionanoparticle conjugates, leading to an exponential increase in the number of publications reporting the use of ES-DMA. A detailed review of the bionanoparticles characterized using ES-DMA will appear in Chapter 3.

1.3 Growth of ES-DMA

Although relatively new, ES-DMA is showing an increasing growth mainly for research purposes as evident from Figure 1.3 below. These plots have been generated using the key words “Electrospray” and “Differential Mobility analysis” in Web of Knowledge (version 5.3). As mentioned in the previous section, the first reported application of ES-DMA to biological molecules was by Kaufman et al in 1996 for characterizing proteins. This work was followed over the next decade by several reports from Allmaier *et al* [11], Wick *et al.* [12] and de la Mora *et al*. [13] related to characterization of several other proteins, viruses and polymers. Starting in 2006 as seen in Figures 1.3A and 1.3B a dramatic increase in the number of publications and citations related to ES-DMA occurred with contributions from Biswas *et al.* [14], Zachariah *et al.* [15], Loo *et al* [16], Hogan *et al* [17], Pergantis *et al* [18], Pease *et al* [19] and Hackley *et al* [20].

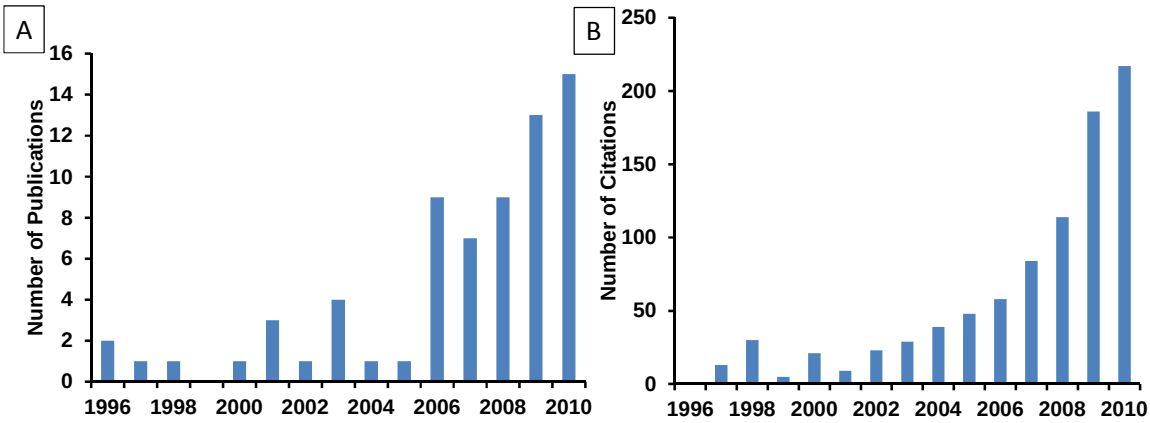

Figure 1.3: (A) Published articles on ES-DMA from 1996 to 2010. (B) Number of citations (including self-citations) from 1996 to 2010.

Although developed primarily for size determination, with an increasing pool of users, several orthogonal utilities have been found for this technique a detailed discussion of which will be appear later in Chapter 3.

1.4 Structure and organization of this dissertation

Having introduced the necessity of ES-DMA in this chapter its different components will be reviewed in the next chapter (chapter 2). In chapter 3, a comprehensive literature survey of applications of ES-DMA (in the context of bionanoparticles) is going to be performed. Based on this survey it will become evident that this technique has certain artifacts and issues. Chapter 4, 5 and 6 will delve into these artifacts and try to eliminate and/or understand them. Subsequently, in chapter 7, 8 and 9 several applications of the ES-DMA are going to be discussed after accounting for the above mentioned artifacts. Chapter 10 will conclude by identifying the areas where further research can be carried out. It should be pointed out that non-spherical bionanoparticles with high values of length to diameter ratios are beyond the scope of this dissertation the reasons for which will become evident later.

Chapter 2: ES-DMA: PRINCIPLES AND OPERATION

The ES-DMA constitutes of four components: the ES for aerosolization of particles, the neutralizer for charge reduction, the DMA for size selection and finally a condensation particle counter (CPC) for counting the size selected particles.

2.1 Electrospray

The first unit of ES-DMA is the electrospray. Usually the analyte solution is housed inside a chamber under pressure (Figure 2.1), which enables the analyte solution to be pushed through a silica capillary. For reliable and stable operation of the ES the solution needs to be conductive. The flow inside the ES capillary can be changed by changing the pressure drop ($\Delta p_{capillary}$) that can be manually controlled externally and is given by the equation below:

$$\Delta p_{capillary} = \frac{128 \mu_{liquid} L_{capillary} Q_{capillary}}{\pi D_{capillary}^4} \tag{2.1}$$

Here μ_{liquid} is the viscosity of the solution passing through the liquid, $L_{capillary}$, $Q_{capillary}$ and $D_{capillary}$ are the lengths, flow rates and inner diameters of the capillary respectively. For simplicity, it is going to be assumed that the viscosity of the buffer used in ES is equal to water. The conductive solution disassociates to form positive and negative ions. As ammonium acetate is used as the solution in this dissertation the respective positive and negative ions formed are ammonium ions and acetate ions. When a positive voltage is applied with a Platinum wire, the positively charged ions migrate away from the wire. The voltage is then manually modified to create a Taylor cone [21, 22] at the tip of the ES capillary. At the tip Columbic repulsion forces the liquid out to form multiple charged droplets. The governing equations for the droplet generation are slightly complex and beyond the scope of this dissertation.

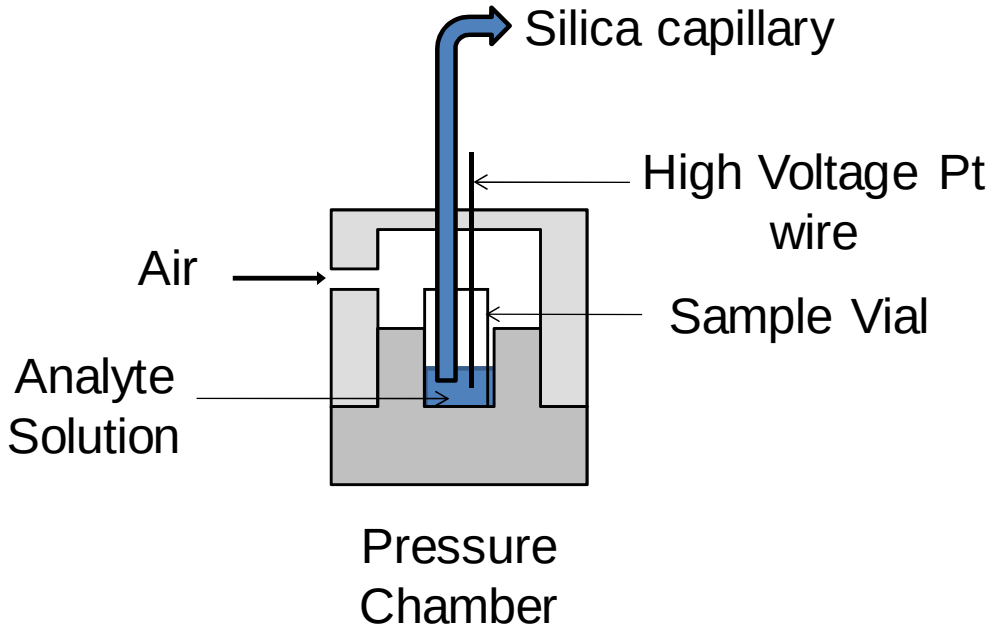

Figure 2.1: A schematic of the section of the ES that aerosolizes the analytes into the gas phase.

After an ES droplet is emitted from the ES silica capillary tip, it holds a charge that is 0.4 – 0.5 times the Rayleigh limit and thus does not disintegrate immediately [23]. The maximum amount of charge q_{max} that an ES droplet of volume R can hold is given by:

$$q_{\max} = 8\pi(\gamma\varepsilon_o R^3)^{\frac{1}{2}} \qquad (2.2)$$

where γ is the surface tension of the solvent and $\varepsilon_o = 8.854\times10^{-12}$ C^2/Nm^2 is the permittivity of free space. Although for cone stability ammonium acetate is added in small proportions with water for ES operations, for simplicity, let it be assumed that the properties of the resultant solution are same as that of pure water and thus $\gamma = 7.28\times10^{-2}$ N/m.

Typically the droplet size at the moment of formation under the operating conditions of the ES used here is 150 nm. A detailed discussion about the operating conditions that produces this droplet size is provided later in section 2.6. The ES droplet moves away from the capillary towards the orifice plate as shown in Figure 2.2 because of the electric field as well as a source of air (and or CO_2). The later also aids in the evaporation of the ES droplet. Further based on force balance on an ES droplet of mass m_R (= $4/3\pi\rho R^3$where ρ is the density of water and is equal to 1000 kg/m^3) one could write:

$$m_R a = F_E + F_D \tag{2.3}$$

Here F_E = qE where $q=0.5q_{max}=2\times10^{-16}$ C and E=V/h where h is the distance from the ES capillary tip to the orifice plate and F_D is the drag force. This is a simplistic assumption as the electrical field, denoted by the blue bold line in Figure 2.2 would vary in the direction perpendicular to the direction of the movement of the ES droplet. Further assuming the equation of drag force to follow Stokes Law [24] for such small objects, one can write, $F_D = 6\pi\mu_{air} vR$. Here v is the velocity of the ES droplet and μ_{air} is the viscosity of air. The voltage V is assumed to be 2 kV and is reasonable as the ES is operated between 1.5 kV to 3 kV. Thus combining the expressions above one could write:

$$\frac{dv}{dt} = \frac{3qV}{4\pi\rho_{water} R^3 h} - \frac{9\mu_{air} v}{2R^2 \rho_{water}} \tag{2.4}$$

For simplicity assuming that the acceleration on the ES droplet is equal to zero and the ES radius is not changing as a function of time the velocity of the ES droplet can be determined to be ~ 16 m/s from equation 2.4 above. Given that the distance where the neutralization chamber begins and the ES tip is located is ~ 1 mm, it takes a ES droplet to traverse this distance in ~ 62 μs.

On the other hand, the time taken for the ES droplet to evaporate to the size such that it reaches the Rayleigh limit can also be independently ascertained. Considering solvent evaporation it can be shown that the time taken to reach a droplet size R_2 is given by the equation below [25],

$$R_2 = R - \frac{\alpha' v' p^o M}{4\rho R_g T} t \tag{2.5}$$

Where α´ is assumed to be ~ 0.04 and is a measure of condensation and is assumed to be almost equal to water, v´ is the thermal velocity and is assumed to be 4.5×10^2 m/s, p^o is the partial vapor pressure = 2.3 kPa at T = 293 K, M = 0.018 kg/mol and R_g= 8.314 J/mol/K.

The ES droplet would continue to evaporate till the Rayleigh limit is reached at which point it will disintegrate into smaller droplets. Thus,

$$8\pi(\gamma\varepsilon_o R_2^{\,3})^{\frac{1}{2}} = 0.5\times 8\pi(\gamma\varepsilon_o R^3)^{\frac{1}{2}} \tag{2.6}$$

Thus for a 150 nm ES droplet, $2R_2$ = ~ 95 nm. Now substituting this value of R_2 in equation 2.5 above, one will get t = 362 µs. As it takes 62 µs for an ES to reach the orifice plate, it implies that a droplet will reach the orifice plate and enter the neutralization chamber much before it starts to disintegrate by Columbic repulsion. In this regard, the 150 nm droplet becomes ~ 140 nm droplet in 62 µs (obtained by replacing 62 µs in equation 2.5).

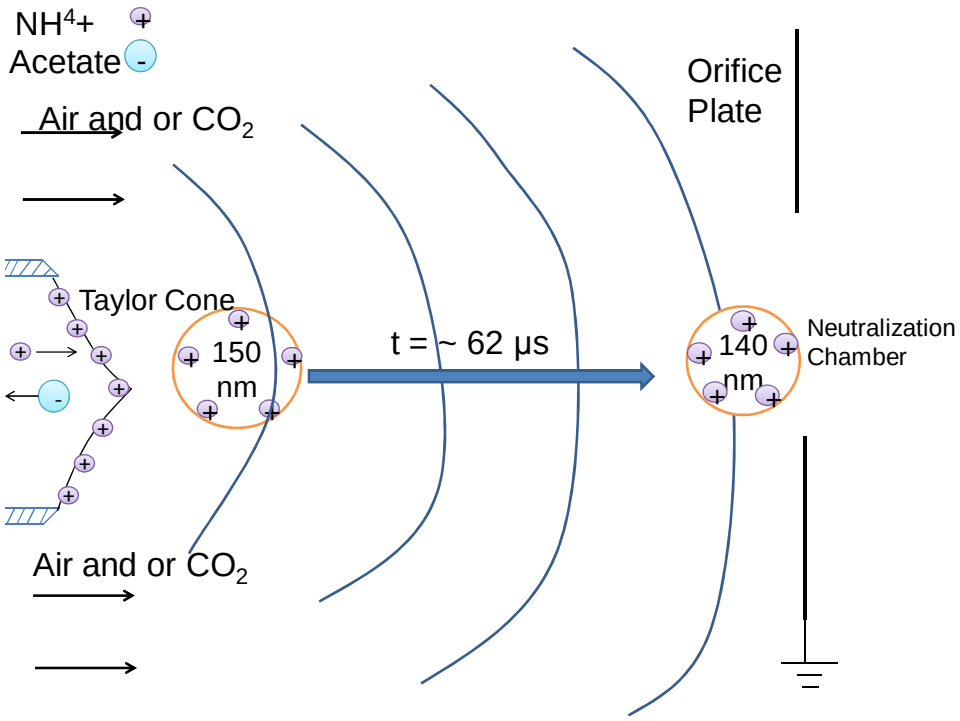

Figure 2.2: The journey of the ES droplet from the tip of the ES capillary to the orifice plate.

This analysis has a very important consequence. It implies that from the time of formation of the ES droplet to the time it reaches the neutralizer, the nanoparticle residing inside the ES droplet will stay intact and unperturbed by the electro-hydrodynamic forces. In the context of this discussion certain operational parameters of the ES are discussed for clarity. A more detailed discussion about the ES operational conditions is further provided in section 2.6 and a detailed descriptions of the mechanism of how ES droplets evaporate and charge is transferred to the analyte are provided elsewhere [23, 26].

2.2 Neutralization chamber

The neutralizer is the second component of the ES-DMA and is the primary way of charging the analytes in ES-DMA unlike mass spectrometry (MS) [23, 26]. Inside the neutralization chamber there is an ionizing source that continuously ionizes

the the N_2, $O_2$and CO_2 to create a bipolar atmosphere of ions as shown in Figure 2.3(A). The alpha particles at first collide with the individual gas molecules to generate positive ions. The electrons emitted from these positive ions then may generate negative ions thus creating a bipolar atmosphere. These ions themselves can collide with each other and create more ions or may agglomerate presumably by electrostatic interactions and form very large ions too. As the 140 nm electrospray droplet passes through, these ions collide with the ES droplet to reduce the charge on the droplets. Thus, the ES droplets can no longer disintegrate by Columbic repulsion.

Given the flow rate of the air that drives the ES droplets and the neutralizer volume, it takes about a few seconds for the ES droplet to transit through the neutralizer and thus the droplet continues to evaporate. If it is assumed that there is an analyte inside that itself has a diameter of 10 nm, then the minimum R_2 is > 5 nm. Using, this value in equation 2.5 above, it takes about ~ 1 ms for the ES droplet to completely evaporate. As the transition time through the neutralizer for the droplet volume is much more, thus one can assume that the ES droplet completely evaporates before exiting the neutralizer. It should be pointed out though that some nanoparticles may have more affinity towards water and because equation 2.5 above does not take into account the interaction of the nanoparticle inside the ES droplet with the solvent thus it may be possible that some water may still stay bound to the nanoparticle before it reaches the DMA.

Figure 2.3B shows a few of the several possible ways a nanoparticle can end up acquiring a neutral, +2, +1 or -1 charge. In context of this dissertation, the ES-DMA's resolution is significantly less compared to a MS and it cannot differentiate between the different charges. Say for example, an analyte acquires a +1 charge either through a N_2^+ ion or through a NH_4^+-$O2^-$-$N2^+$,all the DMA "sees" is a particle which

is charged with +1 charge .Further, as ammonium acetate-water as a solvent is not very common amongst the ES-MS users, it is not clear what is the most prevalent chemical composition of the charges. However, extensive studies have been conducted on the fraction of charges (irrespective of the chemical nature) [24, 27] generated by such a diffusion mechanism and thus one can collect either the positive or negatively charged particles using a technique discussed in the next section to calculate back the actual gas phase concentrations of the particles.

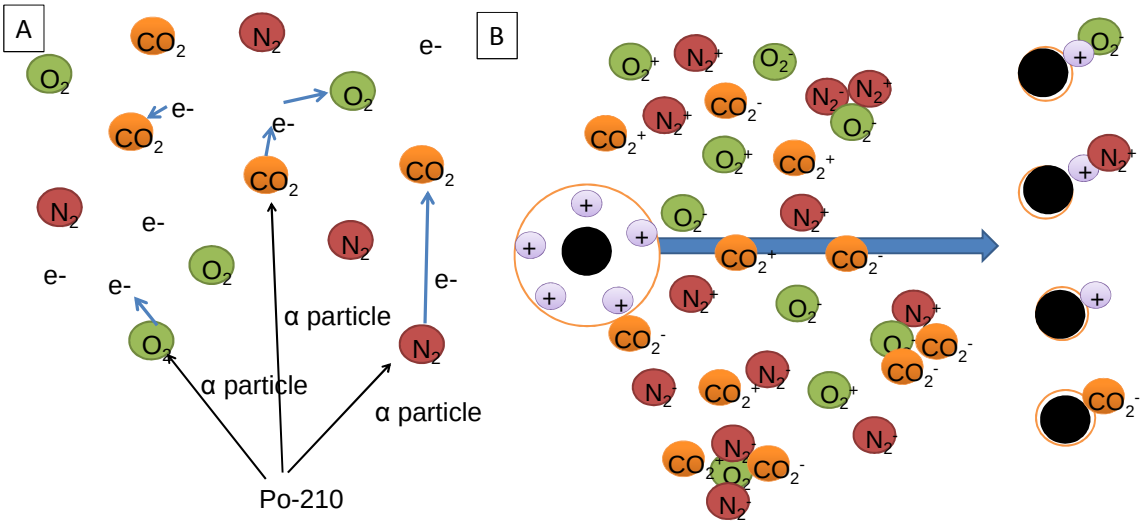

Figure 2.3: (A) An alpha source, typically Po-210, is used in commercial ES-DMA for neutralizing the charges on the electrospray. (B) The journey of the ES droplet and the analyte inside the neutralization chamber.

Combining the neutralizer with the ES opens up a really interesting avenue for ES units that are usually not applicable to ES-MS systems. Although it is usually believed that an ES does not break up non-covalent bonds, it is possible that as the droplets disintegrate by Columbic repulsion once the Rayleigh's limit is reached during evaporation, the stresses on the non-covalent nanoparticle systems residing inside a ES droplet could be significant (consider a dimer or trimer of protein getting

disintegrated by stresses generated during disintegration of the ES droplet). As the ES droplet is not allowed to disintegrate by Columbic forces in a ES-neutralizer system, such a unit can potentially sample intrinsic aggregate populations of different nanoparticles more accurately which will become evident in chapters 5 and 8.

The combination of the ES-neutralizer also allows one to measure and monitor the ES droplet size. As the ES droplet does not disintegrate, it implies that if known concentration of a non-volatile salt is ESed and if the droplet residue size ($D_{residue}$) can somehow be measured then the ES droplet size can be extracted from it. Assuming $C_{sucrose}$ is a known concentration of sucrose being ESed through such a system and the droplet upon complete or near complete evaporation can be measured then:

$$(2R) = \frac{1}{C_{sucrose}^{\frac{1}{3}}} D_{residue} \tag{2.7}$$

Further, it has been experimentally observed that the residue particle size is strongly correlated with the capillary flow rate [28]:

$$D_{residue} \sim Q_{capillary}^{\frac{1}{3}} \tag{2.8}$$

Further as the pressure drop through the capillary is correlated with the capillary flow rate (equation 2.1), thus, changing the pressure drop in the ES can enable one to change the ES droplet volume. The consequence of this demonstration will be illustrated later in chapter 5 and 8.

Figure 2.4A shows the residue size of sucrose at two different capillary pressure drops of 3 PSI and 3.7 PSI using 0.67 % volume/volume sucrose concentration. Figure 2.4B shows the corresponding ES droplet sizes determined using equation 2.7. The sucrose residue size as shown above can be most conveniently measured using a differential mobility analyzer which is discussed in the next section.

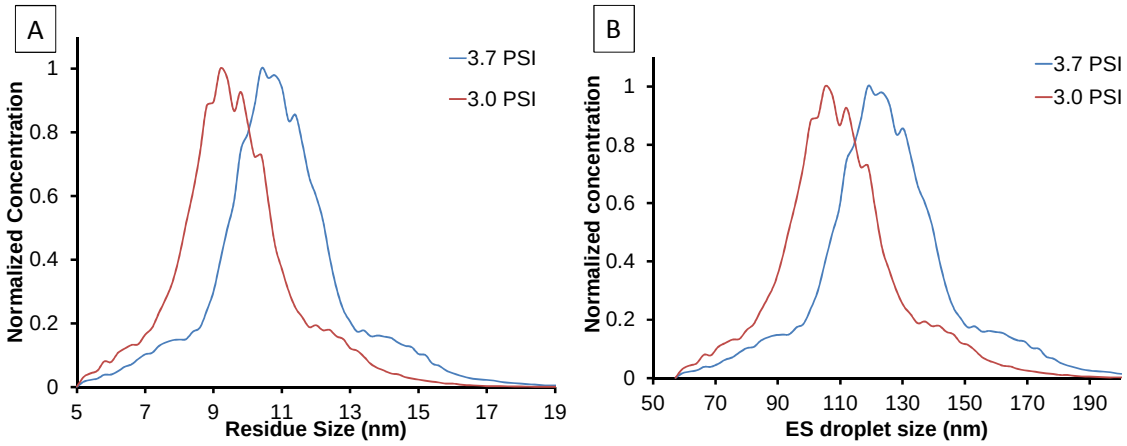

Figure 2.4: (A) Size distribution of the sucrose residue size. (B) Size distribution of the ES droplet size for the same sucrose residue size.

2.3 Differential Mobility Analysis

The DMA which is a mobility analyzer is the third component of the ES-DMA system. There are many types of analyzers for mobility classification, which fall broadly into two classes; time-of-flight and differential mobility. While the former separates particles temporally, the later separates particles spatially. There are other available varieties of mobility classifiers such as, drift tube – ion mobility, high field asymmetric ion mobility, and travelling voltage wave ion mobility, but these techniques are beyond the scope of this dissertation. For a brief overview of these techniques the reader can refer elsewhere [27].

Irrespective of the type of classifier the mobility velocity (v) of a charged particle is proportional to the electrical field (E):

$$v = ZE \tag{2.9}$$

where Z is the proportionality constant and is called the electrical mobility [27]. This equation is valid for low electric fields as at higher field strengths charged particles may exhibit preferential orientations and thus electrical mobility may not remain constant [21]. This is especially true for non-spherical particles (especially particles

with large values of length to diameter ratios) and as pointed out in chapter 1, these particles won't be dealt with in this dissertation.

Within the class of DMA's, the cylindrical configuration is the most widespread, primarily because its electrodes can be manufactured with exacting spatial specifications, and thus, electric fields are highly uniform and precisely controlled. The cylindrical DMA consists of two electrodes, one that is held at a high voltage (usually the inner electrode), and another that is grounded (usually the outer cylinder) as shown in Figure 2.5.

Once the analyte enters the DMA, it almost immediately "relaxes" under the new conditions of forces. The expression for the "relaxation time" of a particle is given by [24]:

$$\tau = \frac{neC_c V}{3\pi\mu_{medium} D_{analyte} h} \tag{2.10}$$

Where, $D_{analyte}$ is the analyte diameters, μ_{medium} is the viscosity of the medium and C_c is the Cunningham slip factor that takes into account the variation in the experimentally determined values of drag force in the different flow domains (free molecular flow, transition flow and continuum flow). The expression for C_c is provided later. Further, V is the voltage applied to an electrode and the h is the spacing inbetween the two electrodes (assuming rectangular electrode configuration for simplicity). Assuming different values of V and $D_{analyte}$ it can be shown that the residence time of an analyte inside the DMA is significantly greater (typically few seconds) than the relaxation time (< 1 sec).

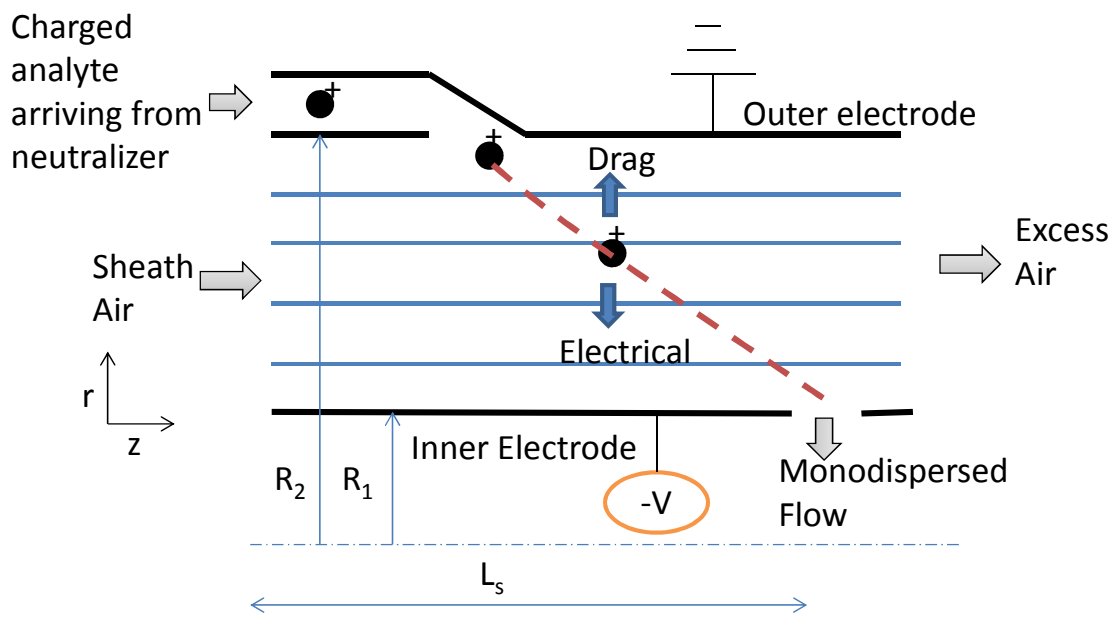

Figure 2.5: Force balance on a charged analyte inside the DMA.

If a negative voltage is applied to the inner electrode as shown in Figure 2.5, a positively charged analyte upon entering the DMA will get attracted towards the inner electrode. As a result a drag force also acts on the analyte in the direction opposite to its motion. The neutral and negatively charged particles are lost to the electrodes by diffusion. The governing equation can then be written as:

$$m_{analyte}\frac{dv_r}{dt} = F_E - F_D \tag{2.11}$$

Where $m_{analyte}$ is the mass of the analyte, v_r is the velocity of the analyte in the r-direction and F_D and F_E are the drag and electrical forces respectively. As the particle is non-accelerating, thus $dv_r/dt = 0$ and hence:

$$F_E = F_D \tag{2.12}$$

The equation for electrical force would be same as presented for ES droplet i.e:

$$F_E = qE \tag{2.13}$$

Here q=ne, where n is the number of charges and e is the charge of 1 electron. In this dissertation, most bionanoparticles dealt with will be singly charged. Note that the

electric field here is inside the DMA and should not be confused with the electric field inside the ES. The expression of drag force is slightly complicated. It is developed by modifying Stokes' Law for very small particles and is given by:

$$F_D = \frac{3\pi\mu_{air} D_{analyte} v_r}{C_c(D_{analyte})} \tag{2.14}$$

Cunningham slip correction factor is dependent on the particle size and is given by $C_c = 1 + \frac{\lambda}{D_{analyte}}[2.34 + 1.05\exp(-0.39\frac{D_{analyte}}{\lambda})]$. Here λ is the mean free path of the medium used. For air, this is ~ 66 nm at standard temperature and pressure. Although strictly speaking, a similar correction should have been employed for the ES droplets in section 2.1, usually C_c becomes constant and ~ 1 for large particles and hence it was not intentionally used in the analysis. In this regard, as discussed before in the context of ES droplets, Stokes Law is used here as the Reynolds number of aerosols is typically less than 1.

Combining equations 2.9, 2.12, 2.13 and 2.14 the electrical mobility is defined by:

$$Z = \frac{qC_c(D_{analyte})}{3\pi\mu_{air} D_{analyte}} \tag{2.15}$$

The variation of this slip factor as a function of particle diameter is well established [20]. For particles smaller than the mean free path of gas (~ 66 nm at 293 K and 100 kPa) it is inversely proportional to $D_{analyte}$, and for larger particles it decreases linearly with increasing particle diameter. Thus, for very small particles (say 10 nm or 20 nm), DMA separates particles based on the difference of projected area, while for larger particles (say 100 nm or above) it separates based on the difference of diameter.

As shown in Figure 2.5, a laminar sheath flow (Q_{sh}) also enters the DMA. The spatial resolution of analyte is achieved by using the sheath flow in the z-direction.

The velocity of a particle in the z-direction is given by

$$v_z = \frac{Q_{sheath}}{\pi(R_2^2 - R_1^2)} \tag{2.16}$$

Further if the amount of time taken for the analyte to traverse the gap between the electrodes is t_r and using equation 2.9:

$$t_r = \int \frac{dr}{v_r} = \frac{\ln(\frac{R_2}{R_1})(R_2^2 - R_1^2)}{2ZV} \tag{2.17}$$

and in that same time the analyte traverses a length L_s because of the sheath flow then,

$$t_z = \frac{L_s}{v_z} = \frac{L_s \pi(R_2^2 - R_1^2)}{Q_{sheath}} \tag{2.18}$$

Combining the above two equations such that $t_r = t_z$

$$\frac{L_s \pi(R_2^2 - R_1^2)}{Q} = \frac{1}{2}\frac{\ln\frac{R_2}{R_1}}{VZ_p}(R_2^2 - R_1^2) \tag{2.19}$$

Thus, for a given applied voltage (V), and Q_{sh} , a given mobility (Z) can be extracted [20]:

$$Z = \frac{Q_{sheath}\ln(\frac{R_2}{R_1})}{2\pi V L_s} \tag{2.20}$$

Above equation implies that a particular voltage corresponds to a particular mobility of a particle. The bold dotted red line in Figure 2.5 shows the specific trajectory of a particular particle for a specific voltage V. Thus by scanning the DMA voltage from low to high voltages, mobility of particles from subnanometer size to several hundred nanometers can be obtained, depending on DMA design. Then, by substituting equation 2.20 in equation 2.15, $D_{analyte}$ of a particle can be determined. One major constraint is that the sheath flow must remain laminar, such that the only force acting

on the particles is in the radial direction because of the applied electric field and flow effects are negligible.

Usually the analyte flow that enters the DMA is referred to as polydispersed flow, and the mobility size selected aerosol flow is referred to as monodispersed flow. Typically, the DMA is operated under balanced condition which implies that the polydispersed flow is equal to the monodispersed flow and thus the sheath air becomes equal to the excess flow.

2.4 Condensation particle counter (CPC)

The CPC, the last component of the ES-DMA is the most sensitive detector available, and is about a thousand times more sensitive than commercially available electrometers. The high counting sensitivity of a CPC is based on condensation of a working fluid (alcohol or water) on the particle, which increases in size to form ~ 10 μm almost uniform droplets (irrespective of the analyte size) so that it can be easily counted optically (Figure 2.6). However, while extremely sensitive, the CPC suffers from a lower size limit of detection of ~ 2.5 nm because the droplet activation efficiency is size dependent (i.e. smaller analytes are more difficult to activate at a given supersaturation of the working fluid). This size dependence is usually accounted for by calibrating CPCs against electrometers and is called the CPC collection efficiency (η_{CPC}) [30]. It should be pointed out that modifications, including use of different working fluids and operating temperatures can lower the size limit to ~ 1 nm [31]. Further discussion about the operating principle of the CPC can be found elsewhere [29].

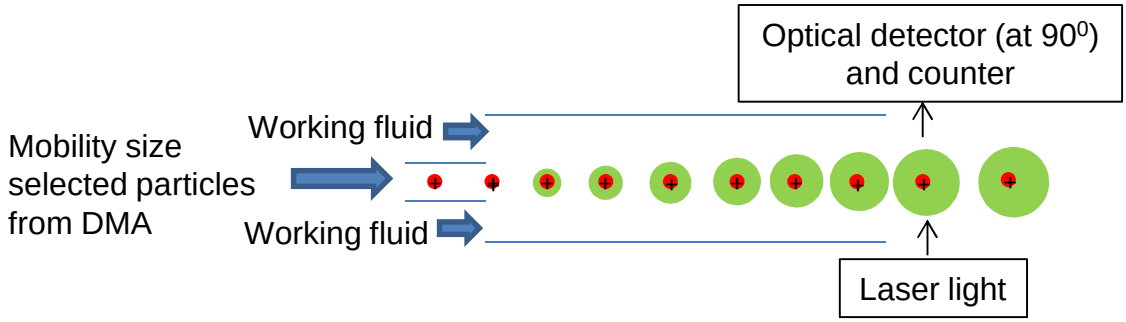

Figure 2.6 Schematic of the operating principle of the CPC

2.5 Data Interpretation

The raw data obtained with ES-DMA is corrected with the response of each of the intermediate components for obtaining the actual gas phase distribution (Figure 2.7). For the neutralizer, the charge distribution on the analyte is a function of particle size and is an absolutely essential correction. As mentioned earlier, upon applying a negative DMA voltage only the positively charged particles are collected. As the actual gas phase particles have positive, neutral and negatively charged particles, one needs to implement a correction to get back the original concentration. The fraction of positive, neutral and negatively charged particles generate by diffusion as a function of size is well-studied and this correction mathematically is given by:

$$\eta_c = 10^{\sum_{l=0}^{5} a_l^{\,j} \left[\log\left(d_p / d_o\right)\right]^l} \qquad (2.21)$$

where d_p represents the diameter of the analyte, d_o = 1 nm, j is the number of charges on a particle, and a_o^1 through a_5^1 are given by empirically fitted values of -2.3484, 0.6044, 0.4800, 0.0013, -0.1553, and 0.0320, while a_o^2 through a_5^2 are given by empirically fitted values of -44.4756, 79.3772, -62.8900, 26.4492, -5.7480, and 0.5049, respectively.

The next correction is for the transfer function of the DMA usually represented by Ω. Because of the finite width of the region where the analyte enters

the DMA, trajectories of different analyte may vary. This means that particles with slightly different trajectory may also enter the CPC for a particular DMA voltage. For example, depending on the operating conditions of the DMA, a 10 nm and a 10.2 nm particle may get collected by the CPC for a particular DMA voltage. Thus, even though these two particle sizes are different an user would think they are the same. Qualitatively these two sized particles are then within the resolution of the DMA. Thus the ultimate resolution and throughput of the DMA can be described by the transfer function and the resolution and transfer function always go hand in hand. Under balanced flow conditions, (i.e. when sheath flow equals excess flow and analyte or aerosol flow in, equals monodispersed size selected flow out) the ratio of the sheath to the analyte flow in provides an ultimate measure of the theoretical resolution [20]. The transfer function can be further broadened by Brownian diffusion and the equations can get extremely complicated. In this dissertation, the effect of diffusion has been neglected for simplicity. For all the bionanoparticles that are discussed in this dissertation, the transfer function is assumed to be equal to 1 as under the operating conditions the influence of transfer function on size distributions was found to be insignificant. In other words, the distribution obtained with DMA reflects the intrinsic distribution width.

Finally, the collection efficiency of the CPC is analyte size dependent and thus needs to be accounted for by the following expression:

$$\eta_{CPC} = 1 - e^{\frac{\alpha_1 - D_{analyte}}{\alpha_2}} \tag{2.22}$$

Where $\alpha_1 = D_{analyte_o}$ and $\alpha_2 = \frac{D_{analyte_{50}} - D_{analyte_o}}{\ln(2)}$. Here $D_{analyteo}$ is the diameter of an analyte for which the collection efficiency is ~ 0 % and $D_{analyte50}$ is the diameter of an analyte for which the collection efficiency is 50%. Typically most CPCs can collect

particle sizes of 5 nm with 50 % efficiency and particles of around 7 nm with ~ 90 % efficiency. In the context of this dissertation, the collection efficiency of most bionanoparticles will be 100 % as they will be larger than or equal to 7 nm.

Incorporating all the responses from the neutralizer, DMA and the CPC, and neglecting the effects of the transfer function it can be shown that the raw data $N_1(V_1)$ from the CPC at a particular voltage V_1 (corresponding to mobility Z_{p1} and diameter D_{p1}) and the size distributions are related by:

$$N_1(V_1) = \eta_{CPC}(D_{p1})\, f_c(D_{p1}) \frac{dN}{dD_{p1}} dD_{p1} \tag{2.23}$$

Where dD_{p1} is the increment of size from D_{p1} to D_{p1}+ dD_{p1} under balanced flow conditions, i.e. the polydispersed flow equals the monodispersed flow and also assuming that the aerosol flow is equal to the flow into the CPC.

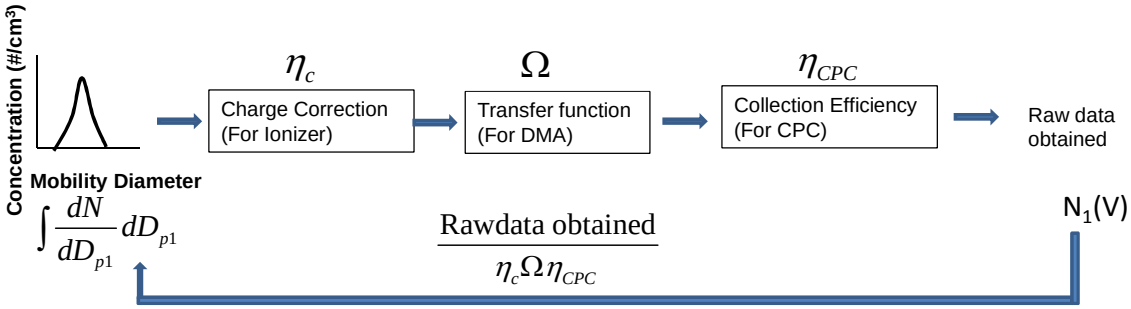

Figure 2.7: Steps for converting the raw data to the actual gas phase distribution.

2.6 Operating parameters of the ES-DMA

Twenty mmol/L ammonium acetate buffer is prepared by adding 0.77 g of ammonium acetate (Sigma Aldrich, St Louis, MO, #631-61-8) to 0.5 L of deionized water (18 MΩ/cm, Barnestead nanopure UV system) and adjusting to the desired pH using ammonium hydroxide (Baker, Phillipsburg, NJ, #9721-01). The concentration of acetate buffer used can also be as low as 2 mmol/L or as high as 80 mmol/L. If the conductivity is too low then the Taylor cone is not clearly visible and it results in big

unstable ES droplets. On the other hand, if the conductivity is too high then the Taylor cone is not stable which results in small droplets but with higher polydispersity. Further details about the "window" of operation of the ES can be found elsewhere [30].

Typically the ES chamber pressure (Figure 2.1 and Figure 2.8A) is maintained at 3.7 PSI which for a capillary with 25 µm inner diameter and 24 cm length gives the liquid flow rate of ~ 70 nL/min and the Reynolds number for this flow is < 1. These capillaries have an outer diameter of 150 µm. The capillaries from TSI Inc also come with an inner diameter of 40 µm but for most of the work in this dissertation 25 µm capillaries were used unless otherwise stated. Further, it should be pointed out that the chamber pressure is also operated at 3.0 PSI the reasons for which will become evident in chapter 4 and 8.

A 5 mCi Po-210 is used as the neutralizer. In Figure 2.8B it is not visible as it resides in the enclosed chamber inside the ES unit. The arrowhead in Figure 2.7B is barely indicative of its position. Although Po-210 has a half-life of ~ 138 days, it can be used upto one year after which the proportion of doubly charged particles even at small sizes (say 20 nm) starts to become significant.

The next component is the DMA (Figure 2.8C). At the highest sheath flow rates (30 L/min) used in this dissertation the Reynolds number inside the DMA is < 1000 and thus the flow is laminar. For calculating the Reynolds number the hydraulic diameter of the concentric cylindrical configuration of the DMA was assumed. In a slightly different context, an example calculation is provided in Appendix A. The inner diameter of the electrode for the DMA used is ~ .94 cm and the outer diameter is ~ 1.905 cm. The model used in this dissertation has length of ~ 5 cm which is considerably lesser than a longer model with a length of 44 cm (referred to as the

long-DMA), and is thus often referred to as a nano-DMA (NDMA, Figure 2.8C). The polydispersed flow, sheath flow and monodiserpsed flow are shown in Figure 2.8. The polydispersed and monodispersed flow connections are made with tygon tubings (from ES to DMA and DMA to CPC, respectively) while the sheath flow connection (from a high pressure dewar set at 40 PSI to the DMA) is through a plastic tubing. The DMA back pressure would vary from ~ 5 mm of H_2O (3 L/min) to ~ 30 mm of H_2O (30 L/min) depending on the sheath flow rate. The excess flow outlet is behind the NDMA and thus cannot be seen in this picture. The last component used for counting the particles size selected by the DMA is the CPC (Figure 2.8D). The model used in this dissertation is 3025A. For all cases in this dissertation, it was operated at high flow mode (1.5 L/min) to reduce the deposition losses of the bionanoparticles the tubing that connects the DMA size selected monodispersed outlet to the CPC.

As the operating conditions can slightly vary from experiment to experiment hence, each chapter (or section) will provide the operating conditions of the ES-DMA pertaining to that chapter (or section).

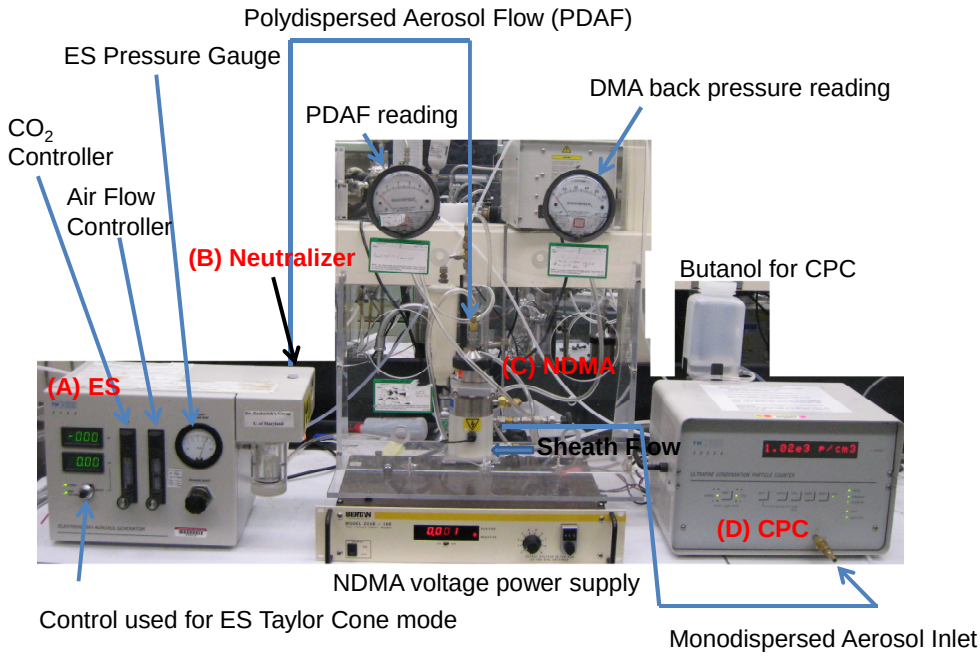

Figure 2.8: Actual ES-DMA experimental set up.

2.7 Summary

To summarize the above sections a schematic of the different components of the ES-DMA system is provided in Figure 2.9. In the ES (Figure 2.9A) the analyte, typically dissolved in a volatile buffer solution is passed through a fused silica capillary under pressure and then electrosprayed to produce multiply charged droplets containing the analyte. The ES in this figure is shown operating in the positive ion mode. The analyte containing droplets are then mixed with air (sometimes also supplemented with CO_2) and are passed through the neutralizer (Figure 2.9B) where solvent from droplets continue to evaporate, and a residual charge on the particles results from diffusion charging from positively and negatively charged ions. Only positively (or negatively) charged particles are then classified by applying a negative (or positive) bias in the DMA (Figure 2.9C). The rest of the particles with zero or negative (or positive) charges will collide with one of the electrodes of the DMA and be lost. Finally analyte particles are eventually detected (Figure 2.9D) by either using a condensation particle counter or an electrometer and thus a size distribution is obtained. Figure 2.9E below shows the size distributions of human serum albumin and MS2 virus (after charge correction) in ammonium acetate buffer. Size distributions adapted with permission from [10], copyright 1996 (American Chemical Society) and [14], copyright 2006 (American Chemical Society).

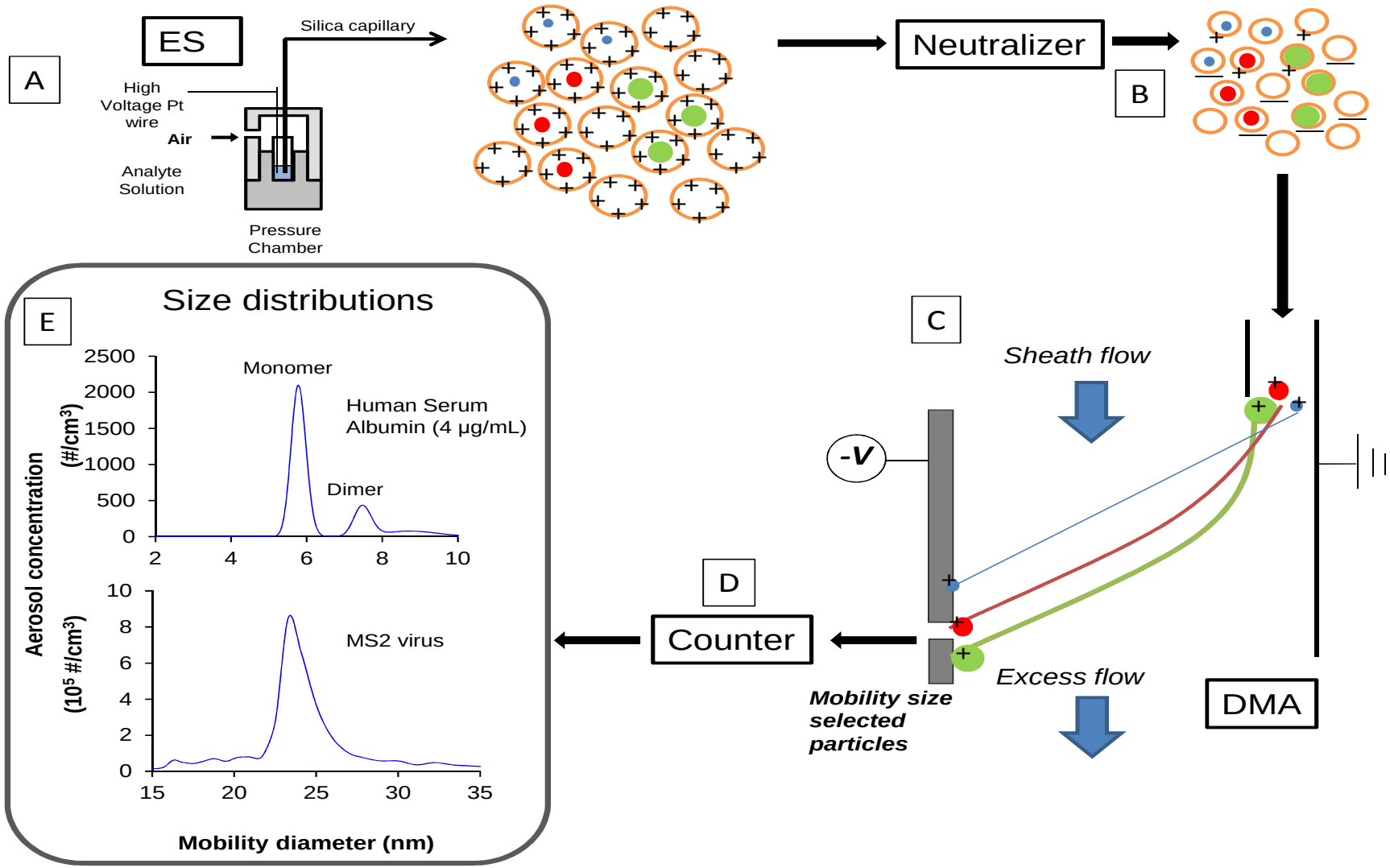

Figure 2.9 Schematic of the ES-DMA used for obtaining size distribution of bionanoparticles.

Chapter 3: LITERATURE SURVEY

Although a few groups of researchers use ES-DMA for characterizing AuNPs, silver nanoparticles (AgNPs) routinely the scope of this dissertation is only limited to nanoparticles in the biological context and thus in this chapter the most relevant examples are discussed.

3.1 Viruses and bacteriophages

Over the last decade, ES-DMA has been applied broadly to characterize phage and virus-like particles. For example, a number of studies measured the size of both large and small viruses as evident from Table 3.1 below. Using ES-DMA size distributions Pease, *et al*. [31] determined the symmetry and number of proteins per capsid for PR772 (Family *Tectiviridae*, Genus *Tectivirus*), a biosafety level 1 (BSL1) simulant of adenovirus. Lute, *et al*. [32] extended ES-DMA analyses to viruses of particular interest to biomanufacturers and filter firms by characterizing the size distributions of several viruses used in virus filtration studies and in the Parenteral Drug Association's (PDA) new nomenclature standards for small and large virus retentive filters. Wick, *et al*., [33] demonstrated that ES-DMA is sufficiently gentle to enveloped viruses such as alphavirus (Family *Togaviridae*) although there was some loss of structure in murine hepatitis virus (Family *Coronaviridae,* Genus *Coronavirus*), and sendai rodent virus (Family *Paramyxoviridae*, Genus *Respirovirus*). Using a novel recombinant virus-like particle as a test article, Pease *et al.,* [34] recently compared ES-DMA size distributions to those of TEM and asymmetric flow field-flow fractionation and found good agreement among the techniques for particle quantitation. Furthermore, it has been shown that icosahedra viruses remain infectious following electrospray [14, 35] though long tubular viruses

appear to lose structural integrity and infectivity in the electrospray. Overall, this technique has the potential to analyze many types of viruses. Table 3.1 below provides a comprehensive list of all viruses that have been studied till date.

Table 3.1: Summary of reported virus identities and mobility sizes. (Adapted from reference [36])

Author and Ref	Capsid Diameter (nm)	Virus	Virus Classification
Wick 2005 [33]	22.5	Kilham rat virus (KRV)	Parvoviridae
Lute 2008 [37]	23.2	PP7	Leviviridae
Kuzmanovic 2008 [38]	23.3	MS2	Leviviridae
Wick 2005 [33]	23.3	MS2	Leviviridae
Cole 2009 [39]	23.4	MS2	Leviviridae
Thomas 2004 [35]	23.6	MS2	Leviviridae
Cole 2009 [39]	24.0	PP7	Leviviridae
Hogan 2006 [14]	24.1	MS2	Leviviridae
Wick 1999 [12]	25.0	MS2	Leviviridae
Kaddis 2007 [40]	25.4	Cowpea chlorotic mottle virus (CCMV)	Bromoviridae
Thomas 2004 [35]	25.9	Cowpea mosaic virus (CPMV)	Comoviridae
Lute 2008 [41]	26.5	□X174	Microviridae
Wick 2005 [33]	26.9	MVM parvovirus	Parvoviridae
Cole 2009 [39]	27.0	□X173	Microviridae
Wick 2005 [33]	28.0	Rice yellow mottle virus (RYMV)	Sobemovirus

Thomas 2004 [35]	28.5	RYMV	Sobemovirus
Wick 2005 [33]	28.9	Sendai Rodent Virus	Paramyxoviridae
Laschober 2008 [42]	29.8	Human Rhinovirus (HRV)	Picornaviridae
Bacher 2001 [11]	29.8	HRV Types 2 & 14	Picornaviridae
Wick 2005 [33]	31.1	GD7 picornavirus	Picornaviridae
Bacher 2001 [11]	31.1	HRV Types 2 & 14	Picornaviridae
Pease 2009 [34]	38.1	VLP	Polyomaviridae
Hogan 2006 [14]	43.9	□-phage	Siphoviridae
Pease 2010 [31]	59.6	PR772	Techtiviridae
Wick 2005 [33]	70.0	Alpha virus	Togaviridae
Wick 2005 [33]	73.7	Murine hepatitis virus (MHV)	Coronaviridae
Wick 2005 [33]	79.1	Reo-3 (rheovirus)	Reoviridae
Thomas 2004 [35]	79.7	Adenovirus	Adenoviridae
Wick 2005 [33]	82.0	Adenovirus	Adenoviridae
Hogan 2006 [14]	87.0	T2	Myoviridae
Hogan 2006 [14]	88.3	T4	Myoviridae
Allmaier 2008 [43]	300.0 x 19.0	TMV	Tobravirus

By collecting viruses post-ES [14] and post-ES-DMA [6] it has been established that some viruses (e.g., MS2, λ) remain viable after the ES process while some others do not (e.g.,T2, T4, [14] and TMV [6]). The latter also appear at mobility diameters smaller than expected, especially if the ES droplet sizes are smaller or comparable to these viruses. It has been speculated that electrical or mechanical

perturbation during the ES evaporation process may disrupt the integrity of these viruses. That some viruses indeed break up during the ES process has also recently been corroborated with TMV [6].

Evaluating the titer (concentration) of viral products as part of a lot release protocol is a key quality control step essential to ensuring their efficacy and safety [44]. Although the specific tests comprising the lot release protocol are prescribed individually for each product as appropriate for each case, the assays and instruments used to evaluate the identity, composition and potency of viral products must meet standards established by the International Committee on Harmonisation (ICH) (ICH Expert Working Group, 2005). Specifically, "ICH Q2 Validation of Analytical Procedures: Text and Methodology" indicates that a quantitative assay must be evaluated based on seven criterion, namely; specificity, linearity, range, accuracy, precision, robustness, and system suitability testing [44]. Although routinely used by several labs, such a systematic study for viruses is lacking in the literature and thus will be systematically studied in chapter 7.

3.2Polymers and proteins

Almost all polymers and proteins of interest are amenable to characterization by ES-DMA, which offers faster characterization times over size exclusion chromatography (SEC), analytical ultracentrifugation (AUC), flow-field fractionation (FFF), and gel electrophoresis, in addition to providing a direct measure of size. ES-MS methods have difficulty measuring high molecular weight proteins and the presence of more than one charge state can complicate data interpretation [45].

The first application of ES-DMA to nucleic acids can be traced back to 1997 when it was used for determining the mobility diameter of single stranded and double stranded DNA from size range 6 kDa to 900 kDa [46]. Polyethylene glycols (PEGs)

in the size range of 4k to 700 kDa were used to establish that molecular weight and mobility diameter could be correlated by a one-third power law [47] a correlation that had already been established for proteins three years prior [11]. Similar behavior has been reported for water insoluble polymers [48]. Using this correlation, ES-DMA can also been used to determine density of polymers (or proteins) [11, 49].

$$\rho = \frac{6MW}{N_{avg}\pi d_{DMA}^{\ 3}} \tag{3.1}$$

Here ρ is the density of the polymer (or protein), MW is the molecular weight, N_{avg} is the Avagadro's number and d_{DMA} is the analyte diameter determined by DMA [46, 50]. It should be pointed out that for a known gas phase density of a particle, equation 3.1 can conversely also be used to determine the molecular weight. Such a correlation is obvious for any globular particle as it resembles a sphere. However, it arises for any non-spherical particle such as a PEG probably because ES droplet evaporation causes it to dry up to a near spherical shape. It should be pointed out that unlike proteins, equation 4 cannot be used to correlate the molecular weight of viruses with mobility diameter most likely because the density of the different internal constituents of viruses can vary [11].

ES-DMA has been used to determine polydispersity in PEGs, although, in this study, the density of PEGs were assumed to be the same as proteins with no justification whatsoever [51]. It was also found that 2 kDa PEG monomers are too small for analysis by ES-DMA. This result is expected because a CPC's sensitivity is nearly zero at particles sizes of ~ 2 nm to 3 nm [52] and the mobility diameter of 2 kDa PEG falls in this range. This limitation can however be overcome by using an electrometer instead of a CPC. Another group has also attempted determining the density of PEGs and there appears to be a significant variation amongst different

groups (0.52 gm/cc to 1.3 gm/cc) [47, 51]. The reason for this variation is discussed later.

ES-DMA has been used to characterize different generations of poly(amido-)amine dendrimers (G2 to G10) and size distributions obtained were found to be in reasonable agreement with atomic force microscopy, transmission electron microscopy, and small angle X-ray or neutron scattering [53]. In this study, using equation 3.1, the densities of the dendrimers were determined to be ~ 0.54 gm/cc. It should be pointed out that for some generations of these dendrimers, the density values obtained using ES-DMA were about a factor of 2 lesser than rated densities of the manufacturer. Silk-elastin-like protein polymers (SELP) are a new class of materials that potentially can be used for gene delivery applications. Recently it has been demonstrated with the ES-DMA that such polymers can be electrosprayed to produce finely-tunable, potentially non-toxic nanoparticles either by changing concentration of the SELPs in solution or by changing solution viscosities [54].

Another potentially valuable application of ES-DMA is characterizing and quantifying proteins and protein aggregates, the latter being a common problem during therapeutic protein development or storage [55]. ES-DMA possesses some distinct advantages relative to other more popular techniques such as SEC, dynamic light scattering (DLS) and field-flow fractionation (FFF). Although not demonstrated before, it is presumed that ES-DMA has a better resolution than SEC. In DLS the intensity of light scattering scales as the sixth power of the hydrodynamic diameter. Thus it cannot characterize heterogeneous populations unless the size difference between the particles is at least more than 3:1. On the other hand, ES-DMA size selects either on the basis of the inverse of projected area (e.g. 10 nm particles) or equivalent diameter (e.g. 100 nm particles) and thus has no such constraint. Further,

ES-DMA should also have a limit of detection which is about a thousand fold lower compared to techniques that use UV detectors such as SEC, AUC and FFF because of the sensitivity of CPC [9]. The first reported use of ES-DMA [10] employed several different globular proteins from molecular weight of 5.7 kDa (bovine pancreas insulin) to 669 kDa (bovine thyroglobulin). It was demonstrated that the monomers of different proteins can be differentiated from their respective oligomers (dimers, trimers) and that there was a strong correlation between the molecular weight and the mobility diameter determined using ES-DMA. Since then, the molecular weight – mobility diameter empirical correlation plotted in Figure 3.1 has been confirmed by several groups of researchers for both globular, as well as non-globular proteins ranging from a few kDa [11, 19, 56, 57] to several MDa [56]. The actual expression is later going to be used in Chapter 8. Recalling that the DMA does not measure mass directly, but rather projected area (for very small particles), the validity of this correlation implies that the proteins (esp. non globular proteins) undergo structural changes and become spherical during the evaporation of the ES droplet. A recent study with GroEL, a 14-mer complex suggested partial collapse of the structure in the gas phase after the ES-DMA thus strengthening this hypothesis although it should be pointed out that a "neutralizer" was not used for charge reduction in this study [58].

ES-DMA has been used to resolve protein aggregates of DNase [59], insulin [30], and various immunoglobulins [19]. It has also been used to gain insight into the function of a number of protein complexes such as vault proteins [56], 20S proteasome [16], ErbB3 [60], hemoglobin (Hb), Hemopure (a crosslinked Hb) [49], and for correlating heart disease risks with the size of lipoproteins [61]. A brief review of some of these results is available elsewhere [49].

The quantification of different oligomers of proteins has been reported for human antibodies [19], bovine serum albumin [10], hemoglobin [59] and 20-S proteasome complex [16]. One potentially confounding factor in these studies is adsorption of proteins to the ES capillary which produces time variant size distributions. However, since the development of ES-DMA this effect has never been systematically studied. Furthermore, studies suggest that proteins aggregate upon adsorption to different surfaces [48], thus one may wonder how adsorbed proteins may effect size distributions when desorbing.

Another potentially significant problem is the quantification of aggregates using ES-DMA. Two or more monomers of a bionanoparticle may get encapsulated in the same ES droplet that upon evaporation of the droplet will be incorrectly measured as an intrinsic aggregate in MS or DMA. This artifact can be minimized either by conducting measurements of proteins at low concentration or by reducing the ES droplet volume [10, 62]. However, no quantitative approach is available to correct this artifact.

ES-DMA can be used to determine the density of proteins. However, density determined using equation 3.1 has been found to vary almost by a factor of two by different groups. The earliest findings of 1 – 1.1 g/cm^3 were close to values reported for the liquid phase density [10, 57]. However, commercial ES-DMAs used later yielded densities close to 0.6 g/cm^3[11, 49]. To explain this difference, it has been hypothesized that the mobility diameters are dependent on the geometric features of DMAs [63]. It has been independently seen that the mobility diameter obtained for same particles but with different DMAs can vary by about 15% [64]. Using uncertainty analysis, it can be shown that a 15% variation in mobility diameter results in a 45% variation in density which partially explains this wide scatter of densities in

the literature and strengthens the above hypothesis. The same rationale may also explain the scatter of densities found in PEGs [47, 51]. Curiously, the lower density in all cases have been reported only with TSI Inc designed DMAs and this perhaps is because of inaccurate or imprecise DMA geometry designed and manufactured by them.

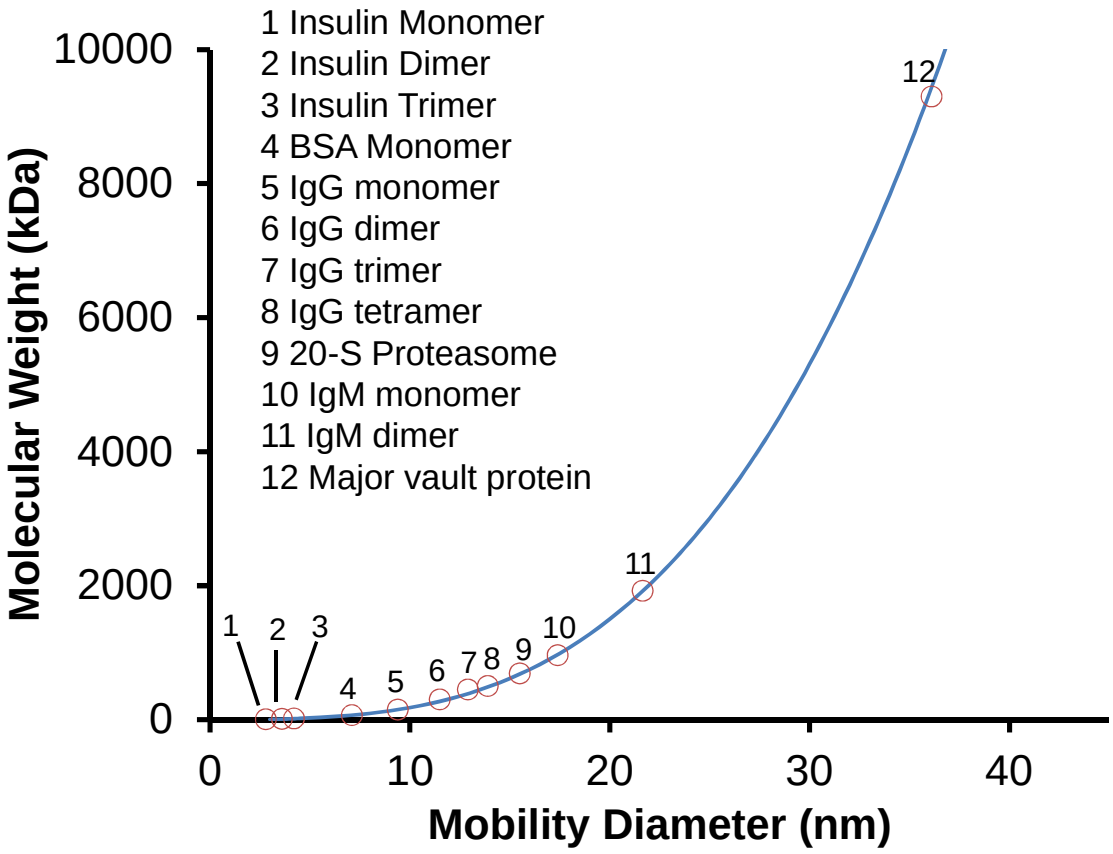

Figure 3.1: Molecular weight and mobility diameter correlation.

3.3 Nanoparticle-biomolecule conjugates

Gold nanoparticles (AuNPs) are being intensely studied for bio-sensing and health diagnostic applications in part because of the ease with which they can be surface functionalized. The adsorption of biomolecular ligands, such as nucleic acids and proteins, to AuNPs often leads to an increase in mobility diameter that can be measured using ES-DMA. This principle has been demonstrated with several different examples [15, 20, 42, 65, 66]. For example, ES-DMA has been used to characterize

and quantify surface coverage of single strand DNA molecules on 10 nm gold nanoparticles [65]. Similar studies have been reported for self-assembled alkane thiol monolayers (SAMs) on 10 and 60 nm AuNPs [15]. This study found that the coverage of SAMs was independent of the size of the AuNPs. BSA was recently used as a model protein to study AuNP-protein interactions as a function of concentration and pH [20]. To further model the complexity inside human plasma where multicomponent species may be present, competitive adsorption – desorption of SAMs and PEGs on AuNPs has been successfully studied [66, 67].

ES-DMA has also been used to characterize a variety of bimolecular complexes, such as oligomerization of subunits of ribonucleotide reductase in the presence of different functional groups [68] and triphosphates [69], PEGylated-Von Willebrand factor (VWF) protein [70], quantification of coverage of antibodies (8F5) on human common cold virus [42], and quantum dots (QDs) on bacteriophages [71, 72].

Two approaches are used to quantify adsorbed ligand (usually peptides and or proteins) on a primary particle (such as AuNP, virus, or protein). One approach for quantification is based on the increase in projected surface area due to adsorption of ligand [15, 20, 65] (AB approach):

$$N_{ligand} = \pi\left(\frac{d^2_{conjugate} - d^2_{primary}}{4A_{ligand}}\right)^2 \qquad (3.2)$$

N_{ligand} is defined as the number of ligands per primary particle, $d_{conjugate}$ and $d_{primary}$ are the mobility diameters of the conjugates and primary particles, respectively, and A_{ligand} is the projected area of the ligand in liquid phase. The above equation has been employed for quantifying surface coverage of polymers and proteins on AuNPs, as

well as QDs on phages. The other approach is to quantify based on the increase in volume due to adsorption of ligand [42] (VB approach):

$$N_{ligand} = \frac{d^3_{conjugate} - d^3_{primary}}{d^3_{ligand}} \tag{3.3}$$

where d_{ligand} is the mobility diameter of the ligand. This has been used for quantifying the number of 8F5 antibodies that bind to human common cold virus, and has also been corroborated with cryo-miscroscopy [42]. For the same mobility diameter increase of a primary particle, each of these approaches gives different ligand coverages, with equation 3.3 always yielding higher coverages (for ligand size greater than 2 nm or more). This is evident from different examples shown in Table 3.2 below. Further, these values obtained only rarely appear to corroborate with other independent measurements (column 7, Table 3.2). Thus it is evident that further systematic studies and comparison with several other orthogonal techniques is required to determine which approach provides more accurate values. It should also be pointed out that both equations assume that a ligand, upon adsorption, does not change in size (or conformation); this assumption may not always hold.

Table 3.2 List of bionanoparticle conjugates and the differences in results depending on equations used.

Complex	Ligand Size	Primary Particle	Conjugate Size	AB approach	VB approach	Independent
HRV2 + mAb-8F5 (1:60)[42]	8.8	30.0	35.8	8	28	30
MS2 + mAb (1:69) [73]	9.0	23.2	31.8	11	27	NA
MS2 + pAb (1:35) [73]	9.0	23.2	24.0	0	2	NA
λ Phage + Strp + QD [71, 72]	14.1	48.4	55.8	5	21	7, 13
10 nm Au + BSA [20]	7.1	13.0	19.3	12	27	3
30 nm Au + BSA [20]	7.1	31.1	37.2	52	116	30
30 nm Au + BSA [20]	7.1	59.0	64.9	161	367	87
60 nm Au + TNF [74]	6.0	60.0	66.4	161	355	1018
30 nm Au + hIgG(Chapter9)	8.8	32.8	39.2	11	37	140

3.4 Advantages and limitations of ES-DMA

3.4.1 Advantages

a) ES-DMA characterization is independent of particle type and thus, no prior information about the particle type, is required. The use of charge neutralizers result in a reduction of the number of charges states per particle compared to ES-MS, and thus makes the data interpretation and the mobility spectra relatively simple to analyze. ES-DMA operates under ambient pressure conditions, and does not require sophisticated pumping. This latter operational characteristic also makes its interface to other instruments (such as counters, substrates and mass spectrometry) much easier.

b) ES-DMA's have been routinely used to characterize particles over a broad size range (~ 3 nm to several hundred nanometers), and has also been validated with several independent liquid and gas phase techniques [14, 30, 34, 75]. Indeed ES-DMA was one of the primary tools in the recent development of NIST traceable nanoparticle size standards [76]. Although the commercialized ES-DMA has been used up to several hundred nanometers, it can be used for characterizing particles up to ~ 2 μm, and thus its operational size-range is significantly greater than both SEC and MS. It should be pointed out however, that for micron sized particles, multiple charging, and a decrease in resolution (at fixed flow rate) can pose difficulties. Multiple charging can be deconvoluted by using Tandem-DMA methods, analogous to MS-MS studies.

c) ES-DMA can be operated in a scanning mode [77] such that the total time of analysis is 2 - 4 minutes, and significantly shorter compared to several other methods. (e.g. SEC and FFF ~ 30 minutes; AUC ~ 3 – 6 hours).

d) ES-DMA requires small sample volumes (a few µLs or less depending on time of analysis).

e) Relative to other methods, ES-DMA has high sensitivity. The lower limit of detection of CPC is a thousand fold less than UV-vis based detectors typically used in SEC, AUC and FFF [9]. A more detailed study of the lower limit of ES-DMA will also be provided in chapter 7 (in context of viruses) and chapter 8 (in context of proteins).

3.4.2 Limitations

a) Liquid phase techniques such as SEC, AUC, FFF and DLS are widely used by the biopharmaceutical industry for characterizing protein stability and aggregate formation. Most of these techniques are capable of analyzing high concentrations of proteins (10 – 100 mg/mL), in non-volatile buffers and at high ionic strengths (100 – 1000 mM). In contrast, ES artifacts that are going to be discussed in chapter 4 and 5, and instability, limits the solution conditions to concentrations of a few hundred µg/mL (protein and ES droplet volume specific), low ionic strength (<100 mM), and volatile buffers. Furthermore, characterization of proteins from cell media require some preprocessing, such as dialysis, to prevent droplet-induced coagulation of the analyte and heterogeneous media and a methodology to overcome it will be provided in Chapter 4.4.

b) The uncertainty in measurements of ES-DMA is typically ± 0.3 nm from a size range of a few nanometers to at least ~ 100 nm [75] and appears to be independent of resolution [78]. However, this uncertainty sometimes may not be adequate to distinguish proteins with slight differences in molecular weight. For example, two proteins with molecular weights of 145 kDa and 150 kDa would have predicted mobility diameters of 9.3 nm and 9.4 nm, respectively. These values are within the

uncertainty, and thus, ES-DMA cannot distinguish between these two proteins. This limitation has been reported for certain cases [79]. On the other hand, a typical ES-MS can easily distinguish differences in molecular weights of a few Daltons.

c) A typical commercially available ES-DMA and CPC detection system will cost ~$100 K (USD) and thus is a greater financial impediment relative to gel electrophoresis, capillary electrophoresis, SEC, DLS and FFF [55]. However, recent developments in DMA technology may potentially reduce the price [80].

3.5 Summary and Motivation

Based on the extensive literature survey in previous sections it is evident that ES-DMA can be used for several different subclasses of bionanoparticles. Besides size determination it can also be used for i) measuring gas phase concentrations and correlating with liquid phase concentrations, ii) measuring the density of proteins and polymers, iii) quantifying ligand adsorption and iv) kinetics of aggregation.

However, there are several outstanding questions and issues. These can broadly be divided into two categories: research oriented and industry oriented. The first one addresses some of the artifacts of ES-DMA from a fundamental standpoint and tries to study them systematically, understand them and if possible eliminate them. Under this category questions are as follows:

1. As proteins can interact with ES capillary walls producing a response that varies as a function of time, can this interaction be quantified?
2. Does the above interaction influence the aggregate distribution?
3. Can quantitative theories be developed for quantifying unintentional non-specific aggregation caused by ES?

4. The two models (AB and VB approaches) developed for quantifying ligand adsorption to bionanoparticles can vary drastically. Can a more acccurate methodology be adapted?

Questions 1 and 2 are addressed in chapter 4, question 3 is addressed in chapter 5 and question 4 is addressed in chapter 6.

To address the second category, different type of bionanoparticles such as viruses (chapter 7), proteins (Chapter 8) and nanoparticle-protein complexes (chapter 9) are going to be taken up and analyzed with the most routinely used analytical methods and then compared to ES-DMA to see how the later fares against these techniques. It should also be pointed out that analyzing bionanoparticles often requires analysis with several orthogonal methods. Thus, in all subsequent chapters other analytical methods are going to be invoked as and when necessary.

Chapter 4: ES ARTIFACTS: ADSORPTION AND DESORPTION OF PROTEINS AND ITS EFFECTS

Depending on the pH of the solution and the type of the protein being electrosprayed, there can be a time variant size distribution obtained with the ES-DMA. The objective of this chapter is three-fold: i) to demonstrate that this time variant size distribution can be harnessed to quantify the adsorption and desorption of a) monomeric and b) oligomeric proteins to ES silica capillaries , ii) to study whether the adsorption and subsequent desorption of proteins to the capillaries influence aggregate distributions and iii) to demonstrate through an exploratory example that ES-DMA can be used for characterizing complex heterogeneous protein mixtures by first adsorbing the mixture to the ES capillary and then characterizing during desorption.

4.1 Monomeric protein adsorption-desorption to ES silica capillaries

4.1.1 Introduction

Protein adsorption is important to many fields including biomaterials and bioprocessing, which has led to many studies to quantify it. The characterization methods employed can be broadly characterized into solution depletion, optical, spectroscopic, imaging and surface force measurement techniques [81, 82]. Most of these techniques operate at stagnant conditions [83, 84] or at low shear [85, 86] (typically 10^2 sec^{-1} to 10^3 sec^{-1}) and have only rarely [87-89] been used for studying competitive adsorption of protein oligomers (i.e. monomers, dimers, trimers etc. of same protein). An understanding of both the effects of shear and competitive adsorption is relatively unexplored problem. It has been reported for example that shear flows increase protein adsorption [86], which is obviously of interest in the

context of the human circulatory system where shear rates can vary from 1 sec^{-1} to 10^5 sec^{-1} [90]. However, while protein aggregation has been studied at high shear flow rates (10^6 sec^{-1}) [91, 92] adsorption to surfaces is yet to be probed under these conditions. Further, it is generally believed that in multi-component systems, smaller proteins adsorb fastest, which are then displaced by larger ones [83, 85]. This effect has been observed in both stagnant [83, 84] and low shear flow conditions (≈ 500 sec^{-1}, 225 sec^{-1} to 2700 sec^{-1}) [85, 86]. However, with a few exceptions, [87-89] there seems to be an overall lack of tools that can study adsorption-desorption of oligomers of same protein other than a few exceptions. Furthermore, it is common to label proteins while studying multi-protein systems or sequential adsorption [92-94] despite the fact that labeling may change conformational stability of proteins and also affect adsorption patterns [95-97].

The objective of this section is to demonstrate that Electrospray-differential mobility analysis (ES-DMA) can also be used for studying protein adsorption. As mentioned in chapter 3 it was pointed out that size distributions of proteins are time dependent implying interaction of proteins with the ES capillary. As ES-DMA can resolve oligomers of the same protein it offers the possibility to study competitive or sequential adsorption of oligomers of the same protein or a mixture of different proteins or both (as long as their sizes are different) without the need for labeling. Because of the ES, particles (proteins in this context) pass through a silica capillary under high shear (typically 10^5 sec^{-1}) thus offering the possibility of studying the effects of protein adsorption at high shear.

4.1.2 Materials and Methods

4.1.2.1 Sample preparation

A monoclonal antibody (IgG1) Rituxamab (RmAb), was purified using Protein A affinity column (GE Healthcare) and stored at -20 ^{o}C in 0.025 mol/L Tris buffer at pH 7.4 and 1×10^{-5} mol/L of NaN_3 was added as a preservative. To desalt the protein sample, a millipore centrifuge filter (30 kDa molecular weight cut off) was used immediately prior to ES-DMA analysis at 13,200 rpm for 12 minutes. For ES-DMA experiments, RmAb was prepared at a concentration of 1.0 mg/ml as determined by UV-vis absorption measurements in 0.020 mol/L ammonium acetate at pH 7, and further diluted to 0.01 mg/mL, 0.02 mg/mL, 0.05 mg/mL and 0.1 mg/mL. For the "proof of principle" experiment described in section 4.1.2, a solution of 0.001% sucrose and 0.01 mg/mL RmAb was prepared at 0.020 mol/L ammonium acetate at pH 7.0.

Bovine IgM (Sigma Aldrich, St Louis, MO, 078K4779) obtained in concentrations of 1 mg/mL was desalted as described for RmAb and diluted 10× to a concentration of 0.1 mg/mL for use in the ES-DMA.

Stock gelatin (KNOX, trade name: Gelatine, # 0-41000-03500-5) solutions were prepared by suspending 1 mg to 1.5 mg in 1 mL to 1.5 mL of 20 mmol/L ammonium acetate at the desired pH in low protein binding vials (Eppendorf). The 1 mg/mL solution was heated to ≈50 ^{0}C for ≈5 minutes for dissolution. The samples were then diluted to 0.1 mg/mL and used to passivated the capillaries. Solutions of gelatin were prepared fresh each time the capillaries were passivated.

The capillaries referred to as unpassivated or bare are those that did not undergo any surface treatment before use. Passivated capillaries are those that

underwent surface treatment with gelatin or BSA. The methodology of passivation is described in great detail in chapter 4.3.

4.1.2.2 ES-DMA

About 1.0 M H_2SO_4 was made to flow through the 25 μm capillaries for 20-30 minutes (equivalent to 11-16 capillary volumes, definition of capillary volume provided later), followed by nano-pure18 MΩ/cm ultrapure water for another 10 minutes (5-6 capillary volumes). Prior to ES-DMA experiments, capillaries were cleaned by flowing 0.020 mol/L ammonium acetate buffer solutions at pH 7.0 for 5 – 10 minutes before introduction of the desired sample. Capillaries undergoing this treatment are referred to as "bare".

The ES-DMA was operated with a sheath flow rate of 10 L/min using nitrogen and an aerosol flow rate of ≈1.5 L/min using air except for the "proof of principle" experiment for which the sheath flow used was 30L/min. Size distributions of RmAb were obtained by scanning from 7.2 nm to 15.5 nm. The CPC was operated at a high flow mode of 1.5 L/min.

A typical adsorption-desorption experiment would constitute the following steps: firstly, insertion of the sample was followed by starting of data collection after 4 minutes, to allow for the sample to elute through the capillary, pass through DMA and get counted by the CPC; mobility distributions were obtained every 90 seconds (unless otherwise mentioned) till steady-state was achieved (within experimental variability) and finally the protein sample was replaced with buffer and further mobility distributions obtained. The system was calibrated for size using 60 nm NIST calibrated polystyrene latex particles [32].

It should be noted that all experiments described after the proof of principle experiment did not incorporate sucrose as a marker, the gas phase data were charge

corrected and mobility distributions were obtained from 7.37 nm to 15.1 nm using commercial TSI Inc. software (Aerosol Instrument Manager) that enables obtaining size distributions more frequently (every 90 seconds) compared to the experiment in "proof of principle" experiment. Also, because the ES community (especially mass spectrometry) uses different capillary diameters and hence the flow volume [28, 53, 98] can vary significantly time was replaced with equivalent capillary volume, which is defined by the product of time with capillary flow rate, and divided by the total volume within the capillary. In this regard, the mass-spectrometry community typically uses different passivations on silica surfaces to reduce protein adsorption which concomitantly reduces the long waiting times before protein breakthrough [99].

4.1.2.3Shear rate calculation

For the 25 μm capillaries and the nominal flow rates used in this study, the shear rate is calculated to be $\approx 10^4$ sec^{-1} as calculated below. This value is about one order of magnitude higher than techniques previously used to study protein adsorption under shear flow conditions such as total internal reflection fluorescence (TIRF) [100], ellipsometer [86] and surface plasmon resonance [101].

In laminar flow the velocity profile inside a tube is given by equation 1,

$$\frac{U}{U_{average}} = 2(1 - 4(\frac{r}{D_{capillary}})^2) \quad (4.1)$$

Where U is the velocity at any radius r and $D_{capillary}$is the capillary inner diameter, and$U_{average}$ is defined as,

$$U_{average} = \frac{4Q_{capillary}}{\pi D_{capillary}^{\ 2}} \quad (4.2)$$

where $Q_{capillary}$ is the flow rate inside the capillary.

The shear rate is then $\gamma = \left| \left. \frac{\partial U}{\partial r} \right|_{r=D_{capillary}/2} \right| = \frac{2 \times U_{average}}{D_{capillary}}$ (4.3)

Using equation 3 the shear rate in a 25 μm capillary at a capillary flow rate of 66 nL/min comes out to be 10756 sec^{-1}.

4.1.3 Proof of Principle Experiment

Sucrose was used as a reference marker in this experiment because it does not significantly interact with the silica surface of the capillary at pH 7. On the other hand, any protein that interacts with the capillary will result in a mobility distribution that should vary with time.

Figure 4.1A plots the size distributions from 3 nm to 13 nm obtained at times of 0, 99, 128, 137.5, and 175.5 minutes for a mixture of 0.001% sucrose (v/v) and 0.01 mg/mL RmAb. At t = 0 minutes and t = 99 minutes a peak for sucrose at 4.6 nm is clearly observed, while no peak is observed for RmAb. At t = 128 minutes, a peak for RmAb at ≈ 9nm is first observed that increases quickly in intensity to a steady-state value with time. These results show that, sucrose does not bind to the capillary, and protein adsorption occurs over a long period of time. The RmAb mobility size needs to be corrected for sucrose that coats the RmAb molecule. The equation for this correction is given by:

$$d_{RmAb} = \sqrt[3]{d_{RmAb,sucrose}^3 - d_{sucrose}^3} \quad (4.4)$$

Where d_{RmAb} is the size of RmAb monomer, $d_{RmAb,sucrose}$ is the RmAb coated with sucrose and $d_{sucrose}$ is the diameter of sucrose. The d_{RmAb} value obtained is in excellent agreement with mobility diameters of immunoglobulins obtained by others [11].

Figure 4.1A also shows small quantities of RmAb dimers at 11.2 nm which appears because of an electrospray artifact of two monomers in the same ES droplet

[102, 103] as discussed in the previous chapter. Other time points have not been shown for clarity. The data has been normalized w.r.t to the sucrose peak. Figure 4.1B includes the adsorption phase (upto ≈ 140 minutes), the steady state phase (upto ≈ 180 minutes) and the desorption phase (upto ≈ 230 minutes).

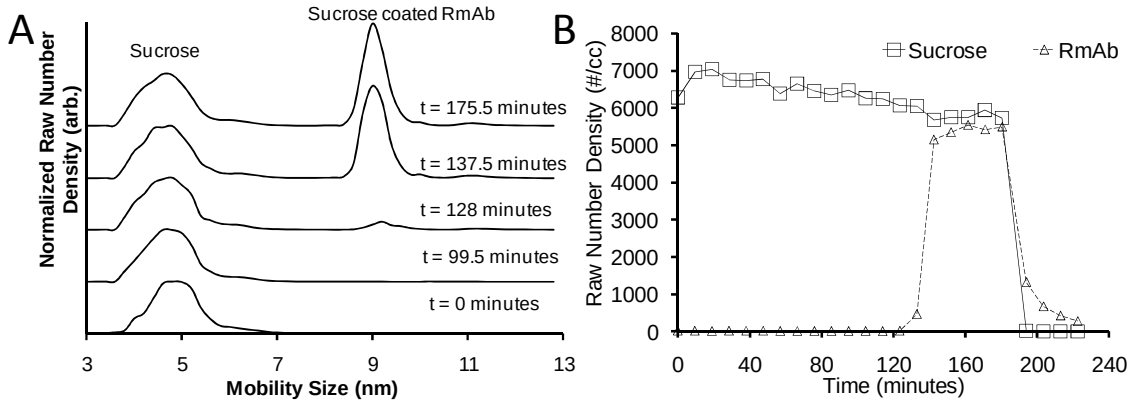

Figure 4.1: Size distributions of 0.001% sucrose (v/v) mixed with 0.01 mg/mL RmAb at pH 7.0 using the ES-DMA as a function of time. 2B shows the integration of the sucrose peak and RmAb peak plotted as a function of time.

After the protein signal has reached steady-state (≈ 180 minutes), the protein solution is replaced with a 20 mmol/L ammonium acetate buffer at pH 7. Upon replacing the sample with buffer, the sucrose signal decreases immediately, in contrast the RmAb signal decays relatively slowly. This is evident from Figure 4.2B that plots the integrated area under the RmAb and sucrose peak as a function of time for the entire experiment. These results are summarized and interpreted as follows. The presence of sucrose signal together with the absence of RmAb signal suggests that RmAb adsorbs to the wall of the glass capillary. From 0 to ≈ 130 minutes RmAb adsorbs until the RmAb surface coverage reaches saturation, at which point protein is first observed and the signal rapidly reaches steady-state. Upon replacing the protein/sucrose solution with pure ammonium acetate buffer the sucrose signal

decreases rapidly, while the RmAb signal falls more slowly. The slowly decaying RmAb signal suggests slow desorption of RmAb from the glass capillary surface.

4.1.4 Surface coverage and adsorption kinetics for monomeric and multimeric proteins

In this section the relationships necessary to extract kinetic parameters and surface coverages from the mobility distributions are formulated and then demonstrated with a monomer protein (RmAb). The reader is reminded that RmAb does not elute from the ES capillary for many minutes (or capillary volumes) for all experiments conducted for this work, hence it is not possible to determine the adsorption rate constants for RmAb using ES-DMA.

To determine the surface coverage, $C_{eluting}^{t(i)}$ is defined as the concentration of protein in liquid phase eluting through the ES capillary, a parameter that varies with time where superscript t_i denotes time i. The DMA-CPC however measures the gas phase concentration, which must be corrected for transport losses and particle charging fraction. While the charge fraction is based on well known relationships which allows one to make the appropriate quantitative corrections (defined by α_{charge}), the transport losses must be empirically calibrated, through a parameter α which takes into account Brownian motion [24] and electrostatic deposition losses and electrospray efficiency [104] as shown in equation 4.5.

$$C_{eluting}^{t(i)} = \alpha C_{gasphase}^{t(i)} \frac{Q_{cpc}}{Q_{capillary}} \tag{4.5}$$

where α is an unknown at this point since $C_{eluting}^{t(i)}$ is unknown and Q_{cpc} and $Q_{capillary}$ are the flow rates inside the CPC and capillary respectively. $C_{gasphase}^{t(i)}$ is given by equation 4.6 and is determined by charge correcting the CPC raw data and then

integrating over the entire size range of observed protein species such as protein monomer, dimer, or larger aggregates.

$$C_{gasphase}^{t(i)} = \int \frac{d(\alpha_{charge} N_{cpc}^{t(i)})}{dD_p} dD_p \quad (4.6)$$

Where $N_{cpc}^{t(i)}$ are the counts obtained by the CPC at a mobility diameter of *Dp*, *dDp* is the increment in mobility diameter and α_{charge} accounts for the charge correction [105]. For RmAb the monomer and dimer counts were obtained by integrating from 7.6 nm to 9.6 nm and 9.8 nm to 11.8 nm respectively.

When the concentration of eluting protein reaches steady state (or in other words assuming *adsorption reaches equilibrium*) $C_{eluting}^{t(ss)}$ can be written as shown below:

$$C_{eluting}^{t(ss)} = C_{solution} \quad (4.7)$$

Where $C_{solution}$ is the total concentration of the protein in solution measured by an independent technique such as UV-vis and the superscript *t(ss)* denotes steady state. Then combining equation 4.5 and 4.7,α can be determined at steady state. Using this approach α was ≈ 4-5 for RmAb at all concentrations and pH values; however α is dependent on system operating parameters such as the aerosol flow and sheath flow as well as protein type. The assumption of equilibrium has been addressed in greater detail in section 4.2. For now assuming steady state corresponds to equilibrium allows one to evaluate the adsorption kinetics under non-equilibrium conditions, because α once evaluated at steady state can then be used at other conditions assuming linearity. Concomitantly, this also allows the amount of protein adsorbed to the capillary surface per unit area Γ_{ads} to be calculated. Because the amount of protein adsorbed varies with time and DMA scans require a finite dwell time Δt, $\Gamma_{ads}^{t(i)}$ is evaluated

over a given time interval and summed over each scan period as given by equation 4.8.

$$\Gamma_{ads} = \sum \Gamma_{ads}^{t(i)} = \sum \frac{(C_{solution} - C_{eluting}^{t(i)}) Q_{capillary} \Delta t}{\pi D_{capillary} L_{capillary}} \quad (4.8)$$

Where $D_{capillary}$and $L_{capillary}$ are the diameter and length of the capillary, and Γ_{ads} is the total coverage obtained.

When the protein is replaced with buffer, $\Gamma_{des}^{t(i)}$ is the amount of protein desorbed

at time period *t(i)* and is given by:

$$\Gamma_{des} = \sum \Gamma_{des}^{t(i)} = \sum \frac{C_{eluting}^{t(i)} Q_{capillary} \Delta t}{\pi D_{capillary} L_{capillary}} \quad (4.9)$$

where Γ_{des} is the total amount of desorbed protein.

Figure 4.2A presents data for 0.01 mg/mL RmAb at pH7 electrosprayed through a bare capillary for up to ≈ 100 capillary volumes, while Figure 4.2B shows size distributions for RmAb as a function of time when the sample is replaced with buffer. In this case, RmAb first appears at ≈ 72 capillary volumes consistent with results obtained before when sucrose was used as a "marker". Figure 4.2C displays the total counts of RmAb as a function of time and the plot is divided into four domains. Domain I is characterized by zero signal intensity due to the adsorption of nearly all protein to the glass capillary surface. Domain II is characterized by a rapid rise in counts following saturation of the RmAb surface coverage. Domain III is where RmAb signal reaches steady state. Domain IV is during buffer rinse where a rapid decay in RmAb signal occurs. It should also be noted that the mobility size of the RmAb monomers and dimers obtained during desorption (domain IV) are equivalent to that obtained during adsorption, and that the desorbing species are primarily

monomers, although from this measurement one cannot be certain that the desorbed monomer is in its native state. Figure 4.2D shows the resulting surface coverage (mg/m^2) as a function of time, determined from equation 4.8. A maximum steady-state coverage of ≈ 4 mg/m^2 is determined, which only slightly decreases during the desorption period. The dotted line in domain I represents no protein eluting and thus the intial rate of protein adsorption is unknown. The next section compares the coverages with previously reported values.

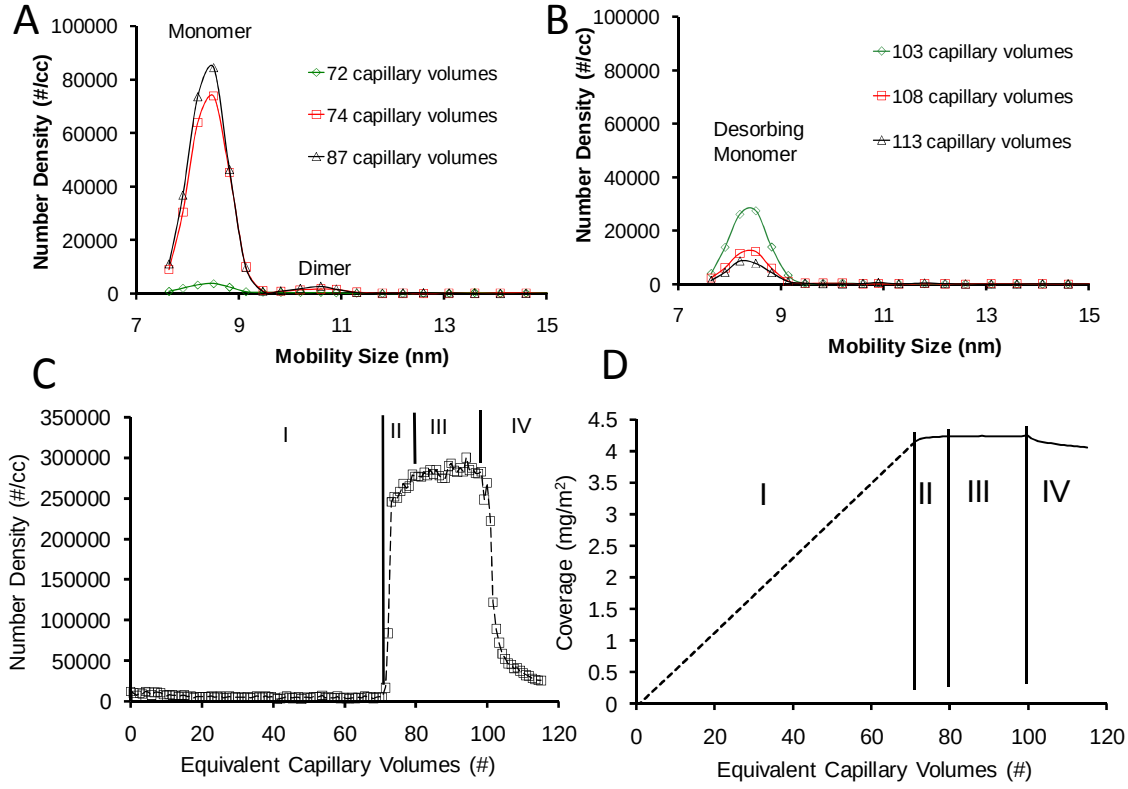

Figure 4.2: (A) Size distributions of RmAb. (B) Size distribution as a function of time. (C) Sum of the monomer and twice the dimer counts as a function of time. (D) Surface coverage as a function of time for RmAb.

4.1.5 Concentration and pH dependent adsorption-desorption of RmAb

As the methodology for determining coverage, and adsorption-desorption kinetics, is now established these parameters can then be determined at different conditions. Experiments like those shown in Figure 4.2 were carried out at four different concentrations of RmAb: 0.01 mg/mL, 0.02 mg/mL, 0.05 mg/mL and 0.1 mg/mL at pH 7.0. The capillary volume at which RmAb started eluting was found to be inversely proportional to solution concentration as shown in Figure 4.3A. For example at 0.01 mg/mL the first evidence of RmAb appears at ≈ 72 capillary volumes as shown in Figure 4.2C before, likewise, RmAb starts eluting after ≈ 38 capillary volumes, ≈ 13 capillary volumes and ≈ 7 capillary volumes for 0.02 mg/mL, 0.05 mg/mL and 0.1 mg/mL respectively. It is also evident from Figure 4.3A that the total gas phase counts is linearly correlated with the liquid phase concentration, i.e. the gas phase density of 0.02 mg/mL, 0.05 mg/mL and 0.1 mg/mL solutions after steady state are about two times, five times and ten times that of the steady state gas phase density of 0.01 mg/mL solution implying that the recovery in all these cases are the same and that the ES-DMA is linear in this concentration range. Size distributions were obtained for 15 to 20 capillary volumes after steady state had been attained for each of the above cases after which, the RmAb samples were replaced with buffer and size distributions obtained for ≈ 15 capillary volumes, to determine the desorption rate. The same methodology was adopted for the pH study. For clarity only one set of experiments have been shown in Figure 4.3A.

Using equation 4.5 and 4.6, the surface coverage of RmAb on the glass capillary surface and the amount desorbed are plotted as a function of RmAb solution concentration in Figure 4.3B. The error bars are standard deviations determined from

2-3 experiments. Within experimental uncertainty, the amounts of both absorbed and desorbed RmAb appear to be relatively independent of protein concentration.

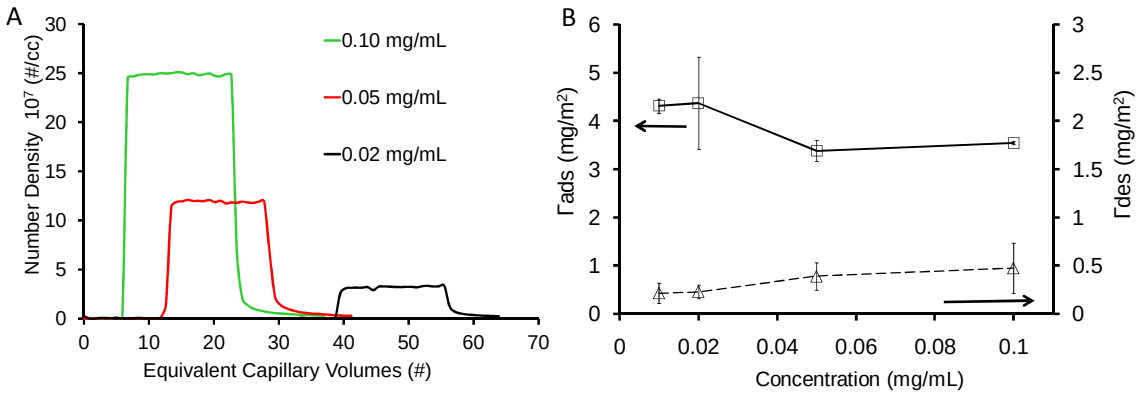

Figure 4.3: (A) The total gas phase density of RmAb as a function of time expressed in equivalent capillary volumes at four different concentrations at pH 7.0. (B) Adsorbed (open square) and desorbed amounts (open triangle, dotted line) of RmAb per unit area as a function of concentration.

Other groups have reported that protein adsorption increases as a function of concentration at both stagnant to high shear flow conditions [106-109] which is in direct contrast to what is shown in Figure 4.3B. Nonetheless, the coverages of 3.5 – 4.3 mg/m^2 determined here for concentrations ranging from 0.01 mg/mL to 0.1 mg/mL fall within the range of 2 – 18 mg/m^2 reported in the literature for silica surfaces [106-115]. The reasons for the breadth of values may be attributed to differences in surface properties [116], ionic strength [106, 107, 117, 118] , pH [113, 114, 117, 119] and different immunoglobulins [113] .

Using simple structural models for RmAb one can estimate if adsorption is monolayered or multilayered. For a typical IgG, the projected side (53 nm^2) and frontal areas (94 nm^2) [19] give corresponding coverages of 4.6 mg/m^2 and 2.6 mg/m^2,respectively. The experimental values of 3.5 – 4.3 mg/m^2 in Figure 4.3B fall within this range suggesting approximately monolayer coverage for RmAb on the

glass capillary surface; however, one cannot exclude the possibilities of mixed orientations or coverages, or surface induced aggregation or conformation changes that would change the adsorbed area of the protein [106, 119-122]. Many studies have proposed monolayer adsorption even for coverages up to 18 mg/m^2 for IgG [119, 123, 124], although multilayer adsorption has been reported by many others [117, 121, 125-127].

The effect of pH on adsorption of RmAb was also examined. Figure 4.4 shows the amount of RmAb adsorbed (primary axis) and desorbed per unit area (secondary axis) of the capillary as a function of pH at a concentration of 0.1 mg/mL and error bars are obtained by obtaining data at least in duplicate. The highest surface coverage was observed near the isoelectric point (pI) of the protein. These results are consistent with the domed shaped profile commonly reported by others [114, 118] suggesting that intermolecular electrostatic repulsion effects may be important in influencing protein surface coverage. It should be pointed out that the pH study was limited to pH 9.0 since buffers at ≈ pH 10 start etching of the silica capillaries that produced significant noise in the size distributions making data interpretation difficult.

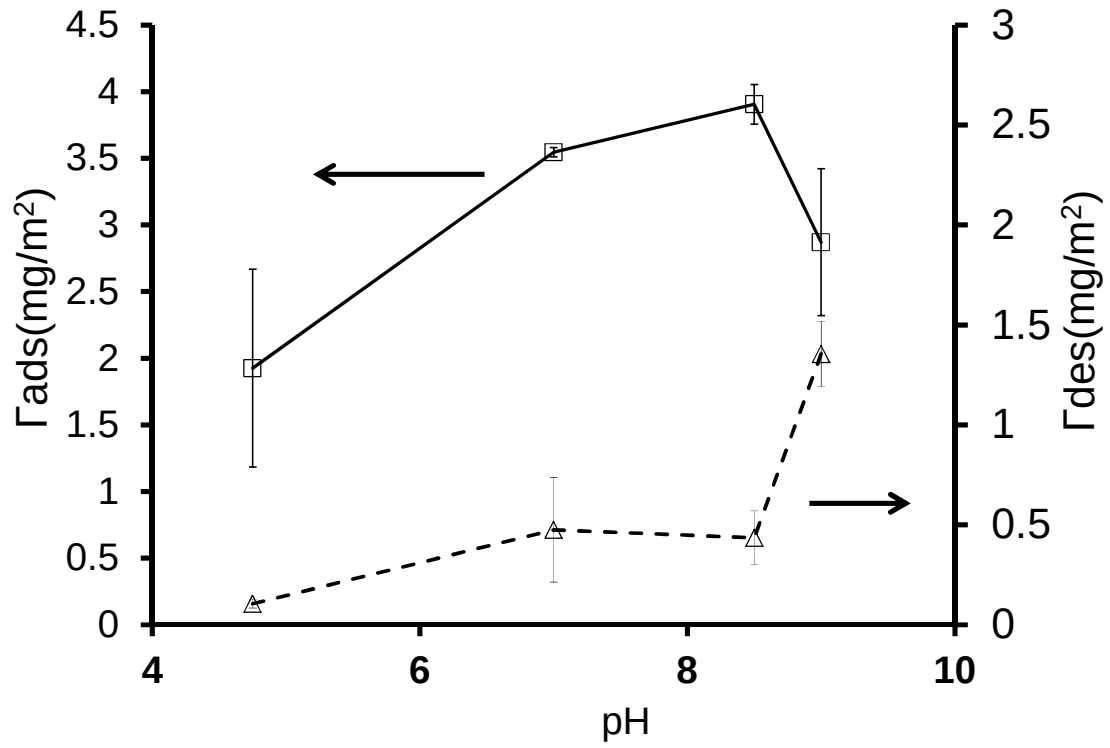

Figure 4.4: Adsorbed and desorbed RmAb per unit area as a function of pH at concentration of 0.1 mg/mL.

The amount of RmAb desorbed was also quantified at pH 4.75, 7.0, 8.5 and 9.0 to be 0.11 ± 0.02 mg/m2, 0.48 ± 0.26 mg/m^2, 0.44 ± 0.13 mg/m^2 and 1.35 ± 0.16 mg/m^2 respectively which translates to 5.5 %, 15.3%, 11.1 % and 47% of the amounts adsorbed. Buijs *et al* [113] using reflectrometry found ≈ 10% desorption of IgG from silica consistent with the findings in this section.

4.1.6 Desorption rate constants

Based on the desorption data, one can also extract kinetic rate constants. Assuming that desorption over the 90 sec scan time is constant, one can determine the number of particles that desorb, $N_{desorb,gas}^{t(i)}$, by integrating the area under the monomer peak. Then the number of particles desorbing is $N_{desorb,liquid}^{t(i)}$, such that

$$N_{desorb,liquid}^{t(i)} = N_{desorb,gas}^{t(i)} Q_{cpc} \Delta t_i \alpha \qquad (4.10)$$

At any time *t(i)*, the amount of particles remaining on the surface, denoted by $N_{surface}^{t(i)}$ is,

$$N_{surface}^{t(i)} = N_{surface}^{total} - N_{desorb,liquid}^{t(i)} \quad (4.11)$$

where the total number of particles on the surface $N_{surface}^{total}$ is calculated from the size distribution as determined by the DMA, the area of the capillary, and assuming monolayer coverage.

The desorption rate is the change of surface concentration with time, which is assumed to be a first order process, and is integrated to give:

$$\log\left(\frac{N_{surface}^{t(i)}}{N_{surface}^{total}}\right) = -K_{desorption}(t(i) - 0) \quad (4.12)$$

Where $K_{desorption}$ is the desorption rate constant

Using equation 4.12, the rate constants of desorption for the concentrations studied are found to be $\approx 10^{-5}$ sec^{-1} and invariant of concentration. The desorption rate constants at pH 4.75, 7.0 and 8.5 were determined to be $\approx 10^{-5}$ sec^{-1}, whereas for pH 9 it was $\approx 10^{-4}$ sec^{-1}. The higher desorption rate at pH 9.0 may be caused by electrostatic repulsion between the silica and adsorbed protein. The desorption rate constants are listed in Table 4.1. Using X-ray photoelectron spectroscopy, Ball *et al* [120] found desorption rate constant for IgG to be $\approx 10^{-5}$ sec^{-1}, consistent with above results. Because the experiments by Ball et al. were performed under stagnant conditions, the reasonable agreement of results implies that shear does not considerably affect desorption rate constant for RmAb on a glass capillary surface.

Table 4.1. Desorption rate constants at different concentrations and pH.

Concentration (mg/mL) varied at pH 7.0	Desorption rate constants (sec^{-1})	pH varied at concentration 0.1 mg/mL	Desorption rate constants (sec^{-1})
0.01	$1.8\times10^{-5}\pm7.1\times10^{-6}$	4.5	$2.2\times10^{-5}\pm2.5\times10^{-6}$
0.02	$1.9\times10^{-5}\pm1.0\times10^{-5}$	7.0	$2.7\times10^{-5}\pm4.2\times10^{-6}$
0.05	$1.9\times10^{-5}\pm3.5\times10^{-6}$	8.5	$2.7\times10^{-5}\pm1.4\times10^{-6}$
0.1	$1.7\times10^{-5}\pm2.4\times10^{-6}$	9.0	$1.2\times10^{-4}\pm5.8\times10^{-6}$

4.1.7 Summary

The ES-DMA method offers the possibility to study 'label-free' competitive as well as sequential adsorption of oligomers of the same proteins and or multiple proteins under high shear ($\approx10^4$ sec^{-1}). pH (4.75 to 9.0) and concentration based studies were performed for RmAb (0.01 mg/mL to 0.1 mg/mL), on silica at pH 7.0. Concentration does not seem to have an effect on the amount of protein adsorbed at high shear flow conditions for RmAb. The pH studies show maximum adsorption around the pI of RmAb consistent with literature. The desorption rate constants were found to be consistent with other studies at static conditions implying that shear may not have a significant effect on desorption kinetics. It should be mentioned that this methodology can also, in principle, be adapted by the mass spectrometry community for studying protein adsorption-desorption on and from silica capillaries although because the number of charges on proteins would be solution pH specific, quantitation of adsorption-desorption would be more complicated. Such an issue does not arise for the ES-DMA since a Po-210 charge neutralizer is used. It should also be pointed out that as a tool ES-DMA cannot provide insights into the thermodynamics of the protein

adsorption process and the reader would have to refer elsewhere for understanding it better [112, 128-130].

4.2 Oligomeric protein adsorption-desorption to ES silica capillaries

4.2.1 Introduction

As already pointed out in chapter 4.1, protein adsorption to surfaces is ubiquitous and is of great importance to the bio-pharma industry and food processing. Often times, to emulate the complexity inside human plasma, the adsorption of multiple protein systems are studied on to different surfaces. For identifying different proteins from such a system it is common to use radio, fluorescent or gold labeling [85, 93, 131]. However, labeling may change the conformation stability of proteins, and affect their adsorption behavior or even promote aggregation in proteins [87, 95, 96]. To avoid the adverse effects of labeling, other “label-free” tools have been employed such as size exclusion chromatography [87, 95, 96], electrophoresis [128], ellipsometry [132, 133], spectroscopy [134], surface plasmon resonance [101], quartz crystal microbalance [135], tensiometry [132], reflectrometry [136], shear rheology [125], surface force apparatus [137] and imaging techniques [138]. However, there are only a few reports where these tools have been employed on oligomers (monomers, dimers etc) of the same protein [87-89]. The objective of this section is to demonstrate that ES-DMA is one such tool that can be employed for routinely studying adsorption-desorption of heterogenous protein mixtures. This is demonstrated by considering bovine IgM that contains large proportions of monomers and dimers.

4.2.2 Sample preparation

4.2.2.1 Protein sample preparation

Bovine IgM (Sigma Aldrich, St Louis, MO, 078K4779) obtained in concentrations of 1 mg/mL was desalted using 10 kDa molecular weight cut off centrifuge filter from Amicon using the same methodology as adapted for RmAb and described in Chapter 4.1. It was then diluted 10 times to concentrations of 0.1 mg/mL for use in the ES-DMA.

4.2.2.2 Capillary surface preparation and passivation

For the electrospray source and adsorption studies, 24 cm long and 25 μm internal diameter fused silica capillaries were used. Capillaries were treated with ~ 1.0 M H2SO4 for 20-30 minutes, and then rinsed with deionized (18 MΩ/cm) ultrapure water for another 10 minutes. Prior to ES-DMA experiments, capillaries were cleaned by electrospraying with 20 mmol/L ammonium acetate buffer solutions for 5 – 10 minutes before insertion of the desired sample. Capillaries undergoing this treatment are referred to as “bare”.

Stock gelatin (Knox, trade name: Gelatine, # 0-41000-03500-5) solutions were prepared by suspending 1 – 1.5 mg in 1 – 1.5 mL of buffer of 20 mmol/L ammonium acetate at the pH 7.0 in low protein binding vials (Eppendorf). The 1 mg/mL solution was then heated to about 50^0 C for approximately 5 minutes to dissolve the protein in solution. The samples were then diluted to 0.1 mg/mL solution, and used to coat the capillaries. Further details of the protocol for coating the capillaries will be provided in Chapter 4.3. Solutions of gelatin were prepared freshly each time the capillaries were coated.

4.2.2.3 ES-DMA

The experimental conditions were same as the previous section and thus are not discussed here.

4.2.3 Results and Discussion

The mathematic modeling for determination of the coverage of IgM onto ES surface would essentially remain the same as before (Chapter 4.1) with slight modifications arising from the heterogeneity of the sample. For example, expression for $C_{eluting}$ in equation 4.5 above needs to be slightly modified for such an oligomeric system. Defining C_{sol}^{M} and C_{sol}^{D} as the measured monomer and dimer solution concentration respectively such that the total concentration C_{tot} is given by (assuming higher order oligomers are negligible in concentration):

$$C_{sol}^{M} + 2C_{sol}^{D} = C_{tot} \tag{4.13}$$

Then the respective monomer and dimer gas phase counts can be obtained by correlating C_{sol}^{M} and $C_{sol}^{D}$with C_{gas}^{M} and C_{gas}^{D}using $\alpha^{M}$and α^{D} in equation 4.5, 4.6, 4.7. Further, different oligomers can have different projected areas upon adsorption depending on their orientation while approaching the surface as shown in Figure 4.5. One needs to especially take this into account for estimating whether the coverage is monolayered or multilayered. Although this aspect is not addressed in this dissertation, the possible orientations are shown in Figure 4.5, nevertheless.

As the surface is a heterogenous mixture of the monomers and dimers, assuming that the heterogeneity is proportional to the maximum coverages of monomers and dimers, the total monomer on the surface $N_{surf}^{M,\ total}$ can be written as below

$$N_{surf}^{M,total} = \Gamma_{M}^{pl} \times \frac{N_{av}}{MW_{monomer}} \times \pi D_{capillary} L_{capillary} \tag{4.14}$$

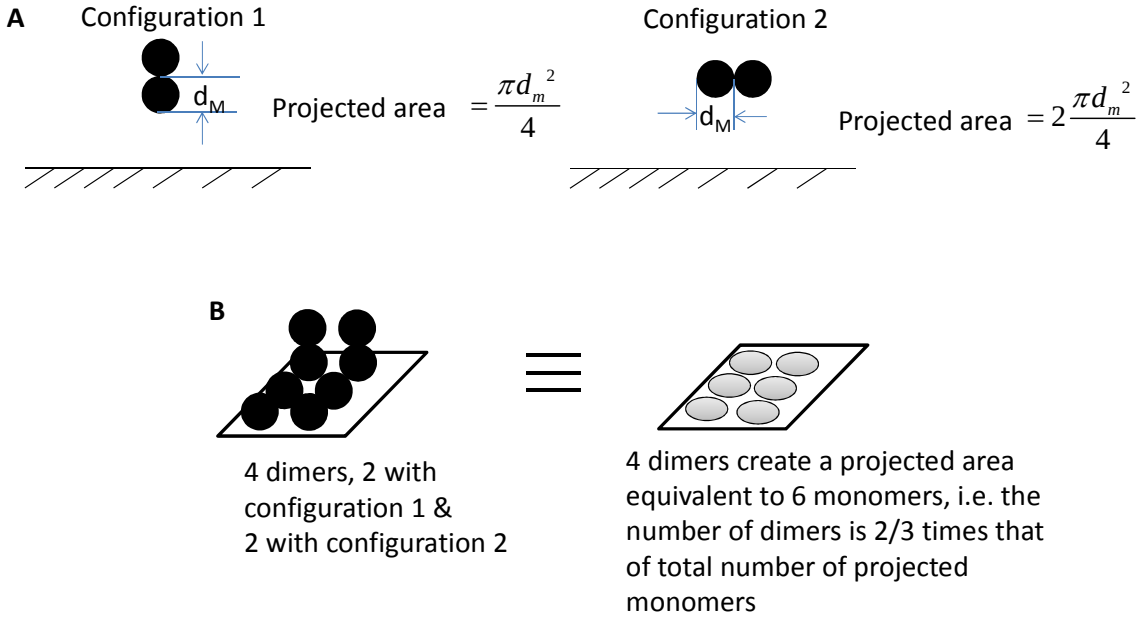

Figure 4.5: (A) Two simplest possible configurations of dimers attaching to the surface of ES capillary. (B) Projected area occupied by dimers assuming equal probability of both configurations.

Where Γ_M^{pl} is the maximum (plateau) monomer coverage, d_M is the diameter of the monomer determined by ES-DMA, $d_{\text{capillary}}$ and $L_{\text{capillary}}$ are the diameters and lengths of the capillary, respectively and N_{av} is Avagadro's number and MW_{monomer} is the molecular weight of the monomers.

As the number of dimers on the surface is irrespective of the orientation, hence the total number of dimers on the surface can be determined using:

$$N_{surf}^{D,total} = \Gamma_D^{pl} \times \frac{N_{av}}{MW_{dimer}} \times \pi D_{capillary} L_{capillary} \qquad (4.15)$$

Where Γ_D^{pl} is the maximum dimer coverage and MW_{dimer} is the molecular weight of the dimers.

Then, following the same methodology as outlined in section 4.1.6, the rate constant for the monomers K_{des}^{M} and dimers, K_{des}^{D} can be determined by replacing

$N_{des,g}^{M,t(i)}$ with $N_{des,g}^{D,t(i)}$, $N_{des,l}^{M,t(i)}$ with $N_{des,l}^{D,t(i)}$, $N_{surf}^{M,t(i)}$ with $N_{surf}^{D,t(i)}$ and $N_{surf}^{M,total}$ with $N_{surf}^{D,total}$ in equations 4.10 to 4.12.

Figure 4.6A shows mobility size distributions of 100 µgm/mL of IgM in 20 mmol/L ammonium acetate buffer at pH 7.0 while Figure 4.6B shows mobility distributions for desorbing IgM when the protein solution was replaced with buffer after about 50 capillary volumes. Both Figure 4.6A and 4.6B consists of two major peaks that can be identified as monomers and dimers of IgM based on an empirical correlation between mobility size and molecular weight. It will be demonstrated in chapter 5 that the size distribution of IgM is intrinsic solution distribution. For now the reader needs to just accept this information. As it is clear from Figure 4.6A that IgM has significant dimers along with monomers hence it is used as an example of a polymeric protein in this section. In Figure 4.6A, the monomers and dimers of IgM increased monotonically immediately after insertion of sample, and the mobility of the monomers and dimers stayed constant at 15.6 nm and 19.2 nm throughout the experiment. Using reasonable numbers for diffusivity (10^{11} m^2/s) for IgM monomers, the characteristic diffusion time can be determined to be ~ 16 s to traverse the radius of the capillary. This is approximately a factor of 8 smaller than the capillary residence time, which in this regard is ≈ 2 min. This implies that the time dependent mobility distributions cannot be ascribed to mass transfer effects, and must be associated with the intrinsic kinetics of adsorption.

The area under the monomer and dimer peaks from each mobility size distribution are integrated and presented in Figure 4.6C as a function of time. Domain I represents the initial phase of adsorption, followed by a step change represented by domain II (capillary volumes 15 onwards), and domain III which is the steady state (capillary volume 33 onwards) condition. Domain IV is when the protein was

replaced with the buffer (capillary volume 52 onwards). From this data, the coverage of protein adsorbed onto ES capillary can also be determined as was demonstrated with RmAb (using C_{sol}^{M} and $C_{sol}^{D}$with C_{gas}^{M} and C_{gas}^{D}using $\alpha^{M}$and α^{D} in equations 4.4 to 4.9). Applying this approach the coverage of IgM monomers and dimers to bare Silica is shown in Figure 4.6D.

Further, by dividing the initial coverage with the initial time (first ~ 20 mins) the initial rate of adsorption was determined to be 0.1 ± 0.02 mg/m^2/min and 0.18 ± 0.05 mg/m^2/min for monomers and dimers respectively. The initial rate of adsorption of IgM dimers is thus about 1.8 times that of IgM monomers. Buijs *et al* [113] found the initial rate of adsorption to be ≈ 1 - 2 mg/m^2/min for IgG at near stagnant conditions using reflectometry, implying that IgM has a much lower affinity to silica than IgG.

The maximum monomer and dimer coverage at steady state were 2.15 ± 0.50 mg/m^2 and 3.75 ± 0.32 mg/m^2 respectively. Tengvall *et al* determined IgM adsorption to hydrophobic silica to be as much as 15 mg/m^2 [139]. On the other hand Lea *et al* found submonolayer (34 %) coverage of murine IgM onto mica surface using AFM [140]. As already described in chapter 4.1, this broad variation in literature could be because of several reasons, such as, different IgMs used, the surfaces, characters of the surfaces, buffers used, ionic strength of solutions, pH etc. Nevertheless, the results obtained here with ES-DMA are well within this broad range of values found in literature.

The desorbed amounts of monomer and dimer per unit area were calculated to be 0.49 ± 0.3 mg/m^2 and 0.08 ± 0.02 mg/m^2, respectively, i.e. 22.8% of monomers desorb while only 2.1% of dimers desorb, implying less dimers come off the surface

when flushed with buffer. This is also evident qualitatively by comparing Figure 4.6A and Figure 4.6B. The dimer/monomer ratio in desorption is significantly smaller than during adsorption that implies that the primary species coming off the surface is monomers. This could be attributed to the larger number of binding sites for IgM dimer compared to its monomer.

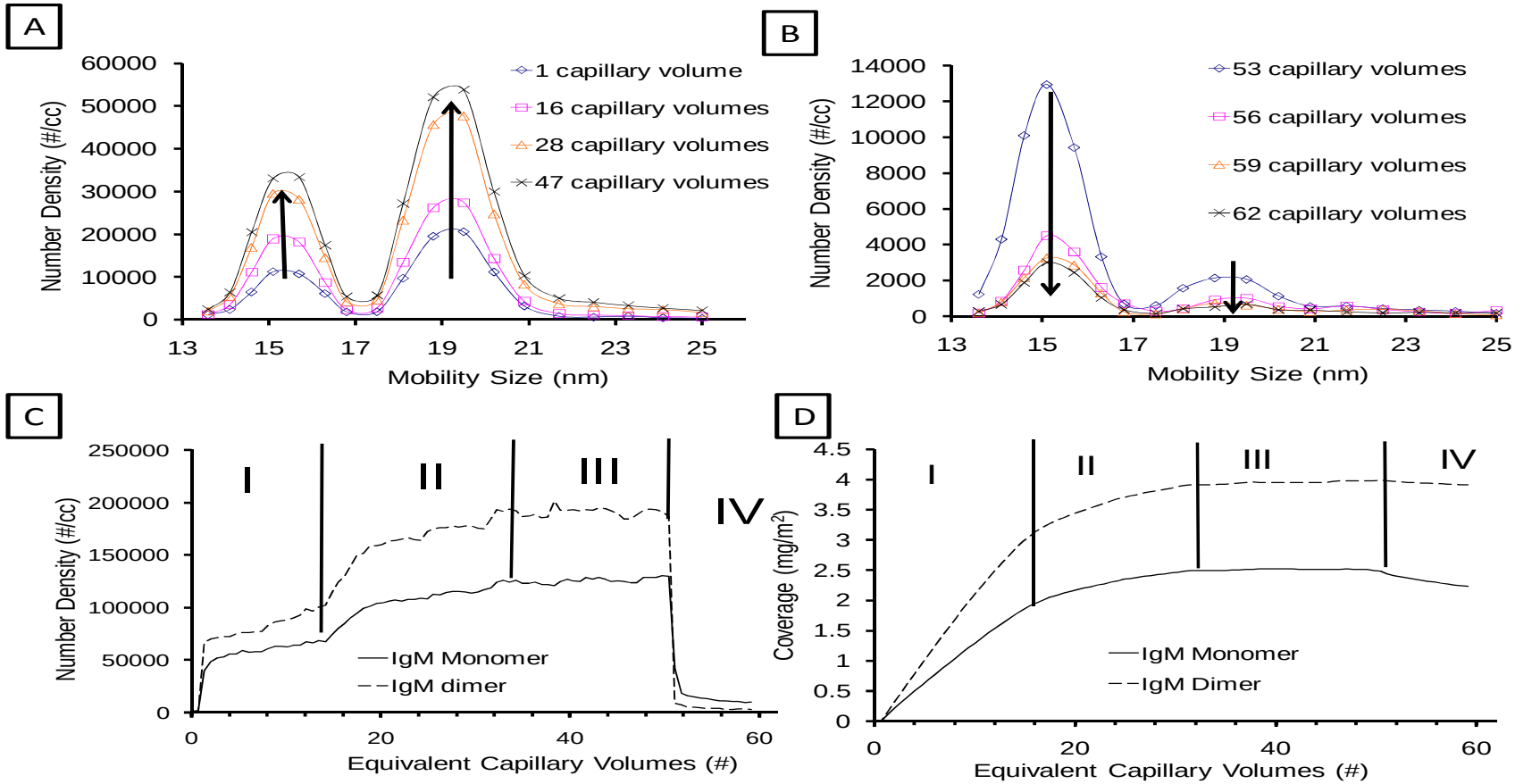

Figure 4.6: (A) Size distributions of monomers and dimers of IgM as a function of capillary volumes during adsorption. (B) Size distributions of monomers and dimers of IgM as a function of capillary volumes during desorption. (C) Integration of the monomer and dimer peaks obtained from size distributions at each capillary volume as a function of capillary volumes. (D) Coverage of monomer and dimers of IgM at the same conditions as a function of equivalent capillary volume.

In chapter 4.3 it will be demonstrated that gelatin passivated silica capillaries prevent adsorption of different immunoglobulins effectively. However, upon electrospraying IgM through such a gelatin passivated surface it was found, significant adsorption, and the adsorption-desorption pattern is also significantly different from a bare surface as discussed here. Firstly no monomer or dimer of IgM elution for ≈ 4 capillary volumes were observed, implying that in contrast to IgG, IgM has a greater affinity towards gelatin and that the kinetics of adsorption is not mass transport limited. This was followed by a sudden increase in monomer intensity (Figure 4.7A) that also corresponds to the appearance of dimers. The monomer intensity then decreased while the dimer intensity continued to monotonically increase till both reach a steady state at 11 capillary volumes significantly quicker than the previous case with the bare capillary. During desorption, as shown in Figure 4.7B, the concentration of dimers desorbing was higher than that of monomers, and indeed higher than dimers desorbing from IgM adsorbed to bare silica. Figure 4.7C shows the integrated concentrations divided into three domains: I where initially no protein eluting was seen to elute, followed by preferential expulsion of monomers, domain II (11 capillary volume onwards) where both monomer and dimers reached a steady state, and domain III (53 capillary volume onwards) when the protein was replaced with buffer. The increase in the monomer signal early on does not show any concomitant temporal variation in the dimer adsorption in Figure 4.7C thus one may qualitatively argue that the dimers were not expelling the monomers. It maybe that higher molecular weight species such as trimers, tetramers and pentamers that were present in small quantities (discussed later in chapter 5, Figure 5.1) were responsible for the displacement of the monomers. This adsorption pattern is also referred to as

the “Vroman effect” after the seminal work of Vroman in 1970s when it was shown that low molecular weight proteins would adsorb to a surface first but would subsequently be displaced by high molecular weight proteins [141, 142]. It is not clear as to why such an adsorption pattern is not seen during the adsorption of IgM to bare silica. Qualitatively, this may be because of differing affinities of IgM to bare silica and to gelatin surfaces.

The maximum IgM monomer and dimer coverages are determined to be 0.49 ± 0.07 mg/m^2 and 2.65 ± 0.4 mg/m^2 respectively, which is about a factor of five (for monomer) and two (for dimer) smaller than on a bare capillary. The amount of IgM monomers and dimers desorbed are 0.28 ± 0.2 mg/m^2 and 0.39 ± 0.1 mg/m^2, respectively, i.e. 57% of monomers and 17% of dimers. Thus it is found that IgM adsorption on a gelatin surface is significantly lower compared to a bare silica surface and desorption of both monomers and dimers is significantly increased.

There appear to be three major similarities for IgM adsorption to bare silica and gelatin coated silica: a) The amount of dimers adsorbed in both the cases is higher than monomers as seen in Figures 4.6D and 4.7D. This is not surprising since the dimer would have nominally twice as many antigen binding sites, b) the monomer and dimer mobilities sizes obtained during desorption are invariant of the two surfaces which may either imply that the two surfaces do not cause a significant change in the protein at least within the uncertainty of the instrument which in this regard is about ~ 0.3 nm [15, 143], or that once the proteins desorb from the surfaces they return to their native state and c) the total protein eluting out is the same irrespective of the surface. The third similarity has an important consequence as discussed here. If IgM adsorption to bare silica and gelatin passivated surfaces would have continued, then the respective steady state size distributions would have been “steady state”

distributions and not “equilibrium” size distributions. Because, these gas phase size distributions are same (implying the protein eluting is the same irrespective of surface type), thus it is likely, that IgM adsorption reached the same steady state for both the surfaces. Thus in all likelihood the recovery of the protein from both the surfaces is 100% and thus “steady state” corresponds to “equilibrium”.

It has been qualitatively pointed out earlier, by comparing Figure 4.6B against 4.6A that dimers have a lower propensity to desorb from the surface. This can further be quantified and explored if one were to assume desorption to be a first order process, using the monomer and dimer concentration decay as a function of time during the buffer flush. The detailed analysis as provided above yields desorption rate constants for IgM monomer and dimer of 0.005 ± 0.001 min^{-1} and 0.0011 ± 0.0002 min^{-1}, respectively, from gelatin surface. On the other hand for IgM desorption from bare silica is 0.004 ± 0.0025 min^{-1} and 0.00035 ± 0.00007 min^{-1} for monomers and dimers respectively. These values are well within the wide range of desorption rate constants ($\approx 10^{-4}$ min^{-1} to ≈ 1 min^{-1}) found in the literature [120, 144-146]. Clearly, there are two important inferences: the monomer desorbs faster than the dimer for both surfaces, and the propensity for both the monomers and dimers of IgM to stay adsorbed on the gelatin-passivated surface is lower.

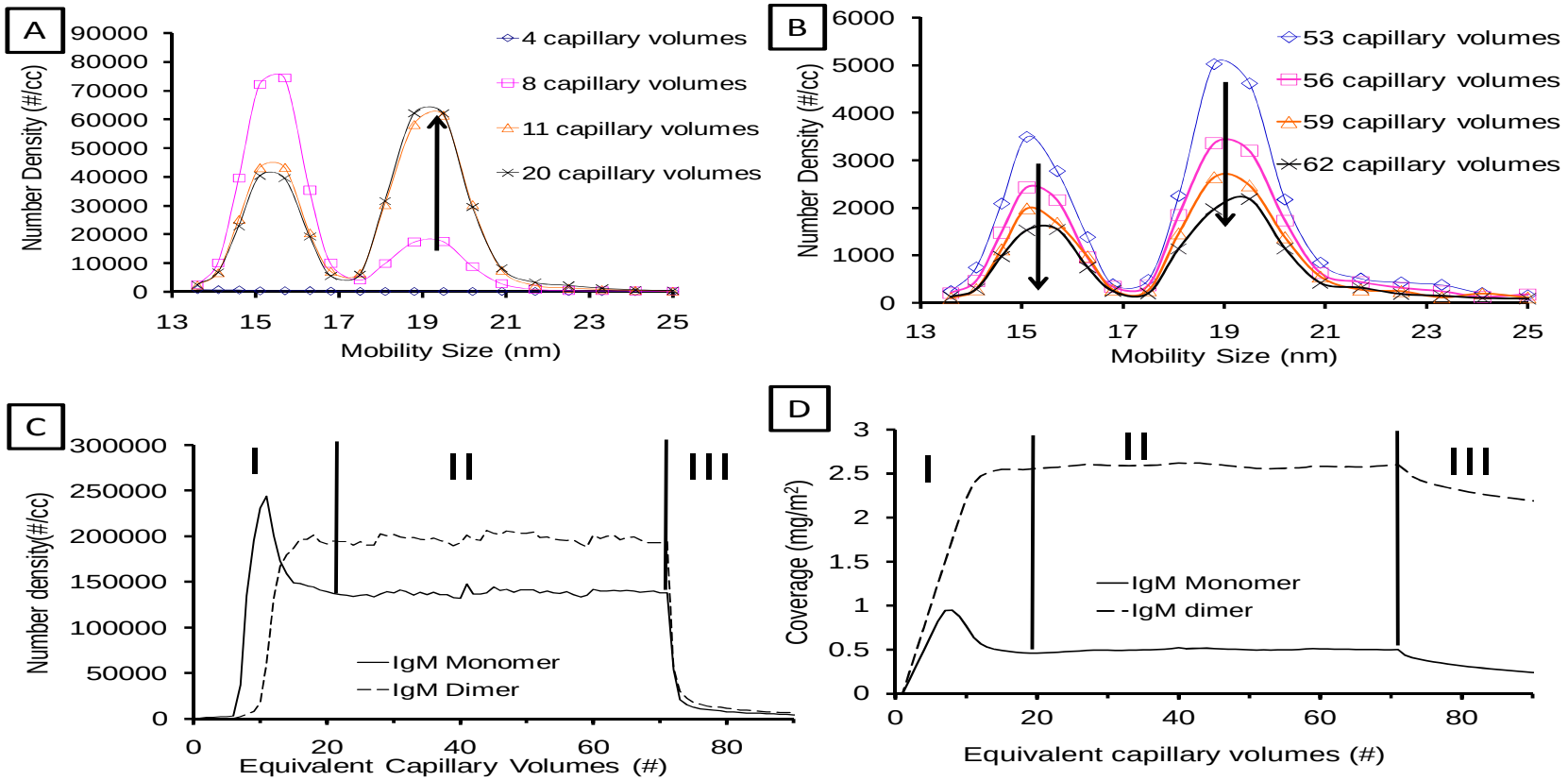

Figure 4.7 (A) Size distributions of monomers and dimers of IgM as a function of capillary volumes during adsorption on a gelatin coated capillary surface. (B) Size distributions of monomers and dimers of IgM as a function of capillary volumes during desorption from the same gelatin coated capillary. (C) Integration of the monomer and dimer peaks obtained from size distributions at each capillary volume as a function of capillary volumes. (D) Coverage of monomer and dimers of IgM at the same conditions as a function of equivalent capillary volumes.

4.2.4 Summary

By selecting a multioligomeric protein, it was demonstrated that ES-DMA can quantify protein-adsorption for heterogenous protein mixtures. For IgM adsorption to bare silica it was found that IgM dimers a) adsorb at a rate faster than IgM monomers and b) have a lesser propensity to desorb compared to IgM monomers. Further, changing the nature of the ES surface showed significant variation of adsorption-desorption trends. For gelatin passivated surface it was found that Vroman effect was observed. For both the surface types, the desorption rate constants are consistent with literature at low shear implying shear does not affect the rate of desorption.

4.3 Influence of protein adsorption-desorption to aggregate distribution

4.3.1 Introduction

One potentially confounding effect in accurately measuring the size distribution of protein oligomers by ES-DMA is the adsorption of the protein to the bare silica capillary. As demonstrated in the last two sections and previously in literature [19, 30] there is compelling evidence that proteinds adsorb to the glass capillary wall. To minimize these effects and for studies were aggregates were quantified measurements of protein size distributions were considered only after the adsorption-desorption process had reached steady-state. However, in these studies, it was assumed that the proteins desorbing from the capillary walls did not influence the size distributions. Recent evidence suggests that proteins adsorbed to surfaces aggregate [147, 148]. Since these aggregated proteins may then desorb, one might reasonably wonder, how these desorbing

proteins may impact size distributions obtained with ES-DMA, an aspect that has never been studied before.

To understand the effect of adsorbed proteins that desorb, the following approach is taken: Experiment I, involves obtaining size distributions of a protein, denoted A, as a function of time until the measured protein monomer signal reaches steady state (which is reached once the surface is saturated with protein A). In experiment II, another protein, denoted B, is used as a blocking agent for passivating a fresh silica capillary until surface saturation. In this case, the size distribution of protein B is obtained again as a function of time as in experiment I. The amount of protein B adsorbed on the surface can be estimated from the time taken for protein B's size distributions to reach steady state and by correlating the gas phase counts obtained with the known liquid phase concentration of this protein at steady state. This determination is described in greater details in chapter 4.1. In experiment III, protein A is electrosprayed through the capillary passivated with B and size distribution of A and its oligomers are measured and compared to results of the bare capillary (experiment I).

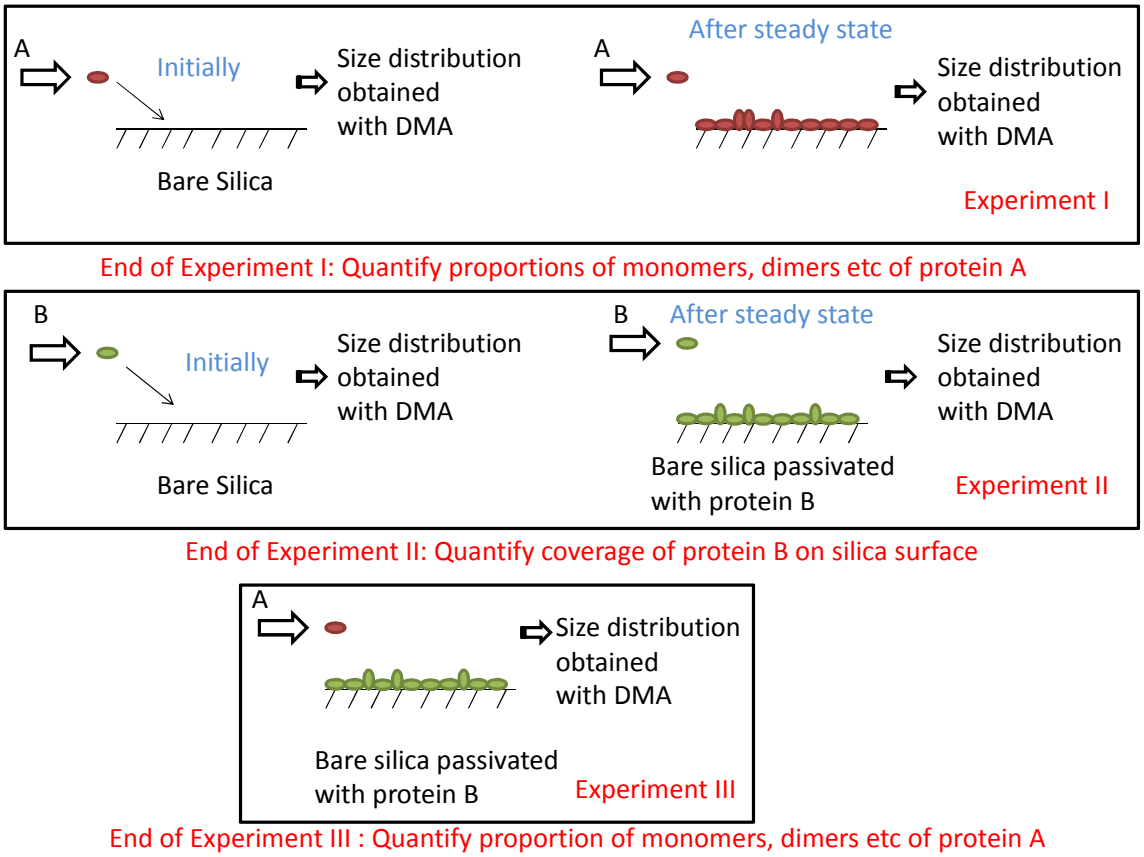

Figure 4.8: Approach taken to study the affect of aggregate distribution as a function of surface passivation.

In this section, the size distributions of four different proteins, bovine serum albumin (BSA), polyclonal human immunoglobulin (hIgG), monoclonal human immunoglobulin (RmAb), bovine immunoglobulin M (IgM) are obtained with ES-DMA using bare and passivated capillaries thus allowing a systematic comparison of the effect of capillary passivation on the quantification of monomers and aggregates of proteins. For surface passivation BSA [149-153] and gelatin [154, 155] were used as blocking agents, each of which can form monolayers or multiple layers on a surface and hence reduce surface adsorption of other proteins.

4.3.2 Materials and Methods

The sample preparation for this samples are already described in sections 4.1 and 4.2. It should be pointed out that in all subsequent experiments in this chapter, upon insertion of the different samples into the ES, one would need to wait about 4 minutes before starting to collect the data, since it would take a finite amount of time for any sample to traverse the full length of the capillary, different tubings and the DMA to eventually reach the CPC. Thus time t = 0 minutes refers to 4 minutes after sample insertion. The total monomer, dimer and trimer counts of the proteins were obtained by integrating the size distributions from 8 nm to 9.4 nm, 9.6 nm to 11.4 nm, 11.6 nm to 12.8 nm for RmAb and hIgG, 6 nm to 7.6 nm, 8 nm to 9.2 nm and from 9.4 nm to 10.2 nm for BSA, and 14.4 nm to 16.4 nm, 18.2 nm to 20.4 nm and 20.6 nm to 22.8 nm for IgM.

4.3.3 Results and Discussion

4.3.3.1 Adsorption of BSA to passivate capillaries

Sections 4.3.3.1 and 4.3.3.2 describe results corresponding to experiment II of Figure 4.8, where BSA and gelatin are used to passivate the capillary surface.

BSA has been widely used as a blocking agent to limit non-specific adsorption of proteins [149-153]. In this section, the protocol for passivating the ES capillaries with BSA is described at pH conditions close to its isoelectric point (pI) of 4.8 [156]. At neutral conditions no significant variation in the size distribution was observed as a function of time using the ES-DMA implying little adsorption.

ES-DMA offers the opportunity to quantify the amount of BSA adsorbed as already described in Chapter 4.1. For BSA passivation, ≈ 0.05 mg/mL of BSA at pH 4.8 is electrosprayed for 1 hour (or approximately 32 capillary volumes) through a new capillary after its surface has been cleaned following the procedure outlined in Section 2.2. In Figure 4.9A, no elution from the capillary is observed for the first 16 capillary volumes, after which the monomer and dimer counts increase monotonically and reach steady state at ≈ 27 capillary volumes. The Y-axis has been offset slightly to show that BSA is not eluting at 16 capillary volumes. After about 60 minutes (32 capillary volumes) the protein sample was replaced with 20 mmol/L ammonium acetate at pH 7.0 and the capillary flushed using this buffer while simultaneously monitoring the size distribution. Figure 4.9B displays mobility spectra during the flushing phase showing that the mobility size of monomers and dimers remained unchanged and that there was a monotonic decrease in the number density of desorbing monomers and dimers.

Figure 4.9C shows the resulting calculated coverage of the BSA as a function of time. Region I in Figure 4.9C, corresponds to when there was no protein eluting, (represented by the dotted line), region II corresponds to when the protein was first observed eluting, and the concentration continued to increase, region III corresponds to steady state, and region IV corresponds to when the protein was replaced with the pH 7.0 buffer. The dotted line represents when no protein is eluting. The monomer, dimer and trimer peaks for each protein are assigned and labeled 1, 2 and 3, respectively, based on well-established empirical correlations between molecular weight and mobility size [11].

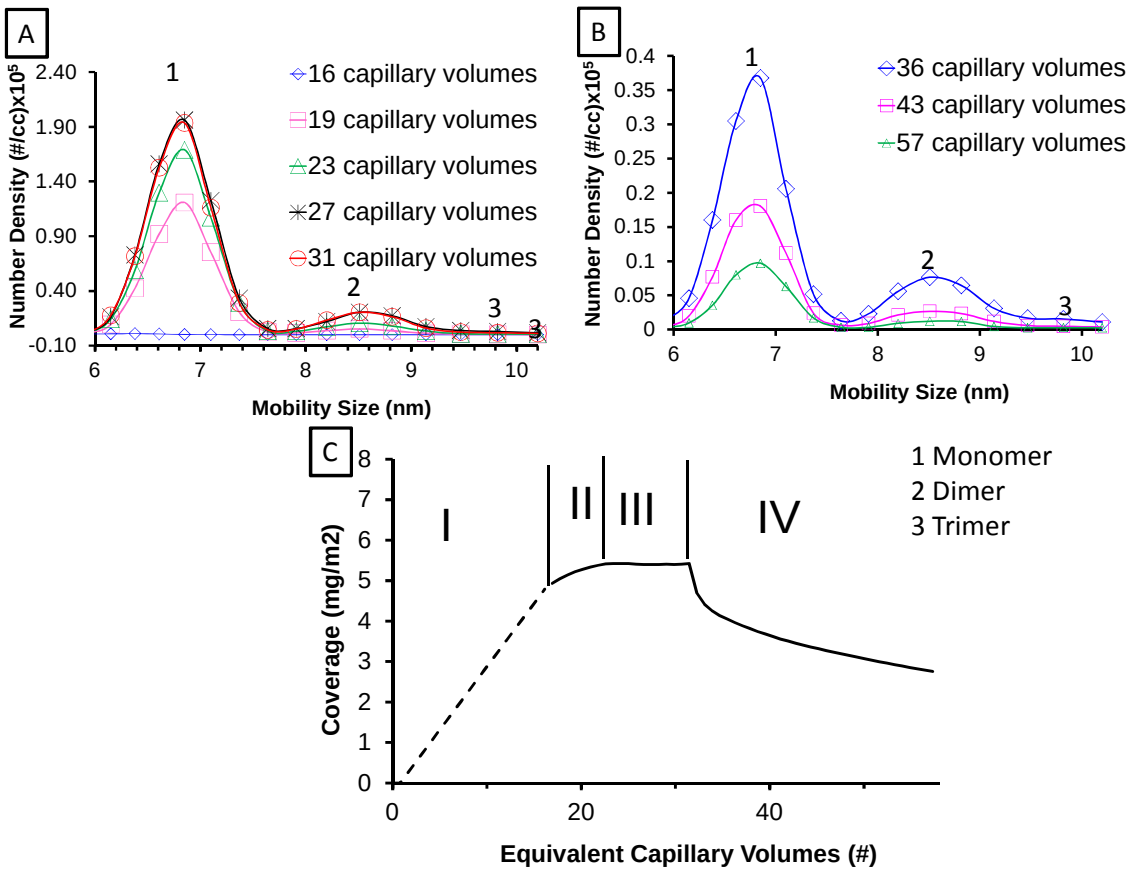

Figure 4.9: (A) Size distributions of monomers, dimers, and traces of trimers (not evident from this figure) of BSA eluting through the capillary as a function of capillary volumes. (B) Size distribution of the desorbing species as a function of capillary volumes when the protein sample is replaced with buffer. (C) Coverage of BSA adsorbed and desorbed as a function of capillary volumes.

The calculated coverage at steady state is determined to be 5.4 mg/m^2 (region III). Assuming that BSA is spherical and using the measured diameter of 6.6 nm obtained by the ES-DMA, then the theoretical coverage of a monolayer is 3.2 mg/m^2, which suggests that adsorption is multilayered. Such a multilayered adsorption scheme can be explained as follows [157]: first a layer of protein adsorbs to the surface and denatures, this promotes the exposure of hydrophobic residues of the first layer of protein which then

attracts a second layer of protein; as the layers build on top of each other, the interaction in between successive upper layers progressively weaken (as the extent of denaturation and exposure of hydrophobic residues are reduced) and thus protein adsorption eventually stops. The coverage obtained here falls within the range of previous studies of BSA adsorption under a variety of conditions where reported coverage values range from 1.2 mg/m^2 to 10 mg/m^2 [158-162]. After ≈ 30 capillary volumes of flushing, the amount of BSA remaining on the surface is estimated to be ≈ 2.8 mg/m^2, which is close to the theoretical coverage of 3.2 mg/m^2 for a monolayer.

4.3.3.2 Adsorption of Gelatin to passivate capillaries

In this section gelatin adsorption is quantified using ES-DMA. The use of gelatin layers to passivate surfaces against protein adsorption has been previously reported [154, 155]. In the current study, gelatin was deposited on glass capillary surfaces by electrospraying ≈ 31 capillary volumes of a gelatin solution through a freshly prepared capillary. The passivation process was also assessed using the DMA. Figure 4.10A shows the mobility distribution as a function of capillary volumes during the passivation. The size distributions are clearly wider than for the other proteins in this paper, and reflect the heterogeneity of gelatin. If the peak mobility is assumed to be 7 nm (Figure 4.10A), and assuming the protein to be an equivalent sphere, the theoretical maximum surface coverage is ≈ 3.0 mg/m^2.

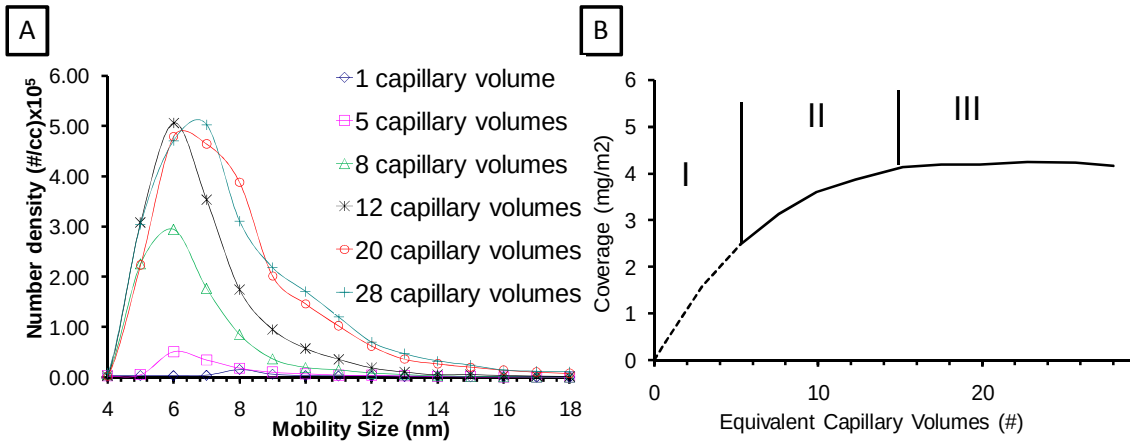

Figure 4.10: (A) Mobility distribution of 0.10 mg/mL gelatin in 20 mmol/L ammonium acetate at pH7. (B) The coverage of gelatin on fused silica as a function of time.

As described above for BSA, one can estimate the surface coverage of gelatin by monitoring the time course evolution of the gelatin signal. Figure 4.10B plots the experimentally determined surface coverage as a function of capillary volume for a gelatin solution concentration of 0.1 mg/ml. Little gelatin is observed initially (upto 5 capillary volumes, domain I). Then the gelatin signal gradually increases and eventually reaches steady state (5 to 20 capillary volumes, domain II), after which there is no significant variation in the size distribution (within experimental variability) as shown in Figure 4.10A (domain III). At steady state the gelatin surface coverage is estimated to be 4.2 mg/m^2, which considering the theoretical estimate of 3.0 mg/m^2 for monolayer coverage, suggests a multilayer gelatin coating. The value of 4.2 mg/m^2 is comparable to coverages obtained for gelatin under different conditions using surface force apparatus, calorimetry and ellipsometry on different types of surfaces [163-167]. An interesting feature of gelatin adsorption is that it appears to be largely irreversible, because little desorption is observed over a wide range of flushing conditions (pH 4.8 to pH 9.0) (data

not shown). It has been suggested that gelatin's strong interaction with surfaces may be due to its ability to form a gel at room temperature by physical entanglement [168]. This behavior is in contrast to the other proteins examined (BSA, RmAb, hIgG and IgM) all of which show significant desorption from unpassivated (i.e. bare) capillaries.

4.3.3.3 Effect of size distribution on passivated, partially passivated and unpassivated capillaries

For bare silica, i.e., for unpassivated surfaces it takes several capillary volumes (10 to 30) for BSA, hIgG, RmAb and IgM size distributions to reach steady state. When a capillary is passivated with BSA the number of capillary volumes to reach steady state is reduced for hIgG, RmAb and IgM (5 to 20 capillary volumes). Although passivation by BSA reduces adsorption of these proteins, some nonspecific adsorption still occurs suggesting protein adsorption to the pre-adsorbed BSA layer thus a BSA passivated capillary will act as a partially passivated surface for hIgG, RmAb and IgM. In contrast, for a capillary passivated with gelatin, it is observed that hIgG and RmAb size distributions reach steady state immediately, while BSA and IgM take time before reaching steady state (5 to 10 capillary volumes). Therefore, one can conclude that the gelatin passivated capillary nearly completely prevents nonspecific adsorption of hIgG and RmAb, while less so for BSA and IgM, i.e. a gelatin passivated capillary is a completely passivated surface for hIgG and RmAb and a partially passivated surface for BSA and IgM.

Because the size distributions of RmAb, hIgG, IgM and BSA were obtained at steady state for unpassivated and gelatin passivated capillaries, and for RmAb, hIgG and IgM steady state size distributions were obtained for a BSA passivated capillary, the

effect of capillary passivation on size distributions can be assessed, i.e. one can compare size distributions obtained in experiment I (Figure 4.8) with those obtained in experiment III (Figure 4.8). Figure 4.11 plots dimer/monomer and trimer/monomer peak area ratios for steady state conditions for unpassivated, BSA passivated, and gel passivated capillaries. The uncertainties are from measurements made in triplicates. The different surfaces appear to have no effect on the observed dimer/monomer and trimer/monomer ratio. Thus, one can conclude that for the proteins and the capillary surface passivation conditions examined here, surface passivation does not alter size distributions measured under steady state condition relative to that obtained using a bare glass capillary (i.e. unpassivated capillary).It should be pointed out that the dimer and trimers seen in these size distributions may not necessarily be intrinsic solution aggregates, as a portion of it may get created by the artificial induction of two or more monomers in the same ES droplet, which is also refered to as “droplet induced aggregation” which will be discussed in the next chapter. This is especially true for RmAb and hIgG as has been demonstrated later. However, in this section the objective is to systematically studying the difference in the distributions before and after passivation. If there was any difference in instrinsic aggregates because of desorbing proteins from unpassivated surfaces, then one would have also seen a difference in the observed distributions as well. The fact that such a difference in aggregate distribution is not seen for different proteins using passivated and unpassivated surfaces implies that the intrinsic solution aggregate proportions for the different proteins considered here also stay the same.

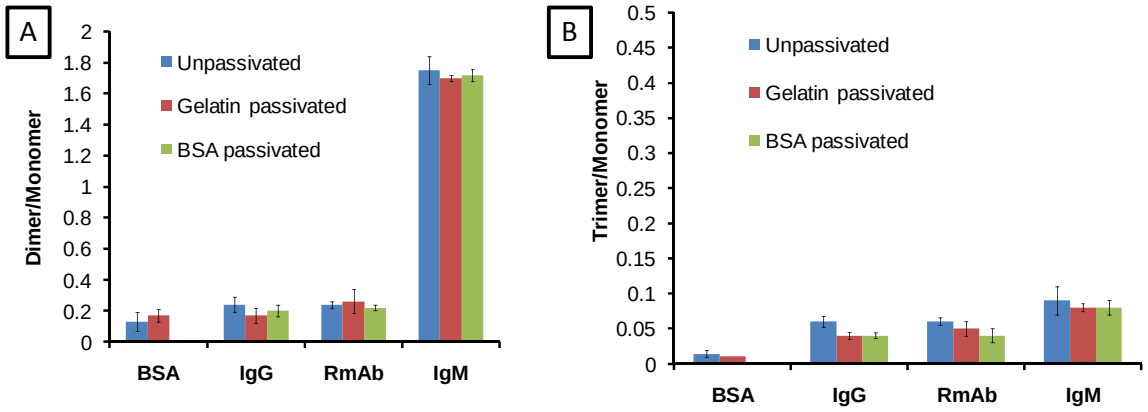

Figure 4.11: (A) Dimer to monomer and (B) trimer to monomer ratios of four different proteins on unpassivated, gelatin passivated and BSA passivated surfaces.

It should be noted that RmAb and hIgG were observed to elute nearly immediately at several different concentrations from gelatin passivated capillaries implying little or no adsorption. These results indicate that protein recovery from a gelatin passivated surface is nearly ≈ 100 %. With an unpassivated or partially passivated surface the eluting monomer, dimer and trimer counts of proteins at steady state are found to be equal (within experimental variability) to the respective counts from a gelatin passivated surface or in other words *steady state in an unpassivated surface also corresponds to equilibrium.*

There could be several possible scenarios for which unpassivated or partially passivated capillaries do not influence the size distributions. Proteins could be desorbing either as monomers or aggregates such as dimers, trimers etc., and could be desorbing in their native form or in denatured state [129, 130, 162]. Careful analysis of the mobility spectra between the desorption and adsorption experiments for all proteins indicate no significant mobility size change in the monomers or dimers indicating that at least to the

level of the instrument resolution, 0.3 nm in mobility diameter [15, 143], there is no discernable changes in protein onformation. Further the desorbing species were primarily monomers. This could either mean the proteins on the surface of the capillary elute as monomers or as dimers or larger aggregates that then dissociate to form monomers during passage through the capillary or the larger aggregates are irreversibly bound to the ES capillary surface and do not desorb at all. Given that the upper limit of the DMA range in its current configuration is 80 nm and that the lower limit of detection is 10^9 particles/mL, it is also possible that large aggregates at low concentration desorb from the surface and pass undetected as well. Irrespective of the mechanism of desorption and the sizes of the desorbing aggregates, it is evident that the desorbing proteins do not influence the aggregate distribution.

4.3.3.4 Efficacy of gelatin passivation in repelling different protein monomers

The strong passivating behavior of gelatin against RmAb and hIgG and the limits of the time resolution of the experiments conducted here precludes one from determining if any adsorption at all is taking place; however, one can perform desorption measurements to estimate the efficacy of passivation. In these experiments, protein is flowed through the capillary until the size distribution reaches steady state and then the capillary (unpassivated and gelatin passivated) is flushed with 20 mmol/L ammonium acetate buffer at pH 7.0. The temporal data for monomer desorption are presented in Figure 4.12 for both unpassivated and gelatin passivated surfaces.

It is evident from Figure 4.12, that desorption of monomers observed from unpassivated capillaries is significantly higher than that seen for gelatin passivated capillaries for RmAb and hIgG. As a metric, a coating efficacy parameter η is defined as:

$$\eta = \frac{Monomer_{unpassivated} - Monomer_{passivated}}{Monomer_{unpassivated}} \quad (4.16)$$

where $Monomer_{passivated}$ and $Monomer_{unpassivated}$ are the desorbed total monomer counts from passivated and unpassivated capillaries at a time of when the buffer starts to elute (at 0 capillary volumes). A value of unity would then imply a perfectly passivating coating or proteins that are adsorbed irreversibly. For Figures 4.12A and 4.12B, data collection for the desorbing RmAb and hIgG from gelatin passivated surfaces were stopped after approximately ≈ 3 to 5 capillary volumes, since the amount of proteins desorbing by then was too little to be quantifiable with the ES-DMA.

Table 4.2 presents the coating efficacy parameter,η, of gelatin for the proteins studied. The gelatin passivation seems to be especially effective in reducing adsorption of antibodies hIgG and RmAb. Gelatin has an isoelectric point (pI) of 4.7 to 5.3 [169] which is close to the pI of BSA (pH 4.8). At pH 7.0, both proteins are negatively charged and yet they show a propensity to adsorb, implying that BSA's affinity towards gelatin results from hydrophobic interactions [113, 156]. On the other hand, hIgG (pI 6.3-9.3) and RmAb (pI 8.5) are fairly neutral or positively charged at pH 7.0, and yet, gelatin which is negatively charged at this pH, repels both the immunoglobulins, the reasons for which are not clear. The pI of the IgM used here is unknown, so it was not possible to determine if the enhanced affinity is due to electrostatic effects or simply because IgM is ≈ five times larger than the hIgG proteins and, thus, has more potential interactions sites per molecule.

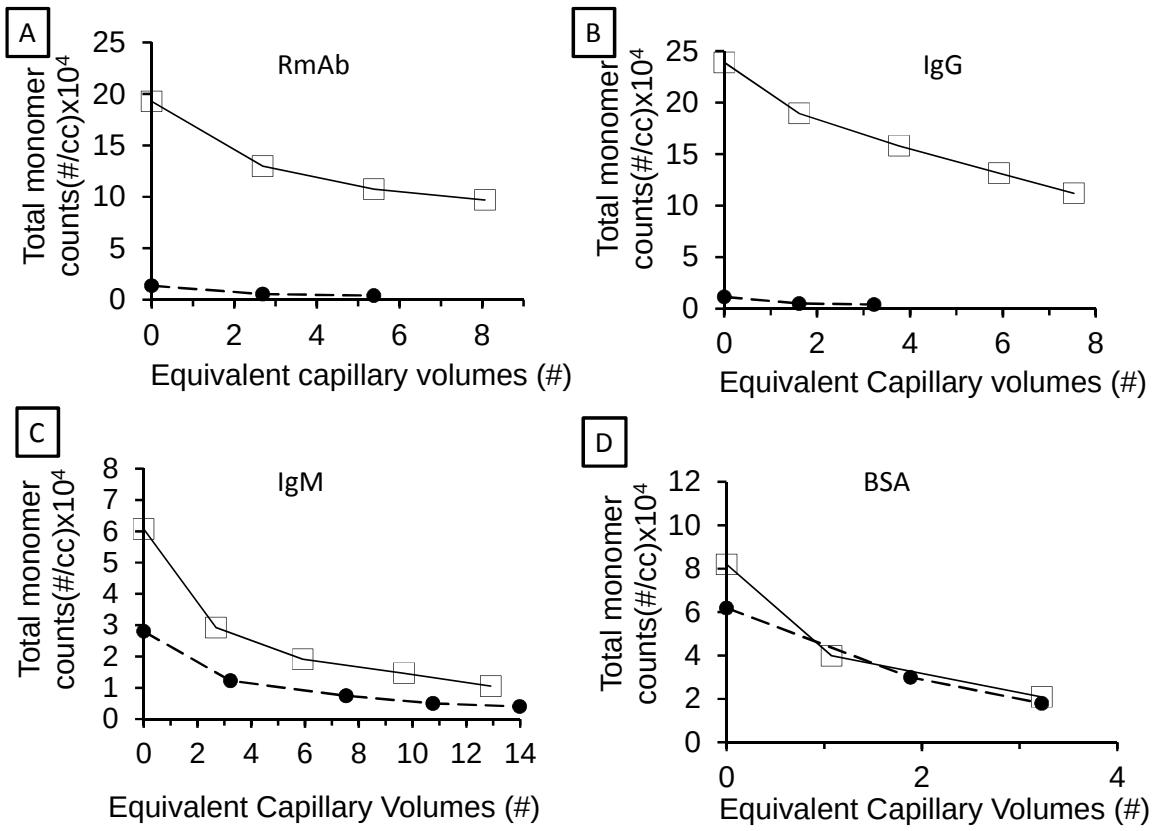

Figure 4.12: Desorption of monomers of RmAb (A), hIgG (B), IgM (C) and BSA (D) for the gelatin passivated (solid circle, dotted line) and unpassivated capillaries (open square, solid line) at pH 7.0.

Table 4.2. Comparison of efficacy of gelatin passivation for each of proteins

Proteins	η
BSA	0.57
hIgG	0.95
RmAb	0.93
IgM	0.54

4.3.3.5 Stability of gelatin passivation

The stability of gelatin passivation over three days was studied by electrospraying RmAb at 0.1 mg/mL at different times. It was found that the size distribution of RmAb reached steady state almost immediately upon sample introduction, indicating that the gelatin passivation was still intact.

Buffers at pH 2.1 to pH 9.0 were flowed through the ES and size distributions obtained with ES-DMA to determine if gelatin was desorbing from gelatin passivated capillaries. No evidence of gelatin desorption was found from pH 4.8 to pH 9.0 although the passivation became unstable under acidic conditions (pH 2.1) and gelatin elution was detected by ES-DMA. Unfortunately gelatin desorption at pH 2.1 could not be quantified directly because the "Taylor cone" at the ES capillary tip was unstable at this pH for an initial period of time, which likely resulted from significant desorption of gelatin. In addition, when RmAb solution (0.1 mg/mL solution, 20 mmoL/L ammonium acetate at pH 7.0) was flowed through a gelatin passivated capillary previously flushed with buffer at pH 2.1 for one hour a significant amount of RmAb was found to adsorb with an estimated coverage of $\approx$ 2.0 mg/m^2. A coverage of $\approx$ 3.4 mg/m^2 for RmAb on a unpassivated glass capillary surface was previously determined using ES-DMA (Chapter 4.1). Thus, it is evident that acid treatment leads to a capillary surface with some exposed silica that act as sites for RmAb adsorption.

4.3.4 Summary

In this section size distributions of four proteins were systematically compared using passivated and unpassivated capillaries at steady state and it was found that size distributions remain unchanged by passivation. Therefore one can conclude, that at least

for the proteins examined in this study, protein adsorption does not influence aggregate distributions measured at steady state by ES-DMA. Although, size distributions of different proteins in this study were obtained using differential mobility analyzer, these findings apply to other techniques that use ES for aerosolization of proteins as well (e.g. mass spectrometry). A simple method of passivating capillaries with BSA and gelatin was presented a coverages of these proteins onto ES capillaries were also quantified in situ using the ES-DMA. Although in the ES-mass spectrometry community it is fairly common to passivate capillaries with polyethylene glycols (PEGs) [48] this is the first time that passivation for ES-DMA has been systematically explored. It was also found that gelatin passivated capillaries are effective in reducing non-specific adsorption of immunoglobulins and are stable upto about 3 days within a pH range of 4.8 to 9.0 although gelatin desorption was observed at low pH (≈ 2.1). In this regard, PEGylation of ES capillaries (data not shown) with 5 kDa and 20 kDa silane PEGs was also undertaken but it was found that gelatin performs significantly better compared to these PEGs. In the future, the coating efficiency of gelatin (or other PEGs or proteins) against several other proteins can also be studied following the above approach.

4.4. Protein Adsorption based Characterization: Preliminary results

4.4.1 Introduction

In the above sections it was shown that several proteins tend to adsorb to the ES silica capillary. For a monomeric protein with high concentration disseminating the size distribution can often be problematic as the same ES droplet can harbor multiple monomers as will be demonstrated in the next chapter. To add further complexity to this problem, if the sample is heterogeneous, constituting different sized proteins then these

proteins may also get encapsulated in the same droplet. Figure 4.13 below demonstrates this problem. Say there is a solution with a heterogeneous mixture of three proteins X, Y and Z. While randomly sampling with ES two monomers of say Protein X or Y or Z may get into the same droplet. If the concentration of all the heterogeneous proteins is known Poisson statistics can be employed to correct for this artifact. This is going to be discussed in further detail in the next chapter. However, in real protein systems, like cell extracts, the concentration of the different mixtures is often very high and unknown. Under such a scenario making sense of the size distribution obtained can be extremely difficult. One approach to overcome this problem is to intentionally adsorb the proteins to the ES columns and then characterize them during desorption as demonstrated below.

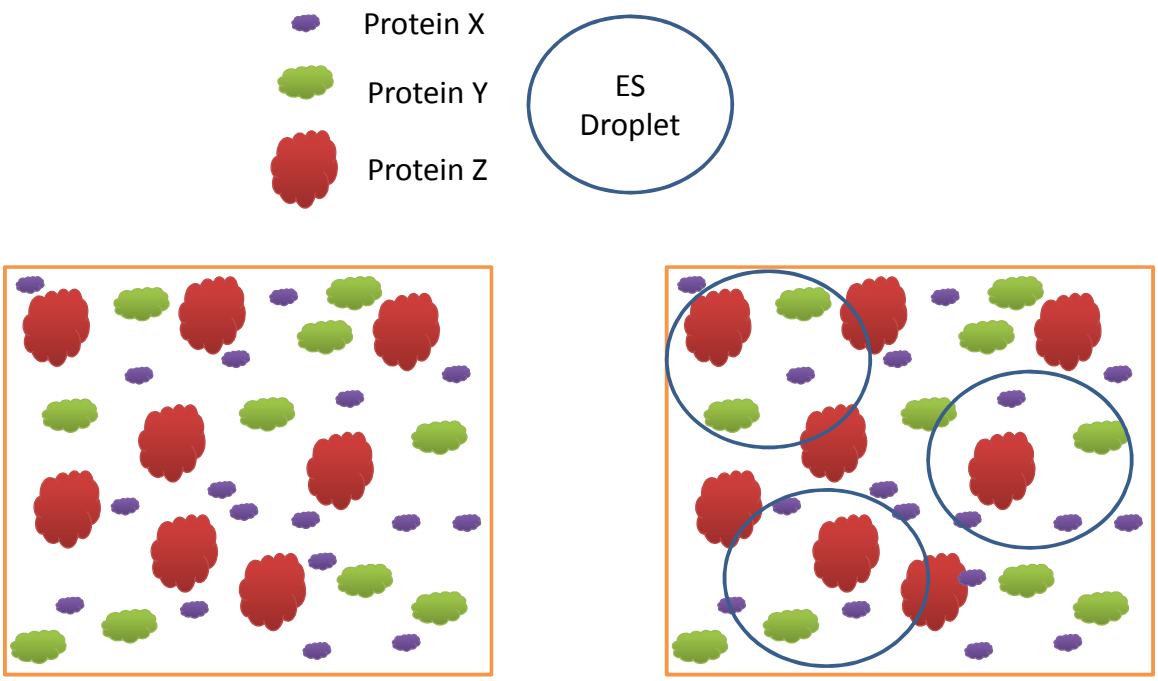

Figure 4.13: (A) A colloidal solution with heterogenous mixture of Protein X, Y and Z. (B) Random sampling with ES droplet might induce different proteins into the same ES droplet.

4.4.2 Materials and Methods

Lyophilized Amelotin (Am) (concentration labeled 0.8 mg) was suspended in 800 µL of 20 mmol/L ammonium actetate at pH 7.0 which produced a 1 mg/mL concentration in solution. It was then diluted 10 times in the same buffer to obtain 0.1 mg/mL sample concentration. A typical experiment conducted would be as follows: after incubating the ES capillary for ~ 1 hour with the above sample, size distributions would be obtained multiple times to ensure that protein adsorption had reached steady state. Then the sample was replaced with 20 mmol/L ammonium acetate buffer and size distributions were obtained every 6 minutes for the protein desorbing from the ES capillary.

4.4.3 Results and Discussion

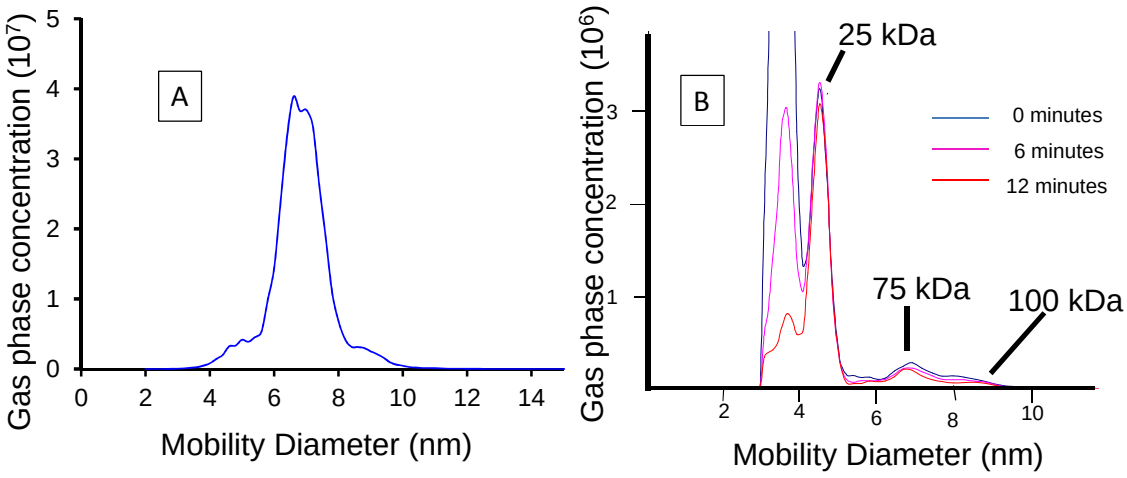

Figure 4.14: (A) Size distribution of 0.1 mg/mL of Am. (B) Size distribution of the same sample during desorption.

Figure 4.14A shows the size distribution of the Am sample at 0.1 mg/mL concentration after steady state. The Am protein has a molecular weight of 25 kDa and thus based on Bacher et al. correlation is expected to appear at a size of ~ 5 nm. Besides

the monomers, the sample was also expected to have larger aggregates although it was not clear what the size of these aggregates would be. Because of the situation explained in Figure 4.13, it was not possible to definitively characterize the sample based on the above size distribution. Instead desorption studies were performed. Figure 4.14B shows the size distribution of the Am desorbing from the ES capillary upon eluting buffer through it. It shows four different peaks. The first peak at size < 4 nm appears to decrease quickly as a function of time implying this species has a low binding strength to the ES silica surface. As its size corresponds to < 20 kDa which is smaller than the Am monomer thus this species is probably smaller protein fragments. The second peak at ~ 5 nm corresponds to the monomer of Am. Two more peaks are identified at ~ 7 nm and ~ 8.5 nm that correspond to the trimers and tetramers of Am.

4.4.4 Summary

Based on the example demonstrated above, it is evident that ES-DMA can be used for highly heterogeneous samples or for sample with high concentrations of proteins by first intentionally adsorbing the proteins to the ES silica capillary and then characterizing them while flushing buffer through the capillary. It should be pointed out that such a study intrinsically assumes that the monomers and larger aggregates do not aggregate or dis-aggregate upon adsorption or during desorption to or from the surface. The experiments shown in this section were exploratory and further experiments need to be conducted in the future.

Chapter 5: ES ARTIFACTS: DROPLET INDUCED AGGREGATION

5.1 Introduction

Although the ES-DMA was primarily developed for size characterization, given the correlation between liquid phase and gas phase, it can also be used for quantification of bionanoparticles as discussed in chapter 3. Of the several classes of bionanoparticles, quantification of protein aggregates is perhaps of most importance (chapter 3). A concern that has only been previously superficially addressed by ES-DMA users is whether the oligomer (or otherwise referred to as aggregate) distributions observed by ES-DMA reflects what is nascent to the liquid solution sampled, or is the analyzed oligomers an artifact of the ES process. It is reasonable to imagine a situation in which during random sampling two or more analyte bionanoparticles occupy a volume encompassing what becomes an electrosprayed droplet (Figure 5.1). In this regard it should be pointed out that particles in liquid follow a Poisson distribution. Eventually as the ES droplet dries up, two or more of these particles would cluster together and would be detected as dimer or trimers by the DMA. As these dimers and trimers were not originally existing in the solution hence they are then artificially induced. In the rest of this dissertation this artifact is going to be referred to as “droplet induced aggregation”.

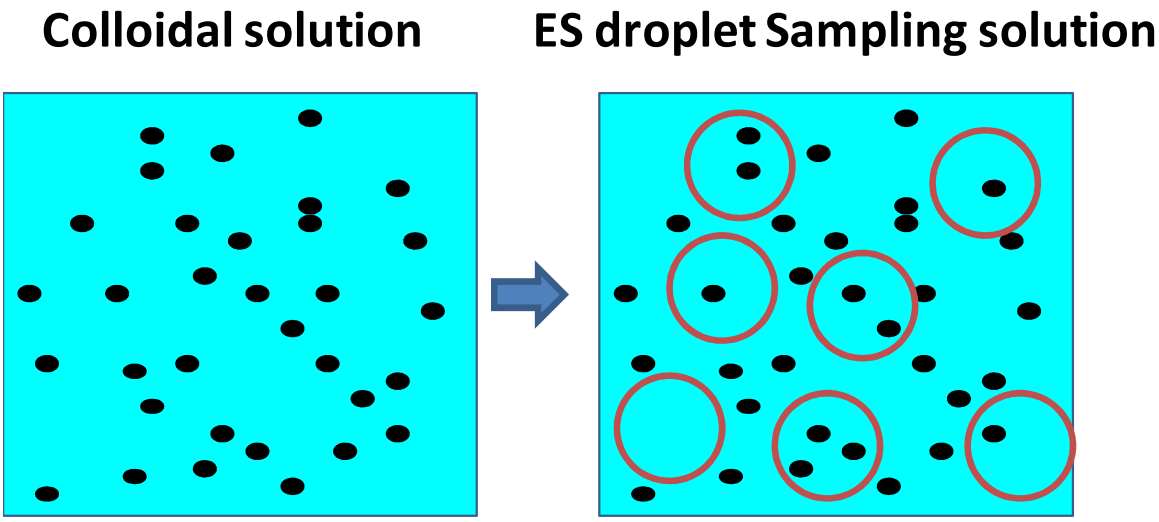

Figure 5.1: (A) Distribution of particles in a colloidal solution (B) Electrospray sampling may create artificially induced dimers or larger aggregates.

Lenggoro *et al.* [170] and Pease *et al.* [19] used a semi-quantitative equation to provide an upper workable concentration above which the artifact described in Figure 5.1 become prominent. According to this criterion:

$$C_p < \frac{6}{\pi D^3_{ES}} \qquad (5.1)$$

Such an approach has some disadvantages. Firstly, it relies on total protein concentration of the sample. If the intrinsic aggregate (say dimers and above) population was more, then this effect would be considerably less. This will become evident from the examples provided in subsequent sections. Secondly, as it is an inequality it is only semi-quantitative. Thirdly, it also poses a limit to the upper range of concentration of bionanoparticles. For example, for an ES droplet size of 140 nm the particle

concentration has to be < 7×10^{14} particles/mL. In real cases, especially in the biopharma industry the protein concentrations range in ~ 10^{15} - 10^{16} particles/mL or more.

This chapter is devoted to discussing an experimentally verified theory that will enable one to distinguish ES induced aggregates from intrinsic aggregates. This theory will eventually be applied in subsequent chapters as and when necessary.

5.2 Materials and Methods

5.2.1 Analytical Ultracentrifugation

In the process of establishing the theory in context of ES-DMA, it would be necessary to validate it using at least one independent technique. In this study such a validation was performed using AUC. AUC is a versatile tool for determining hydrodynamic and thermodynamic properties of proteins [5]. AUC allows direct observation of sedimentation dynamics of proteins in solutions under the influence of centrifugal field without interaction with any substrate or matrix. The centrifugal force causes the depletion of protein particles at the meniscus and thus the concentration boundary moves towards the bottom with time. The material boundary position is recorded via absorbance measurement at regular radial intervals and time points within the sector shaped cell. The sedimentation coefficient for a macromolecule is related to molecular parameters via the Svedberg equation and thus size distributions can be obtained. AUC measurements were made using Beckman-Coulter XL-I Proteomelab (Brea, CA). The temperature of the centrifuge chamber was equilibrated to 20 °C. The reference cell was filled with a sample solution equivalent ammonium acetate buffer of matching molarity. 400 µL volumes of the same sample as prepared for ES-DMA were spun at 30000 RPM

(3142.857 rad/s). Radial absorption measurements were recorded every 180 s at 280 nm wavelength with a radial position step size of 0.005 cm. The protein particles in the suspensions were subjected to a relative centrifugal force (rcf, relative to gravity) ranging from 62384 g to 72245 g, depending on their position with respect to the rotor center in the sector shaped cell. The radial scans were then analyzed using the Continuous Sedimentation Coefficient Distribution method in SEDFIT [171, 172], fitting the baseline with a resolution of 200. Confidence level of 1σ was used while fitting the AUC data using SEDFIT. The peak values in the c(S) versus 'S' distributions were then converted to molecular weight using SEDFIT, correspondingly exhibiting the existence of monomers, dimers and trimers. The monomer and dimer concentrations for hIgG were determined by integrating from 6.3 to 7.8 Svedbergs and 9.4 Svedbergs to 11.6 Svedbergs, respectively, while for IgM they were determined by integrating from 15.58 to 25.12 Svedbergs and 29.15 to 42.21 Svedbergs.

5.2.2 Sample preparation

The methodology adopted for preparing proteins in this chapter have already been described in chapter 4.

5.3 Results

Using equation 5.1 one can ascertain the upper concentration for different proteins. Assuming that the ES droplet size is ~ 140 nm the corresponding upper limit of concentration is ~ 7×10^{14} particles/mL. Keeping this value in mind, one could take up two different examples, of 100 μg/mL hIgG (4.4×10^{14} particles/mL) and 100 μg/mL of IgM (6.4×10^{13}particles/mL). Both these concentrations satisfy the above criterion and thus the size distribution obtained with the ES-DMA should in principle reflect the

intrinsic aggregate population. Figure 5.2 compares the intrinsic dimer and monomer proportions obtained with ES-DMA and AUC for bovine IgM and hIgG, respectively. Integrating the area under the monomers and dimers using the two techniques it becomes evident that for IgM both techniques quantify almost the same amount of aggregates such that the dimer to monomer ratio is ~ 150% whereas the dimer to monomer proportions obtained for hIgG is ~ 35 % and ~ 10 % with ES-DMA and AUC, respectively. The subsequent sections describe how the differences between ES-DMA and AUC can be reconciled with the developed theory.

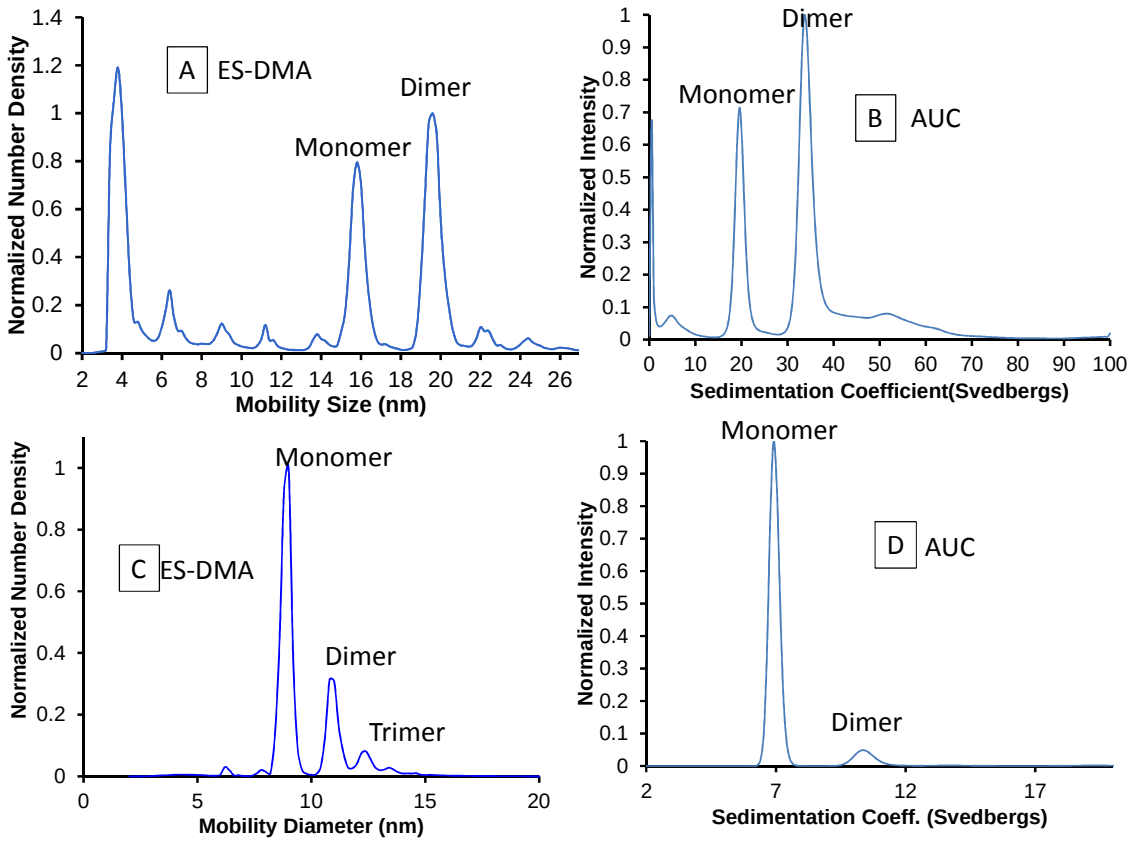

Figure 5.2 (A) Size distribution of bovine IgM using ES-DMA. (B) Size distribution of bovine IgM using AUC. (C) Size distribution of hIgG using ES-DMA. (D) Size distribution of hIgG using AUC.

5.3.1 Intrinsic monomers

Because the spatial distribution of analytes in solution is statistical, a theoretical treatment was developed based on probabilistic analysis. If a droplet generated at the tip of a capillary in ES is a random sample of the solution, and the particles in the solution areidentical and independent, the probability of ***k*** particles in a given droplet obeys a Poisson distribution and is given by

$$P(k,\lambda) = \frac{e^{-\lambda}\lambda^{k}}{k!} \qquad (5.2)$$

where $\lambda = V_d C_p$, V_d is the droplet volume and C_p is the concentration of the analyte in solution and *k* is the order of aggregation. Here λ physically signifies number of particles per droplet.

As mentioned previously in chapter 2 the droplet size is a function of size, i.e. it is not a specific value but rather a distribution, thus one needs to account for this distribution. For a droplet size distribution $f(D_d)$, the average value of parameter λ is then given by

$$\overline{\lambda} = \sum_i f(D_{d,i})\lambda = C_p \sum_i \frac{1}{6}\pi D_{d,i}^{3} f(D_{d,i}) = C_p \overline{V_d} \qquad 5.3)$$

Now if it is assumed that a solution only constitutes of monomers, then the Poisson distribution of the monomers will be given by:

$$P(1,\lambda) = \frac{e^{-\lambda}\lambda^{1}}{1!} \qquad (5.4)$$

And the Poisson distribution of the dimers will be given by:

$$P(2,\lambda) = \frac{e^{-\lambda}\lambda^{2}}{2!} \qquad (5.5)$$

Thus the probability of the dimers to monomers will be given by:

$$\frac{Dimer}{Monomer} = \frac{P(2,\lambda_1)}{P(1,\lambda_1)} = \frac{\lambda}{2} = \frac{C_p \overline{V_d}}{2} \qquad (5.6)$$

Assuming the average droplet volume to be ~ 140 nm, and for the known concentration of bovine IgM, the dimer to monomer ratio was determined to be 0.1, i.e if all particles were monomers there would be 5 % dimers that would be induced by the ES droplets for the given concentration. Because the proportion of dimers in Figure 5.2A were significantly greater this implies that this proportion was intrinsic and also explains the reasons for similarity with AUC results. Following the same approach for hIgG, the dimer/monomer proportion comes out to be ~ 30% implying most dimers and droplet induced. Thus equation 5.6 above provides a semi-quantitative approach that helps one to decide how much effect "droplet induced aggregation" has. Naturally, one may wonder if there is a methodology that could be adopted to correct for this artifact. This is described in the next section.

5.3.2 Intrinsic monomers and dimers

For reconciling the results obtained with ES-DMA and AUC for hIgG let it be assumed that there were monomers and dimers existing in the solution (based on the AUC data in Figure 5.2D). This is not an unreasonable assumption as AUC results in Figure 5.2B suggested so.

A schematic description of how intrinsic and induced oligomers may be distributed within ES droplets is shown in Figure 5.3. Consider there are C_{p1} monomers and C_{p2} dimers in solution. Following ES, N_{o1} monomers, N_{o2} dimers, and N_{o3} trimers

are observed with probabilities P_1, P_2 and P_3. There is only one possible condition for observation of monomers; that is, only one monomer in a single droplet generated by ES has a probability of P_1. For observed dimers, there are two possibilities. One is that two monomers are captured within a single droplet with probability P_{21}, creating an induced dimer, and the other possibility is that there is one intrinsic dimer in a single droplet with probability P_{22}.

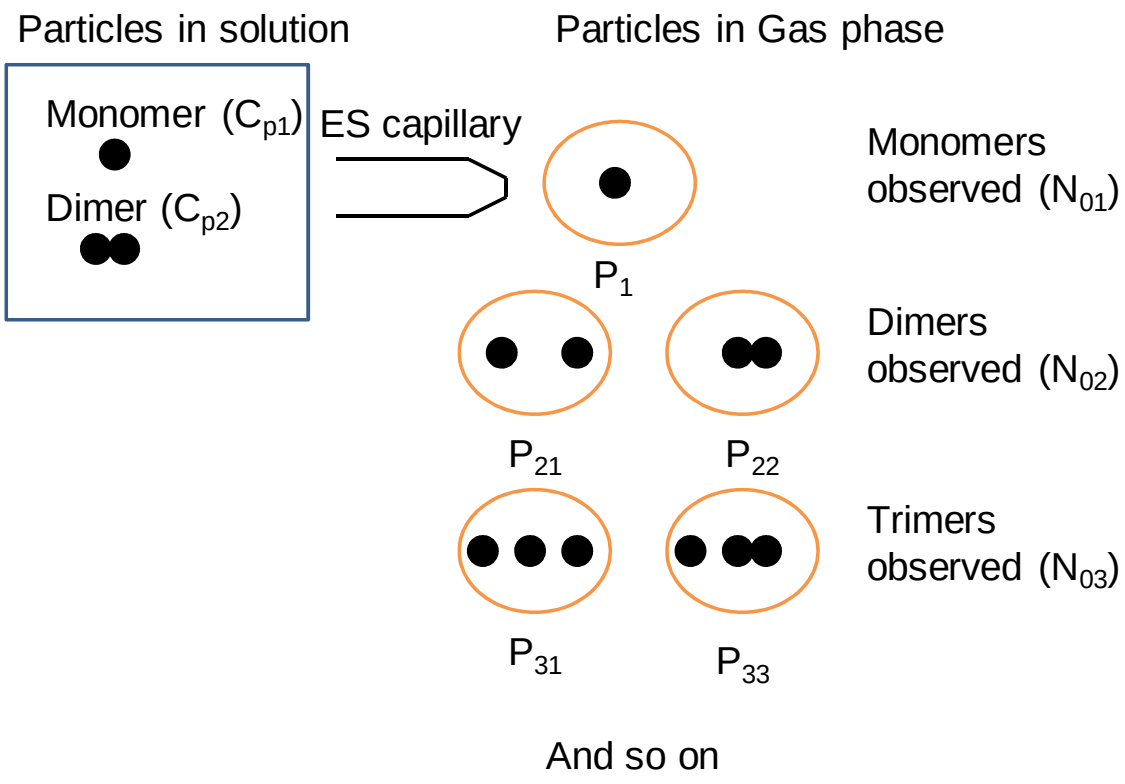

Figure 5.3. Physical representation of the probability distribution of induced and intrinsic aggregate distributions from electrospray.

With this construct one can obtain the following two relationships:

$$\frac{N_{o2}}{N_{o1}} = \frac{P_2}{P_1} = \frac{P_{21} + P_{22}}{P_1} \qquad (5.7)$$

Similarly for trimers, there are two situations, three monomers captured into a droplet with probability P_{31} or one monomer and one dimer captured within the same droplet with probability P_{32} as shown in Figure 5.3. Thus,

$$\frac{N_{o3}}{N_{o1}} = \frac{P_3}{P_1} = \frac{P_{31} + P_{32}}{P_1} \tag{5.8}$$

Likewise for tetramers, there are three situations, four monomers captured into a droplet with probability P_{41}, or two dimers with the probability of P_{42} or two monomers and one dimer captured within the same droplet with probability P_{412}. Thus,

$$\frac{N_{o4}}{N_{o1}} = \frac{P_4}{P_1} = \frac{P_{41} + P_{42} + P_{412}}{P_1} \tag{5.9}$$

Similarly for pentamers, considering probability of five pentamers, one monomer and two dimers or one dimer and three monomers:

$$\frac{N_{o5}}{N_{o1}} = \frac{P_5}{P_1} = \frac{P_{51} + P_{512} + P_{521}}{P_1} \tag{5.10}$$

Further now that there are monomers and dimers in solution the Poisson distribution needs to be generalized for different aggregates:

$$Q(k, \overline{\lambda_i}) = \frac{e^{-\overline{\lambda_i}} \overline{\lambda_i}^k}{k!} \tag{5.11}$$

Where,

$$\lambda_i = V_d C_{pi} = \frac{1}{6}\pi D_d{}^3 C_{pi} \tag{5.12}$$

C_{pi} is the number concentration of monomers in solution.

The Poisson distributions of monomers and dimers are independent of each other. Thus:

$$P_1 = Q(1,\lambda_1)Q(0,\lambda_2) = e^{-(\lambda_1+\lambda_2)}\lambda_1 \tag{5.13}$$

$$P_{21} = Q(2,\lambda_1)Q(0,\lambda_2) = e^{-(\lambda_1+\lambda_2)}\frac{\lambda_1^2}{2} \tag{5.14}$$

$$P_{22} = Q(0,\lambda_1)Q(1,\lambda_2) = e^{-(\lambda_1+\lambda_2)}\lambda_2 \tag{5.15}$$

$$P_{31} = Q(3,\lambda_1)Q(0,\lambda_2) = e^{-(\lambda_1+\lambda_2)}\frac{\lambda_1^3}{6} \tag{5.16}$$

$$P_{32} = Q(1,\lambda_1)Q(1,\lambda_2) = e^{-(\lambda_1+\lambda_2)}\lambda_1\lambda_2 \tag{5.17}$$

$$P_{41} = Q(4,\lambda_1)Q(0,\lambda_2) = e^{-(\lambda_1+\lambda_2)}\frac{\lambda_1^4}{4!} \tag{5.18}$$

$$P_{42} = Q(0,\lambda_1)Q(2,\lambda_2) = e^{-(\lambda_1+\lambda_2)}\frac{\lambda_2^2}{2!} \tag{5.19}$$

$$P_{412} = Q(2,\lambda_1)Q(1,\lambda_2) = e^{-(\lambda_1+\lambda_2)}\frac{\lambda_1^2\lambda_2}{2!} \tag{5.20}$$

Then combining 5.7, 5.13 and 5.14,

$$\frac{N_{o2}}{N_{o1}} = \frac{\overline{V_d} C_{p1}}{2} + \frac{C_{p2}}{C_{p1}} \tag{5.21}$$

And combining 5.8, 5.13 and 5.16 and 5.17 it can be shown that:

$$\frac{N_{o3}}{N_{o1}} \approx \frac{P_3\big|_{V_d=\overline{V_d}}}{P_2\big|_{V_d=\overline{V_d}}} = \frac{\overline{V_d}^2 C_{p1}{}^2}{6} + \overline{V_d} C_{p2} \tag{5.22}$$

Further combining 5.9, 5.13, 5.18, 5.19 and 5.20 it can be shown that:

$$\frac{N_{o4}}{N_{o1}} \approx \frac{P_4\big|_{V_d=\overline{V_d}}}{P_1\big|_{V_d=\overline{V_d}}} = \frac{\overline{V_d}^3 C_{p1}{}^3}{24} + \frac{\overline{V_d}^2 C_{p2}{}^2}{2\overline{V_d} C_{p1}} + \frac{\overline{V_d}^2 C_{p1} C_{p2}}{2} \tag{5.23}$$

Further for pentamers it can be shown following the same approach,

$$\frac{N_{o5}}{N_{o1}} \approx \frac{P_5\big|_{V_d=\overline{V_d}}}{P_1\big|_{V_d=\overline{V_d}}} = \frac{\overline{V_d}^4 C_{p1}{}^4}{120} + \frac{\overline{V_d}^2 C_{p2}{}^2}{2} + \frac{\overline{V_d}^3 C_{p1}{}^2 C_{p2}}{6} \tag{5.24}$$

Following the same approach the proportion of larger induced aggregates can be determined.

Although this section laid down the equations that can be used for ascertaining the extent of droplet induced aggregation the next section discusses the approach that is required for correcting for this artifact.

5.4 Discussion

Although the objective of this chapter is to demonstrate and quantify droplet induced aggregation, it should emphasized that the methodology adapted here open up the avenue for measuring the absolute liquid phase number concentrations and the two are interlinked. A key feature of this statistical approach is that by measuring the relative oligomer mobility size distributions, one is able to work backwards to determine the absolute number concentration in solution. What is particularly attractive about this method is that by only measuring the relative oligomer concentrations, one eliminates the

need for sample-specific calibration standards or detailed analysis of transport losses. For a solution constituting of monomers and dimers, there are many approaches one could take:

Approach 1

Recalling that in chapter 2 it was mentioned that one can use two different ES droplet volumes at two ES capillary pressure drops, if one were to obtain the size distribution of RmAb at both these capillary pressures, then one would obtain equation 5.21 at both different pressure drops. Assuming equation 5.21 is at an arbitrary ES pressure of p_{ES}, then at another arbitrary pressure of p'_{ES} one could write:

$$\frac{N_{o2}'}{N_{o1}'} = \frac{\overline{V_d}' C_{p1}}{2} + \frac{C_{p2}}{C_{p1}} \tag{5.25}$$

Then solving 5.21 and 5.25 simultaneously one can determine the absolute liquid phase number concentrations of monomers and dimers and thus determine the intrinsic monomer and dimer proportions. This approach will be again invoked in chapter 8 where Figure 5.2C and Figure 5.2D are going to be quantitatively discussed. It should be pointed out that this is a time consuming experiment as it needs the size distributions and droplet volumes to be obtained at two different dilutions.

Approach 2

If one were to assume that the dimers were covalent aggregates and would not be affected by dilution (irreversible aggregation), then one can dilute the solution to say 50% and then obtain the size distributions at this dilution. This would be given by:

$$\frac{N_{o2}\big|_{2X}}{N_{o1}\big|_{2X}} = \frac{\overline{V_d} C_{p1} / 2}{2} + \frac{C_{p2} / 2}{C_{p1} / 2} \qquad (5.26)$$

Then solving equation 5.21 and 5.26 simultaneously, C_{p1} and C_{p2} can be obtained. This also is a time consuming experiment as, like the approach 1, it needs size distributions and droplet volumes to be obtained at two different dilutions.

Approach 3

If the concentration of the solution (say by using UV-vis) is known then one can write:

$$C_p = C_{p1} + 2C_{p2} \qquad (5.27)$$

Then solving equations 5.21 and 5.27 simultaneously, one can obtain C_{p1} and C_{p2}.

Approach 4

The easiest approach is to combine equations 5.21 and 5.22 above simultaneously to obtain the intrinsic aggregates as this can be achieved by carrying out two experiments: one for size distribution and another for droplet volume. However, although theoretically possible it poses two challenges. If the concentration of the induced trimer is low then quantification may be inaccurate. Otherwise, if the concentration of the solution is too high, then separation of trimers and larger aggregates from one another may be limited. This second limitation and other limitations of this mathematical approach is provided in detail in the next section.

Although the same principle demonstrated in the last two sections can be applied to a solution with intrinsic monomers, dimers and trimers, one could imagine that the mathematics can get extremely challenging. Further validating such a model would be

even more challenging because of certain experimental limitations as discussed in the next section. Thus developing such an approach was not been pursued.

5.4.1 Limitations

Although the above approach can be used for quantification of intrinsic aggregates or for correction of non-specific analyte aggregation, it has certain limitations that are mostly experimental.

Firstly, it becomes difficult to use the above set of equations if the droplet size varies from one experiment to another. As the droplet size is usually determined by a separate experiment, any small fluctuation in the droplet size can also affect quantification. This is even more true for the larger induced aggregates as the dependence of these aggregates on the droplet size is more pronounced. For example, an uncertainty analysis on equation 5.22 above would show that a 10 % run to run variation in the ES droplet size would result in a 17% variation in the observed trimer to monomer ratio arbitarily assuming about 4×10^{14} particles/mL of monomers and 2×10^{13} particles/mL of dimers and a droplet volume corresponding to ~ 130 nm of ES droplet size.

$$\frac{\Delta\frac{N_{o3}}{N_{o1}}}{\frac{N_{o3}}{N_{o1}}}\times100=\frac{\frac{2\overline{V_d}C_{p1}{}^{2}\Delta\overline{V_d}}{6}+\Delta\overline{V_d}C_{p2}}{\frac{\overline{V_d}^{2}C_{p1}{}^{2}}{6}+\overline{V_d}C_{p2}} \qquad (5.28)$$

Secondly, the upper concentration regime would still be limited by the resolution of the DMA. For example, the size distribution of BSA is shown at a concentration of 0.1 mg/mL (that corresponds to ~ 10^{15} particles/mL) using 2 mmol/L ammonium acetate that generates a droplet size much larger than 140 nm at a DMA resolution of 25:1. Qualitatively this implies that most large aggregates would be droplet induced (Figure

5.4). For this size distribution because the separation between tetramers, pentamers and larger aggregates is not good, thus trying to quantify the induced aggregates would be difficult. Thus the resolution of the DMA also poses a restriction on the above approach for relatively higher concentrations of particles.

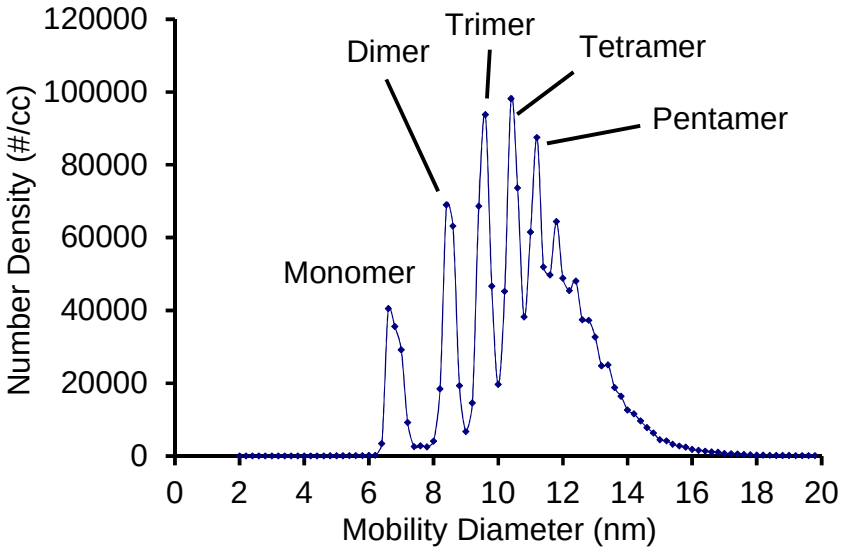

Figure 5.4 Size distribution of BSA at 0.1 mg/mL using 2mmol/L ammonium acetate.

Thirdly, this approach inherently requires induced aggregates. If the proportion of these induced aggregates is low or absent, then neither can one quantify the proportion of intrinsic aggregates nor can one use this approach for measuring the absolute number concentration. Often times the concentration of bionanoparticles can be low, and concentrating them for quantification may be undesirable. In such a case, a bionanoparticle can be quantified by calibrating the system with another bionanoparticle and then assuming the losses in the ES-DMA system to be the same for both. This approach will be discussed in detail in chapter 7.

Finally, the above analysis can be used for monodispersed samples. In several real applications, nanoparticles can be polydispersed and for such cases this methodology is difficult to implement.

5.5 Summary

"Droplet induced aggregation" in the past had been tackled through semi quantitative approach. This chapter described how this artifact can be eliminated using Poisson statistics and *a priori* knowledge of the ES droplet size. The developed approach also allows one to determine the absolute liquid phase number concentration of different oligomers. There are certain experimental limitations to this approach that are also discussed in detail. In chapter 8 this methodology is going to be adopted to obtain intrinsic monomer and dimer populations of two different immunoglobulins.

Chapter 6: DMA ARTIFACTS: CONFORMATIONAL CHANGES OF LIGANDS UPON ADSORPTION TO NANOPARTICLES

6.1 Introduction

Gold - nanoparticles find regular use in the realm of nanotechnology because of its non-toxic nature, size dependent optical properties, high image contrast, high-yield synthesis and easiness in conjugation with other moieties for achieving desirable properties [173]. Amongst several moieties that are used, conjugation with proteins is extremely important in the context of drug delivery. Protein adsorbed to a nanoparticle can act as a "corona" that then defines the identity of the nanoparticle-protein conjugate, allowing easy camouflaging and entry into the human body. At the later phase of its journey inside the body, the nanoparticle can be triggered to release the protein at affected region inside the body [174].

Quantifying protein adsorption to different bionanoparticles is an important subclass of problems in the context of nanoparticles for drug delivery. The nature of the protein, its charge as well as the nature of the surface and its charge are important parameters that drive protein adsorption to bionanoparticles [173]. To gain an understanding of the relative importance of these factors several methods are used for quantification of the protein to the nanoparticles. A few techniques that are routinely used are: UV-vis [160], fluorescence spectroscopy [175], reflectometry [113], quartz crystal microbalance [176], surface plasmon resonance [177] and bicinchoninic assay [178]. As already mentioned in chapter 3, another technique that is gaining momentum in

applications to quantifying protein adsorption to nanoparticles is electrospray-differential mobility analysis. Although primarily developed for measuring size of different bionanoparticles such as nanoparticles, viruses and proteins, it can also be used for quantifying ligand adsorption to another bionanoparticle. As this principle of ES-DMA is independent of material property hence it has been used for a variety of different nanoparticles [42, 65, 71, 72] that include nanoparticles-proteins, viruses-proteins, protein-proteins and viruses-quantum dots and is already discussed in great detail in Chapter 3. Thus although this chapter is going to focus only on protein adsorbing to nanoparticles, the principles employed here may not be limited to such a case. Keeping this in mind, any bionanoparticle adsorbing to an anlyte is defined as a ligand.

There are two different approaches that are regularly used for quantifying ligand adsorbed to nanoparticles as already discussed in Chapter 3. One is the area based approach (referred to as AB approach, henceforth, equation 3.2) and another is volume based approach (referred to as VB approach, henceforth, equation 3.3). Both approaches significantly deviate from each other. This is evident from the results assimilated in Table 3.2 of chapter 3. One of the most significant disadvantages of both these equations is that it is assumed that the protein does not change in conformation upon adsorption to the surface. Such an assumption is highly protein specific. Whether a protein will change in conformation after adsorption would depend on several factors such as: size of the nanoparticle, type of protein and the relative charges on the protein and the surface. Comparing case 1 and case 2 in Figure 6.1, it is evident a situation might arise when a ligand adsorbs to a nanoparticle, changes its conformation and forms multiple layers. In this case the increase in mobility size upon adsorption to the surface (case 2) could be

equal to a single layer of protein without any significant conformational changes (case 1). Conversely, if a protein adsorbs and denatures substantially which results in a significant increase in the size of the conjugate, the number of ligand adsorbed per nanoparticle would be over predicted by ES-DMA. Secondly, mobility diameters of bionanoparticles determined can often be instrument specific. As the equations 3.2 and 3.3 rely on the mobility diameter of the ligand, any inaccurate determination of its size would also affect the quantification as well.

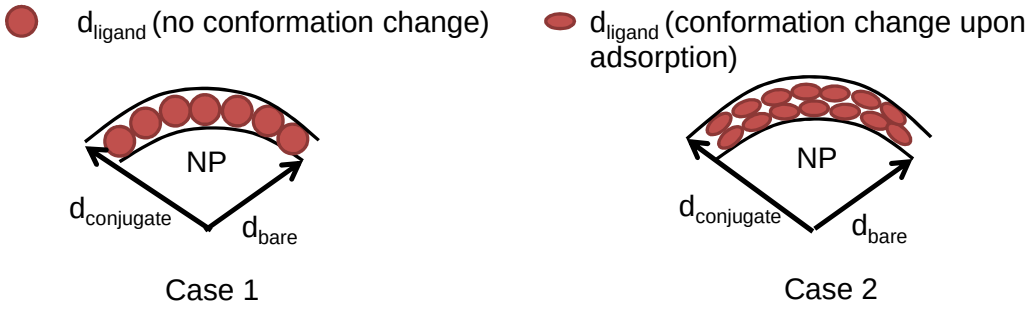

Figure 6.1: Mobility increase does not take into account changes in conformation changes of protein upon adsorption to a nanoparticle.

Thus, measuring the mass is a more accurate approach for quantifying ligand adsorption using ES-DMA. As DMA cannot directly provide a measure of mass, hence it is necessary to invoke another gas phase technique. The technique chosen in this context is called aerosol particle mass analyzer (APM). APM size selects particles by the balance of electrical and centrifugal forces [179]. It constitutes of two concentric rods much like the DMA and particles are selected based on the balance of drag and electrical forces. The governing equation is as given below:

$$m_{particle} = \frac{n_{particle} e V_{APM}}{\omega^2 r_a^{\,2} \ln(\frac{r_2}{r_1})} \qquad (6.1)$$

Here $m_{particle}$ is the mass of the particle, $n_{particle}$ is the charge on the particles, e is the elementary charge, V_{APM} is the corresponding APM voltage, ω is the rotations speed of the APM, r_2 and r_1 are the outer and inner radius of the APM cylinder, r_a is the average of r_1 and r_2.

It can be easily hyphenated with DMAs to measure mass of particles preselected by the DMA as has been demonstrated before [78]. In principle, depending on the resolution of the APM it can also be used to measure the mass of ligand adsorbed to nanoparticles and thus eliminates the shortcoming of the ES-DMA that may arise because of configuration changes in the protein.

The objective of this chapter is to demonstrate that DMA-APM can be used in tandem to quantify ligand adsorption to nanoparticles. This is demonstrated with two model examples: gold nanoparticles to bovine serum albumin at variable concentrations and polystyrene latex beads to RmAb (a monoclonal human immunoglobulin) at variable pH.

6.2 Materials and Methods

6.2.1 Sample preparation

Thirty nanometer citrate stabilized gold nanoparticles were acquired from Ted pella Inc. Bovine serum albumin was acquired from Sigma Aldrich and suspended in 2 mmol/L ammonium acetate buffer at pH 7.0 prepared by adding about 0.077 gm of ammonium acetate to 500 mL of deionized water and then by adding about 10 µL of ammonium hydroxide to adjust the pH. Subsequently BSA was added to the citrate stabilized gold such that the concentration of BSA would be 2 µmmol/L, 5 µmmol/L, 10 µmmol/L, 20 µmmol/L, 50 µmmol/L and 100 µmmol/L, respectively. The volume of these samples were 500 µL. These samples are then allowed to sit at 4 ^{0}C overnight and then spun down for 10 minutes at 10 krpm each after which about 485 µL of the supernatant would be removed and replaced with 2 mmol/L ammonium acetate buffer. This step was subsequently repeated two times to remove the excess protein. The unconjugated sample was only centrifuged once, as otherwise multiple centrifugations would aggregate the sample.

About 35 µL of 60 nm polystyrene latex beads (NIST SRM 1963) were added to 965 µL of 2 mmol/L ammonium acetate buffer to which dialyzed RmAb suspended in 2 mmol/L ammonium acetate buffer (pH varied) would be added such that the total protein concentration in the solution would be 1 mg/mL. Four such samples were prepared at pH values of 5.0, 7.0, 8.5 and 9.0. The methodology adapted for dialyzing the RmAb samples is available elsewhere. The samples would then be allowed to incubate overnight at room temperature. As the density of PSL is almost equal to that of water, the excess protein could not be removed by centrifugation. This raises one artifact of multiple

proteins getting encapsulated in the same droplet with the conjugate and thus creating non-specific adsorption to the conjugate (as mentioned in chapter 5). This artifact is a function of the concentration of the free protein in solution, the ES droplet size and the concentrations of the conjugates in solution. By measuring the size distributions of the prepared samples at different dilutions no observable difference in mobility size were found for the PSL-RmAb conjugates implying that the effect of this artifact was negligible (data not shown). It should be pointed out that such an artifact was insignificant even more so for the Au-BSA samples as the excess protein was removed through centrifugation.

6.2.2 ES-DMA-APM

A 40 µm capillary (TSI Inc 3900126) was used in the ES (TSI Inc 3480). The ES chamber pressure was maintained at 3.7 PSI. The aerosolized nanoparticles were carried from the ES towards the DMA using a supplement of 1 L/min of air and 0.2 L/min of CO_2 (referred to as the polydispersed flow henceforth). The DMA was operated with a polydispersed flow rate of 1.2 L/min and sheath flow of 3 L/min. The CPC was operated at a high flow mode of 1.5 L/min. A step size of 1 nm was used for obtaining each size distribution. The APM (Model 3600, Kanomax, Japan) was operated at 4500 RPM for all samples and the aerosol flow in and out of it was maintained at 1.5 L/min.

The methodology adapted for quantification using DMA-APM is demonstrated in Figure 6.2 below. At first a size distribution of the bare sample (say Au or PSL) would be obtained by varying the DMA voltage which can be correlated to the mobility size and thus would give a gas phase size distribution. Then the peak mobility size of this distribution would be obtained by fitting a Gaussian through this distribution using

Kaleidograph. This is shown in step 1 of Figure 6.2. Then the DMA voltage would be fixed at the value that corresponds to the peak mobility size and the APM voltage would then be varied at conditions mentioned above to obtain a plot of voltage versus gas phase concentration. This distribution would be obtained by increasing the voltage in steps of 2 V from 8 V to 30 V for the PSL and PSL-RmAb samples and in steps of 1 V from 22 V to 40 V for the AuNP and AuNP-BSA samples and obtaining the gas phase counts at each of the voltages for about 30 to 60 s. The aerosol counts thus obtained would be first averaged at each respective APM voltage and thus a voltage corresponding to mass and gas phase distribution would be obtained. This distribution would then be again fit through a Gaussian to determine the mass of the peak size. This step would then be repeated for the conjugates to obtain the mass of the peak size of the conjugate (Step 3). Then, for the known surface area of the bare nanoparticle, the coverage can be determined (Step 4).

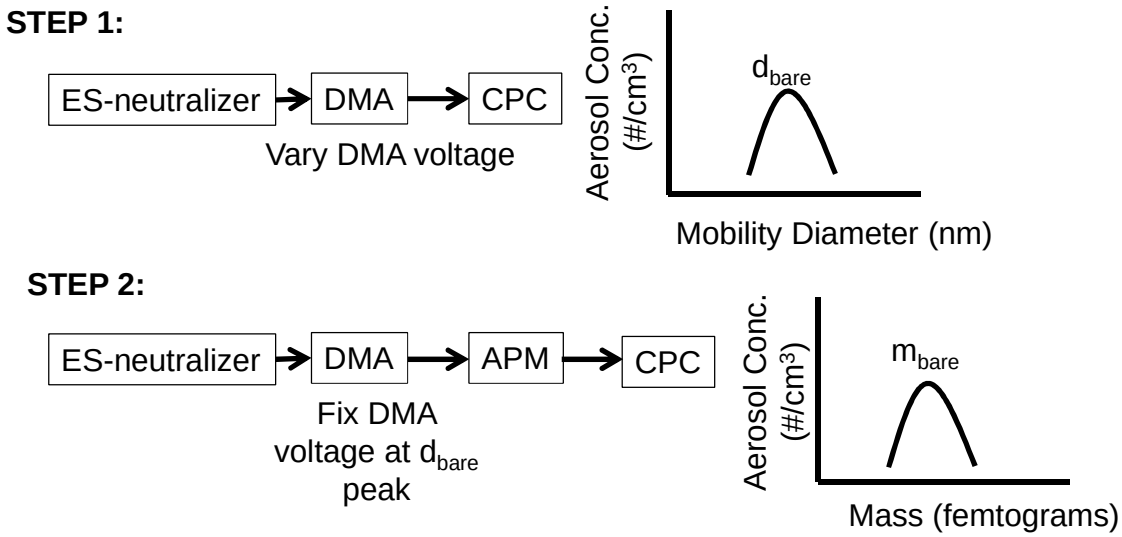

End result: Obtain mass of the nanoparticle m_{bare}

STEP 3: Repeat 1 and 2 for conjugate to obtain $m_{conjugate}$

STEP 4:

$$\Gamma = \frac{m_{conjugate} - m_{bare}}{\pi d_{bare}^2}$$

Figure 6.2: The different steps involved that eventually provides the number of ligands adsorbed/nanoparticle using a DMA-APM system.

6.3 Results and Discussion

Using the approach outlined in the previous section, the amount of protein adsorbed was calculated for AuNP-BSA samples as a function of increasing BSA concentration. The results obtained with DMA-APM are shown in Figure 6.3 below. It is seen that the coverage of BSA to increase with concentration. This trend has been consistently seen with several other proteins on different surfaces as discussed in chapter 4.1. At low concentrations, adsorption-desorption at the nanoparticle surface reaches a steady state slowly, thus allowing time for the protein to spread on the nanoparticle

surface. At higher concentrations, proteins reach the surface of the nanoparticle faster thus allowing less time for proteins to spread. Concomitantly the nanoparticle surface area available for protein adsorption is more. This explains the increase in BSA adsorption as a function of concentration. Strikingly, the values obtained with DMA-APM are in excellent agreement with coverages of BSA obtained on planar Au surface using QCM-D. This agreement of results between ES-DMA and QCM-D also implies that the adsorption coverage for 30 nm nanoparticle and planar Au is the same. This is not unreasonable as Teichroeb et al found that coverages are independent of particle size from ~ 30 nm onwards.

Using the AB and VB approaches one could also determine the coverages. Using either of the approaches requires the mobility diameter of BSA which can vary from 6.7 nm to 7.1 nm [11, 180]. Assuming the later value and knowing the average mobility diameters of the bare nanoparticles and the conjugates allows quantification of the ligands and are plotted in Figure 6.3 below. Comparing the values obtained APM with those obtained by using equation 3.2 and 3.3 it is evident that: a) the AB approach fairs poorly and consistently underreports compared to VB approach and b) the volume based approach works fairly well at low concentrations and starts to under report the amount of ligand adsorbed significantly at larger concentrations of BSA. The agreement at low concentrations for the VB approach is probably because at lower concentrations of added BSA, the protein probably takes an expanded conformation closer to the assumed value of 7.1 nm. As already mentioned this is not surprising as others have also reported that different proteins can take expanded conformations at lower concentrations. As the concentration increases, more BSA molecules cuddle together, creating a more compact

conformation. For such a case the VB approach can still be used to better fit the coverage obtained by DMA-APM and QCM-D by assuming a lower value of ligand diameter, although it would then need to be determined by other orthogonal techniques.

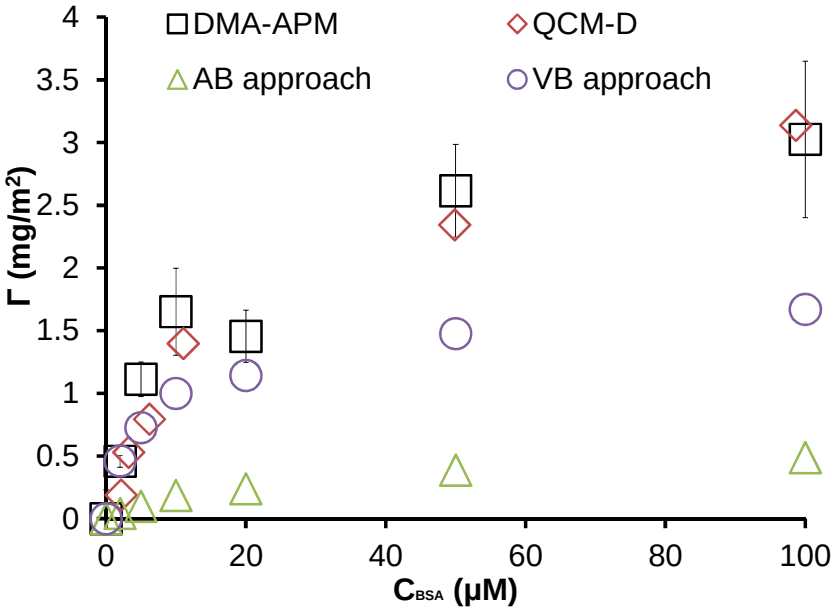

Figure 6.3: Coverages of BSA on 30 nm AuNP as a function of concentration obtained with DMA-APM (square-black), on planar Au surface obtained with QCM-D (diamond-red), using VB approach (circle-purple) and AB approach (triangle-green).

Knowing the dimensions of BSA (5.5x5.5x9 nm^3 [181]) allows one could estimate if the adsorption is monolayered. Depending on side-on (foot print area 5.5x5.5 nm^2) or end-on adsorption (5.5x9 nm^2) the coverage would be 2.2 mg/m^2 or 3.6 mg/m^2, respectively, under the simplest conditions (i.e. neglecting electrostatic repulsions, solute effects etc). As the maximum coverage lies in between these values, it is reasonable to infer that the adsorption of BSA to the Au nanoparticles is monolayered and is a heterogenous mixture of both these configurations.

As a second application the coverages of RmAb on NIST SRM PSLs were also studied. As the pI's can vary significantly for different IgGs, thus for conveniently comparing the DMA-APM data with the selected literature, all the pH values have been offset with respect to the pI of the respective IgG. For example, the adsorption coverage of IgG 2B shown in Figure 6.4A below has an isoelectric point of ~ 5.0 and the pH values at which it was studied [182] were pH 4, 4.5, 5, 6, 6.5, 7 and 8 . It is offset in a way such that its isoelectric point appears at 0 units in Figure 6.4A below. Similarly, IgG 7B (mouse IgG type 1), Mab-1 (mouse IgG type 1) and RmAb (human IgG type 1) had pIs of ~ 5.5, ~ 5.4 and ~ 8.5, respectively. IgG 2B and IgG 7B were adsorbed to negatively charged 501 nm PSLs [159] and Mab-1 was adsorbed to negatively charged 297 nm PSLs [183]. From Figure 6.4A it is evident that the adsorption of RmAb reaches a maximum at the pI and decreases significantly away from the pI. Based on the results obtained with other immunoglobulins IgG 2B, IgG 7B and Mab -1 it is evident that the dome shaped adsorption pattern for RmAb corroborates with studied conducted on other monoclonal IgGs with different techniques. Further, the adsorption pattern of RmAb on silica as a function of pH in 20 mM ammonium acetate buffer has been studied previously as discussed in chapter 4.1. It is evident that amount of RmAb adsorbed to silica was considerably smaller in that study. Others have also reported increased adsorptions at lower ionic strengths [106, 112, 118]. Thus it is evident that the results obtained with ES-DMA-APM is consistent with literature [113, 144, 182, 183] and implies that electrostatic forces (between protein-protein and protein-sorbent) play the most dominant role in influencing coverage.

Based on the dimensions of an immunoglobulin, the maximum monolayered theoretical coverage that could be obtained is 3.8 mg/m^2. Further, considering electrostatic effects, this could be as low as 2.1 mg/m^2 [184]. The experimental maximum coverage obtained with DMA-APM is higher, suggesting multilayered adsorption. Quantifying the amount adsorbed with DMA-APM also enables comparisons with values predicted by VB and AB approaches. Consistent, with the observations discussed for BSA adsorbed to Au NPs, it is found the AB approach under-reports significantly at all pH values whereas VB appears to corroborate well with DMA-APM at low pH values (~ 5) but significantly deviates at higher pH especially when adsorption is multilayered.

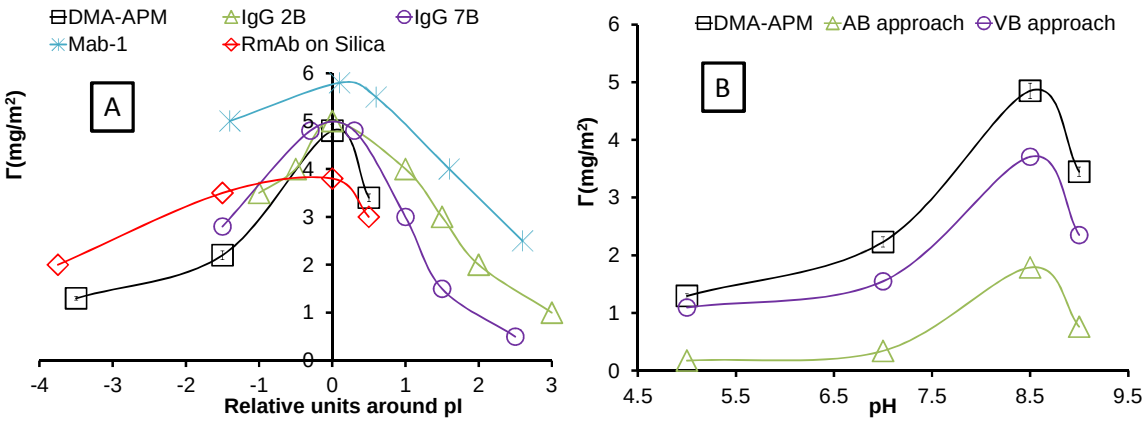

Figure 6.4: (A) RmAb adsorbed to on negatively charged 60 nm PSL (NIST SRM 1964) quantified with DMA-APM (square, black) and comparisons with literature: IgG 2B (mouse IgG type 1) (triangle, green), IgG 7B (mouse IgG type 1) (circle, purple) and Mab-1 (asterisk, blue) and RmAb on Silica (diamond, red). (B) Coverage of RmAb at

different pH values obtained using DMA-APM (square-black), and predictions based on VB (circle-purple) and AB approach (triangle-green).

It should be pointed out that the DMA-APM in the context of ligand quantification also has certain limitations imposed by the resolution and lower limit of detection of the APM. Such examples are: a) NPs that are very heavy (say 100 nm AuNPs) or have a broad mass distribution for a fixed mobility size (the relative percentage increase in mass after protein adsorption can often be < 0.2 % which is the lower limit of detection for the APM), b) Bionanoparticles that are light (say 10 nm or 20 nm PSLs or 5 nm gold nanoparticles or different protein complexes cannot be quantified as the mass is below the detection limit) or c) light weight polyethylene glycols and self assembled monolayers (as the relative increase in mass after ligand adsorption can be small). Such limitations can however be eliminated with higher resolution APMs.

6.4 Summary

By integrating an aerosol mass analyzer with the conventional ES-DMA, a new methodology for quantifying ligand adsorption to bionanoparticles was developed that allows for accurate quantification and eliminates the intrinsic sensitivity issues with DMA. This also permits systematic investigations of the area based and volume based approaches that are available for quantification using ES-DMA. This investigation suggested that both volume based and area based approaches are not accurate as ligands can change conformation and adsorb in multiple layers on different bionanoparticles.

Chapter 7: APPLICATIONS: VIRUSES

7.1 Introduction

Common tests used to identify the concentration and composition of viruses includes transmission electron microscopy (TEM), scanning electron microscope (SEM), analytical ultracentrifugation and dynamic light scattering. Although each of these methods possesses particular strengths for evaluating viral products, they all have disadvantages. Some of these disadvantages were already discussed in chapter 1. In the context of characterizing viruses, resolving particles that are close in size is an important criteria, as viral degradation often leads to mixtures of intact and partially degraded viruses that can differ in diameter by 10 nm or less which are difficult to distinguish with TEM and DLS (because of lack of contrast between the proteins and TEM grids and because of the intrinsic principles of operation of DLS, respectively).

ES-DMA can be potentially used for analysis in biomanufacturing environments (e.g. evaluation of gene therapy produces, vaccines for routine lot release, etc.) where relatively concentrated solutions of particles 20 nm to 200 nm in size are measured. The advantages of ES-DMA for characterizing vaccines include its ability to provide a direct read-out of particle size distributions, to measure rapidly statistically significant populations of nanoparticles, and to detect changes in nanoparticle diameter as small as 0.3 nm, far below the size of the smallest viruses [15, 143]. In addition, viruses can be identified based on particle size, thereby ruling out contaminating adventitious agents unless they are of the same size. Size measurement by ES-DMA also does not rely on chemical specificity between the host (say a bacteria) and the virus. Given these salient features of ES-DMA it is evident that it has the potential to become an important tool in

decision making in biomanufacturing environments. However, before ES-DMA can be accepted as a tool it requires to demonstrate that it meets the ICH Q2 principles first which is the objective of this chapter.

7.2 Materials and Methods

7.2.1 Test article preparation

Phage PP7 and its host *Pseudomonas aeruginosa* were obtained from the ATCC (Manassas, VA; accession numbers 15692-B4 and 15692). Coliphage PR772 and host *E. coli* strain K-12 J-53-1 were obtained from the Félix d'Hérelle Reference Center for Bacterial Viruses (Université Laval, Québec, Canada). These bacteriophage models were used instead of actual mammalian viruses because they can be easily grown to high titer and can be prepared and studied under BSL1 conditions. Stocks were prepared by CsCl gradient ultracentrifugation methods, and live intact phages were enumerated by plaque assays using their respective hosts, as described elsewhere [37, 185]. The phages were then dialyzed into 2.0 mmol/L ammonium acetate, pH 7.4, in preparation for the electrospray. Studies showed that short term storage (≈ months) in this buffer system did not significantly impact phage infectivity (results not shown). For PR772 the dialyzed sample at an initial concentration of 1.5×10^{12} plaque forming units/mL (pfu/mL) was diluted to prepare a serial dilution of 4×, 10× 50×, 500× and 5000× and have been henceforth referred to as PR772a, PR772b, PR772c, PR772d and PR772e, respectively. For PP7, dialysis a parent stock resulted in an initial concentration of 2.5×10^{13}pfu/mL. Then a fifty times dilution from the above stock was prepared from which serial dilutions of 2×, 5×, 50×, 500× and 1000× were prepared and have been henceforth referred to as PP7a, PP7b, PP7c, PP7d and PP7e, respectively.

Analysis in this chapter was limited to viral particles in solutions in which nonvolatile salts, surfactants, or other materials present in formulation buffers had largely been removed. The presence of these species were found to cause clogging of electrospray capillaries, destabilizating the electrospray and resulting in noisy size distributions. Other factors that affect the stability of the electrospray include capillary diameter, ionic strength outside of a specific conductivity window, and protein or buffer species that affect the surface tension.

To create partially degraded test samples, dialyzed PR772 and PP7 samples were placed in 1.5 mL protein low binding centrifuge vials (Eppendorf North, Westbury, NY, USA, #022431081) and heated using a BLOK heater (Labline Instruments Inc, Melrose Park, IL, USA, #2003) to temperatures from 50 ^{o}C to 80 ^{o}C. The samples were heated within 2 minutes to the desired temperature, and maintained within ± 1.0 ^{o}C as measured by a type K thermocouple (Omega, Stamford, Connecticut, USA) inserted directly into sample vials via holes punctured through their caps. After 30 minutes the samples were removed from the BLOK heater. Control samples for comparison were held at ambient temperature (25 ^{o}C) for 30 minutes.

For infectivity assays, dilutions of the virus stocks and heat treated samples were prepared and added to mid-log-phase host and liquefied top agar, which was spread over tryptic soy agar plates.

7.2.2 Buffer Preparation

The protocol for buffer preparation for ES-DMA was same as that already described in chapter 2.6.

7.2.3 Gold nanoparticles Preparation

For quantitative number concentration calibration of the ES-DMA, gold nanoparticle reference standards were used. One milliliter aliquots of as received 20 nm and 60 nm Ted Pella gold initially at particle concentrations of 7.0×10^{11} particles/mL and 2.6×10^{10} particles/mL were centrifuged for 20 minutes and 10 minutes, respectively, at 13,200 rpm which were subsequently concentrated to prepare stock concentrations of 3.4×10^{12} particles/mL and 2.6×10^{11} particles/mL for 20 nm and 60 nm samples respectively. Two different sizes were selected because the sensitivity of ES-DMA depends on size, with sensitivity increasing with particle size. Serial dilutions of 2, 4, 8, 16, 32, and 64 times for the 20 nm and 2, 4, 8, and 16 times for 60 nm were then prepared from this stock.

7.2.4 ES-DMA operation and data analysis

The ES was operated under the same conditions as described in chapter 2.6. A 25 µm capillary was used. The DMA was operated with a sheath flow of 30 L/min for PP7 or 10 L/min for PR772. By stepping through different electric fields, a size distribution was obtained, in increments of 0.2 nm. The CPC was operated in the high flow mode as described in chapter 2.6.

Gold nanoparticles (Ted Pella) prepared in ammonium acetate buffer or 60 nm polystyrene latex particles (NIST SRM® 1963) were used as system suitability standards to confirm operation of the instrumentation [15, 78, 143].

7.2.5 Gold calibration approach

In order to correlate gas phase concentration with liquid phase, Cole *et al.,* [39] used known concentrations of gold nanoparticles to calibrate the ES-DMA system to

determine the concentration of virus particles. The ratio of particles in solution and signal intensity from the DMA gave the response function of the DMA system. The response function was then used to obtain virus concentration in solution. Virus concentration values determined this way were found to be in good agreement with amino acid analysis [39]. A similar protocol was used in this article to determine concentrations of PP7 and PR772.

Two different gold nanoparticles sizes of known concentrations were selected; nominally 20 nm and 60 nm, to approximate particles close in size to PP7 and PR772. Serial dilutions of 20 nm citrate stabilized Ted Pella gold nanoparticles, as mentioned in section 2.3, were created to obtain a response function for the ES-DMA of $6.21\times10^{-8} \pm 4.6\times10^{-9}$ (particles/cm^3)/(particles/mL) for PP7 where the response function is defined as the ratio of the concentration measured in gas phase using ES-DMA and the actual particle concentration in solution. Similarly using 60 nm particles, a response function of $9.15\times10^{-8} \pm 8.0\times10^{-9}$ (particles/cm^3)/(particles/mL) for PR772 was obtained. The difference in response functions for PP7 and PR772 was likely due to different ES-DMA settings and operational parameters used (e.g. particle size dependent diffusional losses).

7.2.6 TEM Characterization

TEM analysis employed a standard negative staining procedure performed by JFE Enterprise (Brookeville, MD). Briefly, a drop of 0.01% of BSA was placed on a formvar/carbon coated grid and wicked off with filter paper. Then 2.0 μL of the virus was applied on the coated grid and allowed to air-dry. The grid was washed with distilled water twice and air dried. Subsequently, 10 μL of 1.0% uranyl acetate was placed on the

grid, allowed to stain for 30 seconds, wicked off and then allowed to air dry again before TEM imaging.

7.3 Results

Like any assay, ICH Q2 should be used to validate ES-DMA for any particular application, e.g., testing particle size distributions of vaccines or gene therapy vectors. According to ICH Q2, "the objective of validation of an analytical procedure is to demonstrate that it is suitable for its intended purpose." This guidance recommends evaluation of a quantitative assay along seven lines of inquiry; namely specificity, linearity, range, accuracy, precision, robustness, system suitability, limit of detection (LoD) and limit of quantitation (LoQ). In the remainder of this chapter, the phages were considered as though they were the models for industrially relevant virus preparations of interest and the performance of ES-DMA was evaluated as a quantitative assay relative to ICH Q2 criteria to measure the viral analyte present in the sample.

7.3.1 Specificity

Demonstration of specificity confirms the ability of an assay to distinguish the species of interest within a sample from extraneous material or closely related species such as contaminating adventitious viruses. ICH Q2 states that specificity must "assess unequivocally the analyte in the presence of components … including impurities, degradants, matrix, etc." [44].

ES-DMA can differentiate intact virus particles from impurities associated with degradation products, e.g., capsids that are partially or completely degraded. To model such impurities, virus particles were thermally degraded for 30 minutes at temperatures up to 70 ^{o}C, and ES-DMA size distributions and TEM images were obtained for PR772

and PP7 before and after thermal treatment (Figure 7.1). ES-DMA size distributions for PR772 (Figure 7.1A) showed two peaks corresponding to degraded viruses (≈ 50nm) at 70^{o}C and intact viruses (≈ 60 nm) at ambient temperature and 60 ^{o}C. The full size distribution (Figure 7.1A) also included a third peak at ≈ 8.0 nm which was assigned to P3 trimers based on Bacher *et al*'s [11] molecular weight correlation. Larger structures that were likely aggregates of the capsid proteins also appeared between 10 nm and 20 nm and increased in intensity with increasing incubation temperatures. The specificity of ES-DMA was confirmed by comparing ES-DMA size distributions to TEM micrographs. The TEM micrographs showed a similar trend of intact particles at ambient conditions, partially degraded particles at 60 ^{o}C and then completely degraded particles at 70 ^{o}C with predominantly intact virus particles (Figure 7.1B) and degraded particles (Fig. 7.1C and Figure 7.1D). Some particles of size 100 nm to 200 nm were seen (Fig. 7.1D) but possibly were below the limit of detection of the ES-DMA, for only a few were found in the TEM micrographs.

The ES-DMA size distribution of PP7 (Figure 7.1E) showed putatively intact virus particles (≈23 nm) and degraded capsid proteins or their aggregates at smaller sizes (≈10 nm) that increased in concentration with incubation temperature. Similarly, the TEM micrographs, at ambient conditions showed no difference from sample heated at 60^{o}C (Figure 7.1F); however, in contrast to ES-DMA data, there was little evidence of degraded capsids proteins. Nevertheless, the agreement confirmed ES-DMA's ability to identify specifically intact and partially degraded capsids or aggregates of capsid proteins.

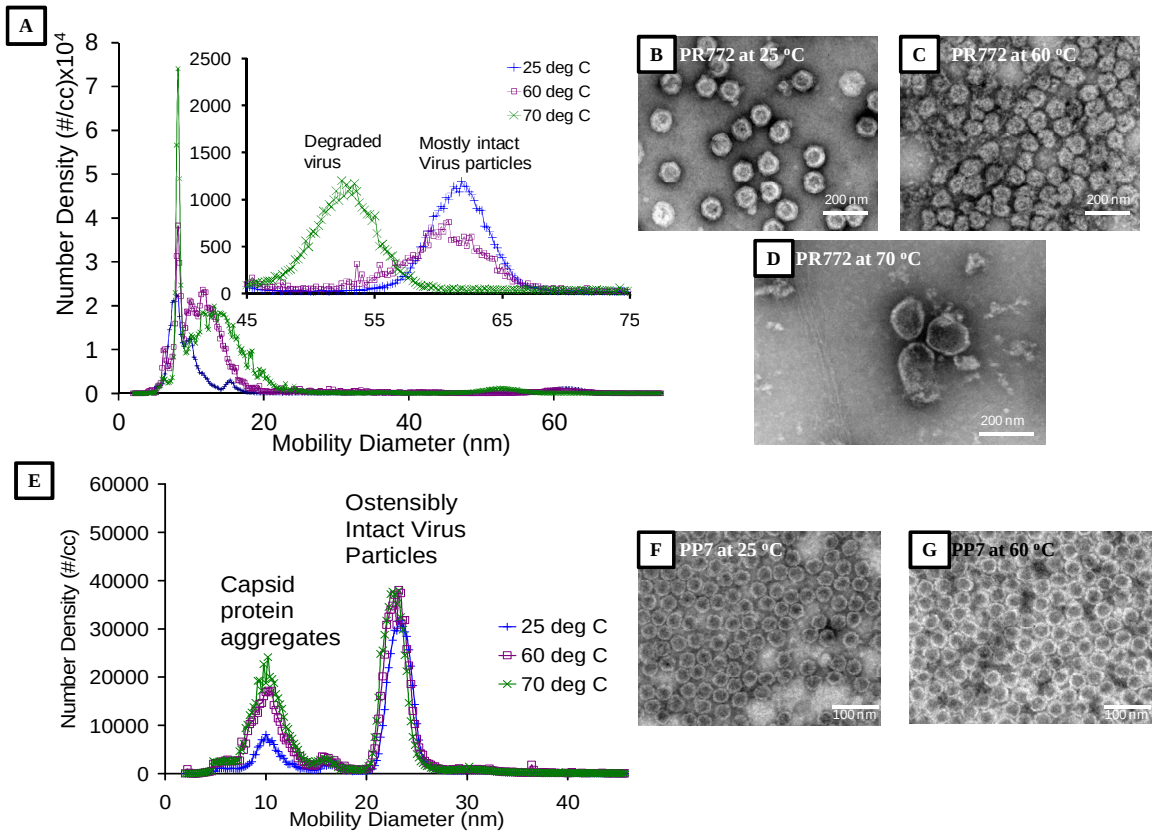

Figure 7.1: (A) ES-DMA size distributions for PR772 and TEM images of PR772 (B) untreated and heated for 30 minutes to (C) 60°C and (D) 70°C. (E) ES-DMA size distributions for PP7 and TEM images of PP7 (F) untreated and (G) heated for 30 minutes to 60°C.

7.3.2 Precision, Linearity and Accuracy

The linearity, accuracy and precision of ES-DMA for measuring the concentration of virus particles were determined. Five different dilutions each of PP7 and PR772 were prepared and their concentrations were determined by a plaque-based assay and ES-DMA. For virus particle concentration measurement, the PP7 peak included counts from 21.0 nm through 26.8 nm and the PR772 peak included counts from 55.0 nm to 67.8 nm. The mean mobility diameter of PR772 and PP7 were determined to be 62.1 nm ± 0.4 nm

and 23.8 ± 0.3 nm respectively for size distributions obtained in triplicate. All linearity studies were performed using the same capillary to rule out any differences arising from different capillaries. ES-DMA gas phase number density as a function of solution concentration of PR772 and PP7 was plotted over a solution concentration range from 4.48×10^{9} particles/mL to 5.15×10^{12} particles/mL and 1.12×10^{10} particles/mL to 9.9×10^{12} particles/mL for PR772 and PP7, respectively (Figure 7.2). The linear fits were $\log_{10}(N)=0.9774\ \log_{10}(C)-5.6782$ with $R^2= 0.9995$(denoted by long blue dash) for PR772 and $\log_{10}(N)=1.09\ \log_{10}(C)-6.1662$ (denoted by short purple dash) with $R^2=0.9993$ for PP7. The linear fits for 60 nm and 20 nm Au were $\log_{10}(N)=0.9425\ \log_{10}(C)+7.2533$ with $R^2= 0.9989$ and $\log_{10}(N)=0.9439\ \log_{10}(C)+7.4424$ with $R^2=0.9996$ respectively. R^2 values in excess of 0.99 for both the cases indicated that the fit was good. The error bars in the Figure 7.2, if not visually apparent, were smaller than the symbols and were from samples run in triplicate. The long (blue) and short (purple) dashed lines guide the eyes. ES-DMA characterizes two properties of particles: size and number concentration.

The accuracy of ES-DMA for determination of size were established for spherical and nearly spherical particles elsewhere [15, 143]. Accuracy of ES-DMA for determination of concentration can be established usually by comparing results with another orthogonal technique although methods are not always directly comparable as given below.

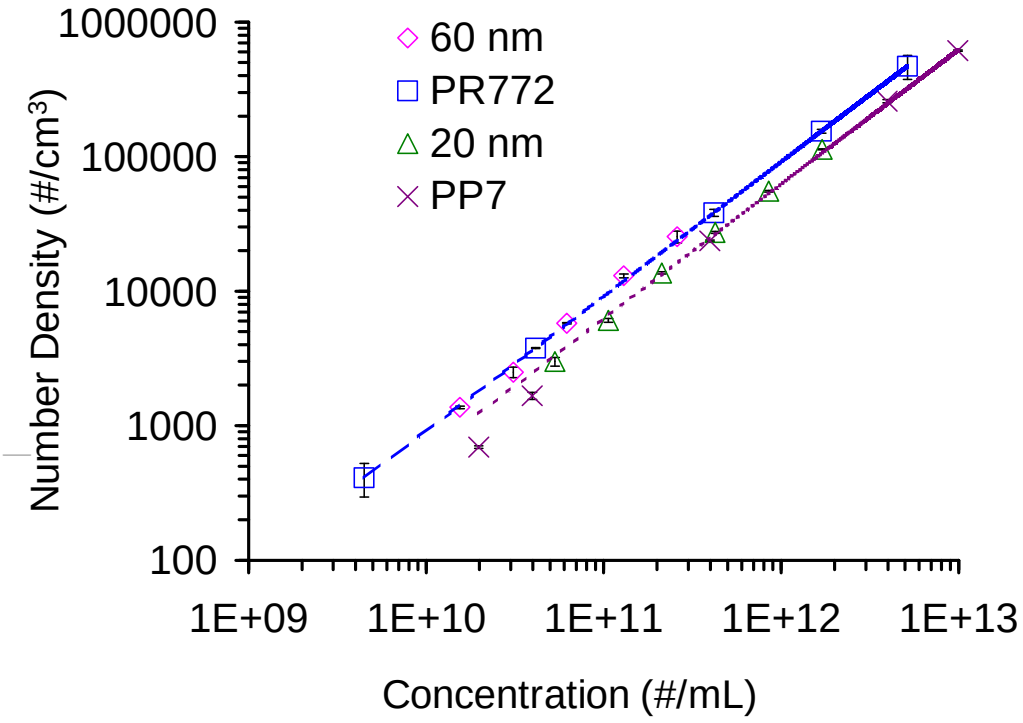

Figure 7.2: ES-DMA aerosol number density, N, versus solution concentration, C, for PP7 and PR772.

To relate ES-DMA counts to concentration of virus particles in solution, ES-DMA was calibrated by analyzing gold nanoparticles of known concentration as already discussed. The absolute liquid phase virus concentration was also determined by ES-DMA (column 4, Table 7.1). Particle measurements were 11-15 fold (PR772) and 22-42 fold (PP7) greater than their infectivity (Table 7.1), showing that these preparations were 2-10% infectious in agreement with previous results [39].

Table 7.1 ES-DMA as compared to plaque assay.

	Plaque Assay derived concentration (pfu/mL)	ES-DMA gas-phase particle counts (particles/cm^3)*	ES-DMA (concentration in solution particles/mL)	Ratio (ES-DMA particles/mL)/(pfu/mL)
PR772a	3.75×10^{11}	471700±96400	5.15×10^{12}	14
PR772b	1.5×10^{11}	154400±5100	1.69×10^{12}	11
PR772c	3.00×10^{10}	38300±2300	4.18×10^{11}	14
PR772d	3.00×10^{9}	2504±200	4.13×10^{10}	14
PR772e	3.00×10^{8}	400±110	4.48×10^{9}	15
PP7a	2.50×10^{11}	614800±7300	9.90×10^{12}	40
PP7b	1.00×10^{11}	258500±6600	4.16×10^{12}	42
PP7c	1.00×10^{10}	23700±330	3.81×10^{11}	38
PP7d	1.00×10^{9}	1700±110	2.69×10^{10}	27
PP7e	5.00×10^{8}	700±20	1.12×10^{10}	22

**Samples run at least in duplicate*

In order to compare the inter-day precision with intra-day precision, samples PR772c and PP7b were measured repeatedly on an individual day to determine the repeatability and across several days to measure the intermediate precision. The data was found to fall within relatively narrow bands (Table 7.2). It was observed that for both PP7 and PR772 the intra-day variations were smaller than the inter-day variation, as is typical for precision studies. The larger inter-day variation was expected because over this time period, the ES-DMA system was shut down (which consists of switching off the ES,

sheath flow and the CPC) and restarted which may have caused modest differences in flow rates or may have affected the performance of the DMA or the CPC. In addition, the effect of changing capillaries was also studied, an issue addressed in greater detail in section 7.3.5.

Table 7.2. Repeatability, intermediate precision and capillary variation statistics for ES-DMA

	Average (particles/cc)	Standard deviation (particles/cc)	Coefficient of variation	Confidence interval*,** (%)
Repeatability PR772c	38300	2300	0.064	6.0
Repeatability PP7b	269300	13500	0.050	4.8
Intermediate precision PR772c	33270	6950	0.209	17.5
Intermediate precision PP7b	265200	17400	0.065	5.5
Capillary variation PR772c	29920	3200	0.107	11.0
Capillary variation PP7b	271140	34750	0.128	13.1

*http://www.itl.nist.gov/div898/handbook/prc/section1/prc14.htm
** *Calculations done at 90% confidence level for samples run in triplicate*

7.3.3 Detection and Quantitation Limits

The limits of detection and quantitation were determined using the signal-to-noise method indicated in ICH Q2. First, the CPC baseline was determined by electrospraying ammonium acetate buffer through a capillary and by obtaining size distributions of this control buffer from 2 nm to 45 nm for PP7 or 2 nm to 75 nm for PR772. Then, the baseline where PP7 (21 nm to 26.8 nm) and PR772 (55 nm to 68 nm) would appear were summed to obtain the limit of detection for these viruses, respectively. This was repeated

in triplicate and the uncertainty in CPC counts in the baseline was determined to be 45 particles/cc ± 14 particles/cc and 7 particles/cc ± 2 particles/cc for the measured size range of PP7 and PR772, respectively (data not shown). This then corresponded to the noise in gas phase. Then by multiplying the average of the gas phase noise with the average response functions of 20 nm and 60 nm Au nanoparticles respectively, the corresponding noise in liquid phase was determined for PP7 and PR772. Further, since ICH Q2 specifications for LoD require a signal-to-noise ratio of 3:1, the liquid phase noise was multiplied by three to obtain LoDs of 7.3×10^{8} particles/mL for PP7 and 2.3×10^{8} particles/mL for PR772 respectively. Expressing these values as plaque assay LoDs (pfu/ml) yielded 2.3×10^{7} pfu/mL (assuming particle:infectivity ratio of ≈ 32) and 1.7×10^{7} pfu/mL (assuming particle:infectivity ratio ≈ 14) for PP7 and PR772, respectively. These values were distinctly higher than the LoD of approximately 10^{6} infectious virus/mL determined by Hogan, *et al*. [14] for bacteriophage viruses although they did not report a baseline uncertainty.

The limit of quantitation (LoQ) was determined using a similar signal-to-noise method. For the LoQ, all steps were similar to that described for LoD except the last one where the liquid phase noise in the above data was multiplied by ten instead of three as per ICHQ2, resulting in LoQs of 2.5×10^{9} particles/mL and 7.5×10^{8} particles/mL for PP7 and PR772, respectively. Expressing the concentration in terms of pfu/mL, the LoQ were determined to be 7.7×10^{7} pfu/mL and 5.6×10^{7} pfu/mL for PP7 and PR772 respectively.

7.3.4 Range

ICH Q2 also requires a determination of the dynamic range of the instrument. The LoQ as specified above defined the lower end of the range. The instrument has an

upper limit of 10^6 particles/cm^3 (in the aerosol phase), but any highly concentrated solution can always be diluted to reduce the concentration to the linear region of the instrument. Thus, the upper range can be defined by the highest particle titer in a test particle.

7.3.5 Robustness

For ES-DMA the primary factors that influence size and concentrations are ambient temperature variations; fluctuations of the gas flow in the electrospray, DMA and CPC; performance of the neutralizer; and variation in capillaries. ICH Q2 calls for investigation of such parameters under the rubric of robustness. Ambient temperature variations may influence the gas flows in the ES, the DMA as well as the CPC. The performance of the DMA depends on the relative rates of a carrier gas in the DMA and the analyte carrying gas that arrives from the ES. Any changes in these flows can cause apparent changes in size and concentration of the particles of interest. Further, inside the CPC, particles are counted by condensing butanol vapors on them, which are also highly sensitive to temperature. Additionally, the flow rates may also vary slightly over time even without temperature changes. Each change may cause variation in counts and size obtained by ES-DMA assay over several hours on the same day or over several days as has been addressed under the rubric of “repeatability” and “intermediate precision”. Further, the neutralizing source used for charge reduction (Po – 210) had a half-life of 138 days and produced enough alpha radiation to neutralize the ionized partices for several months. Had the experiments been conducted over several years, the charging efficiency would have varied in this time frame. This would result in less singly charged particles and concomitantly more doubly charged and triply charged particles as the

efficiency of the neutralizer would reduce. Since all experiments were carried out in a time frame (seven days) much smaller than the half-life of the source, hence the source would not have a significant effect on the results. Capillaries in the electrospray, another robustness parameter, often need to be changed because of clogging from either very large impurities (micron sized) in the solution or from deposition of particles on the electrospray tip with time, which affects ES-DMA concentration measurements. To study this variation, the PP7 and PR772 samples were kept the same and size distributions of these samples were obtained using three different capillaries on the same day. In this regard, the PP7 and PR772 samples had concentrations of 4.2×10^{12} particles/mL and 4.2×10^{11} particles/mL, respectively. For PP7 and PR772 the mean diameters obtained were 23.7 nm ± 0.1 nm and 61.9 nm ± 0.3 nm in conjunction with linearity studies, which implied that changing the capillaries did not affect the size. However, concentrations determined by the ES-DMA were found to vary with change of capillaries (last two rows, Table 7.2). These variations were found to be comparable to the intermediate precision, i.e. changing capillaries on one day had as much effect as did other day-to-day factors (such as flow and temperature fluctuations).

7.4. Discussion and Summary

Manufacturers routinely characterize vaccines and gene delivery products when releasing lots or performing stability studies. Determining the purity of final product and assessing concentration at various stages of product processing are of paramount interest. While techniques such as TEM and dynamic light scattering can be used, drawbacks include long analysis times (TEM), skewing of size for multimodal distributions (dynamic light scattering) and dependence of results on infectivity (plaque assays). Other

characterization techniques such as antigen detection and nucleic acid detection and amplification are also popular but they either require specific antibodies or high concentrations [186]. Also, plaque-forming assays cannot distinguish between a single virus or an aggregate of several viruses which could potentially disassociate upon administration to humans and cause an over dose [187]. MS is gaining popularity for characterization [188], but has been primarily applied to analysis of proteins of viruses [189, 190] and rarely for entire capsids because of their large sizes (> 1 MDa) resulting in high *m*/*z* ratios [191]. But, as mentioned in chapter 3, MS spectra can be complex and size distributions can be difficult to interpret because of multiple charging of particles.

In contrast, ES-DMA is a near real time method that operates at atmospheric pressure, and can resolve the whole size distribution from capsid proteins to the whole virus as has been demonstrated in section 7.3.1. ES-DMA can achieve this objective by correlating identity with size. Thomas *et al.*, [35] has shown that the components of mixtures of very similar sized viruses can be distinguished based on size by ES-DMA. For example, they differentiated MS2 from RYMV based on a 4.3 nm size difference. Even though a database correlating size with identity has not yet been assembled using ES-DMA yet, a broad range of viruses can be distinguished based on their distinct mobility diameters as discussed in the introduction.

It is possible that two or more viruses may overlap in size such as MS2 and PP7 or HRV and GD7, making positive identification and complete discrimination difficult despite the subnanometer resolution of ES-DMA. However, in the case of industrial virus production, risk mitigating factors, such as stock characterization and adventitious agent testing, lower the risk of cross contamination of the widely different viruses.

To make the ES-DMA conducive to biomanufacturing, ES-DMA was evaluated in the context of ICH Q2. The ratio of particles/mL to pfu/mL for a given virus remained approximately constant as a function of decreasing virus concentration (Table 7.1). This suggested that the ES-DMA behaved linearly for the concentration range examined. However, the ES-DMA and plaque assay data did not yield the same counts (Table 7.1), which implied that not all phage particles were infectious such that a direct comparison to infectivity data led to a 10 to 40 fold disparity in the measured values, a common observation in virology when comparing the infectivity assay to methods that physically count particles [192, 193]. This discrepancy between the plaque assay and the ES-DMA measured concentrations presumably involves several factors. ES-DMA is a physical measurement and counts all virus particles whether "live" or "dead", while the plaque assay is infectivity count. To be infectious, a phage must land on the bacteria, penetrate the cell membrane, take over the cellular machinery, and then make copies of itself and finally lyse the bacteria. Each of these processes has an efficiency of less than 100% thus a 1:1 particle to infectivity ratio is rarely achieved for any type of virion. This also explains why the LoDs and LoQs had different limits depending on whether they were expressed with respect to particles/mL or pfu/mL. The plot of linearity (Figure 7.2) showed that the data did not extrapolate through the origin, an observation consistent with that of Hogan, *et al.*, [14] for MS2, T2, and T4 viruses suggesting possible variability in the plaque assay measurements or differences in depositional losses that arise from particles sticking to surfaces (with smaller particles showing a greater propensity to stick because Brownian diffusion is more) which may be size and species specific. PP7 gas phase counts obtained with the ES-DMA started to deviate from

linearity at concentrations below ≈ 10^{10} particles/mL perhaps because of imprecision at the LoD.

Concentration measurements with ES-DMA yielded an uncertainty of ≈ 10-20% (obtained by dividing the standard deviation with the average in Table 7.2), a value close to that reported in a previous study [39] and slightly lower than that of the virus infectivity assay, which has an uncertainty of up to ≈ 30% (unpublished observations, FDA). Additional advantages of ES-DMA compared to infectivity assays include faster analysis time (minutes compared to a day for plaque assay) and that the genetic sequence of the virus or a viral host is not required for analysis.

The LoD was found to be size dependent. As indicated by Hinds *et al.* [24], deposition losses due to particle diffusion increase strongly as the particle size decreases. These losses may occur in the neutralizer, DMA, entrance to the CPC, or all the intermediate connective tubings. Therefore, it is unsurprising that the LoD for PP7 would modestly exceed that for PR772 solely due to diffusion deposition losses.

In summary, as the first step towards potential industry use and acceptance, ES-DMA was examined as a tool for vaccine and gene therapy product characterization in the context of ICH Q2 guidelines. The ES-DMA characterizes both “alive” or inactivated viruses, potentially tracks their degradation, and can resolve aggregated species. Further ES-DMA is rapid, non-biologically based quantitative assay, effective for non-enveloped viruses, with a lower detection limit of ≈ 10^9 particles/mL, and was found to meet the requirements set forth by ICH Q2.

CHAPTER 8: APPLICATIONS: PROTEINS

8.1 Introduction

Detection and characterization of protein aggregates in formulations is of prime importance to the biopharmaceutical industry [194-196]. A concentration-size chart summarizing the most commonly used methods for sizing aggregates is presented in Figure 8.1 [197, 198]. The solid and dashed lines represent boundaries for constant mass of protein particles assuming a spherical density of 1 gm/cc.

Because protein aggregates span a wide range of sizes, and quantification of aggregates depends on the technique employed, there is no one analytical tool that can measure all classes of aggregates [3, 199, 200], and multiple methods are typically used for cross validation [5, 197, 199]. The objective of this paper is to evaluate electrospray – differential mobility analysis (ES-DMA) as another method to add to the suite of protein aggregate characterization tools.

The current configuration of the ES-DMA used in this dissertation, can characterize particles from approximately 3 nm up to approximately 150 nm spherical equivalent diameters. From prior work it has been determined that the lower limit of detection of ES-DMA is in picomolar range [14, 19, 30, 201]. While, the upper limit of concentration till recently, has been limited by the inability to differentiate between intrinsic aggregates, from aggregates formed from different oligomers residing in the same ES droplet, it was demonstrated in chapter 5 that such an artifact can be eliminated. As shown by Figure 8.1, ES-DMA, size exclusion chromatography (SEC), analytical ultra-centrifugation (AUC) and field-flow fractionation (FFF), overlap in the range of analyte sizes they

characterize. However ES-DMA offers a limit of detection that is at least two orders of magnitude lower.

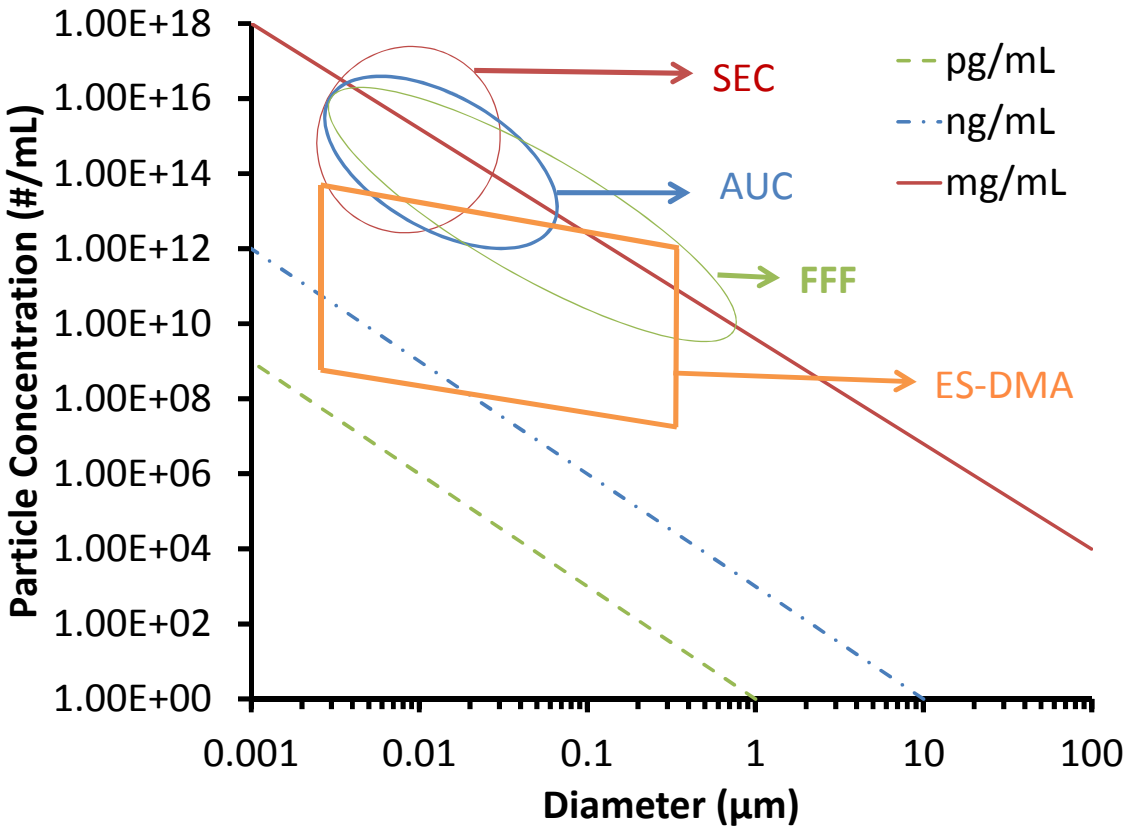

Figure 8.1: The concentration and size landscape of the most popular characterization tools namely size exclusion chromatography (SEC), analytical ultra-centrifuge (AUC) and field-flow fractionation (FFF). (Adapted and modified from [198])

In this study using SEC with ES-DMA two proteins, a monoclonal antibody therapeutic of the IgG1 class, Rituxamab® (RmAb) and a polyclonal human antibody (hIgG) are characterized. The proteins are systematically heat stressed, to promote the formation of aggregates, which are characterized using both techniques.

8.2 Sample Preparation

8.2.1 Protein Sample Preparation

RmAb and hIgG samples were prepared by the same procedure as outlined in chapter 4. All samples were subsequently diluted to concentrations of about 0.1 mg/mL in 20 mmol/L ammonium acetate buffer at pH 7 for analysis with ES-DMA and SEC. This diluted concentration was not verified by UV/vis spectrometer as it was below the limit of quantitation of the instrument in this chapter. Samples that were not heat treated were used as controls. Aggregate formation was accelerated by subjecting samples to 70 ^{o}C for 30, 60, 90, and 120 minutes for RmAb and for 10, 20, 30, 60, 90 and 120 minutes for IgG to monitor the time evolution of the aggregate formation. The heat incubated samples were preserved in the refrigerator at 4 ^{o}C before analysis. Because the heat treated samples showed evidence of large aggregates that could potentially clog up electrospray capillaries and size exclusion columns, hence the samples were filtered using 0.22 μm filters (Millex GV – Catalogue #: SLGV004SL) prior to characterization.

8.2.2 Size Exclusion Chromatography (SEC)

SEC was performed with a Agilent 1200 system using a TSK 3000 gel filtration column at ambient temperature. Using 20 mmol/L ammonium acetate buffer in the SEC column caused the IgGs to adsorb to the SEC column and no protein would elute for several hours. Thus 100 mmol/L potassium phosphate at pH 7.0 along with 300 mmol/L sodium chloride was used as reported in other studies [184, 202]. The injection volume was 50 μL at 0.5 mL/min flow rate with UV detection at 280 nm. Because the

concentration of the protein injected and recovered were below the limit of quantitation of the UV/vis spectrometer used in this study hence the recovery could not be calculated for hIgG and RmAb. However, several steps were taken, that qualitatively suggest that protein adsorption (esp. the monomers) to the SEC column was low. Before running the actual heat treated samples for analysis the columns were pretreated with heat incubated samples (t = 30 minutes sample for hIgG and t = 60 minutes for RmAb) three times (approximately 30 minutes each). SEC chromatograms obtained for these samples did not show any difference from run to run. Further, after finishing all experiments for the day, the column would be flushed with buffer (100 mmol/L potassium phosphate at pH 7.0 along with 300 mmol/L sodium chloride) for 1.5 hours followed by a 10% methanol wash during which only nominal protein would desorb from the column, implying nominal adsorption to the column. For quantitative analysis it was also assumed that the recovery of monomers at different incubation times stay the same for the proteins.

The dimers and monomers were quantified by integrating from elution time of 14.33 minutes to 20.81 minutes and 11.62 minutes to 14.32 minutes respectively. The fractional percentages of dimers were determined by first integrating the area under the monomer and dimer peaks at that particular incubation time, and then dividing dimer peak area by the monomer peak area at the same incubation time. The background noise for the SEC was determined by integrating the area under the monomer and dimer peaks after running 20 mmol/L ammonium acetate buffer in triplicates. The respective average values obtained were 534 arbitrary units and 222 arbitrary units.

8.2.3 ES-DMA

The voltage and current measured in the ES unit were approximately in between 1.6 kV to 1.8 kV and – 170 nA to – 180 nA, respectively, for all samples. To achieve sufficient resolution from the DMA, the ratio of sheath-to-aerosol flow rates within the DMA was set to 25, which provides a theoretical resolution of ~0.4 nm for the antibodies. Under these conditions, data were collected with a voltage scanning step size of 0.2 nm and a dwell time of 10 seconds from 2 nm to 45 nm, i.e. it would take approximately 36 minutes to obtain each ES-DMA size distribution, comparable to SEC experiment. The ES capillary was passivated using gelatin following an approach outlined in chapter 4.3.

From the size distribution (number concentration vs. size) the area under the monomer, dimer, trimer, tetramer and pentamer peaks were determined by integrating from 7.8 nm to 9.8nm, 10.0 nm to 11.6 nm, 11.8 nm to 13.0 nm, 13.2 nm to 13.8 nm and 14.0 nm to 14.8 nm, respectively. Oligomers were identified by an empirical correlation, between mobility diameter and molecular weight that is discussed in greater detail later. The average background noise in ES-DMA under the monomer, dimer, trimer, tetramer and pentamer peaks was found to be 241 particles/cm^3, 125 particles/cm^3, 54 particles/cm^3, 23 particles/cm^3 and 18 particles/cm^3 respectively.

About 20 μLto 30 μL aliquots of samples were for used for analysis, but only 2 – 3 μL was consumed during the course of an experiment, i.e. the sample volume requirement of ES-DMA is significantly less compared to SEC.

The reader should note that the signal produced by the ES-DMA can be material dependent. Similar observations have been made by the mass spectrometry community [203]. However, despite the material dependency, ES-DMA size distributions (after

correcting for ES artifacts) can reflect the intrinsic levels of aggregates of different particles in solution, or in other words, ES-DMA can be used for determining absolute liquid phase concentrations irrespective of material property [102, 103].

8.3 Results and Discussion

8.3.1 Size distributions obtained with ES-DMA

Figure 8.2A shows the size distributions of the RmAb obtained by ES-DMA for unstressed (t= 0 minutes) sample and samples that were incubated at 70 ^{o}C for increasing incubation times. For peak identification the correlation from Bacher *et al* [11]between mobility size (d) and molecular weight (MW) expressed in kDa:

$$MW = - 22.033 + 9.83\ d - 1.247d^{2} + 0.228\ d^{3} \quad (8.1)$$

Using this correlation, the monomer, dimer, trimer, tetramer and pentamer peaks for IgG with a molecular weight of 150 kDa should appear at 9.3 nm, 11.7 nm, 13.4 nm, 14.7 nm and 15.8 nm, respectively. This correlation was specific to their experimental set-up and operating conditions, and can vary up to 1 nm for different DMAs [64]. In this work the monomer, dimer, trimer, tetramer and pentamer peak appeared at 8.8nm, 10.8nm, 12.6nm, 13.4nm and 14.4 nm, respectively, in reasonable agreement with the predicted values. Pease *et al*. [19] have also shown that the sizes of IgG oligomers as measured by the ES-DMA are in excellent agreement with the structural dimensions obtained from protein crystallographic database. Thus oligomer peaks from ES-DMA size distributions can be identified with a high degree of confidence. Besides these, there are three peaks that are characterized at sizes 3.6 nm, 6.2 nm and 7.6 nm. The proportion of these peaks are insignificant (<< 1 %) compared to all other peaks and correspond to the non-volatile solute that may still be present in the solution after the desalting step, doubly charged

monomers of RmAb (not intrinsic to the solution, produced during neutralization in the gas phase), and dimers of F-ab fragments of RmAb, respectively.

The size distributions in Figure 8.2A, show a decreasing trend for monomers (labeled 1), dimers (labeled 2) and trimers (labeled 3) with increasing incubation time, while the tetramers (labeled 4) and pentamers (labeled 5) increase initially (t = 30 minutes and t = 60 minutes), but subsequently decrease at later times. While larger oligomers are clearly evident in the spectra the resolution is insufficient to make a definitive assignment. The maximum intensity of the aggregates for the sample incubated for 120 minutes appear at mobility diameter of 19 nm to 20 nm. Assuming Bacher's correlation the molecular weight at this mobility diameter corresponds to approximately 1300 kDa to 1500 kDa i.e. the most of these aggregates are probably enneamers (9-mers) and decamers (10-mers) of RmAb.

Figure 8.2B shows the size distributions for hIgG where the oligomers are again identified using Bacher's correlation. Like RmAb, the monomers (labeled 1), dimers (labeled 2) and trimers (labeled 3) decrease with incubation, however, unlike RmAb, the larger aggregates do not increase with incubation time. The size distribution also shows two smaller peaks (<< 1% compared to other peaks) at 6.2 nm and 7.8 nm which correspond to the doubly charged monomers (not intrinsic to the solution, produced during neutralization in the gas phase) and dimers of F-ab fragments, respectively. It is possible that larger aggregates of RmAb and hIgG (> 50 nm) form with increasing incubation time at concentrations below the limit of detection of ES-DMA. In fact, at longer incubation times, visible precipitation was observed for both proteins. Flow imaging methods indicated increasing concentrations of particulates with incubation time

ranging in size from 4 μm to 100 μm for both RmAb and hIgG (data not shown). For both the Figures 8.2A and 8.2B the normalization has been done with respect to the area under the monomer peak at t = 0 minutes. All distributions are at an ES capillary pressure drop of 3.7 PSI. Size distributions obtained at 3.0 PSI pressure have not been shown but show similar trend.

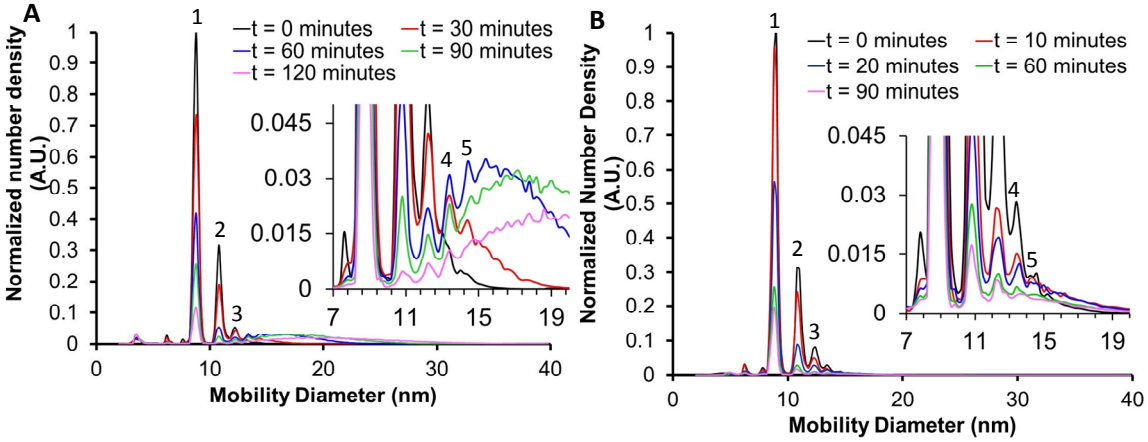

Figure 8.2(A) Size distribution of RmAb for increasing incubation times at 70 ^{o}C. The inset shows a magnification of different aggregates as a function of incubation time. (B) Size distribution of IgG prepared at different incubation times at 70 ^{o}C.

Because of "droplet induced aggregation" introduced in chapter 5, the data obtained with ES-DMA needs to be corrected. For simplicity it is being assumed that only monomers and dimers exist in the solution. This is a reasonable assumption based on previous findings using other aggregate characterization techniques [103, 184, 202] and by using SEC, as discussed in the next section, for IgG and RmAb. In all such cases, the proportion of the intrinsic trimers was negligible (< 1%). Then equations 5.21 and 5.25 could be invoked at two different pressure drops to obtain the intrinsic liquid phase

monomer and dimer concentrations. The percentage of the intrinsic dimers determined following this approach is discussed later.

The larger aggregates, as measured by the ES-DMA, are quantified and plotted as a percentage of all oligomers present at each incubation time in Figure 8.3 below. It is evident that for RmAb the proportion of tetramers and larger oligomers increases as a function of incubation time (Figure 8.3A) whereas for IgG the proportion remains constant (Figure 8.3B). The percentages have been determined by first integrating the area under the respective oligomer (trimer, tetramer and pentamer) peak at the each incubation time divided by the integrated area under the monomer + 2×dimer + 3×trimer + 4×tetramer + 5×pentamer peak.

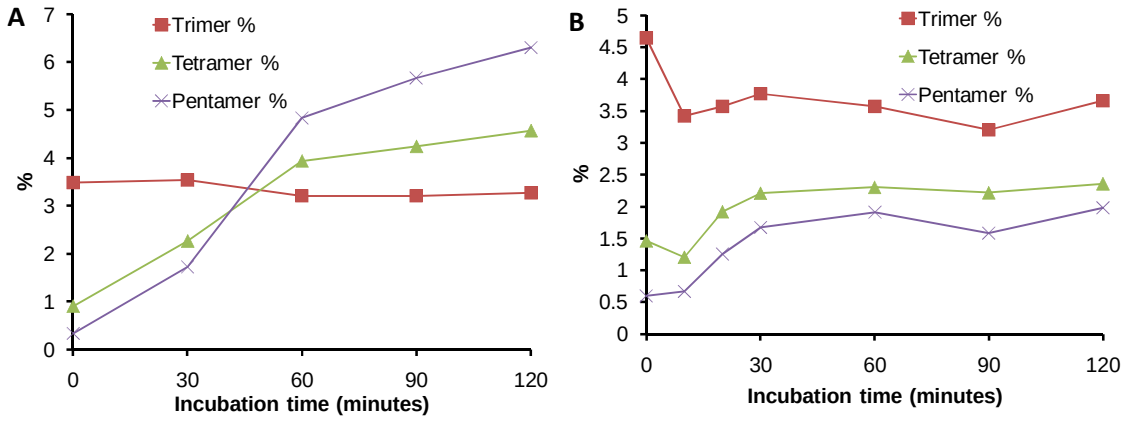

Figure 8.3 (A) Percentages of the trimers, tetramers and pentamers of RmAb and (B) IgG as a function of incubation time as obtained by the ES-DMA.

8.3.2 SEC Chromatograms

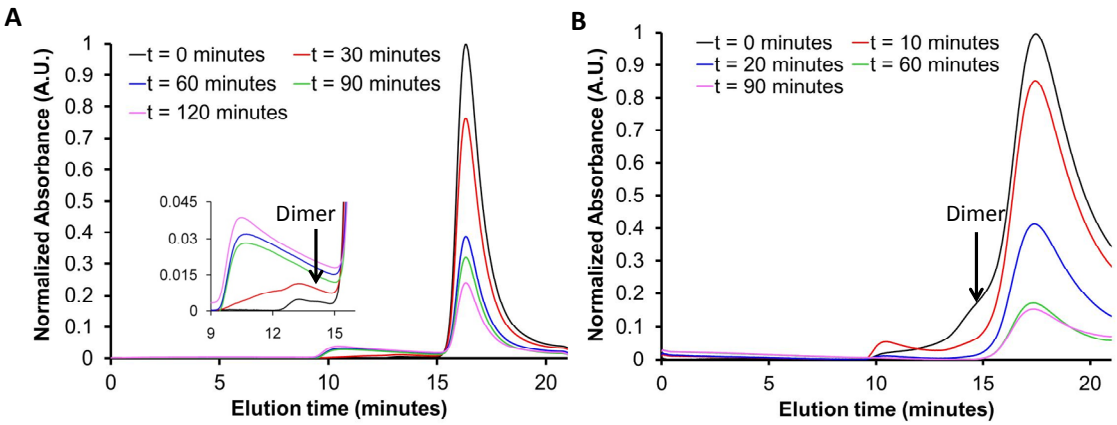

Figure 8.4 **(**A) Chromatograms of RmAb obtained with the SEC for heat treated samples at increasing incubation times at 70 ^{o}C. The inset shows a magnification of the aggregate region (B) Chromatograms of hIgG obtained with the SEC for heat treated samples at different incubation times at 70 ^{o}C.

Figure 8.4A shows SEC chromatograms of RmAb for increasing incubation times at 70 ^{o}C. In SEC larger aggregates will elute first, so the last peak is assigned to the monomer. Little evidence of dimers and trimers in the t= 0 minutes and t = 30 minutes samples are seen. Larger aggregates appear after t=60 minutes that increase in intensity with incubation time. Figure 8.4B shows SEC chromatograms of hIgG. The mode of the monomer peak for both RmAb and hIgG are at approximately 16.3 minutes, but the full width at half max for hIgG is approximately 5.43 minutes compared to only approximately 1.38 minutes for RmAb implying that hIgG interacts with the SEC column longer. Evidence for larger aggregates are observed, for short incubation periods, but drop below the background after 10 min of incubation. The fact that the monomer peak is dropping, with no observation of higher aggregates at long incubation times would indicate that larger oligomers grow very rapidly depleting the system of intermediates

(dimers, trimers etc). In Figure 8.4, for both RmAb and hIgG, the acetate peak elutes first (before 20 minutes) in all samples and has not been shown for clarity. Also, for both the plots (A) and (B) the normalization has been done with respect to the area under the monomer peak at t = 0 minutes.

8.3.3 Comparison of ES-DMA with SEC

Table 8.1, compares the dimer proportions obtained by SEC and ES-DMA (before and after correcting for "droplet induced aggregates") for RmAb and hIgG. The standard error bars are calculated from measurements on three samples. For columns 2, 4, 5 and 7 of Table 8.1 the dimer to monomer proportions have been determined by dividing the area under dimer peaks with the area under the monomer peaks at that incubation time. For columns 3 and 6, the dimer to monomer ratio represents C_{p2}/C_{p1} determined after using equations 5.21 and 5.25 to solve for C_{p1} and C_{p2} respectively. It is evident from the ES-DMA results that a major proportion of the dimers detected were droplet induced. Even after correction for "droplet induced aggregates", it was found that ES-DMA indicates a higher fraction of dimers than SEC at t = 0 minutes. In order to understand the possible sources for the discrepancy in between these two techniques AUC was used to quantify the dimer to monomer proportions for the t = 0 minute samples; the dimer/monomer ratio for RmAb and hIgG were determined to be 4.8%±0.8% [103] and 11.7%±1.9%, respectively (for hIgG refer Chapter 5). Thus the dimer to monomer ratio obtained using AUC and ES-DMA appear to be the same and slightly greater than SEC. Out of the three techniques, the error bars in the dimer percentage measurement of ES-DMA is highest perhaps because of the variability in the measurement of ES droplet sizes. It was not possible to quantify the percentage of the dimers and larger oligomers

for the heat incubated samples using AUC, as the dimer and other oligomer proportions in these samples were below the limit of detection of the AUC, but, as evident from Table 8.1, for all heat incubated samples the dimer to monomer proportion obtained with ES-DMA was greater than SEC (except hIgG at t = 0 minute for which the dimer/monomer proportion obtained with ES-DMA and SEC are comparable). There are several possible reasons for these differences. Firstly, both in ES-DMA and SEC protein is subject to shear forces, which could potentially induce aggregation or alternatively break small oligomers apart. Secondly, high salt concentrations in the mobile phase of the SEC are used to minimize adsorption of protein, but it is known that high salt concentrations can also break up aggregates [5]. Thirdly, prior work by others has indicated that dimers may preferentially absorb in the SEC column [200, 204]. Inaccuracies can also arise in determining the dimer/monomer ratio using the ES-DMA. There could be two sources for this: a) as mentioned in chapter 5 the correction for "droplet induced aggregation" requires the droplet volumes of the ES and any inaccuracy in these measurements can propagate in the determination of the dimers/monomer ratio and b) for RmAb it was initially assumed there are monomers and dimers in solution, however, with increasing incubation time (after 60 minutes) there was evidence of trimers, tetramers and larger aggregates that are intrinsic to the solution (Figure 8.3A) which was not accounted for in the modeling.

Table 8.1. Dimer/Monomer ratio for ES-DMA before and after correcting for "droplet induced aggregates" and SEC at different incubation times at 70 ^{o}C.

Time	RmAb			hIgG		
	ES-DMA before correction	ES-DMA after correction	SEC	ES-DMA before correction	ES-DMA after correction	SEC
minutes	Dimer %	Dimer %	Dimer %	Dimer %	Dimer %	Dimer %
0	33.0 ± 2.0	5.0 ± 2.0	1.0 ± 0.4	37.0 ± 5.0	12.0 ± 6.0	7.0 ± 2.0
10	-	-	-	25.0 ± 1.0	7.0 ± 2.0	4.0 ± 2.0
20	-	-	-	18.0 ± 2.0	7.0 ± 2.0	ND[2]
30	27.0 ± 2.0	5.0 ± 2.0	2.0 ± 0.1	16.0 ± 2.0	8.0 ± 4.0	ND[2]
60	15.0 ± 1.0	2.0 ± 1.0	ND[1]	13.0 ± 2.0	7.0 ± 2.0	ND[2]
90	11.0 ± 2.0	3.0 ± 2.0	ND[1]	11.0 ± 1.0	6.0 ± 2.0	ND[2]
120	6.0 ± 1.0	2.0 ± 1.0	ND[1]	9.0 ± 2.0	4.0 ± 2.0	ND[2]

ND[1] (not determined) For these samples the SEC was not able to resolve the dimers from the larger aggregates hence the dimers were not quantified

ND[2] (not determined) The signal-to-noise ratio for the dimers for these samples were less than 3

Based on the signal to noise (S/N) ratio of the monomers and larger aggregates for the different samples obtained with SEC and ES-DMA the detection limits for these two methods were compared. For ES-DMA, considering RmAb sample at t = 120 minutes the monomer, dimer, trimer, tetramer and pentamer average counts were 158961 particles/cm^3 (not corrected for droplet-induced artifacts), 8371 particles/cm^3 (not

corrected for droplet-induced artifacts), 13467 particles/cm^3, 18780 particles/cm^3 and 25913 particles/cm^3, respectively. Comparing these values to the background noise (provided in materials and methods section) it is evident that the S/N ratio was 2 to 3 orders of magnitude higher than the background noise. On the other hand for the same sample the average monomer counts obtained with SEC was 5342 arbitrary units, and thus the monomer S/N ratio was ~ 10 (the background noise for SEC monomers is provided in materials and methods section) whereas the S/N ratio for dimer was < 3. Thus, ES-DMA appears to have a lower limit of detection.

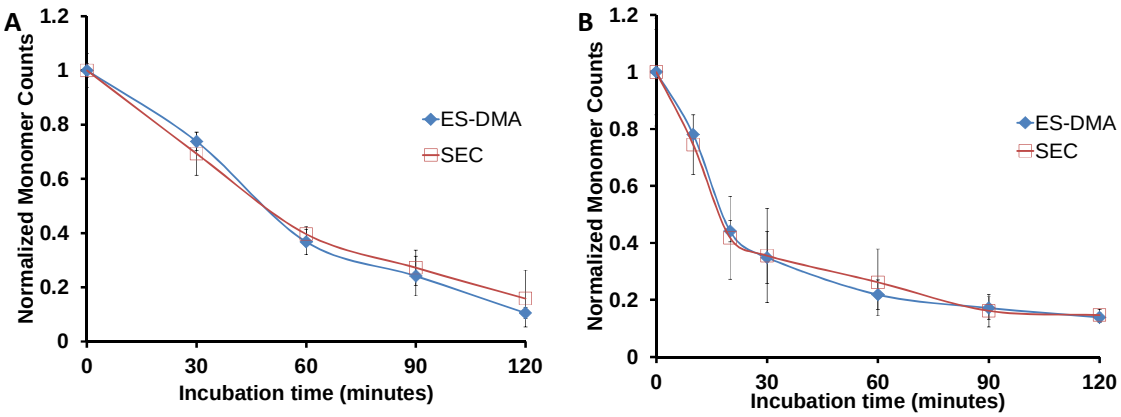

Figure 8.5: (A) Normalized monomer counts for RmAb as a function of incubation time at 70 ^{o}C obtained with SEC and ES-DMA (after correcting for "droplet induced aggregation"). (B) Normalized monomer counts for hIgG as a function of incubation time 70 ^{o}C obtained with SEC and ES-DMA (after correcting for "droplet induced aggregation").

Despite the differences in the dimer fractions, there appears to be good agreement in the relative amount of monomer decay between ES-DMA and SEC, as can be seen in the normalized monomer plots of RmAb (Figure 8.5A) and hIgG (Figure 8.5B) as a function of incubation time. The error bars are for measurements made in triplicate. For the SEC

normalization has been done with respect to the total area under the monomer peak at t = 0 minutes. For ES-DMA the normalization has been done with respect to the absolute monomer concentration at t=0 minutes.

The monomer decay can be described by a general rate equation:

$$\frac{dC}{dt} = -kC^n \tag{8.2}$$

where C is the concentration of the monomer in the liquid phase at time t, k is the rate constant, and n is the reaction order.

For n=1, assuming C_o is the initial monomer concentration, the concentration of monomers, C_t at time t is:

$$\ln(\frac{C_t}{C_o}) = -kt \tag{8.3}$$

For $n \neq 1$, the general rate equation can be solved to get:

$$(\frac{C_t}{C_o})^{1-n} = 1-(n-1)kC_o^{n-1}t \tag{8.4}$$

Further kC_o^{n-1} can be replaced with an apparent rate constant k', such that

$$(\frac{C_t}{C_o})^{1-n} = 1-(n-1)k't \tag{8.5}$$

For IgGs a wide range of reaction orders have been proposed, n = 1.0 [205, 206], 1.2 [207], 1.5 [208, 209], 2.0 [210, 211] or 2.5 [212]. The order of the reaction is typically determined by fitting the experimental data using different reaction orders, and assigning the order with highest R^2 value.

The reaction-order fitting results are presented in Table 8.2. In the case of RmAb it was found that both ES-DMA and SEC indicated a reaction order of approximately unity. Physically, this may either imply that the aggregation process is unfolding limited or occurs via monomer addition to oligomers [213]. Despite being completely different techniques, the difference in the decay rate constants are within 5% of each other and in good agreement with those reported previously [211, 214] for the temperature range, 55 ^{o}C to 70 ^{o}C.

Table 8.2. Rate constants and R^2 values obtained for RmAb and IgG using ES-DMA and SEC by fitting different reaction orders.

	RmAb				hIgG			
	ES-DMA		SEC		ES-DMA		SEC	
n	k' (min^{-1})	R^2	k' (min^{-1})	R^2	k' (min^{-1})	R^2	k' (min^{-1})	R^2
1	**0.0073**[a]	**0.97**	**0.0069**[a]	**0.99**	0.0096	0.84	0.0083	0.84
1.2	0.0210	0.94	0.0175	0.98	0.0235	0.89	0.0230	0.90
1.5	0.0292	0.88	0.0226	0.96	0.0316	0.95	0.0304	0.97
2	0.0540	0.77	0.0364	0.88	**0.0549**[b]	**0.99**	**0.0517**[b]	**0.99**
2.5	0.1095	0.66	0.0625	0.79	0.1023	0.98	0.0939	0.96
3	0.2430	0.57	0.1137	0.71	0.2024	0.95	0.1809	0.91

[a] The uncertainty in rate constant measurement for ES-DMA and SEC were determined to be ±0.001 min^{-1} and ±0.0016 min^{-1}, respectively, based on measurements on three samples.

[b] The uncertainty in rate constant measurement for ES-DMA and SEC were determined to be ±0.003 min^{-1} and ±0.011 min^{-1}, respectively, based on measurements on three samples.

For hIgG, a second order reaction yielded the best fit for both SEC and ES-DMA. This physically implies that the rate of dimer formation controls the rate of monomer

depletion. The apparent rate constant k' obtained for hIgG is in good agreement with values obtained elsewhere [207, 210, 215] at 65 ^{o}C to 70 ^{o}C. In addition, the rate constants obtained by both methods agree well, differing by only ≈ 6%.

8.4 Summary

Using two heat incubated IgGs the ability of ES-DMA and SEC to characterize oligomers were compared. Results of this study indicated that ES-DMA can be a useful method for monitoring protein stability and for characterizing protein aggregates and its capabilites are at par and in some cases (e.g., resolution, detection limit) better than those of SEC. ES-DMA observes a higher fraction of dimers, and due to its inherent higher resolving power, and lower limit of detection was able to characterize the larger oligomers that were not apparent in SEC at the concentrations used in this chapter (≤ 0.1 mg/mL). In addition ES-DMA generally has shorter analysis time and lower sample volume requirements than SEC. Although ES-DMA has certain constrains as discussed in chapter 3, it is anticipated that the above demonstration will make it a popular process analytical tool in the future.

CHAPTER 9: APPLICATIONS: NANOPARTICLE-PROTEIN COMPLEXES

The objective of this chapter is two-fold: i) to demonstrate that ES-DMA can be used to monitor nanoparticle-protein conjugate (or otherwise also referred to as complex) stability and ii) to demonstrate through an exploratory experiment that ES-DMA can also be used for glycan analysis.

9.1. Nanoparticle-protein conjugate stability

9.1.1 Introduction

The importance of nanoparticle-protein conjugates was already established in chapter 6. One desirable property of conjugates is that they should be very stable [173]. If not stable, conjugates may aggregate and these aggregates can appear in sizes spanning from few nanometers to several micrometers. This size range is within the operational range of both dynamic light scattering (DLS) and transmission electron microscopy (TEM) and thus both these techniques are routinely used for monitoring conjugate stability [20, 67, 100, 173]. However, each of these techniques has certain disadvantages. For example in DLS, the scattered light intensity scales as the sixth power of the hydrodynamic diameter of particles, thus although it is sensitive to aggregation, it fails to provide multimodal size distributions for highly polydispersed systems. Further, it is difficult to correlate intensity obtained with DLS to the liquid phase concentration of particles. TEM on the other hand is expensive and time consuming. The objective of this chapter is to demonstrate that ES-DMA can also be routinely used for monitoring conjugate stability.

9.1.2 Materials and Methods

9.1.2.1 Sample preparation

Ammonium acetate, a volatile buffer, at a concentration of 2 mmol/L, was prepared in 0.5 L volumes by adding 0.077 g of ammonium acetate and the pH was increased to 9.4 by adding about 250 µL of ammonium hydroxide. Polyclonal human IgG (Sigma Aldrich, isoelectric point pH 4.8 – 9.3) was suspended in the above mentioned buffer at pH 9.4 to prepare a protein solution of concentration 1 mg/mL. These pH and IgG concentrations were intentionally chosen as it was found that choosing a lower pH or significantly lower concentration of IgG causes significantly more gold-nanoparticle-protein conjugate monomer loss as a function of centrifugation.

Commercial Tedpella 30 nm gold nanoparticles were taken in 450 µL aliquots to which about 2 µL of ammonium hydroxide was added to increase the pH to ~ 10 after which 50 µL of 1 mg/mL IgG solution was then added and then allowed to interact for 0.5 hours (Figure 9.1B). This sample will be referred to as 0× AuNP-IgG henceforth. For removing the excess protein, another aliquot was centrifuged for 10 minutes at 10,000 rpm (Figure 9.1C), then 450 µL of the supernatant replaced with 450 µL ammonium acetate buffer at pH 9.4 (Figure 9.1D and 9.1E). This sample will be referred to as 1× AuNP-IgG. Likewise, steps c to e were repeated to prepare samples that were centrifuged twice and thrice and will be referred to as 2× AuNP-IgG and 3× AuNP-IgG respectively. Control protein solutions were also prepared which involved centrifuging the samples zero, one, two and three times and will be referred to as 0× IgG, 1× IgG, 2×IgG and 3×IgG respectively.

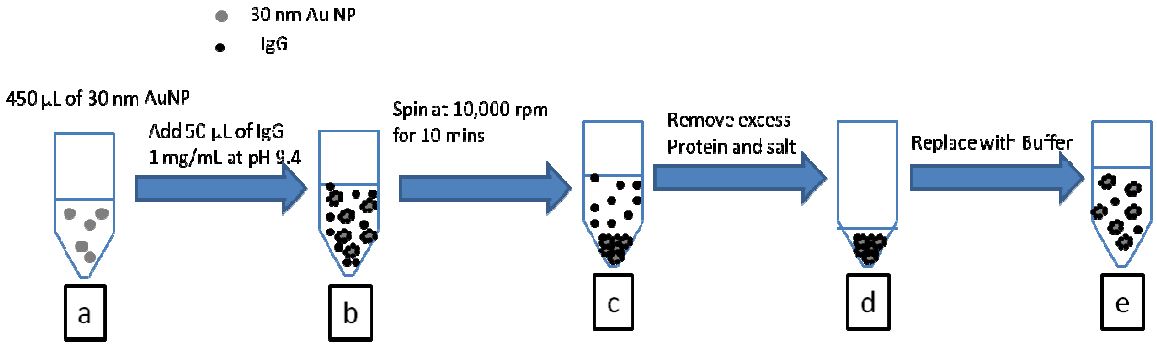

Figure 9.1: Demonstrates the steps involved in preparation of AuNP-IgG sample. Step b and e will be refered to as 0× Au NP-IgG and 1× Au NP-IgG samples respectively. After Step e, c to e are repeated to prepare 2× Au NP-IgG and 3× Au NP-IgG samples.

9.1.2.2 ES-DMA operation

A 40 µm capillary with an outer diameter of 150 µm and length of 24 cm was used to electrospray the conjugates and AuNP samples as it is difficult to achieve stable Taylor Cone with 25 µm capillary while using low ionic strength solutions (~ 2 mmol/L). The ES chamber pressure was maintained at 3.7 PSI. The DMA was operated at 10 L/min and the CPC was operated at high flow mode (1.5 L/min).

As mentioned in chapter 5, one of the artifacts of using the ES is if the concentration of particles is high (say > 10^{13} particles/mL or the ES droplet size is large (say > 100 nm) then two or more particles (conjugates in this context) can get encapsulated in the same ES droplet and appear as "droplet induced aggregates". For this particular study, the concentration of the AuNPs was 2×10^{17} #/m^3 (provided by manufacturer), i.e., it was low enough such that "droplet induced aggregation" did not play any dominant role. It should be pointed out that this rationale applies to the bare

AuNP particles as well as the conjugate samples since this artifact is independent of material property.

9.1.2.3 TEM

A JEOL 2100 TEM was used for obtaining micrographs of the AuNP, IgG and AuNP-IgG conjugates in the size range of 10 nm to ~ 5 μm. About 3 – 5 μL of sample volume would be applied on ultrathin carbon film on a 400 mesh copper grids (Ted Pella Inc.). The samples would then be dried in a vacuum chamber (Thermo Scientific) for ~ 2 hours and then stored in the refrigerator at 4 ^{o}C prior to analysis.

9.1.2.4 Fluid Imaging

FLOWCAM (Fluid Imaging Technologies Inc.) [216] was used for for determining size distributions of conjugate aggregates in the size range of 4 μm to 50 μm. A 10X Olympus lens was used for taking images of the aggregates. The flow cell used had a cell depth of 100 μm and width of 2000 μm. The solution of interest was pumped through the flow cell at the rate of 0.05 mL/min. For the given cell dimensions, this rate were fast enough to eliminate the possibility of capturing the image of same aggregate multiple times. A particle segmentation threshold was defined with dark pixels of 8.0 and light pixels of 6.0. These parameters were used to differentiate particles from the background. The distance to nearest aggregate neighbor was selected as 3 μm to eliminate the possibility of counting smaller aggregates within larger ones. An auto image rate of 10 frames/sec was selected. Usually a solution would be run until 5000 particles had been imaged which ensured repeatable and good statistical data. Increasing the data acquisition time further had no influence on the size distributions.

9.1.3 Results and Discussion

The conjugate samples were centrifuged upto three times and their stability was monitored and compared against the uncentrifuged conjugate as well as bare gold nanoparticles using DLS, ES-DMA, TEM and FLOWCAM. Figure 9.2A shows the hydrodynamic diameter of the bare gold and conjugates samples as a function of centrifugation. The bare AuNP appeared at size 35.3 nm in reasonable agreement with the labeled size of 33.2 nm of the parent stock solution. After addition of IgG and subsequent incubation for 30 minutes, the size increases to 52.0 nm implying successful conjugation of AuNP with IgG. The 17 nm increase with the DLS is more than the 10 nm size of IgG and seems to indicates that IgG forms multiple layers on AuNP surface. In order to accurately quantify the number of layers of IgG adsorbed a fluorometer was used. For a typical IgG the projected side, end and frontal areas are 53 nm^2, 68 nm^2 and 94 nm^2 respectively. This implies that depending on the conformation of IgG, upon adsorption about 40 to 70 IgG monomers can adsorb to a single 33 nm AuNP to form a complete monolayer. The results with fluorometer suggested that about 140±40 IgG monomers adsorbed per AuNP (i.e. 2 to 3 layers depending on conformation). This could either imply that IgG undergoes significant structural change upon adsorption to the AuNP so that the surface can accommodate more monomers than the theoretical estimates above or that IgG adsorbs to form multiple layers on to AuNP. As already discussed, DLS results appear to suggest the later. Such multilayered adsorption of proteins to AuNPs or planar surfaces has also been observed before as already mentioned in chapters 4 and 6.

Upon centrifuging the conjugate samples, the hydrodynamic diameter was found to increase almost linearly as shown in Figure 9.2A. The error bars are from measurements on three samples and if not visually apparent are smaller than the symbols used. This can either imply that more IgG is adsorbing to the AuNP as a function of centrifugation or that centrifugation is creating aggregates that is biasing the DLS hydrodynamic diameter to larger sizes as has been reported in previous studies [20, 66, 67]. The former explanation is unlikely, as with each centrifugation step significant IgG was removed from the solution and was replaced with buffer (for example, after 1st centrifuge about 10% free IgG is left in solution, after 2nd centrifuge about 1% free IgG is left in solution and so on), which means that the amount of free IgG left in the solution after each centrifugation step is lesser so the likelihood of more protein adsorbing to the AuNP is also reduced. Further, there is further evidence with ES-DMA, TEM and FLOWCAM that supports the samples were indeed aggregating and is discussed below.

Figure 9.2B shows size distributions of the bare AuNP samples and the conjugated samples as a function of centrifugation using ES-DMA. Like DLS, the ES-DMA for AuNP-IgG 0X shows an increase in mobility size compared to the bare AuNP sample implying successful conjugation. The increase in size with the ES-DMA is just about 7 nm from 33 nm to 40 nm. This is a factor of two lower than the increase seen in DLS. This contradiction is not unreasonable as DMA is a gas phase technique and the measurements are not done under the same hydrated conditions unlike DLS. In fact, a systematic comparison of size measurements obtained with DLS and DMA previously has shown that mobility size increase measured for ligands adsorbed to nanoparticles always comes out to be lesser than increase in hydrodynamic size [20, 66, 67]. The

increase of mobility size obtained for AuNP-IgG-0X sample can also be used for quantifying the amount of protein adsorbed per NP. However, ES-DMA can under-report protein adsorbed especially for multilayered protein adsorption to NP, as has already been discussed in Chapter 6 and was thus not used in this study for quantifying the proteins adsorbed.

From the size distributions of centrifuged samples in Figure 9.2B, it is evident that unlike DLS, the mobility size of the conjugate monomers stayed the same with subsequent centrifugations although the monomer counts decreased along with the appearance of small quantities of aggregates at sizes ~ 50 nm and ~ 60 nm. It has been shown using ES-DMA, that dimers of particles appear at size ~ 1.26 times that of the monomer while trimers appear at size ~ 1.5 times that of the monomers [217]. Based on this information, the aggregates at ~ 50 nm and ~ 60 nm are identified to be dimers and trimers of the conjugates. For quantifying the extent of aggregation, one can integrate the area under the monomer, dimer and trimer peaks and plot them as a function of centrifugation (Figure 9.2C). It is evident from Figure 9.2C that the total monomer concentration decreases to ~ 50 % whereas the average mobility diameter remains invariant of centrifugation. The decrease of monomers and concomitant increase of larger aggregates appears to qualitatively explain the increase in hydrodynamic size obtained with DLS. Although trimers are the largest aggregates seen with ES-DMA, there could also be larger aggregates existing in the solution that were not detected by ES-DMA because they were below the detection limit of the instrument, which in this regard is 10^9 particles/mL as pointed out in chapter 7. Infact, for samples that were centrifuged twice

and thrice, aggregates were visually confirmed as well. In order to characterize and validate the existence of larger aggregates TEM was used.

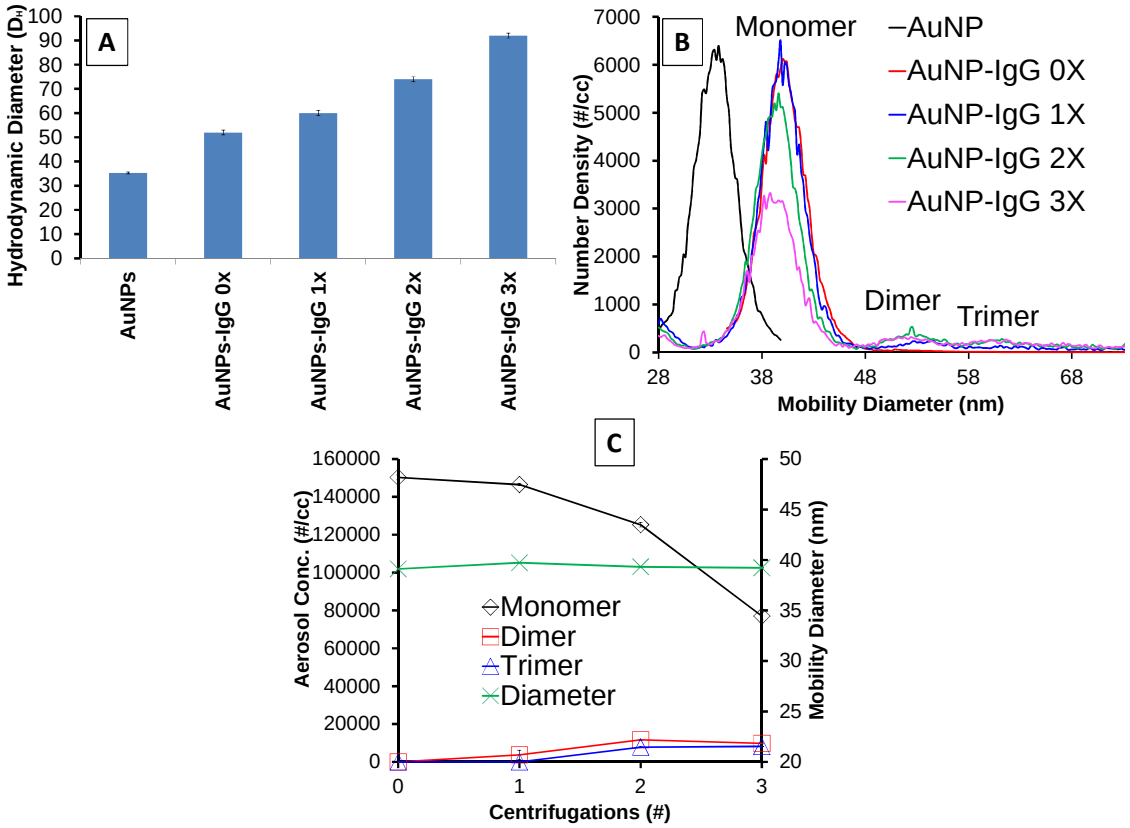

Figure 9.2: (A) The hydrodynamic diameter of AuNP (not centrifuged) and AuNP-IgG samples as a function of centrifugation. (B) ES-DMA size distributions of the same samples. (C) The total gas phase counts (primary Y-axis) of monomers, dimers and trimers and mobility diameter (secondary Y-axis) as a function of centrifugation.

Figure 9.3A shows 0× AuNP-IgG conjugate sample as seen under the TEM. The commercial AuNP solution had non-volatile citrate salt that dried up on the TEM grids and created background with dark patches making it difficult to discern the monodispersed AuNP-IgG conjugates. The fact that these dark patches indeed are from citrate was validated by taking TEM images of uncentrifuged AuNP samples (in citrate

buffer) and IgG samples (in acetate buffer). AuNP samples clearly had the same characteristic as Figure 9.3A (data not shown) while such dark patches were not evident from IgG samples in acetate buffer (data not shown). Upon zooming up of Figure 9.3A the conjugates become visible (Figure 9.3D) and appear to be monodispersed. Further zooming even upto 10 nm (data not shown) does not show any evidence of protein adsorbed to the conjugates. This is not surprising, as it is known from studies in literature [173], proteins adsorbed to nanoparticles are often times not clearly evident even with high resolution TEM, although independent evidence from DLS, ES-DMA and fluorometer suggests otherwise. Figures 9.3B and 9.3C clearly showed a mixture of conjugates monomers along with structures that ranged in size from few hundred nanometers to more than a micrometer. A zoom up of one of these larger structures (Figure 9.3E) confirmed that these structures were made up of individual AuNP-IgG conjugates and were thus aggregates of these conjugates. Usually AuNP aggregates (that are not functionalized) fuse at the grain boundary [143], whereas the individual AuNP particles in these aggregates appear to be slightly apart from neighbouring AuNP particles. This implies that these individual units were AuNP-IgG particles and not bare AuNP particles. This aggregation also appears to explain the conjugate monomer loss observed with ES-DMA and the increasing hydrodynamic diameter seen using DLS.

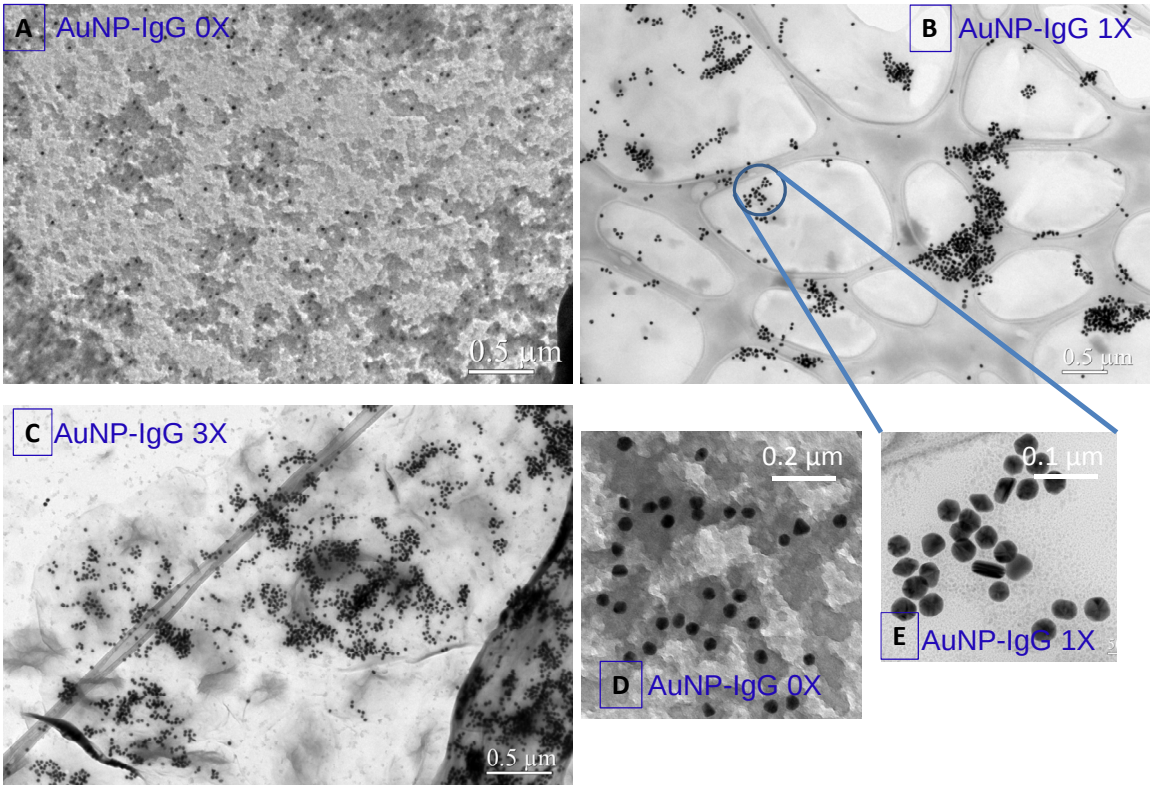

Figure 9.3: TEM images of (A) AuNP-IgG 0X, the black dots represet the individual AuNP-IgG conjugates, the dark grey color patches are from citrate, and the light grey color is from the carbon background of TEM grids, (B) AuNP-IgG 1X, (C) AuNP-IgG 3X, (D) zoom up AuNP-IgG 0X (also showing patches of dark grey citrate background along with light gray carbon background) and (E) zoom up AuNP-IgG 1X.

From the TEM data, it would be possible to obtain multimodal size distribution over the size range of a few nanometers to several micrometers. However, such a task would be extremely time consuming to the extent that it would be impractical from the industrial perspective to use it. On the other hand, FLOWCAM which is fairly inexpensive (~ $20k USD) can provide size distributions of micrometer sized particles in the order of few minutes and thus can be conveniently used for monitoring stability. A

FLOWCAM constitutes of a flow cell (Figure 9.4A) through which the sample passes at a known flow rate. As the aggregates pass through they are counted and photographed. For a known sample analysis time (usually 3 to 5 minutes, but can be longer for better statistics if aggregate concentration is low), the aggregate concentration can be determined. The photographed images are then analyzed and the equivalent spherical diameter of particles determined. Figure 9.4B shows some of aggregates that were photographed for the AuNP-IgG 3X sample. As seen in Figure 9.4B some aggregates appear to be spherical, while others appear fibrillar. Thus, even for the same sample, the morphological characteristics for the aggregates can widely vary. Most particles shown in the Figure 9.4B were greater than 10 μm although majority of the aggregates in solution were less than 10 μm as is evident from the size distributions obtained from FLOWCAM (Figure 9.4C). As the smaller aggregates were closer to the lower size limit of the instrument (4 μm) their morphological characteristics were not clear from the photographs. It should be pointed out that no difference was found in the characteristics of the aggregates for different samples (0X to 3X). In Figure 9.4B some aggregates are in better focus of the objective lens of the camera and thus appear to have sharper edges compared to others. The end result of analysis is a size distribution of the sample of interest in the size range of 4 μm to 100 μm (or larger). Figure 9.4C shows such size distributions for the conjugate samples (AuNP-IgG 0X to AuNP-IgG 3X) along with an AuNP control sample which has very little aggregates. The FLOWCAM used in this study is not set up to distinguish protein particulates biophysically (such as fluorescence) from other aggregates. Thus it is not evident from the data if these aggregates were protein aggregates or AuNP-IgG aggregates. Thus to explore this further, 0.1 mg/mL IgG

samples were subjected to the same centrifugal stress as the conjugate samples and size distributions were obtained with the FLOWCAM subsequently. This way, one could compare the extent of aggregation for these samples with that of the conjugates by integrating the area under the size distributions. Figure 9.4D plots the integrated size distributions for IgG and AuNP-IgG centrifuged different number of times (from 0 to 3 times). It is evident that the IgG samples do not aggregate significantly under centrifugal stress while the conjugates do, thus implying these aggregates must be conjugates. This is in conjunction with the decrease of monomers of conjugates seen with ES-DMA (Figure 9.2B) and the increase of Au-NP conjugates seen with TEM (Figure 9.3B, 9.3C).

One can attempt to quantitatively reconcile the increase in the aggregates with FLOWCAM with the decrease in the conjugate monomers with ES-DMA. Because the concentration of the AuNP particles in solution were known, the gas phase counts obtained with ES-DMA could be, in principle, correlated with liquid phase concentration and thus ES-DMA can be used to determine the total volume loss in the liquid phase because of monomer loss. Similarly, as the aggregate sizes and their concentrations are known, the FLOWCAM can be used to determine the total volume increase because of aggregate formation. Following this approach, it was found that the increase in volume with FLOWCAM was 10 fold more than what is expected based on ES-DMA results. ES-DMA has been successfully used for correlating the liquid phase concentrations with the gas phase on several occasions before as demonstrated in Chapters 4, 7 and 8, thus this 10 fold offset is not because ES-DMA but rather FLOWCAM. Fluid imaging methods such as FLOWCAM is relatively new and size distributions and aggregate sizes obtained with it can widely vary depending on several factors such as a) background contrast, b) liquid

flow rates, c) lenses used etc. even if the instrument is operated within the recommended settings of the manuals. Such variations are surprising as this technique is fairly new and more research is currently underway for understanding these above effects better [218]. Thus, at this point the FLOWCAM results can only be regarded semi-quantitatively until a better understanding of these factors are thoroughly understood.

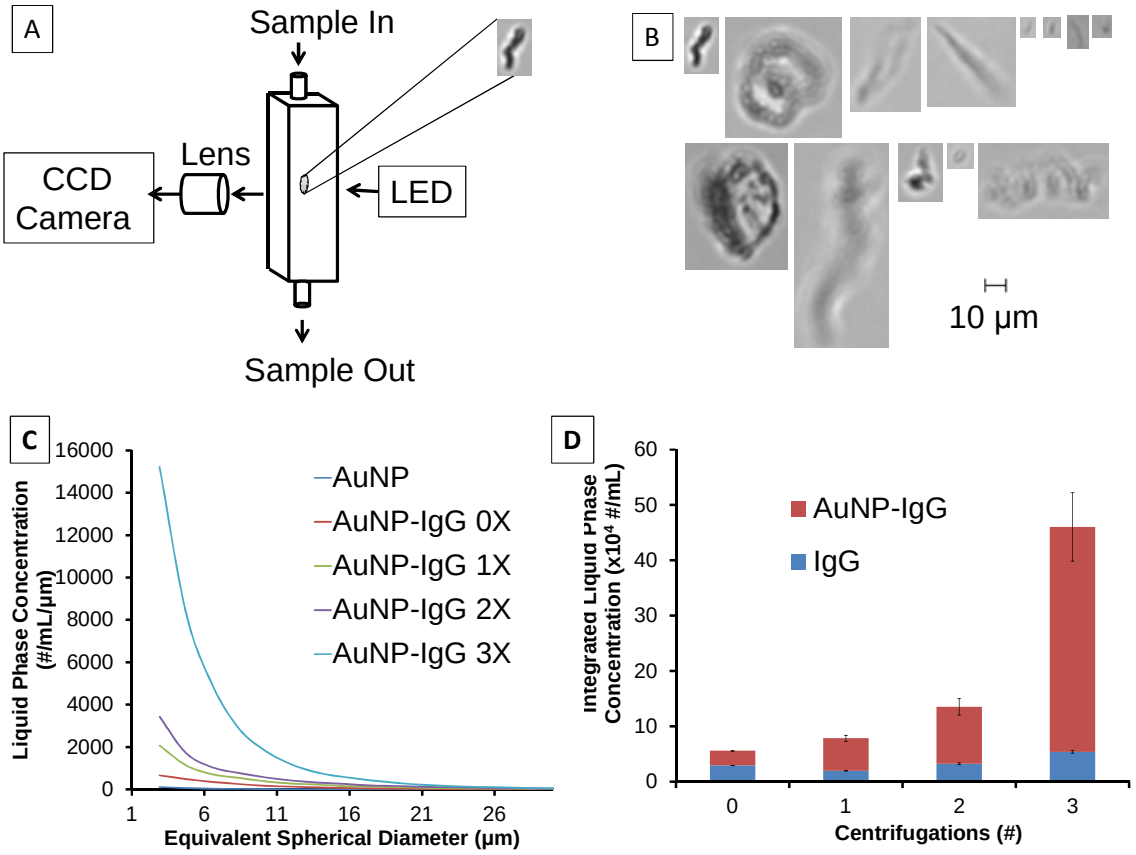

Figure 9.4: (A) Simplified schematic of the internal constituents of a FLOWCAM. (B) Photographs of different conjugate aggregates for AuNP-IgG 3X sample. (C) Size distribution of centrifuged samples and of the control AuNP. (D) The integration of size distributions obtained with FLOWCAM for the AuNP-IgG conjugate and IgG samples as a function of centrifugation.

9.1.4 Summary

AuNP-IgG conjugate aggregates were intentionally produced by centrifugation and were then characterized using ES-DMA, DLS, TEM and FLOWCAM. ES-DMA can provide more quantitative information about conjugate stability compared to DLS and is significantly quicker than TEM. FLOWCAM, a fluid imaging method was also explored in this context and although the results were in qualitative agreement with ES-DMA, DLS and TEM, it was not quantitative enough to close the volume balance.

9.2 Glycan Analysis: Preliminary results

9.2.1 Introduction

The majority of approved protein therapeutics possess some type of glycans which are sugar molecules covalently attached to the protein. There can be significant heterogeneity in the type of glycans carried the same protein which can concomitantly affect the safety and efficacy of a drug [219, 220]. Thus glycans are usually comprehensibly characterized by enzymatic deglycosylation followed by chromatographic [219] and/or mass spectrometric techniques [221]. Although these methods provide rigorous characterization of glycan structure, they can be time consuming and expensive, and require highly trained personnel. In contrast, lectin based assays, in principle, are simple, inexpensive, and rapid alternative for monitoring identifying glycans [222]. In such an approach, a protein X with a glycan Z is incubated with gold nanoparticles. Then a lectin Y is added that is capable of identifying glycan Z. Thus the lectin Y upon incubation with the above sample attaches to another AuNP-X

conjugate and also may adsorb to other AUNP-X conjugates thus creating a network of aggregates. The schematics of the approach is shown in Figure 9.5.

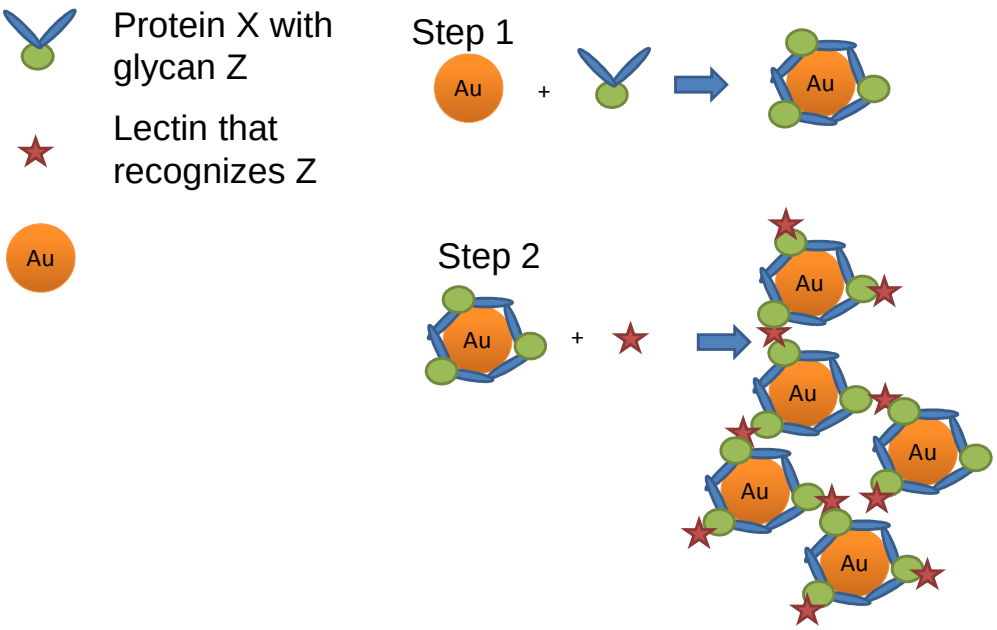

Figure 9.5: Schematics of a lectin based assay for identifying glycans.

9.2.2 Materials and Methods

Concanavalin A, was purchased from Vector Laboratories and used without further purification. Ribonuclease B (RNase B, from bovine pancreas, >80 %), sodium chloride (99.9 %), manganese chloride tetrahydrate (99.99 %), calcium chloride dihydrate (98 %), 4-(2-hydroxyethyl) piperazine-1-ethanesulfonic acid (HEPES, 99.5 %), and indium foil (99.99 %) were purchased from Sigma-Aldrich and used as received. Citrate-stabilized gold nanoparticles (average diameter ≈10 nm) were purchased from Ted Pella. The manufacturer reported concentration is 5.7 x 10^{12} particles/mL. Lectin and bovine serum albumin solutions were prepared to the desired concentrations by dissolving in HEPES buffered saline, HBS (pH 7.4, 150 mmol/L NaCl, 0.01 mol/L HEPES, 1 mmol/L

Ca^{2+}, 1 mmol/L Mn^{2+}). Type I water (UV treated; 18 MΩ-cm; 0.2 micrometer final filter) was used for all solution preparations.

To prepare protein-modified gold nanoparticles, the protein was first dissolved in water at a concentration of 1 mg/mL. The pH of the as received 10 nm gold nanoparticle solution was raised to ≈10 with 0.1 mol/L NaOH (measured by EMD colorpHast pH test strips). Protein solution was added to the gold nanoparticle solution at a volume ratio of 1:10. The solution was mixed and allowed to incubate at room temperature for at least 30 min before analysis or use.

9.2.3 Results and discussion

In the context of Figure 9.5, protein X is RnaseB, and the lectin that recognizes the glycan mannose (Z in Figure 9.5) of RnaseB is ConA. Figure 9.6 shows size distribution of 10 nm Au and its peak mobility appears at ~ 11 nm in conjunction with previous findings. After adsorption with RnaseB it shows an increase in size by about 2 nm. It also shows small fractions of dimers at ~ 17 nm. These dimers of the conjugates were probably induced during centrifugation of the sample. After adsorption of ConA to this sample, a wide distribution is obtained and its intensity is clearly much less than the Au and Au-RnaseB conjugates and is thus plotted with a seconday axis. In this regard, the Au-RnaseB-ConA sample has been normalized with respect to the Au-RnaseB sample. This wide distribution is indicative of an aggregating sample which was also confirmed visually (by change in color of the solution), UV-Vis and DLS [223].

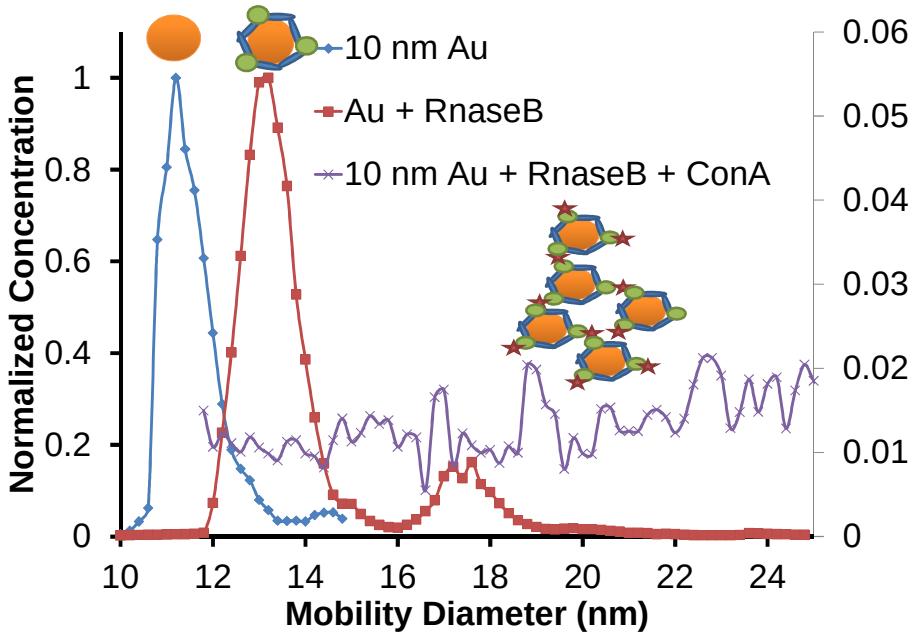

Figure 9.6: Size distributions of Au, Au-RnaseB and Au-RnaseB-ConA.

9.2.4 Summary

The above example thus qualitative demonstrates that ES-DMA can be used for monitoring lectin bindings to glycans. Further, experiments need to be conducted for quantitative measurements. However, there are several challenges that may hamper its application in this area. For example, the above analysis is rather qualitative because of the rapid decay of the concentration of AuNP-RnaseB-ConA conjugates. If the rate of aggregation was slower, then indeed ES-DMA could be used used to obtain mechanistic information about the aggregation. Another issue that might hinder ES-DMA's usage in this area is that usually the lectin binding chemistry is carried out in high concentrations of non-volatile buffers which is not electrosprayable. This poses two challenges: i) change of buffer might affect the kinetics and ii) buffer exchange typically is time consuming (several minutes if centrifuged, several hours without centrifugation) and the kinetics of aggregation has to be slower than the time required for buffer exchange.

Chapter 10: CONCLUSIONS

This chapter briefly describes the intellectual contributions and the anticipated benefits because of the research conducted in the context of this dissertation. It also identifies the directions of future research.

10.1 Intellectual Contributions and Anticipated Benefits

As it is difficult to disseminate the contributions from the resultant benefits hence they are hereby being discussed together. It should also be pointed out that this list is not necessarily in the order of importance.

1. **Review of ES-DMA:** Chapter 3 provides the first comprehensive literature review of all applications of the ES-DMA since its development in the context of bionanoparticles. As a peer reviewer noted: “I have followed the subject reviewed from its very beginning as an interesting curiosity, and was pleasantly surprised to learn from this review that it is in its way to making some impact.” This work has since been accepted for publication at *Trends in Biotechnology* and is tentatively scheduled to appear in the May, 2012 issue [224]. The author anticipates, given the wide audience of this journal and given the wide variety of information that can be extracted by using ES-DMAs, it will become a popular tool in the near future.

2. **Adsorption-Desorption of proteins to ES surface and its effects:** Protein adsorption has been a nuisance that has bothered the ES community for about three decades. The author demonstrated, that by simply correlating the liquid phase concentrations with gas phase ES-DMA can be used to quantify the protein adsorbed and desorbed. As one of the peer reviewers pointed out: “The systematic study undertaken of the phenomenon is of considerable interest, as it establishes a relatively powerful method for protein adsorption

studies." The reviewer in this case was referring to section 4.1 which was published in *Langmuir* [144]. Section 4.2 extended this to oligomeric proteins. Because the shear rates inside ES capillaries are comparable to that inside human blood vessels, thus it also makes ES-DMA the one of the few tools that can be used at such high shear. Given the ease with which surfaces can be modified (as shown in section 4.3, published in *Journal of Colloids and Interface Sciences* [180]) the author anticipates that ES-DMA can become a powerful tool that can be eventually implement by the biopharma and food industry for studying adsorption-desorption of complex heterogeneous proteins on surface-modified ES capillaries. Section 4.3 also ameliorates the concern that protein desorbing from silica capillaries do not influence aggregate distributions. This essentially implies that prior publication that had been carried out without passivating capillaries were accurate in the context of quantification of aggregates.

3. **Validated ES-DMA in the context of ICH-Q2:** Although ES-DMA has been in use for more than 15 years it has been mostly limited to research labs. This in part was because no systematic study was available in the context of ICH-Q2. In essence a technique needs to be "validated" by demonstrating that it meets the stringent criterion set by ICH. In view of that, a systematic study was undertaken to demonstrate that ES-DMA does indeed meet ICH's criteria. As one peer reviewer commented "it looks quite systematic and can be served as a solid validation of ES-DMA for practical usage." This work (Chapter 7) was published in *Journal of Virological Methods* [201]. The assays that are currently used for viral characterization and concentration measurements are extremely time consuming (order of hours and days, respectively). ES-DMA on the other hand is extremely quick (order of few minutes) and thus can streamline

biomanufacturing. Thus the author anticipates that as it has been validated, ES-DMA can become an important process analytical tool in the near future.

4. **Characterization of Protein Aggregates:** Chapter 8 determines that ES-DMA has a better resolution and lower limit of detection compared to the industrial workhorse - SEC and yet shows excellent agreement with SEC in monitoring monomer stability. Given that ES-DMA is also quicker than SEC and requires significantly less sample volume, it is only a matter of time before it is accepted by the biopharma industry as an at-line process for streamlining manufacturing and also for improving the quality of drug products. As the editor of the *Journal of Pharmaceutical sciences* pointed out this "… manuscript contains original and significant new findings …". In this case he was referring to data presented in Chapter 8. This work is already published in the above mentioned journal [225].

5. **Droplet Induced Aggregation:** The probability of two or more particles residing in the same ES droplet and producing an artificial dimer has been long thought to be an issue with ES units. However, no experimental methodology was available to eliminate this artifact. The author assisted Mingdong Li, who is currently a graduate student under Prof. Michael R. Zachariah in developing a methodology that eliminates this artifact. The work described in Chapter 5 is published in *Aerosol Science and Technology* [103] and *Langmuir* [102]. This approach depends substantially on the accuracy of the ES droplet volume determined. Unfortunately, current capillaries that are produced by commercial companies such as TSI and New Objective do not produce ES droplet volumes that have low variability and hence the applicability of the approach is currently limited. However, it is anticipated that with better capillaries, the methodology can be commercialized so

that “droplet induced aggregates” can be corrected for during data analysis. Concomitantly, this may increase the current upper limit of particle concentration that is currently used with ES-DMA systems.

6. **Quantifying Ligand Adsorption to Nanoparticles:** Although traditionally DMA-APM has been used for obtaining mass of very large aggregates (of the order of 100 nm) this is the first application of ES-DMA-APM for quantifying liquid phase protein adsorption to nanoparticles. Obtaining the mobility size using DMA and then the mass using DMA-APM can be useful in understanding the orientations of proteins after adsorption. Thus in the near future ES-DMA-APM can prove to be an useful tool in this context at least in the research labs.

7. **Increased the Library of Bionanoparticles Characterized:** In the past 15 years ES-DMA has been used to characterize a variety of nanoparticles. The author increased this library by characterizing more than 50 different bionanoparticles. In order to make this dissertation a coherent story it was beyond the scope to include all particles characterized. However, Figure 10.1 provides a glimpse of the most important nanoparticles characterized by the author. The letters within parenthesis stand for: P – published, U – unpublished, M – manuscript under preparation, and S – submitted.

Proteins	Nanoparticles	Viruses	Complexes
1. Insulin (P)	1. 10 - 200 nm Au (P)	1. PP7 (P)	1. Au-BSA (M)
2. RnaseA (U)	2. 10 – 100 nm Si (U)	2. PR772 (P)	2. Au-hIgG (M)
3. RnaseB (U)	3. 40 – 80 nm Ag (U)	3. Influenza (U)	3. Au-PEG (5k -20k) (U)
4. TnF (P)	4. 60 nm PSL (P)		4. Au-TnF (P)
5. Amelotin (U)	5. 100 nm PSL (P)		5. Au-RnaseA (U)
6. BSA (S)	6. 4 – 40 nm Sucrose (P)		6. Au-RnaseB (U)
7. RmAb (P)			7. Au-RnaseB-ConA (U)
8. hIgG (P)			8. Au-RnaseA-ConA (U)
9. IgG3 (FDA) (U)			9. Au-PEG (5k-20k)-IgG (U)
10. IgG3 (U .Mass.) (U)			10. MS2-Ab (P)
11. IgM (P)			11. Au-PP7 (U)
			12. Au-SAMs (P)
			13. PSL – RmAb (M)

Figure 10.1: List of most important bionanoparticles characterized from Jan, 2008 to Feb, 2012.

10.2 Future Research

Usually lab-driven research and industry-driven research take separate paths. Keeping that in mind, this section provides the potential future directions of research in each of these categories. As far as the industry is concerned there are at least two frontiers:

1. **Automation of Sample Analysis:** Much like current industrial ES-MS units and LC-MS units, the entire process from sample insertion to data analysis could automated by incorporating the transfer functions of the different ES-DMA components (chapter 2) (currently implemented in TSI Inc. built units) as well by integrating "droplet induced aggregation" theory (chapter 5).

2. **High-throughput Analysis and Lowering Limit of Detection of ES units:** Another direction would be to make significant modifications in current ES units, to enable multi-

capillary systems that could potentially enable high throughput analysis. Further, design modifications in ES units could also be made to lower the limit of detection.

In the context of lab research there are several areas that require further investigation. They are listed as follows:

1. **Adsorption Based Analysis for proteins:** The affinity of most proteins to ES silica capillary can be harnessed to characterize complex heterogeneous protein mixtures. This is demonstrated with an example in section 4.4.

2. **Glycan Analysis:** One approach of identifying different glycans in a protein is a lectin based approach, whereby addition of the right lectin to a glycoprotein solution causes aggregates to form that can then be characterized. Given the excellent resolution of ES-DMA and the first analysis time, it could potentially be used to understand the aggregation mechanisms of such aggregation. This is discussed in greater detail in 9.2.

3. **Structural changes of proteins (esp. non globular proteins) inside the ES-DMA:** Although this was pointed out in Chapter 3, pursuing this study would require multiple spectroscopic techniques such as circular dichroism (CD), Fourier transform infrared spectroscopy (FTIR) etc. Because such techniques require large quantities of protein, it would require very long (several hours) of sample collection time at the end of the ES-DMA unit to pursue such a study.

4. **Do the proteins retain any water post DMA:** Although it is presumed that the ES droplet completely dries up, there is yet to be any experiment proof in the context of ES-DMA to validate this.

5. **Proteins produce different signal outputs compared to nanoparticles:** It is interesting that different proteins produce different signal outputs that is significantly less

compared to inorganic nanoparticles (such as gold or sucrose). This is seen in ES-MS too, but given that the charging mechanism of ES-neutralizer is presumably material independent, such a material dependent response is unexpected and definitely requires further research.

6. **Better capillary passivations to reduce protein adsorption:** It was shown in chapter 4 that gelatin is able to significantly reduce immunoglobulin adsorption. However, gelatin fairs poorly against other proteins. Thus it would be interesting to investigate other types of passivations to reduce protein adsorption to ES capillaries.

Finally, the author anticipates that in the coming decade the popularity of ES-DMA would continue to increase exponentially and will continue to provide answers to different questions in the realm of bionanotechnology.

APPENDIX A: CFD simulations of a modified DMA design

A.1. Introduction

The objective of this project was to explore a new DMA design that could be implemented for increasing the electric field exerted on particles passing through DMA using CFD. This description is being provided in the appendix section as it is unrelated to the dissertation and yet is of sufficient importance for proper documentation. In this context, for spherical particles because of their isotropic nature, the electric field (low or high) does not influence the mobility inside the DMA. However, non-spherical particles may orient differently especially at high electric fields thus producing a electric field dependent mobility which can then be used to extract the shape information of the particle [226]. As mentioned earlier, it is beyond the scope of this dissertation to discuss such non-spherical particles. This particular project was undertaken to assist a graduate student Mingdong Li working under Prof. Zachariah for his own dissertation related work.

CFD simulations on DMAs are extremely rare in literature [227, 228]. This study undertaken here was the first of its kind using FLUENT (commercial CFD simulation software).

A.2 Design and Preprocessing

Traditionally DMAs manufactured by TSI have 10 mm spacing in between the outer (R_2) and inner DMA (R_1) electrodes. A DMA was selected that had the design dimensions as shown in Figure A1 below. In this figure all dimensions are in millimeter. While designing the reduction in spacing, it should be kept in mind that the flow inside

should stay laminar. Further for concentric cylinders the diameter needs to be redefined with respect to the hydraulic diameter [229].Thus,

$$\mathrm{Re} = \frac{v_z D_H}{\gamma} \qquad \text{(A1)}$$

Where, v_z is obtained from equation 2.16 and γ is the viscosity of air. Here $D_H = \frac{2A}{P}$ where $A = \pi(R_2^2 - R_1^2)$ and $P = 2\pi R_2 + 2\pi R_1 + 2(R_2 - R_1)$.

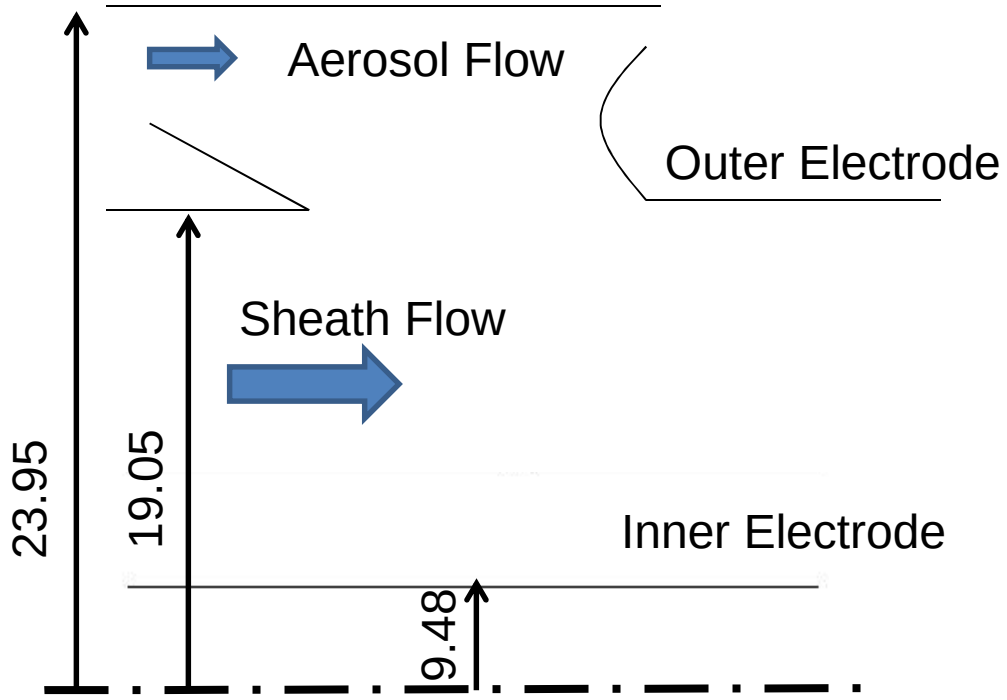

Figure A1: The original DMA design.

Substituting, the respective dimensions and using 10 L/min as the sheath flow, it appears from Figure A2 below, that the Reynolds number only increases marginally with decrease in inner and outer electrode spacing (the inner electrode is fixed at 9.48 mm). This is because although the velocity increases with reduction in spacing, the hydraulic diameter also decreases causing only a small increase in the Reynolds number. Further, assuming 2000 to be critical Reynolds number for a cylindrical tube, for a concentric

cylinder this critical value would then be 1000 as the critical Reynolds number in a concentric cylinder is half of that in cylindrical tubes [230]. As the theoretically predicted Reynolds number is significantly less than this critical value thus one may conclude that the flow will remain laminar even if the gap between the electrodes is reduced to as low as 2 mm (Figure A2).

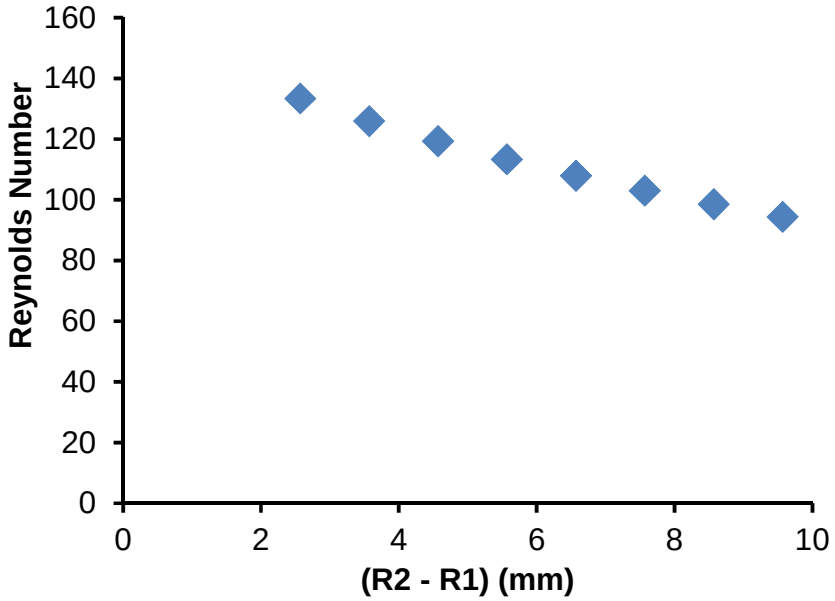

Figure A2: Increase in Reynolds number with decrease in spacing between inner and outer electrodes.

The spacing was arbitrarily chosen to be 3 mm such that for the same voltage, the electric field on a particle would be ~ 3 times more. This reduction in gap was achieved by inserting two inserts labeled 1 and 2 in Figure A3. Of these inserts, insert 1 makes a 30^0 angle with the horizontal. Further the entrance of the aerosol flow where it mixes with the sheath flow (shown in Figure A4) was reduced to $1/10^{th}$ of this spacing to reduce electric fields penetrating the aerosol flow space further upstream. This is important as

penetration of the electric field further upstream of aerosol flow may affect the mobility size (by exerting electrical forces on the particle before it can relax to sheath flow).

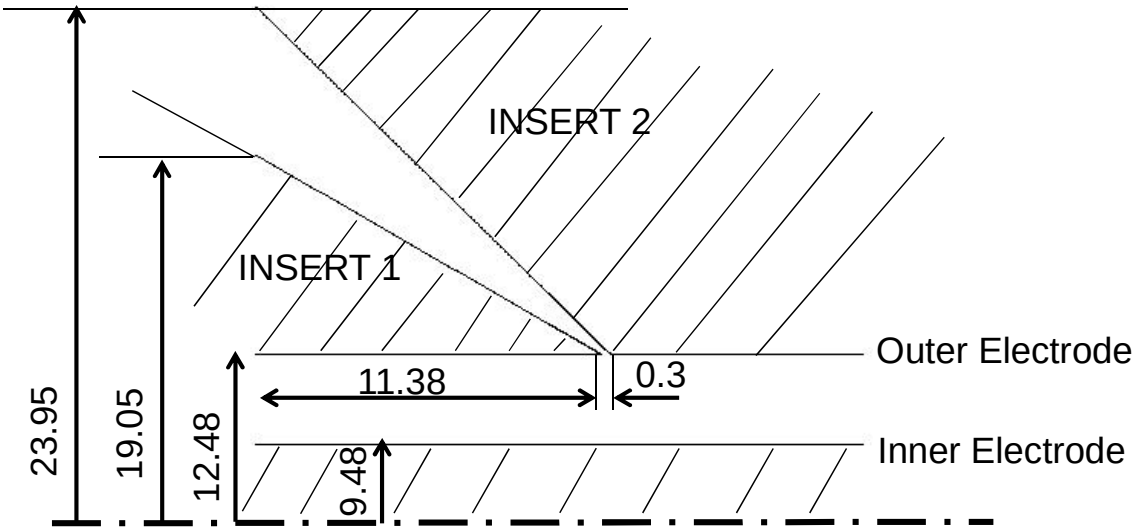

Figure A3: The modified DMA design.

A.2.1 GAMBIT

For creating the computational domain GAMBIT 2.4.6 was used. Quadrilateral meshes were arbitrarily selected with a spacing of 0.01 for the entire computational geometry and was significantly better resolved compared to previous literature [227, 228]. Ideally, further optimization of the mesh size could be done by optimizing the solution obtained and the time taken for convergence of residuals. Such a comprehensive approach was however not undertaken as these simulations were merely exploratory. After creating the mesh the boundaries were labeled and the type of boundary conditions defined (Figure A4). For aerosol and sheath flow velocity inlet conditions were used. For the outlet, outlet boundary condition was used. The interior was chosen to be a fluid. The rest of the boundaries were defined as walls. Although the aerosol flow actually enters at an angle of ~ 30^0 but for simplicity it is assumed that it enters perpendicular to the

surface (implemented in FLUENT). After defining the boundary conditions, the file was exported as a 2-D *.msh file.

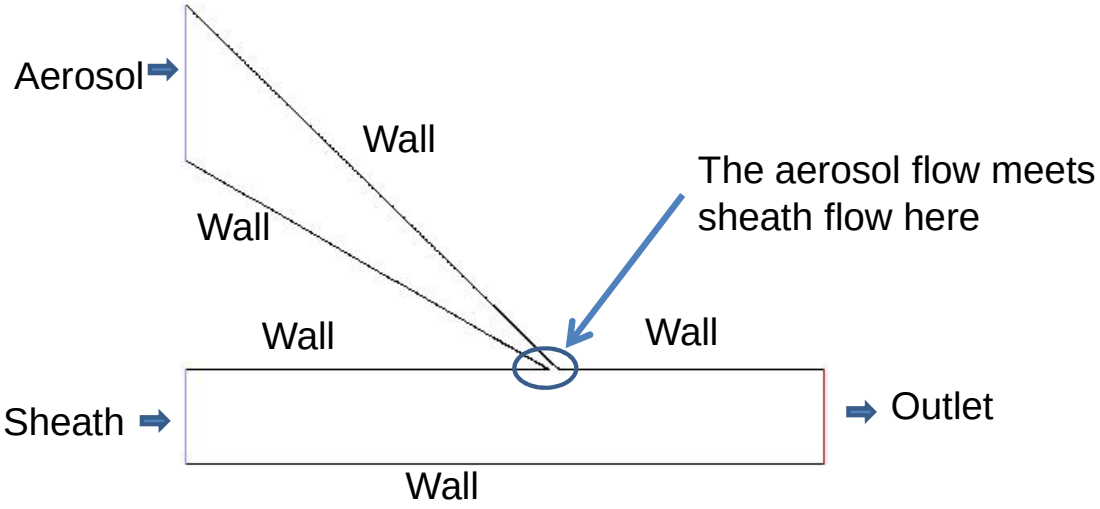

Figure A4: Computational domain and boundary conditions.

A.2.2 FLUENT

FLUENT 6.3 (2D-dp) was used for solving the flow. It should be pointed out that for simplicity, the electric field inside the DMA was not considered. After importing the data the scale was set to mm (note that GAMBIT does not have any scales and works with arbitrary numbers). The geometry was defined to be axi-symmetric and the flow was defined to be steady and laminar. The aerosol velocity was assumed to be 0.01 m/sec (corresponds to 0.3 L/min) and the sheath flow was defined to be 0.8 m/sec (corresponds to 10 L/min). Air was chosen as the working fluid and the pressure in the computational domain was defined as atmospheric. All other conditions such as convergence criterion, pressure-velocity couplings, relaxation factors etc. were left unaltered.

A.3 Results and Discussion

For most boundary conditions (different aerosol and sheath flow velocities) the solutions would be obtained in under 10 – 15 minutes using University of Maryland

virtual computing lab services. Figure A5A and A5B shows the velocity contours and magnitudes respectively. It is difficult to interpret this data without carefully investigating locally, especially at the confluence of the aerosol and sheath flows. One of the issues that need to be accommodated during designing is whether the flow velocities of sheath and aerosol match at the junction where the aerosol enters the DMA. This is of great importance as any substantial mismatch could create local flow perturbations. One way of investigating this mismatch is to create several sections near the confluence of the aerosol and sheath flow and then monitor the magnitude of the axial and radial velocities. From Figures A5C and A5D it appears based on 8 different sections that were created in this above mentioned region that the axial velocity of the aerosol flow matches very well with sheath flow. These sections with respect to the computation domain are labeled in the inset of both A5C and A5D. At the exact region where the aerosol flow enters the DMA, there is some radial velocity. This is unavoidable but can be reduced further by reducing the angle of entry by redesigning the insert 1. As mentioned before the angle of entry of insert 1 is 30^0. Had this been lesser then the radial velocity could have been reduced. However, as the modifications were made to a pre-existing DMA, this redesigning would have required substantially more changes in the DMA that would have been logistically difficult. Hence this design modification was not pursued. Physically, this implies that some aerosol particles that enter the DMA would actually cover certain distance radially which might consequently affect the determined mobility for such particles. However, it should be noted that the above design is currently producing reproducibly good results experimentally (not discussed) implying the above issue is not playing a dominant role.

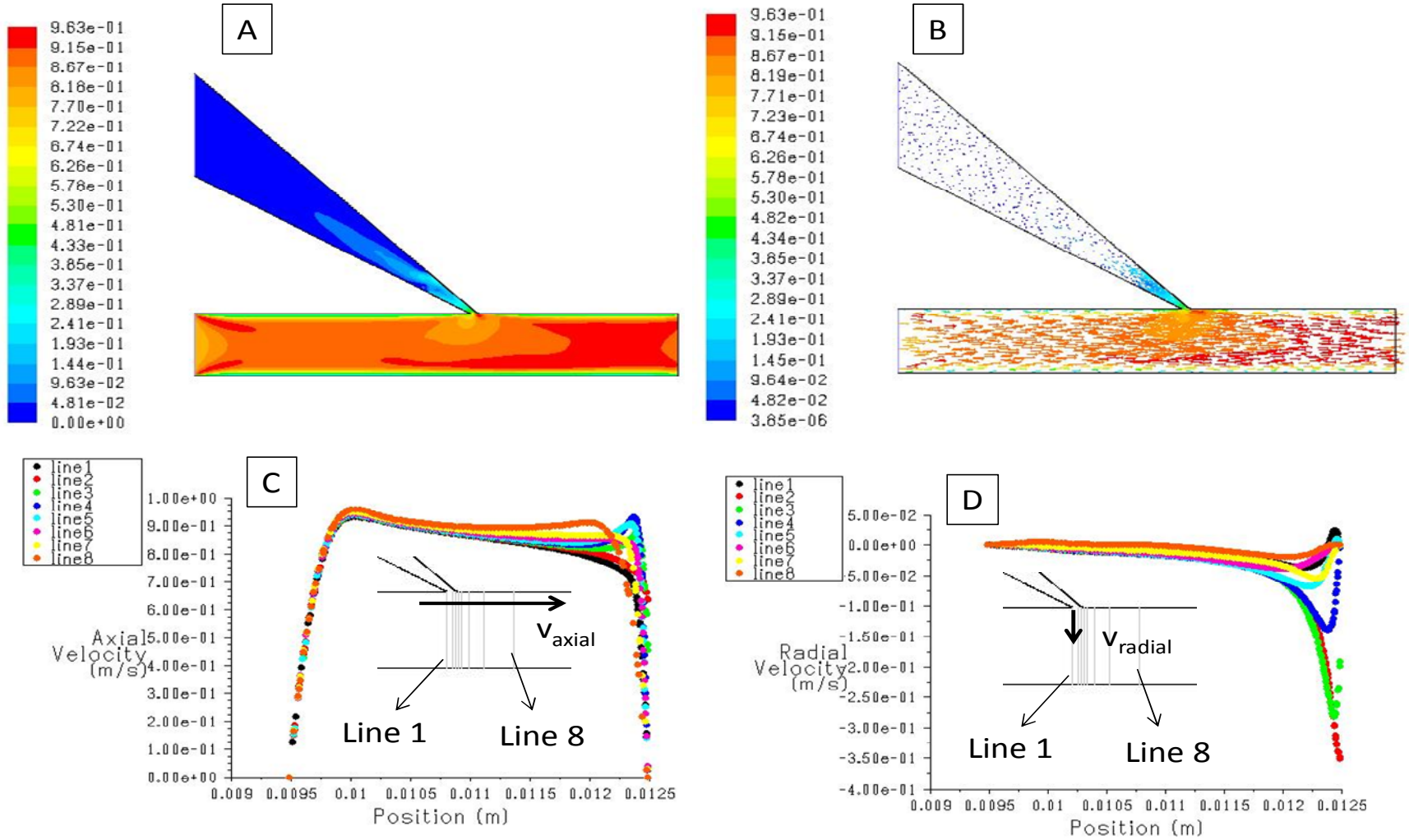

Figure A5: (A) Velocity contours and (B) velocity vectors in the computational domain. Magnitude of axial (C) and radial velocities (D) at 8 different sections.

A.4 Summary

Modifications were first made to an already existing DMA design to reduce the spacing between the electrodes. It was found that decreasing the spacing only marginally increases the Reynolds number. Further, exploratory simulations were carried out on this modified DMA design with reduced inner and outer electrode spacing of 3 mm. For simplicity the electric field inside the DMA was not coupled with the flow. By investigating the region where the aerosol flow meets the sheath flow it was found that the axial velocity components of aerosol flow at 0.3 L/min matches very well with the sheath flow of 10 L/min. Thus, this design should work under these flow conditions.

BIBLIOGRAPHY

1 Bhushan, B. (2010) Introduction to Nanotechnology. In *Springer Handbook of Nanotechnology*, 1-14

2 phRMA (2011) 2011 Profile Pharmaceutical Industry.

3 Philo, J. (2006) Is Any Measurement Method Optimal for All Aggregate Sizes and Types? *The AAPS Journal* 8, 564-571

4 Filipe, V., *et al.* (2010) Critical Evaluation of Nanoparticle Tracking Analysis (NTA) by NanoSight for the Measurement of Nanoparticles and Protein Aggregates. *Pharmaceutical Research* 27, 796-810

5 Carpenter, J.F., *et al.* (2010) Potential Inaccurate Quantitation and Sizing of Protein Aggregates by Size Exclusion Chromatography: Essential Need to Use Orthogonal Methods to Assure the Quality of Therapeutic Protein Products. *Journal of Pharmaceutical Sciences* 99, 2200-2208

6 Chen, D.R. and Pui, D.Y.H. (2010) Electrospray and Its Medical Applications. In *Nanoparticles in Medicine and Environment: Inhalation and Health Effects* (Marijinissen, J. and Gradon, L., eds), pp. 59-75, Springer Science

7 Fenn, J.H., *et al.* (1989) Electrospray Ionization for Mass Spectrometry of Large Biomolecules. *Science* 246, 64-71

8 Flagan, R.C. (1998) History of Electrical Aerosol Measurements. *Aerosol Science and Technology* 28, 301-380

9 Lewis, K.C., *et al.* (1994) Electrospray-Condensation Particle Counter: A Molecule-Counting LC Detector for Macromolecules. *Analytical Chemistry* 66, 2285-2292

10 Kaufman, S.L., *et al.* (1996) Macromolecule analysis based on electrophoretic mobility in air: Globular proteins. *Analytical Chemistry* 68, 1895-1904

11 Bacher, G., *et al.* (2001) Charge-reduced nano electrospray ionization combined with differential mobility analysis of peptides, proteins, glycoproteins, noncovalent protein complexes and viruses. *Journal of Mass Spectrometry* 36, 1038-1052

12 Wick, C. and McCubbin, P. (1999) Characterization of purified MS2 bacteriophage by the physical counting methodology used in the integrated virus detection system (IVDS). *Toxicology Methods* 9, 245-252

13 de la Mora, J.F., *et al.* (2006) The potential of differential mobility analysis coupled to MS for the study of very large singly and multiply charged proteins and protein complexes in the gas phase. *Biotechnol.J.* 1, 988-997

14 Hogan, C.J., *et al.* (2006) Charge reduced electrospray size spectrometry of mega- and gigadalton complexes: Whole viruses and virus fragments. *Analytical Chemistry* 78, 844-852

15 Tsai, D.H., *et al.* (2008) Gas-phase ion-mobility characterization of SAM-functionalized Au nanoparticles. *Langmuir* 24, 8483-8490

16 Loo, J.A., *et al.* (2005) Electrospray ionization mass spectrometry and ion mobility analysis of the 20S proteasome complex. *J Am.Soc.Mass Spectrom.* 16, 998-1008

17 Maiáer, A., *et al.* (2011) Determination of gas phase protein ion densities via ion mobility analysis with charge reduction. *Physical Chemistry Chemical Physics* 13, 21630-21641

18 Carazzone, C., *et al.* (2008) Nanoelectrospray Ion Mobility Spectrometry Online with Inductively Coupled Plasma-Mass Spectrometry for Sizing Large Proteins, DNA, and Nanoparticles. *Analytical Chemistry* 80, 5812-5818

19 Pease, L.F., *et al.* (2008) Determination of Protein Aggregation With Differential Mobility Analysis: Application to IgG Antibody. *Biotechnology and Bioengineering* 101, 1214-1222

20 Tsai, D.H., *et al.* (2011) Adsorption and Conformation of Serum Albumin Protein on Gold Nanoparticles Investigated Using Dimensional Measurements and in Situ Spectroscopic Methods. *Langmuir* 27, 2464-2477

21 Fenn, J.B., *et al.* (1990) Electrospray Ionization-Principles and Practice. *Mass Spectrometry Reviews* 9, 37-70

22 Taylor, G. (1964) Disintegration of Water Drops in Electric Field. *Proceedings of the Royal Society of London Series A-Mathematical and Physical Sciences* 280, 383-+

23 Kebarle, P. and Peschke, M. (2000) On the mechanisms by which the charged droplets produced by electrospray lead to gas phase ions. *Analytical Chimica Acta* 406, 11-35

24 W.C.Hinds (2010) *Aerosol Technology : Properties, Behavior and Measurement of airborne particles*. John Wiley and Sons

25 Tang, L. and Kebarle, P. (1993) Dependence of ion intensity in Electrospray mass-spectrometry on the concentration of the analyte in the electrosprayed solution. *Analytical Chemistry* 65, 3654-3668

26 El-Aneed, A., *et al.* (2009) Mass Spectrometry, Review of the Basics: Electrospray, MALDI, and Commonly Used Mass Analyzers. *Applied Spectroscopy Reviews* 44, 210-230

27 Flagan, R.C. (2008) Differential Mobility Analysis of Aerosols: A Tutorial. *KONA particle and powder journal* 26, 254-268

28 Chen, D.R., *et al.* (1995) Electrospraying of Conducting Liquids for Monodisperse Aerosol Generation in the 4 Nm to 1.8 Mu-M Diameter Range. *Journal of Aerosol Science* 26, 963-977

29 (2011) Model 3025A Ultrafine Condensation Particle Counter.

30 Pease, L.F., *et al.* (2010) Probing the Nucleus Model for Oligomer Formation during Insulin Amyloid Fibrillogenesis. *Biophysical Journal* 99, 3979-3985

31 Pease, L.F., *et al.* (2011) Rapid Physical Characterization of Icosahedral Virus Ultrastructure, Stability and Integrity using Electrospray Differential Mobility Analysis. *Analytical Chemistry* 83, 1753-1759

32 Lute, S., *et al.* (2008) A Consensus Rating Method for Small Virus-Retentive Filters. I. Method Development. *PDA journal of Pharmaceutical Science and Technology* 62, 318-333

33 Wick, C.H., *et al.* (2005) Detection and Identification of Viruses using the Integrated Virus Detection System (IVDS). (Army, D.o., ed), pp. 1-43, Edgewood Chemical Biological Center Aberdeen Proving Ground, MD

34 Pease, L.F., *et al.* (2009) Quantitative Characterization of Virus-like Particles by Asymmetrical Flow Field Flow Fractionation, Electrospray Differential Mobility Analysis, and Transmission Electron Microscopy. *Biotechnology and Bioengineering* 102, 845-855

35 Thomas, J.J., *et al.* (2004) Electrospray ion mobility spectrometry of intact viruses. *Spectroscopy-An International Journal* 18, 31-36

36 Pease, L.F. (2011) Physical analysis of virus particles using electrospray differential mobility analysis. *Trends in Biotechnology*, 30, 216-224

37 Lute, S., *et al.* (2007) Phage passage after extended processing in small-virus-retentive filters. *Biotechnology and Applied Biochemistry* 47, 141-151

38 Kuzmanovic, D.A., *et al.* (2008) A novel application of small-angle scattering techniques: Quality assurance testing of virus quantification technology. *Radiation Physics and Chemistry* 77, 215-224

39 Cole, K.D., *et al.* (2009) Particle concentration measurement of virus samples using electrospray differential mobility analysis and quantitative amino acid analysis. *J Chromatogr.A* 1216, 5715-5722

40 Kaddis, C.S., *et al.* (2007) Sizing large proteins and protein complexes by electrospray ionization mass spectrometry and ion mobility. *Journal of the American Society for Mass Spectrometry* 18, 1206-1216

41 Lute, S., *et al.* (2010) A Consensus Rating Method for Small Virus-Retentive Filters. I. Method Development. *PDA journal of Pharmaceutical Science and Technology* 62, 318-333

42 Laschober, C., *et al.* (2008) Gas-phase electrophoretic molecular mobility analysis of size and stoichiometry of complexes of a common cold virus with antibody and soluble receptor molecules. *Analytical Chemistry* 80, 2261-2264

43 G.Allmaier, *et al.* (2008) Nano ES GEMMA and PDMA, new tools for the analysis of nanobioparticles - Protein complexes, lipoparticles, and viruses. *Journal of the American Society for Mass Spectrometry* 19, 1062-1068

44 ICHEWG (2005) Validation of analytical procedures: text and methodology Q2(R1). In *Internation Conference on Harmonisation of Technical requirements for Registration of Pharmaceuticals for Human Use*

45 Scalf, M., *et al.* (1999) Controlling charge state of large ions. *Science* 283, 194-197

46 Mouradian, S., *et al.* (1997) DNA analysis using an electrospray scanning mobility particle sizer. *Analytical Chemistry* 69, 919-925

47 Saucy, D.A., *et al.* (2004) Mass Analysis of Water-Soluble Polymers by Mobility Measurement of Charge-Reduced Ions Generated by Electrosprays. *Analytical Chemistry* 76, 1045-1053

48 Ku, B.K. and de la Mora, J.F. (2004) Mass Distribution Measurement of Water-Insoluble Polymers by Charge-Reduced Electrospray Mobility Analysis. *Analytical Chemistry* 76, 814-822

49 Kaddis, C.S. and Loo, J.A. (2007) Native protein MS and ion mobility large flying proteins with ESI. *Anal.Chem.* 79, 1778-1784

50 Allmaier, G., *et al.* (2008) Nano ES GEMMA and PDMA, new tools for the analysis of nanobioparticles-protein complexes, lipoparticles, and viruses. *J Am.Soc.Mass Spectrom.* 19, 1062-1068

51 Kemptner, J., *et al.* (2010) GEMMA and MALDI-TOF MS of reactive PEGs for pharmaceutical applications. *J Pharm.Biomed.Anal.* 52, 432-437

52 Mordas, G., *et al.* (2008) On Operation of the Ultra-Fine Water-Based CPC TSI 3786 and Comparison with Other TSI Models (TSI 3776, TSI 3772, TSI 3025, TSI 3010, TSI 3007). *Aerosol Science and Technology* 42, 152-158

53 Muller, R., *et al.* (2007) Determination of Molecular Weight, Particle Size, and Density of High Number Generation PAMAM Dendrimers Using MALDI-TOF-MS and nES-GEMMA. *Macromolecules* 40, 5599-5605

54 Anumolu, R., *et al.* (2011) Fabrication of Highly Uniform Nanoparticles from Recombinant Silk-Elastin-like Protein Polymers for Therapeutic Agent Delivery. *ACS Nano* 5, 5374-5382

55 Wang, W. and Roberts, C.J. (2010) Aggregation of Therapeutic Proteins. John Wiley & Sons Inc

56 Poderycki, M.J., *et al.* (2006) The vault exterior shell is a dynamic structure that allows incorporation of vault-associated proteins into its interior. *Biochemistry* 45, 12184-12193

57 Kaufman, S.L. (1998) Analysis of biomolecules using electrospray and nanoparticle methods: The gas-phase electrophoretic mobility molecular analyzer (GEMMA). *Journal of Aerosol Science* 29, 537-552

58 Hogan, C.J., Jr., *et al.* (2011) Tandem differential mobility analysis-mass spectrometry reveals partial gas-phase collapse of the GroEL complex. *J Phys.Chem.B* 115, 3614-3621

59 Kaufman, S.L., *et al.* (1998) Analysis of a 3.6-MDa hexagonal bilayer hemoglobin from Lumbricus terrestris using a gas-phase electrophoretic mobility molecular analyzer. *Anal.Biochem.* 259, 195-202

60 Kani, K., *et al.* (2005) Oligomers of ERBB3 have two distinct interfaces that differ in their sensitivity to disruption by heregulin. *J Biol.Chem.* 280, 8238-8247

61 Caulfield, M.P., *et al.* (2008) Direct determination of lipoprotein particle sizes and concentrations by ion mobility analysis. *Clinical Chemistry* 54, 1307-1316

62 Loo, J.A. (1997) Studying noncovalent protein complexes by electrospray ionization mass spectrometry. *Mass Spectrometry Reviews* 16, 1-23

63 Hogan, C.J., Jr. and de la Mora, J.F. (2011) Ion mobility measurements of nondenatured 12-150 kDa proteins and protein multimers by tandem differential mobility analysis-mass spectrometry (DMA-MS). *J Am.Soc.Mass Spectrom.* 22, 158-172

64 Laschober, C., *et al.* (2007) Comparison of various nano-differential mobility analysers (nDMAs) applying globular proteins. *Journal of Experimental Nanoscience* 2, 291-301

65 Pease, L.F., *et al.* (2007) Quantifying the Surface Coverage of Conjugate Molecules on Functionalized Nanoparticles. *Journal of Physical Chemistry C* 111, 17155-17157

66 Tsai, D.H., *et al.* (2010) Competitive adsorption of thiolated polyethylene glycol and mercaptopropionic acid on gold nanoparticles measured by physical characterization methods. *Langmuir* 26, 10325-10333

67 Tsai, D.H., *et al.* (2011) Quantitative Determination of Competitive Molecular Adsorption on Gold Nanoparticles Using Attenuated Total Reflectance-Fourier Transform Infrared Spectroscopy. *Langmuir* 27, 9302-9313

68 Rofuogaran, R., *et al.* (2008) Oligomerization status directs overall activity regulation of the Escherichia coli class Ia Ribonucleotide Reductase. *Journal of Biological Chemistry* 283, 35310-35318

69 Crona, M., *et al.* (2011) Assembly of a fragmented ribonucleotide reductase by protein interaction domains derived from a mobile genetic element. *Nucleic Acids Research* 39, 1381-1389

70 Seyfried, B.K., *et al.* (2010) PEGylated recombinant von Willebrand factor analyzed by means of MALDI-TOF-MS, CGE-on-a-chip and nES-GEMMA. *International Journal of Mass Spectrometry* doi:10.1016/j.ijms.2010.10.028

71 Pease, L.F., *et al.* (2010) Structural analysis of soft multicomponent nanoparticle clusters. *ACS Nano* 4, 6982-6988

72 Yim, P.B., *et al.* (2009) Quantitative characterization of quantum dot-labeled lambda phage for Escherichia coli detection. *Biotechnol.Bioeng.* 104, 1059-1067

73 Tsai, D.-H., *et al.* (2011) Process Analytical Technology for Recombinant Pandemic Flu Vaccines: Viral Ultrastructure, Aggregation and Binding. In *AiCHE*

74 Tsai, D.H., *et al.* (2012) Tumor Necrosis Factor Interaction with Gold Nanoparticle. *Nanoscale* (DOI: 10.1039/C2NR30415E)

75 Pease, L.F., *et al.* (2009) Length Distribution of Single-Walled Carbon Nanotubes in Aqueous Suspension Measured by Electrospray Differential Mobility Analysis. *Small* 5, 2894-2901

76 N.I.S.T (2007) Report of Investigation: Reference Material 8011. (Division, C.D.a.M.M., ed), pp. 1 - 10

77 Wang, S.C. and Flagan, R.C. (1989) Scanning Electrical Mobility Spectrometer. *Journal of Aerosol Science* 20, 1485-1488

78 Lall, A.A., *et al.* (2009) Online Nanoparticle Mass Measurement by Combined Aerosol Particle Mass Analyzer and Differential Mobility Analyzer: Comparison of Theory and Measurements. *Aerosol Science and Technology* 42, 1075-1083

79 Guha, S., *et al.* (2010) Electrospray-Differential Mobility Analysis for characterization of heat induced antibody aggregates. In *26th Southern Biomedical Conference*, pp. 232 - 235, Springer Verlag

80 Mei, F., *et al.* (2011) A cost-effective differential mobility analyzer (cDMA) for multiple DMA column applications. *Journal of Aerosol Science* 42, 462-473

81 Hlady, V., *et al.* (1999) Methods for studying protein adsorption. *Methods in Enzymology* 309, 402-429

82 Claesson, P.M., *et al.* (1995) Protein Interactions at Solid-Surfaces. *Advances in Colloid and Interface Science* 57, 161-227

83 Nylander, T., *et al.* (1994) The Effect of Solution Behavior of Insulin on Interactions Between Adsorbed Layers of Insulin. *Journal of Colloid and Interface Science* 164, 136-150

84 Elgersma, A.V., *et al.* (1992) Adsorption Competition Between Albumin and Monoclonal Immunogammaglobulins on Polystyrene Lattices. *Journal of Colloid and Interface Science* 152, 410-428

85 Wojciechowski, P., *et al.* (1986) Phenomenology and Mechanism of the Transient Adsorption of Fibrinogen from Plasma (Vroman Effect). *Journal of Colloid and Interface Science* 111, 455-465

86 Ortega-Vinuesa, J.L., *et al.* (1998) Stagnant versus dynamic conditions: a comparative adsorption study of blood proteins. *Biomaterials* 19, 251-262

87 Lensen, H.G.W., *et al.* (1984) High-Performance Liquid-Chromatography As A Technique to Measure the Competitive Adsorption of Plasma-Proteins Onto Lattices. *Journal of Colloid and Interface Science* 99, 1-8

88 Okubo, M., *et al.* (1990) Preferential Adsorption of Bovine Serum-Albumin Dimer Onto Polymer Microspheres Having A Heterogeneous Surface Consisting of Hydrophobic and Hydrophilic Parts. *Colloid and Polymer Science* 268, 598-603

89 Zsom, R.L.J. (1986) Dependence of Preferential Bovine Serum-Albumin Oligomer Adsorption on the Surface-Properties of Monodisperse Polystyrene Lattices. *Journal of Colloid and Interface Science* 111, 434-445

90 G.A.Trusky, *et al.* (2004) *Transport Phemomena in Biological Systems*. Pearson Education

91 Maa, Y.F. and Hsu, C.C. (1997) Protein denaturation by combined effect of shear and air-liquid interface. *Biotechnology and Bioengineering* 54, 503-512

92 Oliva, A., *et al.* (2003) Effect of high shear rate on stability of proteins: kinetic study. *Journal of Pharmaceutical and Biomedical Analysis* 33, 145-155

93 Pitt, W.G., *et al.* (1986) Sequential Protein Adsorption and Thrombus Deposition on Polymeric Biomaterials. *Journal of Colloid and Interface Science* 111, 343-362

94 Borovetz, H.S., *et al.* (1982) Protein Adsorption in Vitro onto Biomaterial Surfaces Covered with Ulti Carbon. *Biomed.Med.Dev., Artif.Organs* 10, 187-203

95 Elhorst, J.K., *et al.* (1978) The effect of radiolabeling of human fibrinogen on its adsorption behaviour on a polystyrene surface. *Int J Artif Organs* 1, 288-292

96 Grant, W.H., *et al.* (1977) Radiotracer Techniques for Protein Adsorption Measurements. *Journal of Biomedical Materials Research* 11, 33-38

97 Vanderscheer, A.T., *et al.* (1978) Feasibility of Radiolabeling for Human-Serum Albumin (Hsa) Adsorption Studies. *Journal of Colloid and Interface Science* 66, 136-145

98 Wyttenbach, T., *et al.* (2001) Design of a new electrospray ion mobility mass spectrometer. *International Journal of Mass Spectrometry* 212, 13-23

99 Razunguzwa, T.T., *et al.* (2006) ESI-MS compatible permanent coating of glass surfaces using poly(ethylene glycol)-terminated alkoxysilanes for capillary zone electrophoretic protein separations. *Analytical Chemistry* 78, 4326-4333

100 Daly, S.M., *et al.* (2005) Adsorption of poly(ethylene glycol)-modified lysozyme to silica. *Langmuir* 21, 1328-1337

101 Green, R.J., *et al.* (1999) Competitive protein adsorption as observed by surface plasmon resonance. *Biomaterials* 20, 385-391

102 Li, M.D., *et al.* (2011) Method for determining absolute number concentration of nanoparticles from electrospray sources. *Langmuir* 27, 14732-14739

103 Li, M.D., *et al.* (2011) Quantification and Compensation of Non-Specific Analyte Aggregation in Electrospray Sampling. *Aerosol Science and Technology* 45, 849-860

104 Magnuson, M.L., *et al.* (2000) Microscale extraction of perchlorate in drinking water with low level detection by electrospray-mass spectrometry. *Talanta* 52, 285-291

105 Wiedensohler, A. (1988) An Approximation of the Bipolar Charge-Distribution for Particles in the Sub-Micron Size Range. *Journal of Aerosol Science* 19, 387-389

106 Jonsson, U., *et al.* (1985) Immobilization of Immunoglobulins on Silica Surfaces - Kinetics of Immobilization and Influence of Ionic-Strength. *Biochemical Journal* 227, 373-378

107 Silva, C.S.O., *et al.* (2006) Adsorption of human IgG on to poly(N-isopropylacrylamide)-based polymer particles. *Biotechnology Letters* 28, 2019-2025

108 Chuang, H.Y.K., *et al.* (1978) Interaction of Plasma-Proteins with Artificial Surfaces - Protein Adsorption-Isotherms. *Journal of Laboratory and Clinical Medicine* 92, 483-496

109 Fair, B.D. and Jamieson, A.M. (1980) Studies of Protein Adsorption on Polystyrene Latex Surfaces. *Journal of Colloid and Interface Science* 77, 525-534

110 J.L.Brash and D.J.Lyman (1969) Adsorption of plasma proteins from solution to uncharged, hydrophobic polymer surfaces. *Journal of Biomedical Materials Research* 3, 175-189

111 Bee, J.S., *et al.* (2009) Monoclonal Antibody Interactions With Micro- and Nanoparticles: Adsorption, Aggregation, and Accelerated Stress Studies. *Journal of Pharmaceutical Sciences* 98, 3218-3238

112 Bremer, M.G.E.G., *et al.* (2004) Electrostatic interactions between immunoglobulin (IgG) molecules and a charged sorbent. *Colloids and Surfaces A-Physicochemical and Engineering Aspects* 250, 29-42

113 Buijs, J., *et al.* (1996) Adsorption dynamics of IgG and its F(ab')(2) and Fc fragments studied by reflectometry. *Journal of Colloid and Interface Science* 178, 594-605

114 Buijs, J., *et al.* (1997) The effect of adsorption on the antigen binding by IgG and its F(ab')(2) fragments. *Colloids and Surfaces B-Biointerfaces* 8, 239-249

115 Kamyshny, A., *et al.* (1999) Adsorption of hydrophobized IgG and gelatin onto phosphatidyl choline-coated silica. *Colloids and Surfaces B-Biointerfaces* 13, 187-194

116 Iler, R.K. (1979) *The Chemistry of Silica*. Wiley Interscience

117 Hook, F., *et al.* (1998) Structural changes in hemoglobin during adsorption to solid surfaces: Effects of pH, ionic strength, and ligand binding. *Proceedings of the National Academy of Sciences of the United States of America* 95, 12271-12276

118 Ramsden, J.J. and Prenosil, J.E. (1994) Effect of Ionic-Strength on Protein Adsorption-Kinetics. *Journal of Physical Chemistry* 98, 5376-5381

119 Bagchi, P. and Birnbaum, S.M. (1981) Effect of Ph on the Adsorption of Immunoglobulin-G on Anionic Poly(Vinyltoluene) Model Latex-Particles. *Journal of Colloid and Interface Science* 83, 460-478

120 Ball, V., *et al.* (1996) Dynamic aspects of protein adsorption onto titanium surfaces: Mechanism of desorption into buffer and release in the presence of proteins in the bulk. *Langmuir* 12, 1614-1621

121 Jung, L.S., *et al.* (1998) Quantitative interpretation of the response of surface plasmon resonance sensors to adsorbed films. *Langmuir* 14, 5636-5648

122 R.L.Beissinger and Leona, E.F. (1980) Immunoglobulin Sorption and Desorption rates on Quartz: Evidence for multiple sorbed states. *American Society for Artificial Internal Organs* 3, 160-175

123 Baszkin, A. and Lyman, D.J. (1980) The Interaction of Plasma-Proteins with Polymers .1. Relationship Between Polymer Surface-Energy and Protein Adsorption-Desorption. *Journal of Biomedical Materials Research* 14, 393-403

124 Oreskes, I. and Singer, J. (1960) Stability and Gamma-Globulin Binding Studies on Polystyrene Latex Particles. *Arthritis and Rheumatism* 3, 273-274

125 Ariola, F.S., *et al.* (2006) Interfacial rheology of blood proteins adsorbed to the aqueous-buffer/air interface. *Biomaterials* 27, 3404-3412

126 Kekicheff, P., *et al.* (1990) Multilayer Adsorption of Cytochrome-C on Mica Around Isoelectric Ph. *Langmuir* 6, 1704-1708

127 Martin, M.M. (1995) Ellipsometry studies of the effects of surface hydrophobicity on protein adsorption. *Colloids and Surfaces B: Biointerfaces* 3, 297-308

128 Arai, T. and Norde, W. (1990) The behavior of some model proteins at solid liquid interfaces .2. Sequential and competitive adsorption. *Colloids and Surfaces* 51, 17-28

129 Norde, W. and Favier, J.P. (1992) Structure of adsorbed and desorbed proteins. *Colloids and Surfaces* 64, 87-93

130 van der Veen, M., *et al.* (2007) Spreading of proteins and its effect on adsorption and desorption kinetics. *Colloids and Surfaces B-Biointerfaces* 54, 136-142

131 Holmberg, M. and Hou, X.L. (2009) Competitive Protein Adsorption-Multilayer Adsorption and Surface Induced Protein Aggregation. *Langmuir* 25, 2081-2089

132 Alahverdjieva, V., *et al.* (2008) Competitive adsorption from mixed hen egg-white lysozyme/surfactant solutions at the air-water interface studied by tensiometry, ellipsometry, and surface dilational rheology. *Journal of Physical Chemistry B* 112, 2136-2143

133 Golander, C.G. and Kiss, E. (1988) Protein adsorption on functionalized and esca-characterized polymer-films studied by ellipsometry. *Journal of Colloid and Interface Science* 121, 240-253

134 Chittur, K. (1998) FTIR/ATR for protein adsorption to biomaterial surfaces. *Biomaterials* 19, 357-369

135 Glasmastar, K., *et al.* (2002) Protein adsorption on supported phospholipid bilayers. *Journal of Colloid and Interface Science* 246, 40-47

136 Lok, B.K., *et al.* (1983) Protein adsorption on crosslinked polydimethylsiloxane using total internal-reflection fluorescence. *Journal of Colloid and Interface Science* 91, 104-116

137 Claesson, P.M., *et al.* (1989) Direct Measurements of the Interaction Between Layers of Insulin Adsorbed on Hydrophobic Surfaces. *Journal of Colloid and Interface Science* 130, 457-466

138 Servoli, E., *et al.* (2008) Quantitative Analysis of Protein Adsorption via Atomic Force Microscopy and Surface Plasmon Resonance. *Macromolecular Bioscience* 8, 1126-1134

139 Tengvall, P., *et al.* (2001) Ellipsometric in vitro studies on the activation of complement by human immunoglobulins M and G after adsorption to methylated silicon. *Colloids and Surfaces B-Biointerfaces* 20, 51-62

140 Lea, A.S., *et al.* (1991) Igm Adsorption-Kinetics Determined by Atomic Force Microscopy. *Abstracts of Papers of the American Chemical Society* 201, 226-COLL

141 Vroman, L. and Adams, A.L. (1967) Possible involvement of fibrinogen and proteolysis in surface activation - a study with recording ellipsometer. *Thrombosis Et Diathesis Haemorrhagica* 18, 510-524

142 Vroman, L. and Adams, A.L. (1968) Fibrinogen as a confusing factor in surface activation. *Thrombosis Et Diathesis Haemorrhagica* 19, 604

143 Tsai, D.H., *et al.* (2009) Aggregation Kinetics of Colloidal Particles Measured by Gas-Phase Differential Mobility Analysis. *Langmuir* 25, 140-146

144 Guha, S., *et al.* (2011) Characterizing the Adsorption of Proteins on Glass Capillary Surfaces Using Electrospray-Differential Mobility Analysis (ES-DMA). *Langmuir* 27, 13008-13014

145 Nye, J. and Groves, J. (2008) Kinetic control of histidine-tagged protein surface density on supported lipid bilayers. *Langmuir* 24, 4145-4149

146 Wegner, G.J., *et al.* (2004) Real-time surface plasmon resonance imaging measurements for the multiplexed determination of protein adsorption/desorption kinetics and surface enzymatic reactions on peptide microarrays. *Analytical Chemistry* 76, 5677-5684

147 McMaster, T., *et al.* (2000) In situ surface adsorption of the protein C hordein using atomic force microscopy. *Langmuir* 16, 1463-1468

148 Mulheran, P.A., *et al.* (2008) Mechanisms and Dynamics of Protein Clustering on a Solid Surface. *Physical Review Letters* 100, 068102-068101-068102-068104

149 Jeyachandran, Y., *et al.* (2010) Efficiency of blocking of non-specific interaction of different proteins by BSA adsorbed on hydrophobic and hydrophilic surfaces. *Journal of Colloid and Interface Science* 341, 136-142

150 Scott, E., *et al.* (2008) Protein adsorption and cell adhesion on nanoscale bioactive coatings formed from poly(ethylene glycol) and albumin microgels. *Biomaterials* 29, 4481-4493

151 Taylor, S., *et al.* (2003) Impact of surface chemistry and blocking strategies on DNA microarrays. *Nucleic Acids Research* 31

152 Tessler, L., *et al.* (2009) Protein Quantification in Complex Mixtures by Solid Phase Single-Molecule Counting. *Analytical Chemistry* 81, 7141-7148

153 Yue, M., *et al.* (2008) Label-free protein recognition two-dimensional array using nanomechanical sensors. *Nano Letters* 8, 520-524

154 Lin, Y., *et al.* (2008) Gelatin multilayers assembled on poly(L-lactic acid) surface for better cytocompatibility. *Journal of Applied Polymer Science* 109, 530-536

155 Lin, Y. and Su, Z. (2008) Layer-by-layer assembly of gelatin. *Journal of Polymer Science Part B-Polymer Physics* 46, 1252-1257

156 Yon, R.J. (1972) Chromatography of lipophilic proteins on adsorbents containing mixed hydrophobic and ionic groups. *Biochemical Journal* 126, 765-767

157 Matsuda, T., *et al.* (1984) The Blood Interface with Segmented Polyurethanes : "Multilayered protein passivation mechanism". *American Society for Artificial Internal Organs*, 353-358

158 Giacomelli, C. and Norde, W. (2001) The adsorption-desorption cycle. Reversibility of the BSA-silica system. *Journal of Colloid and Interface Science* 233, 234-240

159 Elgersma, A.V., *et al.* (1990) The adsorption of Bovine Serum Albumin on positively and negatively charged polystyrene lattices. *Journal of Colloid and Interface Science* 138, 145-156

160 Larsericsdotter, H., *et al.* (2005) Structure, stability, and orientation of BSA adsorbed to silica. *Journal of Colloid and Interface Science* 289, 26-35

161 McClellan, S. and Franses, E. (2005) Adsorption of bovine serum albumin at solid/aqueous interfaces. *Colloids and Surfaces a-Physicochemical and Engineering Aspects* 260, 265-275

162 Kondo, A., *et al.* (1992) Circular-dichroism studies on conformational changes in protein molecules upon adsorption on ultrafine polystyrene particles. *Biotechnology and Bioengineering* 40, 889-894

163 Erny, G., *et al.* (2006) Capillary electrophoresis using copolymers of different composition as physical coatings: A comparative study. *Electrophoresis* 27, 1041-1049

164 Curme, H.G. and Natale, C.C. (1964) Adsorption of gelatin to Silver Bromide sol. *Journal of Physical Chemistry* 68, 3009-3016

165 Kamiyama, Y. and Israelachvili, J. (1992) Effect of pH and salt on the adsorption and interactions of an amphoteric polyelectrolyte. *Macromolecules* 25, 5081- 5088

166 Vaynberg, K., *et al.* (1998) Structure and extent of adsorbed gelatin on acrylic latex and polystyrene colloidal particles. *Journal of Colloid and Interface Science* 205, 131-140

167 Maternaghan, T.J., *et al.* (1980) Adsorbed layer of gelatin on silver bromide - its nature and photographic significance. *Journal of Photographic Science* 28, 1-14

168 Nakanishi, K., *et al.* (2001) On the adsorption of proteins on solid surfaces, a common but very complicated phenomenon. *Journal of Bioscience and Bioengineering* 91, 233-244

169 Johlin, J. (1929) The isoelectric point of gelatin in relation to its minimum physical properties. *Proceedings of the Society For Experimental Biology and Medicine* 26, 702-704

170 Lenggoro, I.W., *et al.* (2002) Sizing of Colloidal Nanoparticles by Electrospray and Differential Mobility Analyzer Methods. *Langmuir* 18, 4584-4591

171 Lebowitz, J., *et al.* (2002) Modern analytical ultracentrifugation in protein science: A tutorial review. *Protein Science* 11, 2067-2079

172 Schuck, P. SEDFIT. http://www.analyticalultracentrifugation.com/default.htm

173 Thobhani, S., *et al.* (2010) Bioconjugation and characterisation of gold colloid-labelled proteins. *Journal of Immunological Methods* 356, 60-69

174 Ghosh, P., *et al.* (2008) Gold nanoparticles in delivery applications. *Advanced Drug Delivery Reviews* 60, 1307-1315

175 Weiss, S. (1999) Fluorescence Spectroscopy of Single Biomolecules. *Science* 283, 1676 - 1683

176 Brewer, S.H., *et al.* (2005) Probing BSA binding to citrate-coated gold nanoparticles and surfaces. *Langmuir* 21, 9303-9307

177 Mrksich, M., *et al.* (1995) Surface-Plasmon resonance permits in-situ measurment of protein adsorption on self-assembled monolayers of alkanethiolates on gold. *Langmuir* 11, 4383-4385

178 Smith, P.K., *et al.* (1985) Measurement of protein using Bicinchoninic acid. *Analytical Biochemistry* 150, 76-85

179 Ehara, K., *et al.* (1996) Novel method to classify aerosol particles according to their mass-to-charge ratio - Aerosol particle mass analyser. *Journal of Aerosol Science* 27, 217-234

180 Guha, S., *et al.* (2012) Protein adsorption-desorption on electrospray capillary walls - No influence on aggregate distribution. *Journal of Colloids and Interface Sciences* (DOI: 10.1016/j.jcis.2012.03.059)

181 Rezwan, K., *et al.* (2004) Bovine serum albumin adsorption onto colloidal Al2O3 particles: A new model based on zeta potential and UV-vis measurements. *Langmuir* 20, 10055-10061

182 Elgersma, A.V., *et al.* (1991) The adsorption of different types of monoclonal immunoglobulin on positively and negatively charged polystyrene lattices. *Colloids and Surfaces* 54, 89-101

183 Galisteo-Gonzales, F., *et al.* (1994) Adsorption of monoclonal IgG on polystyrene microspheres. *Colloid and Polymer Science* 272, 352-358

184 Bee, J.S., *et al.* (2010) Aggregation of a Monoclonal Antibody Induced by Adsorption to Stainless Steel. *Biotechnology and Bioengineering* 105, 121-129

185 Lute, S., *et al.* (2004) Characterization of coliphage PR772 and evaluation of its use for virus filter performance testing. *Applied and Environmental Microbiology* 70, 4864-4871

186 EPIDI (2009) Manual of rotavirus detection and characterization methods. WHO Document Production Service.

187 Malloy, A. (2010) Characterizing Viral Titers in Manufacturing. In *Genetic Engineering and Biotechnology News*, 42-44

188 S.Becht, *et al.* (2007) Vaccine characterization using advanced technology. *Biopharm International* 20, 16

189 Davison, A.J. and Davison, M.D. (1995) Identification of structural proteins of channel catfish virus by mass-spectrometry. 206, 1035-1043

190 Yao, Z.P., *et al.* (2002) Mass spectrometry-based proteolytic mapping for rapid virus identification. *Analytical Chemistry* 74, 2529-2534

191 Tito, M.A., *et al.* (2000) Electrospray time-of-flight mass spectrometry of the intact MS2 virus capsid. *Journal of the American Chemical Society* 122, 3550-3551

192 Brorson, K., *et al.* (2002) Evaluation of a quantitative product-enhanced reverse transcriptase assay to monitor retrovirus in mAb cell-culture. *Biologicals* 30, 15-26

193 Xu, Y. and Brorson, K.A. (2001) An overview of quantitative PCR assays for biologicals: Quality and safety evaluation. *Developments in Biologicals* 113, 89-98

194 Chi, E.Y., *et al.* (2003) Physical stability of proteins in aqueous solution: Mechanism and driving forces in nonnative protein aggregation. *Pharmaceutical Research* 20, 1325-1336

195 Fink, A.L. (1998) Protein aggregation: folding aggregates, inclusion bodies and amyloid. *Folding & Design* 3, R9-R23

196 Rosenberg, A.S. (2006) Effects of protein aggregates: An immunologic perspective. *Aaps Journal* 8, E501-E507

197 Mahler, H.C., *et al.* (2009) Protein Aggregation: Pathways, Induction Factors and Analysis. *Journal of Pharmaceutical Sciences* 98, 2909-2934

198 Singh, S.K., *et al.* (2010) An Industry Perspective on the Monitoring of Subvisible Particles as a Quality Attribute for Protein Therapeutics. *Journal of Pharmaceutical Sciences* 99, 3302-3321

199 Carpenter, J.F., *et al.* (2009) Overlooking Subvisible Particles in Therapeutic Protein Products: Gaps That May Compromise Product Quality. *Journal of Pharmaceutical Sciences* 98, 1201-1205

200 Arakawa, T., *et al.* (2010) The Critical Role of Mobile Phase Composition in Size Exclusion Chromatography of Protein Pharmaceuticals. *Journal of Pharmaceutical Sciences* 99, 1674-1692

201 Guha, S., *et al.* (2011) Evaluation of electrospray differential mobility analysis for virus particle analysis: Potential applications in biomanufacturing. *Journal of Virological Methods* 178, 201-208

202 Bolli, R., *et al.* (2010) L-Proline reduces IgG dimer content and enhances the stability of intravenous immunoglobulin (IVIG) solutions. *Biologicals* 38, 150-157

203 Cech, B.C. and Enke, C.G. (2000) Relating Electrospray Ionization Response to Nonpolar Character of Small Peptides. *Analytical Chemistry* 72, 2723-2723

204 Gabrielson, J.P., *et al.* (2007) Quantitation of Aggregate Levels in a Recombinant Humanized Monoclonal Antibody Formulation by Size-Exclusion Chromatography,

Asymmetrical Flow Field Flow Fractionation, and Sedimentation Velocity. *Journal of Pharmaceutical Sciences* 96, 268-279

205 Fukumoto, L.R., *et al.* (1994) Stability of Membrane-Sterilized Bovine Immunoglobulins Aseptically Added to Uht Milk. *Journal of Food Science* 59, 757-759

206 Lichan, E., *et al.* (1995) Stability of Bovine Immunoglobulins to Thermal-Treatment and Processing. *Food Research International* 28, 9-16

207 Cao, J.S., *et al.* (2007) Comparative studies on thermoresistance of protein G-binding region and antigen determinant region of immunoglobulin G in acidic colostral whey. *Food and Agricultural Immunology* 18, 17-30

208 Law, A.J.R., *et al.* (1994) Denaturation of the Whey Proteins in Heated Milk and Their Incorporation Into Cheddar Cheese. *Milchwissenschaft-Milk Science International* 49, 63-67

209 Dominguez, E., *et al.* (1997) Effect of heat treatment on the antigen-binding activity of anti-peroxidase immunoglobulins in bovine colostrum. *Journal of Dairy Science* 80, 3182-3187

210 Resmini, P., *et al.* (1989) Thermal denaturation of whey protein in pasteurized milk. *Italian Journal of Food Science* 1, 51-62

211 Lucisano, M., *et al.* (1995) Milk Pasteurization - Evaluation of Thermal-Damage. *Industrie Alimentari* 6, 185-197

212 Indyk, H.E., *et al.* (2008) Analysis of denaturation of bovine IgG by heat and high pressure using an optical biosensor. *International Dairy Journal* 18, 359-366

213 Roberts, C.J. (2003) Kinetics of irreversible protein aggregation: Analysis of extended Lumry-Eyring models and implications for predicting protein shelf life. *Journal of Physical Chemistry B* 107, 1194-1207

214 Hartmann, W.K., *et al.* (2004) Characterization and analysis of thermal denaturation of antibodies by size exclusion high-performance liquid chromatography with quadruple detection. *Analytical Biochemistry* 325, 227-239

215 Mainer, G., *et al.* (1997) Kinetic and thermodynamic parameters for heat denaturation of bovine milk IgG, IgA and IgM. *Journal of Food Science* 62, 1034-1038

216 Ma, X., *et al.* (2008) Particle size analysis of dispersed oil and oil-mineral aggregates with an automated ultraviolet epi-fluorescence microscopy system. *Environmental Technology* 29, 739-748

217 Pease, L.F., III, *et al.* (2010) Packing and size determination of colloidal nanoclusters. *Langmuir* 26, 11384-11390

218 Huang, C., *et al.* (2009) Quantitation of Protein Particles in Parenteral Solutions Using Micro-Flow Imaging. *Journal of Pharmaceutical Sciences* 98, 3058-3071

219 Rudd, P.M., *et al.* (1994) Glycoforms modify the dynamic stability and functional-activity of an enzyme. *Biochemistry* 33, 17-22

220 Rudd, P., *et al.* (2001) Glycosylation and the immune system. *Science* 291, 2370-2376

221 Dell, A. and Morris, H. (2001) Glycoprotein structure determination mass spectrometry. *Science* 291, 2351-2356

222 Chen, S., *et al.* (2007) Analysis of cell surface carbohydrate expression patterns in normal and tumorigenic human breast cell lines using lectin arrays. *Analytical Chemistry* 79, 5698-5702

223 Zangmeister, R.A., *et al.* Method of Characterizing Glycans Attached to Glycoproteins (Attorney docket number: 1109016)

224 Guha, S., *et al.* (2012) Electrospray differential mobility Analysis of Bionanoparticles. *Trends in Biotechnology* (DOI: 10.1016/j.tibtech.2012.02.003)

225 Guha, S., *et al.* (2011) Electrospray differential mobility analysis as an orthogonal tool to size exclusion chromatography for characterization of protein aggregates. *Journal of Pharmaceutical Sciences* (DOI: 10.1002/jps.23097)

226 Kim, S.H., *et al.* (2007) Understanding ion-mobility and transport properties of aerosol nanowires. *Journal of Aerosol Science* 38, 823-842

227 Chen, D. and Pui, D. (1997) Numerical modeling of the performance of differential mobility analyzers for nanometer aerosol measurements. *Journal of Aerosol Science* 28, 985-1004

228 Chen, D., *et al.* (1998) Design and evaluation of a nanometer aerosol differential mobility analyzer (Nano-DMA). *Journal of Aerosol Science* 29, 497-509

229 White, F.M. (1974) *Viscous Fluid Flow*. McGraw-Hill

230 Hanks, R.W. (1963) The laminar-turbulent transition for flow in pipes, concentric annuli, and parallel plates. *Aiche Journal* 9, 45-48